



**University of  
Nottingham**

UK | CHINA | MALAYSIA

Fundamental studies of ionic liquid  
electrolytes aiming at application in  
Na metal-based batteries

Laís Dias Ferreira, BSc.

Thesis submitted to the University of Nottingham for the degree of  
Doctor of Philosophy

August 2020

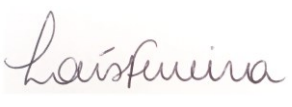


*I dedicate this thesis to the memory of my mum, the most loving, dedicated, and encouraging person I was ever lucky enough to have.*



## Declaration

This thesis is the result of my own investigations, except where otherwise stated and acknowledged by giving explicit references. This thesis has not previously been accepted in substance for any degree and is not being concurrently submitted in candidature for any degree.

Signed: 

Date: 17<sup>th</sup> August 2020



## Abstract

In this thesis, the tunability of ionic liquids was explored to design a series of ILs and evaluate the impact of different IL-based electrolytes on metallic Na electrode cells. This was done by performing a comprehensive investigation involving Na<sup>+</sup> plating/stripping and electrode surface resistance over time (resting and cycling time). In addition, a novel study of solid-electrolyte interphase (SEI) structure and composition was carried out with 3D Orbitrap™ secondary ion mass spectroscopy (3D OrbiSIMS) in depth profiling mode. The unique sensitivity and mass resolution of the 3D OrbiSIMS, and the use of an Ar cluster primary ion beam as a sputtering and analysis beam allowed us to obtain vast and detailed information relating to the nature and distribution of the SEI-products in the interphase. Consequently, we were able to accurately determine the effects of anion and cation variation on the SEI structure. This allowed us to identify key structural features to design high performing stable electrolytes for use in Na-electrode cells. It was demonstrated that the distribution of SEI-products into an organised structure is critical to achieve a stable SEI. In addition, low overpotential during Na symmetrical cycling, and stabilisation of surface resistance was achieved with the IL that demonstrated the most organised SEI structure. Furthermore, the impact of the commonly used [PF<sub>6</sub>]-based salt as an additive was also investigated. It was found that the presence of [PF<sub>6</sub>] additive improves SEI stability and cycling time of symmetrical cells. 3D OrbiSIMS studies of the SEI with the [PF<sub>6</sub>] additive revealed that the organisation of the structure of the SEI has a greater influence on the improved performance of cells than the presence of fluoride products in the SEI itself.

The designer aspect of ILs was further used to obtain electrolytes aiming for application in Na-O<sub>2</sub> cells. The fundamentals of the oxygen reduction reaction (ORR) in the ILs were thoroughly studied, and O<sub>2</sub> concentration and diffusion coefficients in new series of ILs were determined as well. It was found that [C<sub>1</sub>(C<sub>2</sub>OC<sub>1</sub>)Pyrr][NTf<sub>2</sub>] and [C<sub>1</sub>(C<sub>2</sub>OC<sub>1</sub>)Pyrr][C<sub>2</sub>F<sub>5</sub>COO] displayed high O<sub>2</sub>

solubility, whilst the higher  $O_2$  diffusion coefficients were found for  $[N_{C_1,C_1,C_2,(C_2OC_1)}][NTf_2]$  and  $[N_{C_1,C_1,C_2,C_4}][NTf_2]$ .

In the presence of  $Na^+$ , both the IL used and the concentration of  $Na^+$  seemed to influence the nature of the ORR product. It was found that with low  $Na^+$  concentration  $O_2^-$  interacted with both  $Na^+$  and IL cations in  $[N_{C_1,C_1,C_2,C_4}][NTf_2]$ ,  $[C_1(C_2OC_1)Pyrr][C_2F_5COO]$  and  $[C_1C_{dma}Pyrr][NTf_2]$ . Furthermore, multiple oxidation peaks and/or shift of the oxidation peaks over cycling were found for  $[N_{C_1,C_1,C_2,(C_2OC_1)}][NTf_2]$ ,  $[C_1C_{dma}Pyrr][NTf_2]$ ,  $[C_1(C_2OC_1)Pyrr][NTf_2]$  and  $[C_1(C_2OC_1)Pyrr][C_2F_5COO]$ . With the aid of rotating ring and disc (RRDE) studies, these peaks were suggested to be associated with formation of  $Na_xO_y$  product in solution or at the electrode surface. This was found to be significantly impacted by the H-bond ability of the IL, and  $[C_1(C_2OC_1)Pyrr][C_2F_5COO]$  displayed soluble products even at high  $Na^+$  concentration.

Finally, following the step-by-step approach of this thesis based on studies of IL electrolytes with metallic Na,  $O_2$  and  $Na^+/O_2$ , a full Na- $O_2$  cell was assembled. Assembly of a full Na- $O_2$  cell was challenging, and a brief overview is given considering the difficulties and solutions for the cell preparation. Preliminary charge and discharge profiles were obtained, and the post discharge carbon electrode was analysed by scanning electron microscopy. It was suggested that  $O_2$  diffusion in the IL electrolytes is one of the major challenges in applying IL-based electrolytes to full Na- $O_2$  cells.

## Acknowledgments

I remember one of my last meetings with Pete during my undergrad year abroad back in 2015 when he offered me to return to England to take on a PhD. I left his office feeling over the moon and I will be forever grateful to Pete for this opportunity. I also must say thanks to Darren for accepting me in his group as well and for being very welcoming. I am also grateful for the support of both my supervisors throughout my PhD, and to Darren for also teaching me what on earth an oxford comma is.

A huge thanks to Conrad, Coby and Neelam for taking their time to proofread chapters of this thesis and providing me with super helpful feedback. A big thanks to the Walsh/NAMI and Licence groups for their support throughout my project, and for making the past three years more fun. A special thanks to Astrid for her help and discussions about electrochemistry and ILs, Aki for his help with multivariate analysis, proofreading docs, and the daily early morning coffees, Calum for helping me with Matlab, Dan for the super helpful discussions and feedback, Sean for his help around the lab and the always knowledgeable discussions, Kostas for his help setting up the symmetrical cells and for sharing my frustration in preparing Na electrodes, Rory and Conrad for their help setting up Na-O<sub>2</sub> cells and the very useful discussions, Patrick, Aki and Coby for trying to keep me sane in my last months in the lab, Ze for the usual annoyance and help whenever I needed to work in the chemistry building, and Luiz for the insightful discussions and for bringing treats from Brazil. I also must thank Clive and Connor for helping me with my not so easy glassblowing requests. Thanks to David and Julie as well for embracing the challenge of running SIMS on my samples, and I am also very grateful to Dr. Gustavo Ferraz Trindade, for being so helpful with my questions about MVA.

I must also thank everyone in the Energy Storage team at Dyson, for teaching me and inspiring me so much during my placement. A special thanks to my line manager Dr. Matthew Roberts for being such an encouraging and present leader, to Dr. Liyu Jin for his guidance and input throughout the placement, and

to Dr. Alex Mansen and Dr. Duncan Smith for the excellent discussions and support.

A huge thanks also goes to my Dad, who has always fully supported me to pursue my dream of completing a PhD abroad. And most importantly, for understanding my absence in so many important days. My deepest gratitude also goes to Tio Zeca, Elenise and Tia Mirian for looking out for my Dad and giving me peace of mind despite being so far away from home.

There are still so many people that helped me in their own unique way throughout my PhD that I must also say thanks. A special thanks to those who make cold England feel like home, Jenny, Camila, Tom, Una, Meia, Steph, Ellie, Sandro, Odette and Aki. Thanks to my friends and family from home as well, Rayana, Jessica, Lucas, Marcelo e Carmen for keeping in touch despite my absence, and for being the same loving people as always. I must also thank Chloé Pissini for helping me to self-develop in uncountable ways, and for helping me to believe in myself, making sure I got to the end of this PhD.

My most special thanks go to Matt. Thank you for being my rock, for reassuring me during the toughest times, and for bringing the best out of me. And finally, thank you for proof reading so many pieces of my work, for your very logical engineering inputs, for listening to my practice talks, and not falling asleep every time I started out with that 'way too deep chemistry chat' on a Friday night.

## Abbreviations and acronyms

$C_{Na^+}$	Concentration of Na <sup>+</sup> species
$i_{lim}$	Mass transport limited current
$k^0$	Standard electrochemical rate constant
$k_{eff}^0$	Effective rate constant
$k_p^0$	Rate constant for a given process p
$m_T$	Mass transport coefficient
$\bar{\mu}$	Electrochemical potential
$\eta_E$	Overpotential
$[A]_0$	Concentration of A at the electrode surface
$[A]_{bulk}$	Concentration of A in the bulk
$\Delta G_p$	Gibbs energy barrier for a given process p
3D OrbiSIMS	3D Orbitrap™ secondary ion mass spectrometry
A	Area of electrode
$A_p$	Arrhenius constant for a given process p
$Ar_{3000}^+$	Argon cluster (3000 atoms in cluster) primary ion source
$Br^-$	Bromide
$C_{dl}$	Double layer capacitor
CE	Counter electrode
CV	Cyclic voltammogram
DME	Dimethoxy ethane
dmFc	Decamethylferrocene
DN	Donor number
DOL	1-3 dioxolane
E	Potential
$E^0$	Standard solution potential
$E^{0'}$	Formal potential
EIS	Electrochemical impedance spectroscopy
$E_{onset,red}$	Onset potential for reduction reaction
ESW	Electrochemical stability window

$F$	Faraday constant
FTIR	Fourier-transform infrared
GC	Glassy carbon
GCIB	Gas cluster ion beam
IL	Ionic liquid
$j$	Flux of species
$k_0$	Reaction rate constant
MCR	Multicurve resolution
MVA	Multivariate analysis
$n$	Number of electrons exchanged
NCA	Lithium nickel cobalt aluminium oxide
NMF	Non-negative matrix factorisation
ocv	Open circuit voltage
$Ox^+$	Oxidised species
PCA	Principal component analysis
PTFE	Polytetrafluoroethylene
qRE	Quasi-reference electrodes
$R$	Ideal gas constant
$R_{ct}$	Charge transfer resistance
RDE	Rotating disc electrode
RE	Reference electrode
$Red^-$	Reduced species
$R_{electrolyte}$	Bulk electrolyte resistance
RRDE	Rotating ring disc electrode
$R_{surface}$	Electrode surface resistance
SEI	Solid-electrolyte interphase
SIMS	Secondary ion mass spectroscopy
SS	Stainless steel
$T$	Temperature
TEGDME	Tetraethyleneglycol dimethylether
WE	Working electrode

WE2	Second working electrode
XPS	X-ray photoelectron microscopy
Z	Electrical charge
Z'	Real impedance
Z''	Imaginary impedance
$\alpha$	Charge transfer coefficient
$\beta$	Kamlet-taft hydrogen bond donating ability parameter
$\delta$	Diffusion layer
$\eta$	Dynamic viscosity
$\nu$	Kinematic viscosity
$\phi$	Electrical potential
$\phi_M$	Electrode potential
$\phi_S$	Solution potential
$\mu$	Chemical potential
$\varphi$	Phase shift
$\omega$	Rotation speed



Table of structural abbreviations of IL cations and anions

Abbreviation	Structure	Nomenclature
[EMIM]		1-ethyl-3-methyl-imidazolium
[Ac]		Acetate
[FSI]		Bis(fluoromethanesulfonyl)imide
[NTf <sub>2</sub> ]		Bis(trifluoromethanesulfonyl)imide
[DCA]		Dicyanamide
[PF <sub>6</sub> ]		Hexafluorophosphate
[N <sub>C<sub>1</sub>,C<sub>1</sub>,C<sub>2</sub>,C<sub>2</sub>(C<sub>2</sub>OC<sub>1</sub>)</sub> ]		N-(2-methoxyethyl)-N,N-dimethyl- N-ethyl-ammonium
[N <sub>C<sub>1</sub>,C<sub>1</sub>,C<sub>2</sub>,C<sub>4</sub></sub> ]		N,N-Dimethyl-N-ethyl-N-butyl- ammonium
[C <sub>1</sub> (C <sub>2</sub> OC <sub>1</sub> )Pyrr]		N-methyl-N-(2-methoxyethyl)- pyrrolidinium
[C <sub>1</sub> C <sub>dma</sub> Pyrr]		N-methyl-N-dimethylacetal- pyrrolidinium
[C <sub>2</sub> F <sub>5</sub> COO]		Pentafluoropropionate
[P <sub>6,6,6,14</sub> ]		Trihexyltetradecylphosphonium



Acknowledgments .....	vii
Abbreviations and acronyms.....	ix
Table of structural abbreviations of IL cations and anions.....	xiii
<b>1. Introduction .....</b>	<b>21</b>
1.1. Energy storage challenges and emerging alternatives.....	21
1.2. Sodium metal electrodes .....	22
1.3. Na-O <sub>2</sub> batteries.....	25
1.4. Electrolytes for electrochemical applications.....	27
1.4.1 Ionic liquids.....	29
1.5. Aims and thesis outline .....	32
1.6. References.....	33
<b>2. Review of techniques and experimental methodology.....</b>	<b>38</b>
2.1. Fundamentals of Electrochemistry .....	38
2.1.1 Electrochemical equilibrium, electron transfer and the Nernst equation .....	38
2.1.2 Electrochemical cells and electrodes: three electrode systems	42
2.1.3 Mass transport in electrochemical cells .....	43
2.1.4 The Cottrell equation .....	46
2.1.5 Kinetics of electrochemical reactions .....	47
2.1.6 Electrochemical reversibility.....	48
2.1.7 Battery cells .....	49
2.2. Electrochemical Techniques.....	51
2.2.1 Cyclic voltammetry .....	51
2.2.2 Voltammetry using microelectrodes .....	53
2.2.3 Chronoamperometry .....	55

2.2.4	Hydrodynamic techniques: rotating disc electrode and rotating ring-disc electrode .....	56
2.2.5	Electrochemical impedance spectroscopy .....	58
2.2.6	Galvanostatic cycling .....	60
2.3.	Secondary-ion mass spectrometry.....	61
2.3.1	The Orbitrap™ detector.....	63
2.4.	Multivariate analysis and the rationale for the process adopted for analysis of 3D OrbiSIMS dataset .....	66
2.5.	Characterisation techniques of ionic liquid properties .....	73
2.5.1	Viscosity .....	73
2.5.2	Donor Number .....	74
2.6.	Materials.....	74
2.7.	Synthesis and characterisation of ionic liquids .....	75
2.7.1	Synthesis of [C <sub>1</sub> (C <sub>2</sub> OC <sub>1</sub> )Pyrr]Br .....	75
2.7.2	Synthesis of [NC <sub>1</sub> ,C <sub>1</sub> ,C <sub>2</sub> ,(C <sub>2</sub> OC <sub>1</sub> )]Br.....	76
2.7.3	Synthesis of [C <sub>1</sub> C <sub>dma</sub> Pyrr]Br .....	77
2.7.4	Synthesis of [NC <sub>1</sub> ,C <sub>1</sub> ,C <sub>2</sub> ,C <sub>4</sub> ]Br .....	78
2.7.5	Synthesis of [C <sub>1</sub> (C <sub>2</sub> OC <sub>1</sub> )Pyrr][NTf <sub>2</sub> ] .....	78
2.7.6	Synthesis of [NC <sub>1</sub> ,C <sub>1</sub> ,C <sub>2</sub> ,(C <sub>2</sub> OC <sub>1</sub> )] [NTf <sub>2</sub> ] .....	79
2.7.7	Synthesis of [C <sub>1</sub> (C <sub>2</sub> OC <sub>1</sub> )Pyrr][C <sub>2</sub> F <sub>5</sub> COO] .....	80
2.7.8	Synthesis of [C <sub>1</sub> C <sub>dma</sub> Pyrr][NTf <sub>2</sub> ] .....	81
2.7.9	Synthesis of [NC <sub>1</sub> ,C <sub>1</sub> ,C <sub>2</sub> ,C <sub>4</sub> ][NTf <sub>2</sub> ] .....	81
2.8.	References.....	82
<b>3.</b>	<b>Electrochemical performance and stability of Na metal electrode with IL-based electrolytes .....</b>	<b>84</b>
3.1.	Introduction.....	84

3.2. Experimental.....	89
3.2.1 Electrolyte preparation .....	89
3.2.2 Cyclic voltammetry .....	90
3.2.3 Electrochemical impedance spectroscopy and symmetrical cell plating/stripping experiments .....	91
3.2.4 SEI composition study with 3D OrbiSIMS .....	92
3.2.5 Multivariate analysis .....	94
3.3. Electrochemical studies of electrolyte effect on Na <sup>0</sup> /Na <sup>+</sup> redox reactions.	94
3.3.1 Rationale for IL selection.....	94
3.3.2 Cyclic voltammetry of Na <sup>+</sup> containing ILs .....	96
3.4. Solid-electrolyte interphase studies with electrochemical impedance spectroscopy.....	99
3.5. Na Na symmetrical cell cycling using selected IL-based electrolytes .....	106
3.6. Na-IL solid-electrolyte interphase studies with depth profiling 3D OrbiSIMS .....	120
3.6.1 Multivariate analysis of 3D OrbiSIMS depth profile of Na-IL interphase .....	125
3.6.2 MVA study remarks, correlation to other analysis and to the original dataset. ....	139
3.7. Evaluating the role of Na[PF <sub>6</sub> ] as an additive in IL-based electrolytes: electrochemical and 3D OrbiSIMS studies.....	143
3.7.1 Effect of Na[PF <sub>6</sub> ] additive on the solid electrolyte interphase evaluated by electrochemical impedance spectroscopy .....	146
3.7.2 Effect of Na[PF <sub>6</sub> ] additive on Na Na symmetrical cell galvanostatic cycling .....	148
3.7.3 3D OrbiSIMS and MVA study of effect of Na[PF <sub>6</sub> ] additive on the Na-IL electrolyte interphase .....	151

3.8. Conclusions and future work .....	158
3.9. References .....	160
<b>4. Fundamental studies on the oxygen reduction reaction in ionic liquids</b>	
<b>167</b>	
4.1. Introduction .....	167
4.2. Experimental.....	169
4.2.1 Electrolyte preparation .....	169
4.2.2 Cyclic voltammetry and chronoamperometry.....	170
4.2.3 Hydrodynamic voltammetry .....	171
4.3. Results and discussion.....	172
4.3.1 Key properties of the ILs studied in this chapter .....	172
4.3.2 Oxygen reduction reaction in ILs .....	173
4.3.3 ORR studies with microdisc electrodes and determination of O <sub>2</sub> solubility and diffusion coefficients in ILs.....	178
4.3.4 Cyclic voltammetry under hydrodynamic conditions and study of electrode kinetics.....	185
4.3.5 Comparison of coefficients determined with Shoup-Szabo to Levich slope values.....	191
4.4. Conclusions and Future Work .....	192
4.5. References .....	194
<b>5. Oxygen reduction reaction in the presence of alkali metal cations, and an application in Na-O<sub>2</sub> cells .....</b>	<b>199</b>
5.1. Introduction .....	199
5.2. Experimental.....	202
5.2.1 Electrolyte preparation .....	202
5.2.2 Cyclic voltammetry .....	203
5.2.3 Hydrodynamic voltammetry .....	203

5.2.4	Na-O <sub>2</sub> cells and galvanostatic charge/discharge experiments	204
5.3.	Oxygen reduction reaction in the presence of alkali metal cations.....	205
5.3.1	Hydrodynamic voltammetry to investigate the type of ORR product in the presence of Na <sup>+</sup> salts .....	220
5.4.	Evaluating a potential application in Na-O <sub>2</sub> cells.....	226
5.5.	Conclusions and future work .....	231
5.6.	References.....	233
	<b>Final remarks and future work.....</b>	<b>238</b>
	References .....	240
	<b>Appendices.....</b>	<b>242</b>



# 1. Introduction

## 1.1. Energy storage challenges and emerging alternatives

According to the data published in 2017, more than half of the greenhouse gas emissions in the UK and the USA came from transportation and energy supply.<sup>1,2</sup> This clearly shows that there must be a move towards greener and renewable sources of energy to reduce greenhouse gas emissions, and to widespread electrification of transport. Nevertheless, the advancement of both these areas strongly relies on the development of energy storage systems.

Since the first Li-ion battery (LIB) was commercialised in 1991, substantial progress has been achieved, with LIBs displaying cycle life in the order of thousands and production expected to reach hundreds of GWh/year.<sup>3</sup> LIBs also power the electric vehicle (EV) with the longest driving range currently on the market, the Tesla Model S Long-Range<sup>4</sup>. Despite the remarkable progress, LIBs are not predicted to attend the demands of future battery packs with high energy content at low cost.<sup>3,5</sup> For this reason, several battery alternatives have been developed, including alkali metal negative electrodes and S-based and O<sub>2</sub>-based positive electrodes.<sup>6</sup>

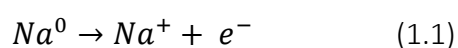
LIB cells are formed by a graphite negative electrode and a variety of metal oxides as the positive electrode and are based on the insertion and extraction of Li<sup>+</sup> into the electrodes. Although the graphite electrode allows outstanding cycling life, the weight and volume of this material considerably limit the specific energy and energy density of LIBs.<sup>3</sup> Replacing the graphite electrode with metallic lithium is expected to increase the specific energy of the cells by approximately 35% and more than double the energy density of the

cells.<sup>3</sup> Furthermore, metallic lithium is also the negative electrode of other emerging technologies such as Li-S and Li-O<sub>2</sub>.<sup>6</sup>

Na batteries have also been developed as an alternative technology to Li-ion. Metallic Na is a promising long-term electrode material with higher abundance and lower costs than Li.<sup>6</sup> This is particularly attractive as it could potentially decrease the cost of batteries. Moreover, Li reacts with Al at the negative electrode, thus in Li-metal batteries Al can only be used as the current collector at the positive electrode, whilst Cu is the current collector in the negative electrode. However, Al and Na do not react under the battery cell conditions, thus Al can also be used as the negative electrode current collector. This is remarkably advantageous from an economic and specific energy point of view, given the lower density and price of Al compared to Cu.<sup>7</sup> Similar to metallic Li, Na is the negative electrode of choice of many next generation batteries.<sup>8</sup> Therefore, the development of alkali metal electrodes is an essential step to advance next generation batteries.

### 1.2. Sodium metal electrodes

Metallic Na, and indeed metallic Li, are highly reactive electrode materials which rapidly react with atmospheric air, moisture, or the majority of solvents they are placed in. This is due to the strong tendency of these metals to oxidise and release an electron according to



The products of the reaction of Na electrode with electrolytes form the solid-electrolyte interphase (SEI). In Li-ion batteries this interphase is typically formed electrochemically on the graphite electrode during the first charge cycle. This is a consequence of the potential of the electrochemical process at the graphite electrode being outside the electrochemical stability window of electrolytes, hence causing electrolyte degradation.<sup>9</sup> Because metallic Na tends to release electrons according to equation 1.1, SEI forms even when the cell is

at open cell conditions.<sup>7</sup> Ideally, the SEI is a protective layer which prevents the flux of electrons, thus stopping further electrolyte degradation reactions, whilst having high ionic conductivity, allowing  $\text{Na}^+$  flux. Moreover, the SEI must be able to withstand volume changes, due to  $\text{Na}^+$  plating and stripping, without cracking and exposing fresh Na. Therefore, the chemical and mechanical properties of the SEI are of extreme importance for a long and stable cycling life of Na electrodes, given its importance in controlling electrolyte consumption as well as dendrite formation and growth.

The spontaneous electron transfer from Na electrodes to the electrolyte can be understood by analysing the energy of the lowest unoccupied molecular orbital (LUMO) and the highest occupied molecular orbital (HOMO) of the electrode and electrolyte. Whenever the electrode chemical potential is at higher energy than the LUMO of the electrolyte, electron transfer can take place, leading to reactions that form the SEI.<sup>7</sup> There is no established understanding of the SEI formation, however, it is believed to form via a surface growth mechanism, in which insoluble species form on the electrode surface. A study using isotope-assisted time-of-flight secondary ion mass spectrometry (SIMS) has suggested that the SEI formation occurs initially with degradation of organic components of the electrolyte, followed by reactions forming more inorganic compounds.<sup>10</sup> The authors also demonstrated that the SEI formation occurs via a bottom-up mechanism. In this mechanism, as the SEI reactions proceed, the initially formed organic layer is pushed outwards towards the bulk electrolyte as the more inorganic layer forms at the vicinity of the electrode.<sup>10</sup> Nevertheless, the study analysed SEI formation on polarized Cu electrodes, in a Cu|Li half-cell, thus some differences could be expected in the SEI formation on Na electrodes.

Another aspect that still needs further investigation is the mechanism of dendrite growth on Na electrodes. It is understood that dendrites are formed due to uneven Na plating when charging Na metal cells, more specifically when Na deposits accumulate at a single spot instead of spreading evenly across the electrode surface. Nevertheless, it is particularly difficult to avoid uneven plating and stripping reactions at the electrode because the uniformity begins on the

electrode itself, or even on the current collector. It is possible that the small protuberances in the irregular surface leads to the formation of uneven SEI and increases the ion flux towards these particular areas. Another factor that also influences dendrite growth is the morphology of the SEI layer. It is believed that in Na metals, dendrite growth occurs from the bottom of the dendrite, rather than at the tip. Consequently, dendrites are more likely to grow through parts of the SEI which are perhaps softer (mechanically), less dense or thinner.<sup>7</sup> Schematics of plating and stripping process leading to formation of dendrites and pits are shown in Figure 1.1.

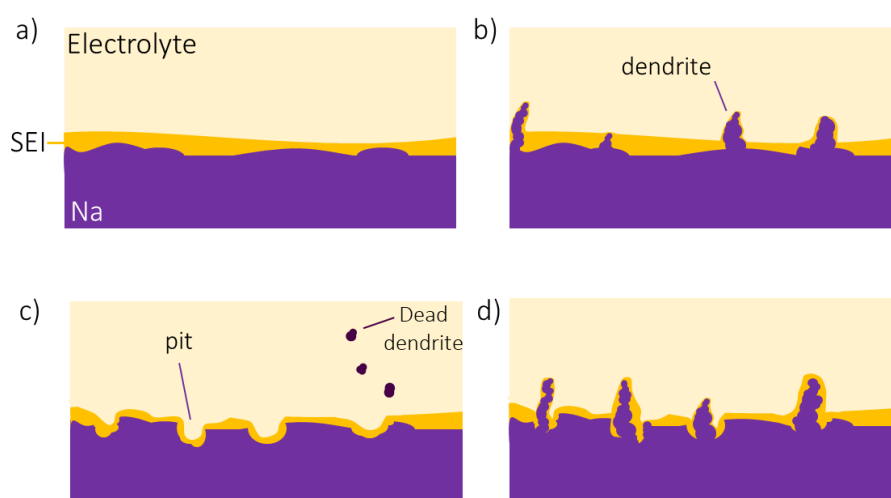


**Figure 1.1.** Schematic of plating and stripping processes in a Na electrode: a) shows uneven electrode and SEI surface, b) shows dendrite growth ( $\text{Na}^+$  plating) on the preferred electrode spots, c) shows Na metal stripping and formation of pits, showing the presence of dead dendrites and d) shows  $\text{Na}^+$  plating preferentially on pits.

The dendrite formation starts with the nucleation step, and once nuclei are formed, dendrites are more likely to grow from those nuclei than to continue nucleation. This may be attributed to the lower impedance of the thinner SEI at the nuclei compared to the already established SEI on the bulk electrode.<sup>11</sup> Hence it is easier for  $\text{Na}^+$  to cross the nuclei SEI and deposit instead of the bulk metal SEI. Moreover, the current density at the nuclei may be higher than at the bulk electrode, increasing ion flux towards these spots.

When discharging Na metal batteries,  $\text{Na}^+$  is stripped from the Na electrode, either from the bulk metal, or from the dissolution of dendrites. When stripping occurs directly from the bulk, pits are formed on the surface where  $\text{Na}^+$  is stripped (see Figure 1.1c). The size and distribution of pits are particularly important, as on the subsequent cycle dendrites are likely to nucleate on the pits first and then on the bulk metal (see Figure 1.1d).<sup>11</sup> If dendrites are already formed at the electrode surface,  $\text{Na}^+$  stripping occurs initially from the dendrites. Uneven stripping from the dendrites causes parts of the dendrite to disconnect from the Na electrode, forming the so-called dead dendrite, or dead Na (see Figure 1.1b and c).<sup>12, 13</sup> This has also been referred to as orphaning of dendrites.<sup>13</sup> Besides losing active material, the formation of dead dendrites can hinder ion transport across the cell due to accumulation of dead dendrites at the electrode surface.<sup>14</sup>

Several strategies have been described in literature to tackle the challenges associated with dendrite formation and unstable SEI when using Na metal electrodes, and these have been reviewed by several authors in the past year.<sup>7, 8, 15-20</sup> In summary, remarkable effort has been put into finding a suitable electrolyte that leads to stable SEI formation, which will be further discussed in Section 1.4. In addition, other methods involve the formation of an artificial SEI and modification of the surface area of the electrode, thoroughly described in the reviews mentioned above.

### 1.3. Na-O<sub>2</sub> batteries

Among the emerging battery technologies using alkali metal electrodes, O<sub>2</sub> batteries draw significant attention because of their high theoretical energy densities. Li-O<sub>2</sub> batteries for instance, have theoretical specific energy of approximately 3505 Wh/kg (based on mass of Li<sub>2</sub>O<sub>2</sub>),<sup>21-23</sup> much higher than the typical 150 Wh/kg of a typical Li-ion cell or even 250 Wh/kg of a prospective Li-metal cell.<sup>3</sup> Remarkable progress has been achieved in Li-O<sub>2</sub> systems, and this has been recently reviewed.<sup>5, 23</sup> Considerable research effort has also been put

into Na-O<sub>2</sub> cells.<sup>20, 24, 25</sup> Na-O<sub>2</sub> are particularly interesting not only because of the lower cost and higher abundance of Na metal as mentioned above, but also because of the lower cell overpotential compared to Li-O<sub>2</sub>, and potentially higher coulombic efficiency.<sup>24</sup>

A schematic of a Na-O<sub>2</sub> battery cell is displayed in Figure 1.2. Na-O<sub>2</sub> batteries are composed of a metallic Na negative electrode and a positive electrode typically consisting of a conductive porous carbon material. As described in the previous section, during the discharge of the cells Na<sup>+</sup> is stripped from the Na electrode and Na plating takes place during the charge cycle. The positive electrode reactions are based on the oxygen reduction reaction (ORR), which in the presence of Na<sup>+</sup> rich electrolyte, forms Na<sub>x</sub>O<sub>y</sub> discharge products. The opposite reaction occurs during cell charging, with oxidation of Na<sub>x</sub>O<sub>y</sub> and O<sub>2</sub> evolution.

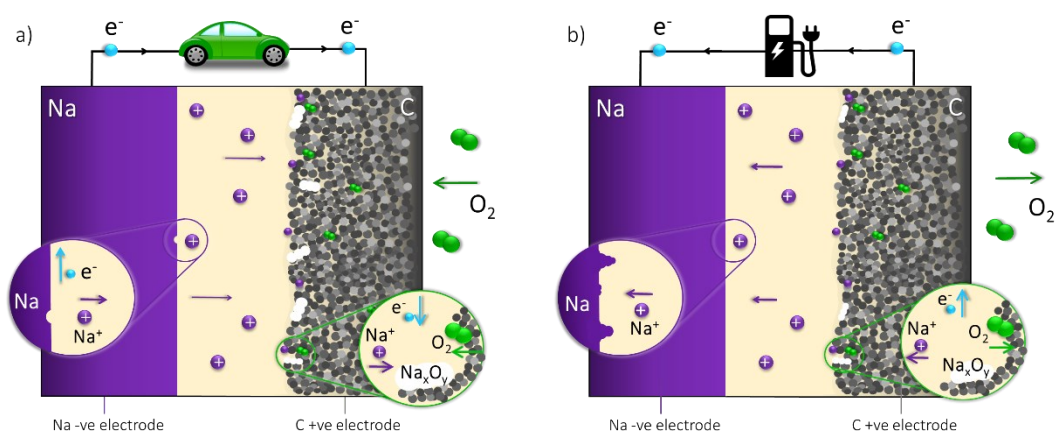


**Figure 1.2.** Schematic configuration of Na-O<sub>2</sub> cells: a) discharge step showing Na oxidation at the negative (-ve) electrode, and O<sub>2</sub> diffusion into the cell followed by O<sub>2</sub> reduction and formation of Na<sub>x</sub>O<sub>y</sub> species at the positive (+ve) electrode; b) charge step showing O<sub>2</sub> evolution at the +ve electrode and Na plating at the -ve electrode.

Unlike Li-O<sub>2</sub>, in Na-O<sub>2</sub> cells NaO<sub>2</sub> is the discharge product reported in the majority of the studies in literature.<sup>26</sup> This is due to the higher stability of NaO<sub>2</sub> compared to LiO<sub>2</sub>, in which the very hard acid Li does not form a stable compound with the softer O<sub>2</sub><sup>-</sup> base. Thus, the softer character of Na<sup>+</sup> forms a stable NaO<sub>2</sub> with the softer O<sub>2</sub><sup>-</sup>, and NaO<sub>2</sub> does not necessarily undergo

chemical disproportionation to  $\text{Na}_2\text{O}_2$ .  $\text{NaO}_2$  is formed via a one-electron reduction of  $\text{O}_2$ , and it is believed that  $\text{NaO}_2$  is formed via a solution-mediated mechanism, in which  $\text{NaO}_2$  is found in solution as contact ion-pairs and precipitates at the electrode surface when the solution reaches saturation, according to:



This has recently been observed via operando transmission electron microscopy using a microbattery setup.<sup>27</sup> Moreover, the authors suggested that there is an equilibrium between  $\text{NaO}_2$  in solution and  $\text{NaO}_2$  at the electrode surface, and during charge the oxidation of  $\text{NaO}_2$  in solution shifts the equilibrium towards formation of the product in solution. Consequently, the charge process does not occur directly via an electron transfer to the solid  $\text{NaO}_2$ , but instead via a solution mechanism.<sup>27</sup>

Despite the promising improved cycling ability of Na- $\text{O}_2$  batteries due to lower overpotentials than Li- $\text{O}_2$ , significant capacity losses have been observed over long-term cycling.<sup>27</sup> This is believed to be associated with parasitic reactions involving the discharge products and the electrode or electrolyte. Therefore, research effort must focus on optimising these cell components, and some strategies have been reviewed recently.<sup>20</sup> This includes improved design of porous electrodes, in terms of materials and morphology, use of additives and development of more stable electrolyte systems. The latter is further discussed in the following section.

## 1.4. Electrolytes for electrochemical applications

The development of an electrolyte that has led to formation of a stable SEI and with minimum degradation over cycling was a crucial step in the advancement of Li-ion batteries. As discussed in the sections above, finding an electrolyte suitable for application in emerging battery technologies is still an ongoing challenge. Although promising reports have been published, which are

## Chapter 1

described in the following paragraphs, the long list of requirements that these electrolytes must meet makes it very challenging to find a suitable candidate. In Na-O<sub>2</sub> batteries, for instance, the electrolyte must not only form a protective, uniform and ion conductive SEI layer on Na, but also display high O<sub>2</sub> diffusion, promote NaO<sub>2</sub> formation preferably via a solution mechanism, and be stable against parasitic reactions with Na-O<sub>2</sub> discharge products. The next paragraphs highlight a few reports in electrolyte design, however a comprehensive overview of the developments to date can be found in several reviews.<sup>15, 19, 20, 24, 28</sup>

Typical electrolytes used in Li-ion technologies, as carbonate solvents, have long been described to be unstable in O<sub>2</sub> cells due to O<sub>2</sub><sup>-</sup> nucleophilic attack,<sup>29</sup> meaning electrolytes based on other solvents must be developed. Previous work described the effect of the solvent donating ability on the discharge mechanism and capacity of Li-O<sub>2</sub> cells.<sup>30</sup> The authors suggested that solvents with high donor number (DN) promote the growth of the Li<sub>2</sub>O<sub>2</sub> discharge product in solution, leading to cells with higher capacity than solvents with low DN. Likewise, the DN of the solvents also has an impact in the mechanism of discharge and on the discharge product in Na-O<sub>2</sub> systems.<sup>31</sup> Aldous and Hardwick observed Na<sub>2</sub>O<sub>2</sub> formation using low DN electrolytes, and suggested that in the absence of Na<sup>+</sup> solvation by the solvent (low DN), discharge occurs via a surface mechanism through which O<sub>2</sub> is further reduced forming Na<sub>2</sub>O<sub>2</sub>. When using high DN solvents, the authors found that NaO<sub>2</sub> was formed via a solution mediated process.<sup>31</sup>

Furthermore, in Na-O<sub>2</sub> cells, dimethoxy ethane (DME) has demonstrated superior discharge capacity compared to tetraethylene glycol dimethyl ether (TEGME), despite higher solubility of NaO<sub>2</sub> in TEGME. This has been attributed to the formation of surface confined NaO<sub>2</sub> in TEGME caused by a higher desolvation barrier in this electrolyte.<sup>32</sup> However, a later study<sup>27</sup> suggested DME suffers parasitic reactions during cell cycling, forming a parasitic layer around the NaO<sub>2</sub> discharge product. Because this layer persists in the electrode surface, it significantly decreases the capacity of the subsequent cycles.

Regarding SEI formation in Na electrodes, a previous study using DME with various types of salts found superior SEI stability with NaPF<sub>6</sub>, whilst Na[NTf<sub>2</sub>] displayed high electrolyte consumption and degradation.<sup>33</sup> The authors associated this finding to a higher concentration of fluoride in the SEI layer when using Na[PF<sub>6</sub>], and this has been described to improve the SEI stability. In fact, other studies have highlighted the positive impact fluoride has on the formation of a stable SEI.<sup>12, 15, 34, 35</sup> Despite several studies suggesting that high fluoride content is essential for a stable SEI, other authors have found better cell performance with fluoride-free electrolytes. Doi *et al*<sup>36</sup> compared the cell performance of Na[PF<sub>6</sub>]-containing electrolytes with electrolytes containing sodium tetrphenylborate (Na[BPh<sub>4</sub>]). The authors found that the Na[BPh<sub>4</sub>]-based electrolyte displayed high coulombic efficiency over 300 cycles of plating and stripping in Na|Na symmetrical cells, with lower overpotential than Na[PF<sub>6</sub>] equivalent electrolytes. Therefore, this demonstrates that although fluoride content seems to be beneficial to achieve a stable SEI, there must be different alternatives to achieve a stable Na cycling, other than simply a fluoride-rich SEI.

Interestingly, many ionic liquids (ILs) are based on the ions discussed in the paragraph above. ILs are a very particular type of electrolyte which have also been evaluated for application in emerging battery technologies. This will be discussed further in the following section.

### 1.4.1 Ionic liquids

Ionic liquids (ILs) are a class of salts with low melting point, with 100 °C being a typical melting temperature to differentiate ILs to molten salts. An extensively studied class of ILs are room temperature ionic liquids (RTILs) which display melting points below 25 °C. Unlike conventional salts, RTILs are mostly comprised of unsymmetrical and bulky ions. Consequently, ILs display lower coulombic interaction and lower lattice energy than typical salts, hence lower melting points.

## Chapter 1

ILs have unique physicochemical properties which attract attention from researchers in a range of fields.<sup>37</sup> Undoubtedly one of their most outstanding properties is the negligible volatility. This is the reason ILs have been referred as green solvents, avoiding the use of volatile organic compounds in certain applications.<sup>38</sup> The low volatility and non-flammability of ILs are particularly attractive properties from a safety point of view. In battery applications, typically used organic electrolytes increase the risk of fires/explosions due to short-circuits and thermal runaways. This is especially important considering large battery packs and electric vehicles applications. The use of non-flammable electrolytes like ILs can have a significant contribution to the overall safety of the cell.<sup>39</sup>

Another remarkable characteristic of ILs is their tunability, a consequence of the innumerable choice of cation and anion pairs, as well as the possibility of attach different side chains to the cations. For this reason, ILs are often called designer solvents, as small changes in the IL structures may lead to distinct solvent properties. This has been explored in several fields such as electrosynthesis,<sup>40</sup> analytical chemistry,<sup>41</sup> and heavy metal extraction.<sup>42</sup>

The ORR has been extensively studied in ILs, and more recently the effect of adding alkali metal cations has also been evaluated.<sup>43-51</sup> Abraham and co-workers have studied the ORR in the presence of  $\text{Li}^+$ ,  $\text{Na}^+$  and  $\text{K}^+$ , in pyrrolidinium and imidazolium ILs. With the aid of electrochemical techniques and a NMR study on the Lewis acidity of cations in solutions, the authors suggested that the ORR products can be understood in terms of hard soft acid base theory.<sup>52</sup>

Tena-Zaera and co-workers have thoroughly investigated  $\text{Na}^+$  and  $\text{O}_2$  electrochemical reactions in  $[\text{C}_1\text{C}_4\text{Pyrr}][\text{NTf}_2]$ .<sup>53</sup> The authors suggested that the salt concentration in the ILs can determine whether the reaction occurs via a solution mechanism or via a surface mechanism. The authors found that the potential of the anodic peaks varied as the salt content was modified. The position of the anodic peaks was associated with the type of reaction mechanism, with the less positive potentials related to oxidation of  $\text{NaO}_2$  in

solution, whilst the oxidation of surface  $\text{NaO}_2$  products occurred at more positive potentials.<sup>53</sup>

Forsyth, Pozo-Gonzalo and co-workers have been pioneers in developing full Na- $\text{O}_2$  cells with purely IL based electrolytes.<sup>54, 55</sup> The authors evaluated the impact of Na salts in the discharge capacity and cycling ability of Na- $\text{O}_2$  cells with  $[\text{C}_1\text{C}_4\text{Pyrr}][\text{NTf}_2]$ -based electrolyte. It was suggested that different salt concentrations affect the  $\text{O}_2^-$  solvation structure,<sup>54</sup> and that concentrated electrolytes enhance the performance of Na- $\text{O}_2$  cells.<sup>55</sup>

To the best of our knowledge, studies of Na electrodes and IL electrolytes are scarce in literature.<sup>35, 39, 56, 57</sup> Nevertheless, a previous study evaluated the stability of Na metal in ILs. X-ray photoelectron spectroscopy (XPS) over a range of etching times was used to study the stability of the Na SEI, and the authors suggested that the SEI formed with  $[\text{C}_1\text{C}_2\text{Im}][\text{NTf}_2]$  was thicker than in  $[\text{C}_1\text{C}_2\text{Im}][\text{FSI}]$ . This was also confirmed by a higher surface resistance observed by electrochemical impedance spectroscopy studies.<sup>57</sup> In addition, another study<sup>35</sup> demonstrated that IL electrolyte with Na[FSI] displayed the lowest overpotential during Na|Na symmetrical cycling. The study evaluated the impact of the type of salt in a  $[\text{C}_1\text{C}_4\text{Pyrr}][\text{DCA}]$ -based electrolyte on cell cycling, electrode surface resistance over time, and on the structure of the SEI.<sup>35</sup>

Finally, an insightful report using atomic force microscopy recently evaluated the structure of the interphase of concentrated Na- $[\text{C}_1\text{C}_3\text{Pyrr}][\text{FSI}]$  electrolyte with a gold electrode.<sup>56</sup> With the aid of molecular dynamics, the study successfully demonstrated that as the Na concentration is increased,  $\text{Na}^+$  aggregates replace ILs at the innermost layers, creating an organised structure of  $\text{Na}_x[\text{FSI}]_y$  species located at the vicinity of the electrode.

Despite the reports described above, there are innumerable cation-anion combinations yet to be explored as electrolytes in emerging battery technologies. Furthermore, finding a suitable electrolyte for both Na- $\text{O}_2$  and other Na-metal based technologies is still an ongoing challenge, given the requirements described throughout this introduction. Therefore, we aim to

investigate whether different cation and anion combinations could be suitable candidates for electrolytes in emerging battery technologies.

### 1.5. Aims and thesis outline

Considering the unique properties of ILs described in the sections above, the overall aim of this thesis is to explore whether the tunability of ILs can affect the performance of electrolytes for emerging battery technologies with Na metal electrodes, with emphasis on Na-O<sub>2</sub> systems. The approach taken in this thesis is to study each element individually due to the complexity of Na-O<sub>2</sub> systems, This is detailed as follows:

- Chapter 3 discusses the Na-IL system, evaluating whether ILs can form a stable SEI with Na metal, and whether Na cells can be cycled with low overpotentials. This chapter also studies the composition and structure of the SEI using a novel methodology;
- Chapter 4 evaluates the fundamental aspects of the O<sub>2</sub> electrochemical reaction in ILs, obtaining mass transport information using a range of electrochemical techniques. This includes determination of solubility and diffusion coefficients of O<sub>2</sub> in the synthesised ILs, and hydrodynamic studies using rotating disc electrodes;
- Chapter 5 studies the ORR in the presence of Na<sup>+</sup> in the range of ILs discussed in Chapters 3 and 4. The type of IL and the concentration of Na<sup>+</sup> salts are evaluated, as well as the impact of these two variables in the solubility of the product of the ORR in the presence of Na<sup>+</sup>. This chapter also displays preliminary results of full Na-O<sub>2</sub> cells using selected IL electrolytes.

In addition, each chapter described above offers a brief introduction highlighting the fundamental aspects and the state of art of each individual system. The techniques used in this thesis and the synthesis of the studied ILs are thoroughly described in Chapter 2.

## 1.6. References

1. Waite, C. Final UK greenhouse gas emissions national statistics. <https://data.gov.uk/dataset/final-uk-greenhouse-gas-emissions-national-statistics> (accessed 27/07/2020).
2. Desai, M.; Camobreco, V. Sources of Greenhouse Gas Emissions. <https://www.epa.gov/ghgemissions/sources-greenhouse-gas-emissions> (accessed 27/07/2020).
3. Albertus, P.; Babinec, S.; Litzelman, S.; Newman, A., Status and challenges in enabling the lithium metal electrode for high-energy and low-cost rechargeable batteries. *Nat. Energy* **2017**, *3* (1), 16-21.
4. Charlton, A. The longest range electric cars of 2020: new EVs with the most charge. <https://www.carmagazine.co.uk/electric/longest-range-electric-cars-ev/> (accessed 25/07/2020).
5. Kwak, W. J.; Rosy, Sharon, D.; Xia, C.; Kim, H.; Johnson, L. R.; Bruce, P. G.; Nazar, L. F.; Sun, Y. K.; Frimer, A. A.; Noked, M.; Freunberger, S. A.; Aurbach, D., Lithium–Oxygen Batteries and Related Systems: Potential, Status, and Future. *Chem. Rev.* **2020**.
6. Sapunkov, O.; Pande, V.; Khetan, A.; Choomwattana, C.; Viswanathan, V., Quantifying the promise of ‘beyond’ Li–ion batteries. *Transl. Mater. Res.* **2015**, *2* (4), 045002.
7. Lee, B.; Paek, E.; Mitlin, D.; Lee, S. W., Sodium Metal Anodes: Emerging Solutions to Dendrite Growth. *Chem. Rev.* **2019**, *119* (8), 5416-5460.
8. Zheng, X.; Bommier, C.; Luo, W.; Jiang, L.; Hao, Y.; Huang, Y., Sodium metal anodes for room-temperature sodium-ion batteries: Applications, challenges and solutions. *Energy Stor. Mater.* **2019**, *16*, 6-23.
9. Berg, H., Lithium battery materials. In *Batteries for Electric Vehicles: Materials and Electrochemistry*, Cambridge University Press: Cambridge, 2015; pp 83-125.
10. Liu, Z.; Lu, P.; Zhang, Q.; Xiao, X.; Qi, Y.; Chen, L. Q., A Bottom-Up Formation Mechanism of Solid Electrolyte Interphase Revealed by Isotope-Assisted Time-of-Flight Secondary Ion Mass Spectrometry. *J. Phys. Chem. Lett.* **2018**, *9* (18), 5508-5514.
11. Wood, K. N.; Kazyak, E.; Chadwick, A. F.; Chen, K.-H.; Zhang, J.-G.; Thornton, K.; Dasgupta, N. P., Dendrites and Pits: Untangling the Complex Behavior of Lithium Metal Anodes through Operando Video Microscopy. *ACS Cent. Sci.* **2016**, *2* (11), 790-801.
12. Rodriguez, R.; Loeffler, K. E.; Nathan, S. S.; Sheavly, J. K.; Dolocan, A.; Heller, A.; Mullins, C. B., In Situ Optical Imaging of Sodium Electrodeposition: Effects of Fluoroethylene Carbonate. *ACS Energy Lett.* **2017**, *2* (9), 2051-2057.
13. Deng, Y.; Zheng, J.; Warren, A.; Yin, J.; Choudhury, S.; Biswal, P.; Zhang, D.; Archer, L. A., On the Reversibility and Fragility of Sodium Metal Electrodes. *Adv. Energy Mater.* **2019**, *9* (39).
14. Chen, K.-H.; Wood, K. N.; Kazyak, E.; LePage, W. S.; Davis, A. L.; Sanchez, A. J.; Dasgupta, N. P., Dead lithium: mass transport effects on voltage,

capacity, and failure of lithium metal anodes. *J. Mater. Chem. A* **2017**, *5* (23), 11671-11681.

15. Matios, E.; Wang, H.; Wang, C.; Li, W., Enabling Safe Sodium Metal Batteries by Solid Electrolyte Interphase Engineering: A Review. *Ind. Eng. Chem. Res.* **2019**, *58* (23), 9758-9780.

16. Wang, H.; Yu, D.; Kuang, C.; Cheng, L.; Li, W.; Feng, X.; Zhang, Z.; Zhang, X.; Zhang, Y., Alkali Metal Anodes for Rechargeable Batteries. *Chem* **2019**, *5* (2), 313-338.

17. Wang, Y.; Wang, Y.; Wang, Y.; Feng, X.; Chen, W.; Ai, X.; Yang, H.; Cao, Y., Developments and Perspectives on Emerging High-Energy-Density Sodium-Metal Batteries. *Chem* **2019**, *5* (10), 2547-2570.

18. Ma, L. B.; Cui, J.; Yao, S.; Liu, X.; Luo, Y.; Shen, X.; Kim, J., Dendrite-free lithium metal and sodium metal batteries. *Energy Stor. Mater.* **2020**, *27*, 522-554.

19. Sun, B.; Xiong, P.; Maitra, U.; Langsdorf, D.; Yan, K.; Wang, C.; Janek, J.; Schroder, D.; Wang, G., Design Strategies to Enable the Efficient Use of Sodium Metal Anodes in High-Energy Batteries. *Adv. Mater.* **2020**, *32* (18), e1903891.

20. Yadegari, H.; Sun, X., Sodium–Oxygen Batteries: Recent Developments and Remaining Challenges. *Trends Chem.* **2020**, *2* (3), 241-253.

21. Bruce, P. G.; Freunberger, S. A.; Hardwick, L. J.; Tarascon, J., Li–O<sub>2</sub> and Li–S batteries with high energy storage. *Nat. Mat.* **2012**, *11* (1), 19-29.

22. Shen, X.; Liu, H.; Cheng, X.-B.; Yan, C.; Huang, J.-Q., Beyond lithium ion batteries: Higher energy density battery systems based on lithium metal anodes. *Energy Storage Materials* **2018**, *12*, 161-175.

23. Liu, T.; Vivek, J. P.; Zhao, E. W.; Lei, J.; Garcia-Araez, N.; Grey, C. P., Current Challenges and Routes Forward for Nonaqueous Lithium–Air Batteries. *Chem. Rev.* **2020**.

24. Landa-Medrano, I.; Li, C.; Ortiz-Vitoriano, N.; Ruiz de Larramendi, I.; Carrasco, J.; Rojo, T., Sodium-Oxygen Battery: Steps Toward Reality. *J. Phys. Chem. Lett.* **2016**, *7* (7), 1161-6.

25. Das, S. K.; Lau, S.; Archer, L. A., Sodium–oxygen batteries: a new class of metal–air batteries. *J. Mater. Chem. A* **2014**, *2* (32), 12623-12629.

26. Bender, C. L.; Schroder, D.; Pinedo, R.; Adelhelm, P.; Janek, J., One- or Two-Electron Transfer? The Ambiguous Nature of the Discharge Products in Sodium-Oxygen Batteries. *Angew. Chem.* **2016**, *55* (15), 4640-9.

27. Lutz, L.; Dachraoui, W.; Demortiere, A.; Johnson, L. R.; Bruce, P. G.; Grimaud, A.; Tarascon, J. M., Operando Monitoring of the Solution-Mediated Discharge and Charge Processes in a Na-O<sub>2</sub> Battery Using Liquid-Electrochemical Transmission Electron Microscopy. *Nano Lett.* **2018**, *18* (2), 1280-1289.

28. Zhao, N.; Guo, X., Cell Chemistry of Sodium–Oxygen Batteries with Various Nonaqueous Electrolytes. *J. Phys. Chem. C* **2015**, *119* (45), 25319-25326.

29. Balaish, M.; Kraytsberg, A.; Ein-Eli, Y., A critical review on lithium-air battery electrolytes. *Phys. Chem. Chem. Phys.* **2014**, *16* (7), 2801-22.

30. Johnson, L.; Li, C.; Liu, Z.; Chen, Y.; Freunberger, S. A.; Ashok, P. C.; Praveen, B. B.; Dholakia, K.; Tarascon, J. M.; Bruce, P. G., The role of LiO<sub>2</sub>

solubility in O<sub>2</sub> reduction in aprotic solvents and its consequences for Li-O<sub>2</sub> batteries. *Nat. Chem.* **2014**, *6* (12), 1091-9.

31. Aldous, I. M.; Hardwick, L. J., Solvent-Mediated Control of the Electrochemical Discharge Products of Non-Aqueous Sodium-Oxygen Electrochemistry. *Angew. Chem. Int. Ed. Engl.* **2016**, *55* (29), 8254-7.

32. Lutz, L.; Yin, W.; Grimaud, A.; Alves Dalla Corte, D.; Tang, M.; Johnson, L.; Azaceta, E.; Sarou-Kanian, V.; Naylor, A. J.; Hamad, S.; Anta, J. A.; Salager, E.; Tena-Zaera, R.; Bruce, P. G.; Tarascon, J. M., High Capacity Na-O<sub>2</sub> Batteries: Key Parameters for Solution-Mediated Discharge. *J. Phys. Chem. C* **2016**, *120* (36), 20068-20076.

33. Lutz, L.; Alves Dalla Corte, D.; Tang, M.; Salager, E.; Deschamps, M.; Grimaud, A.; Johnson, L.; Bruce, P. G.; Tarascon, J.-M., Role of Electrolyte Anions in the Na-O<sub>2</sub> Battery: Implications for NaO<sub>2</sub> Solvation and the Stability of the Sodium Solid Electrolyte Interphase in Glyme Ethers. *Chem. Mater.* **2017**, *29* (14), 6066-6075.

34. Seh, Z. W.; Sun, J.; Sun, Y.; Cui, Y., A Highly Reversible Room-Temperature Sodium Metal Anode. *ACS Cent. Sci.* **2015**, *1* (8), 449-55.

35. Forsyth, M.; Hilder, M.; Zhang, Y.; Chen, F.; Carre, L.; Rakov, D. A.; Armand, M.; Macfarlane, D. R.; Pozo-Gonzalo, C.; Howlett, P. C., Tuning Sodium Interfacial Chemistry with Mixed-Anion Ionic Liquid Electrolytes. *ACS Appl. Mater. Interfaces* **2019**, *11* (46), 43093-43106.

36. Doi, K.; Yamada, Y.; Okoshi, M.; Ono, J.; Chou, C. P.; Nakai, H.; Yamada, A., Reversible Sodium Metal Electrodes: Is Fluorine an Essential Interphasial Component? *Angew. Chem. Int. Ed. Engl.* **2019**, *58* (24), 8024-8028.

37. Singh, S. K.; Savoy, A. W., Ionic liquids synthesis and applications: An overview. *J. Mol. Liq.* **2020**, *297*, 112038.

38. Earle, M. J.; Seddon, K. R., Ionic Liquids: Green Solvents for the Future. In *Clean Solvents*, American Chemical Society: 2002; Vol. 819, pp 10-25.

39. Sun, H.; Zhu, G.; Xu, X.; Liao, M.; Li, Y.; Angell, M.; Gu, M.; Zhu, Y.; Hung, W.; Li, J.; Kuang, Y.; Meng, Y.; Lin, M.; Peng, H.; Dai, H., A safe and non-flammable sodium metal battery based on an ionic liquid electrolyte. *Nat. Commun.* **2019**, *10* (1), 3302.

40. Delorme, A.; Sans, V.; Licence, P.; Walsh, D. A., Tuning the Reactivity of TEMPO during Electrocatalytic Alcohol Oxidations in Room-Temperature Ionic Liquids. *ACS Sust. Chem. Eng.* **2019**, *7*.

41. Anderson, J. L.; Clark, K. D., Ionic liquids as tunable materials in (bio)analytical chemistry. *Anal. Bioanal. Chem.* **2018**, *410* (19), 4565-4566.

42. Chen, Z.; Zhang, S., Extraction of Heavy Metal Ions Using Ionic Liquids. In *Encyclopedia of Ionic Liquids*, Zhang, S., Ed. Springer Singapore: Singapore, 2019; pp 1-8.

43. Zhang, Y.; Pozo-Gonzalo, C., Variations and applications of the oxygen reduction reaction in ionic liquids. *Chem. Commun.* **2018**, *54* (31), 3800-3810.

44. Pozo-Gonzalo, C., Oxygen Reduction Reaction in Ionic Liquids: An Overview. In *Electrochemistry in Ionic Liquids: Volume 2: Applications*, Torriero, A. A. J., Ed. Springer International Publishing: Cham, 2015; pp 507-529.

45. Walsh, D. A.; Goodwin, S., The Oxygen Reduction Reaction in Room-Temperature Ionic Liquids. In *Encyclopedia of Interfacial Chemistry*, Wandelt, K., Ed. Elsevier: Oxford, 2018; Vol. 5.2, pp 898-907.
46. Pozo-Gonzalo, C.; Howlett, P. C.; MacFarlane, D. R.; Forsyth, M., Highly reversible oxygen to superoxide redox reaction in a sodium-containing ionic liquid. *Electrochem. Commun.* **2017**, *74*, 14-18.
47. Galiote, N. A.; Jeong, S.; Morais, W. G.; Passerini, S.; Huguenin, F., The Role of Ionic Liquid in Oxygen Reduction Reaction for Lithium-air Batteries. *Electrochim. Acta* **2017**, *247*, 610-616.
48. Monaco, S.; Arangio, A. M.; Soavi, F.; Mastragostino, M.; Paillard, E.; Passerini, S., An electrochemical study of oxygen reduction in pyrrolidinium-based ionic liquids for lithium/oxygen batteries. *Electrochim. Acta* **2012**, *83*, 94-104.
49. Elia, G. A.; Hassoun, J.; Kwak, W. J.; Sun, Y. K.; Scrosati, B.; Mueller, F.; Bresser, D.; Passerini, S.; Oberhumer, P.; Tsiouvaras, N.; Reiter, J., An advanced lithium-air battery exploiting an ionic liquid-based electrolyte. *Nano Lett.* **2014**, *14* (11), 6572-7.
50. De Giorgio, F., Soavi, F., Mastragostino, M., Effect of lithium ions on oxygen reduction in ionic liquid-based electrolytes. *Electrochem. Commun.* **2011**, *13*, 3.
51. Soavi, F.; Monaco, S.; Mastragostino, M., Catalyst-free porous carbon cathode and ionic liquid for high efficiency, rechargeable Li/O<sub>2</sub> battery. *J. Power Sources* **2013**, *224*, 115-119.
52. Allen, C. J.; Hwang, J.; Kautz, R.; Mukerjee, S.; Plichta, E. J.; Hendrickson, M. A.; Abraham, K. M., Oxygen Reduction Reactions in Ionic Liquids and the Formulation of a General ORR Mechanism for Li-Air Batteries. *J. Phys. Chem. C* **2012**, *116* (39), 20755-20764.
53. Azaceta, E.; Lutz, L.; Grimaud, A.; Vicent-Luna, J. M.; Hamad, S.; Yate, L.; Cabanero, G.; Grande, H. J.; Anta, J. A.; Tarascon, J. M.; Tena-Zaera, R., Electrochemical Reduction of Oxygen in Aprotic Ionic Liquids Containing Metal Cations: A Case Study on the Na-O<sub>2</sub> system. *ChemSusChem* **2017**, *10* (7), 1616-1623.
54. Pozo-Gonzalo, C.; Johnson, L. R.; Jónsson, E.; Holc, C.; Kerr, R.; MacFarlane, D. R.; Bruce, P. G.; Howlett, P. C.; Forsyth, M., Understanding of the Electrogenerated Bulk Electrolyte Species in Sodium-Containing Ionic Liquid Electrolytes During the Oxygen Reduction Reaction. *J. Phys. Chem. C* **2017**, *121* (42), 23307-23316.
55. Zhang, Y.; Ortiz-Vitoriano, N.; Acebedo, B.; O'Dell, L.; MacFarlane, D. R.; Rojo, T.; Forsyth, M.; Howlett, P. C.; Pozo-Gonzalo, C., Elucidating the Impact of Sodium Salt Concentration on the Cathode-Electrolyte Interface of Na-Air Batteries. *J. Phys. Chem. C* **2018**, *122* (27), 15276-15286.
56. Rakov, D. A.; Chen, F.; Ferdousi, S. A.; Li, H.; Pathirana, T.; Simonov, A. N.; Howlett, P. C.; Atkin, R.; Forsyth, M., Engineering high-energy-density sodium battery anodes for improved cycling with superconcentrated ionic-liquid electrolytes. *Nat. Mater.* **2020**.
57. Hosokawa, T.; Matsumoto, K.; Nohira, T.; Hagiwara, R.; Fukunaga, A.; Sakai, S.; Nitta, K., Stability of Ionic Liquids against Sodium Metal: A Comparative

## Chapter 1

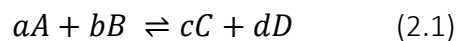
Study of 1-Ethyl-3-methylimidazolium Ionic Liquids with Bis(fluorosulfonyl)amide and Bis(trifluoromethylsulfonyl)amide. *J. Phys. Chem. C* **2016**, *120* (18), 9628-9636.

## 2. Review of techniques and experimental methodology

### 2.1. Fundamentals of Electrochemistry

#### 2.1.1 Electrochemical equilibrium, electron transfer and the Nernst equation

From thermodynamics, it is known that the minimal Gibbs energy for a given chemical reaction is achieved at its equilibrium. By minimising the Gibbs energy of a chemical system ( $dG = 0$ ), the gain in energy by forming the products is equal to the loss in energy by consuming the reactants. If this were not true, then the energy of the system could still be lowered by either consuming more reactants or reacting the products back. In addition, under constant pressure and temperature, the changes in the Gibbs energy ( $dG$ ) are dictated by the chemical potential of each species in the system, Therefore, a generic chemical reaction such as:



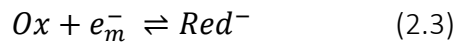
achieves equilibrium when:

$$c\mu_C dn + d\mu_D dn = a\mu_A dn + b\mu_B dn \quad (2.2)$$

where  $\mu$  is the chemical potential of A, B, C or D (with their respective stoichiometric coefficients a, b, c or d).

Similarly, equilibrium is also attained in electrochemical systems by minimising the Gibbs free energy, however it takes place at the electrode surface, and includes not only the species in solution, but also the electrode.

Considering a solution composed of oxidised species (Ox) and reduced species (Red<sup>-</sup>) in contact with a metal electrode:



When an equilibrium is achieved, the rate at which the Red<sup>-</sup> releases an e<sup>-</sup> to the metal electrode (m), is the same rate at which the electrode gives an e<sup>-</sup> to the Ox. The relative charge at the metal electrode and the solution will vary depending whether the equilibrium is accomplished when the reaction above lies to the left or to the right. For instance, if the equilibrium lies towards the right (forming Red<sup>-</sup>), the solution will be negatively charged, compared to the positively charged electrode. Therefore, a charge separation is likely to take place between the solution and the metal electrode, and consequently, a difference in electrical potential.

The electron transfer discussed above for a system formed by Ox, Red<sup>-</sup> and the metal electrode, can be understood by looking at the energy levels in both the electrode and the species in solution. The electronic structure of metals is formed by continuous bands of electrons, with the highest energy level called the Fermi level. Looking at the solution phase Ox, for example, has atomic or molecular orbitals in its electronic structure, with an unfilled orbital which can receive an e<sup>-</sup> to form Red<sup>-</sup>. Considering that the Fermi level of the metal electrode is at a higher energy than the unfilled orbital of Ox, it is energetically favourable for the metal electrode to transfer electrons to the species in solution to decrease the energy of its Fermi level, as demonstrated in Figure 2.1. On the other hand, the increase in electrons in the solution raises the energy level of the solution species' orbitals. A dynamic electrochemical equilibrium is reached when the energy of the orbitals of the solution species and the electrode balances out. The energy level of the metal conducting band is such that the rate at which the electrode transfers an e<sup>-</sup> to the solution is the same as the rate at which Red<sup>-</sup> transfers an e<sup>-</sup> to the metal. It is worth mentioning that the Fermi level of metal electrodes in electrochemical cells can be manipulated by applying different potentials to the electrode, which will be further discussed in section 2.2.1.

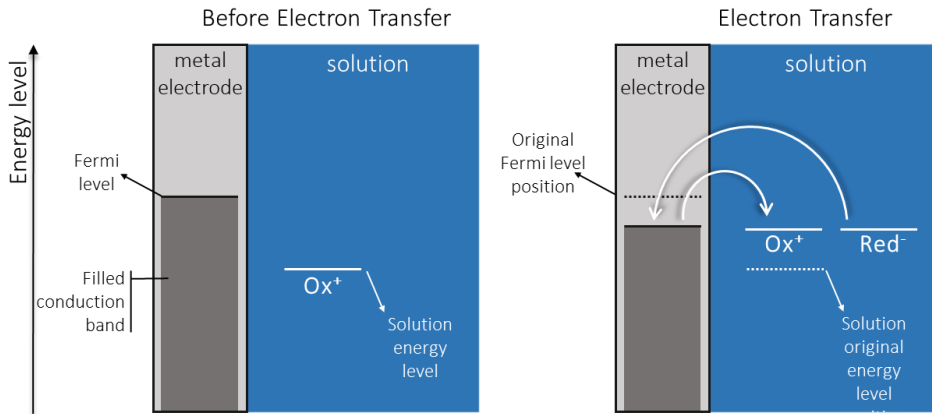


**Figure 2.1.** Energy of metal electrode and species in solution before and during an electron transfer; the narrows on the second quadrant indicate that a dynamic equilibrium has been reached, so that the rate at which electrons are transferred from (or to) the electrode to (or from) the solution are the same.

Considering the discussion above, one can realise that both the chemical potential of the species in solution, and the electrical energy of the electrode and the species in solution affect the electrochemical equilibrium. This can be demonstrated with the concept of electrochemical potential ( $\bar{\mu}$ ) as described in the following equation:

$$\bar{\mu} = \mu + ZF\phi \quad (2.4)$$

where  $\bar{\mu}$  is the electrochemical potential composed of the chemical potential ( $\mu$ ) and the electrical energy of either the electrode or the species in solution ( $ZF\phi$  = electrical energy per mol,  $Z$  the charge,  $F$  the Faraday constant and  $\phi$  the potential of the solution or solid phase).

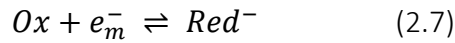
As per a chemical equilibrium, an electrochemical equilibrium is achieved when  $dG = 0$ , and consequently:

$$\bar{\mu}_{Ox} + \bar{\mu}_{e^-} = \bar{\mu}_{Red} \quad (2.5)$$

As the chemical potential ( $\mu$ ) of a given species can be described by the activity of the species ( $a$ ):

$$\mu = \mu^0 + RT \ln (a) \quad (2.6)$$

Thus, the electrochemical equilibrium for a generic redox reaction such as:



can be described by:

$$\mu_{Ox}^0 + RT \ln(a_{Ox}) + ZF\phi_S + ZF\phi_M = \mu_{Red}^0 + RT \ln(a_{Red}) + ZF\phi_S \quad (2.8)$$

where  $\phi_S$  and  $\phi_M$  are the solution and electrode potentials, respectively. By replacing  $Z$  with the corresponding charge of the species and rearranging the equation, the relationship between the electrode-solution potential difference ( $\phi_M - \phi_S$ ) and the species concentration can be observed:

$$\phi_M - \phi_S = \frac{(\mu_{Ox}^0 - \mu_{Red}^0)}{F} + \frac{RT}{F} \ln\left(\frac{a_{Ox}}{a_{Red}}\right) \quad (2.9)$$

The relationship shown in the equation above summarises how the electrochemical system would rearrange to reach dynamic equilibrium.

However, the measurement of the potential difference of a single electrode in solution is not viable. For this reason, the practical potential is measured and given by:

$$E = (\phi_M - \phi_S)_{reaction} - (\phi_M - \phi_S)_{ref} \quad (2.10)$$

where  $(\phi_M - \phi_S)_{reaction}$  is the electrode-solution potential difference of the reaction to be studied and  $(\phi_M - \phi_S)_{ref}$  is the potential of a reference electrode (reference electrodes will be further described in the following section). Finally, the chemical potentials are incorporated into a new variable called standard reduction potential ( $E^0 = \frac{(\mu_{Ox}^0 - \mu_{Red}^0)}{F}$ ), which is the potential for when  $a=1$ . This gives rise to the Nernst equation:

$$E = E^0 + \frac{RT}{F} \ln\left(\frac{a_{Ox}}{a_{Red}}\right) \quad (2.11)$$

which describes the relationship between the measured potential and the activity of the active species in solution. As the activities of species in solution are often unknown and expressed in terms of concentrations, a more practical

way of expressing the Nernst equation is replacing  $E^0$  by the formal potential  $E^{0'}$ :

$$E = E^{0'} + \frac{RT}{F} \ln \left( \frac{[Ox]}{[Red]} \right) \quad (2.12)$$

The Nernst equation describes the changes occurring in an electrochemical reaction in equilibrium, if any of the system properties (*e.g.* potential or concentration of species) are altered. Electrochemical reactions that obey the Nernst equation in the equilibrium are said to attain Nernstian equilibrium.

### 2.1.2 Electrochemical cells and electrodes: three electrode systems

Section 2.1.1 introduced the use of a reference electrode to determine the electrode potential. In practice, when studying electrochemical cells, a potential is applied between the electrode where the reaction of interest takes place at the working electrode (WE), and the reference electrode (RE). The potential of the RE should be constant throughout the experiment, so the potential at which the reactions occur can be determined accurately.

REs should display the behaviour of an ideally non-polarisable electrode, which means that a flow of current does not affect the potential of this electrode. Practically, there is no such a thing as a non-polarisable electrode, so reference systems should have highly reversible and very fast reactions taking place at its surface. This minimises the changes in the RE potential, hence approaching ideal behaviour.

Nevertheless, if enough current passes through a RE, the potential is likely to change. Consequently, three electrode systems are often used to minimise the amount of current passed through the RE. A third electrode is introduced in the system, the counter electrode (CE). The CE is connected in parallel to the RE, meaning that the current flow from the WE will be split between CE and RE. The current flow through the RE can be minimised by placing a resistor of high resistance in series with RE, so that the current reaching

the RE is very low. Therefore, the potential in a three-electrode cell is measured between the WE and the RE, whereas the resulting current flows (mostly) between the WE and CE.

Ag/AgCl is a typical example of RE used in cells with aqueous solutions. This electrode is composed of a silver wire covered in AgCl inside an aqueous solution containing  $\text{Cl}^-$  anions. This electrode displays behaviour close to an ideally non-polarisable electrode for the following reasons. According to the Nernst equation for this system, the electrode potential is only dependent of the activity coefficient of  $\text{Cl}^-$  (Ag and AgCl activity = 1). When small currents pass through this electrode,  $\text{Cl}^-$  will be rapidly formed or consumed, because of the high kinetics and reversibility of this electrode reactions. Therefore, if the concentration of  $\text{Cl}^-$  does not vary significantly, the overall potential will also not vary, making it an almost ideal non-polarisable electrode.

However, RE for non-aqueous systems are more difficult to find. Consequently, many electrochemical cells with non-aqueous solutions use quasi-reference electrodes (qRE). The potential of qRE is not as stable as in RE and is likely to change with changes in the cell environment. qRE can be calibrated by using internal references, whose redox potential should be minimally affected by the cell solution. Decamethylferrocene (dmFc) is an example of internal reference, which has been demonstrated to be slightly more stable than ferrocene (IUPAC recommended internal reference).<sup>58</sup> The increased stability comes from the lower interactions with species in solution, caused by the steric effect of the methyl groups on the cyclopentadienyl ring.<sup>58</sup>

### 2.1.3 Mass transport in electrochemical cells

For electrochemical reactions to occur in an electrochemical cell, active species must move from the bulk solution to the electrode surface. Mass transport of species in solution is observed in three modes: migration, diffusion, and convection. Briefly, migration is the movement of species caused by a charge gradient. For example, positively charged species are likely to migrate

towards negatively polarised electrodes. In practice, this type of mass transport is suppressed using concentrated electrolytes, which populate the solution with an excess of other charged species, minimising such migration effects. Diffusion is the most common mode of transport of active species to the electrode and is further discussed below. Mass transport by convection in electrochemical cells are observed via forced convection, which is the movement of species in solution by mechanical means (e.g. stirring). Convection is observed when using hydrodynamic techniques, such as Rotating Disc Electrodes, which are further discussed in section 2.2.4.

For undisturbed electrochemical cells, diffusion is the dominant mode of transport of active species in solution to the electrode surface. According to Fick's first law of diffusion, the flux of species ( $j$ ) in one dimension, through a unit area in a unit time, is proportional to the negative of the concentration gradient  $\left(\frac{\partial c}{\partial x}\right)$ , summarised by:

$$j = -D \frac{\partial c}{\partial x} \quad (2.13)$$

where  $D$  is the diffusion coefficient (expressed in  $\text{cm}^2/\text{s}$ ). The negative sign demonstrates that the flux of species will be given by the diffusion of species from higher to lower concentration within a distance  $x$ .

Taking as an example a generic solution of species  $A$ , with bulk concentration  $[A]_{\text{bulk}}$  in an electrochemical cell. If the electrode is polarised in such a way to promote the electrochemical reduction of  $A$  to  $B$ :



and assuming this reaction occurs promptly (fast kinetics), then the concentration of  $A$  at the electrode surface ( $[A]_0$ ) will be equal to zero ( $[A]_0=0$ ), since all of  $A$  at the electrode surface is instantly reduced to form  $B$ . This forms a concentration gradient of species  $A$ , between the electrode surface to the bulk. Thus, a flux of species  $A$  from the bulk solution to the electrode surface takes place in the electrochemical cell, following Fick's first law of diffusion, as shown in Figure 2.2b. In addition, Figure 2.2c shows that as time passes and  $A$  is

consumed, the concentration gradient of A becomes smaller. Consequently, the flux of species to the electrode decreases, according to equation 2.13 shown above. The  $\partial x$  distance in which this concentration gradient develops is called the diffusion layer ( $\delta$ ), and it is shown in Figure 2.2d).

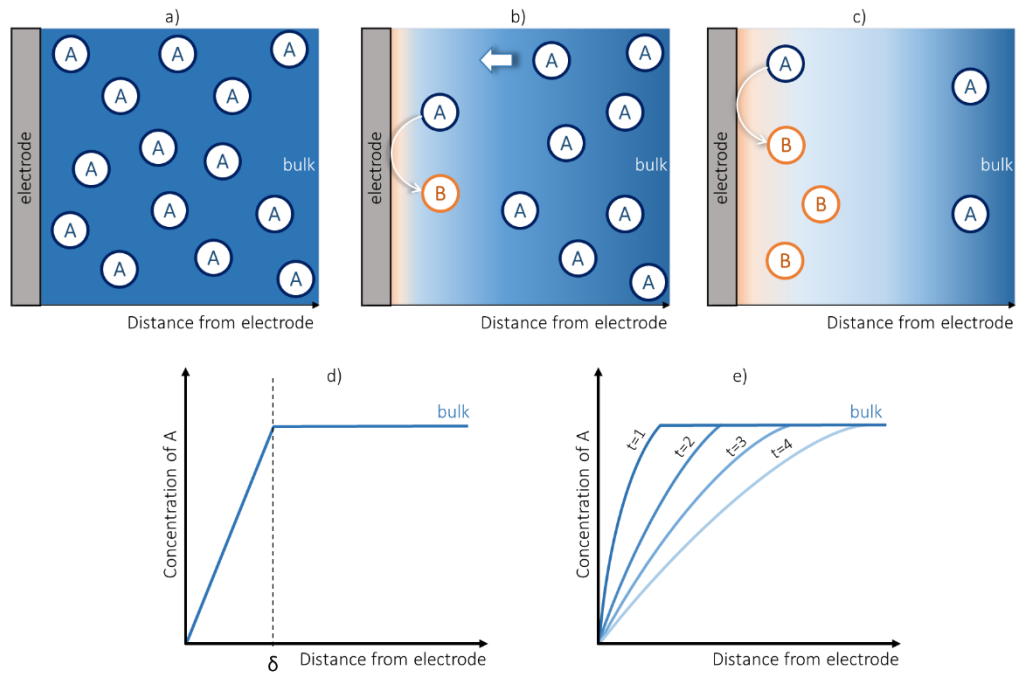


**Figure 2.2.** Mass transport in electrochemical cells: a) Cell before any potential has been applied, b) Potential applied such that A promptly reduces to B, c) Solution composition after time a certain time t, d) Concentration profile of A as a function of the distance from electrode showing the diffusion layer ( $\delta$ ), and e) concentration profile of A over time, across distance x from the electrode).

The practical current developed at the electrode during a generic reaction of A forming B, is given by:

$$I = nFAj \quad (2.15)$$

where  $n$  is the number of electrons involved in the electrochemical reaction,  $F$  is the Faraday constant,  $A$  the area of the electrode and  $j$  the flux of species. Fick's first law states that the flux is proportional to the concentration gradient  $\left(\frac{\partial c}{\partial x}\right)$ , however, as discussed in the above paragraph, the concentration changes only within the diffusion layer of thickness  $\delta$ , being constant in the rest of the

solution ( $[A] = [A]_{bulk}$ , when  $x > \delta$ ). Therefore, the current at the electrode can be described as follows:

$$I = nFA \frac{D([A]_{bulk} - [A]_0)}{\delta} \quad (2.16)$$

A new term called the mass transport coefficient ( $m_T$ ) can be introduced and it is the ratio of the diffusion coefficient and the thickness of the diffusion layer. Additionally, as A reacts as soon as it reaches the electrode surface, the surface concentration of A is zero ( $[A]_0 = 0$ ), thus the current is described by:

$$I = nFA[A]_{bulk}m_T \quad (2.17)$$

#### 2.1.4 The Cottrell equation

The previous section discussed the decrease of the flux of species over time caused by an increase in the diffusion layer formed at the electrode surface. The scenario displayed in Figure 2.2 can be observed when a potential step is applied to the electrode. Cottrell introduced an equation showing the current response when a potential step is applied to a disc electrode:

$$I = \frac{nFA\sqrt{D}[i]_{bulk}}{\sqrt{\pi t}} \quad (2.18)$$

where  $[i]_{bulk}$  is the bulk concentration of species  $i$  in solution. The current response over time estimated by the Cottrell equation is shown in Figure 2.3.

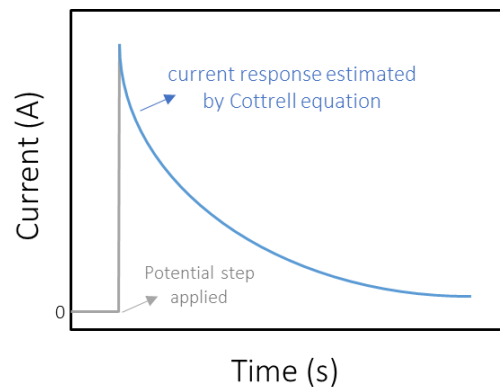


**Figure 2.3.** Current transient resulting from a potential step according to the Cottrell equation (in blue), also showing the current before and when the potential step is applied (in grey).

### 2.1.5 Kinetics of electrochemical reactions

The previous sections discussed generic reactions with high reversibility that occur very quickly, so that no kinetic limitations needed to be considered. Nevertheless, the rate of heterogeneous electron transfer affects the rate of electrochemical reactions, and it will be discussed in this section. For a generic redox reaction between species A and B:



the flux ( $j$ ) of species A undergoing electrochemical reduction, assuming a first order heterogeneous reaction, is given by:

$$j = k_R[A]_0 \quad (2.20)$$

with  $k_R$  being the rate constant for the reduction reaction, and  $[A]_0$  the concentration of species A at the electrode surface. As seen in the previous section, the current developed at the electrode is given by  $I = nFAj$ , hence:

$$I = nFAk_R[A]_0 \quad (2.21)$$

Considering the overall process, the net current can be written

$$I = nFAk_O[B]_0 - nFAk_R[A]_0 \quad (2.22)$$

with  $k_O$  being the rate constant for the oxidation process. As per homogeneous rate constants for chemical reactions,  $k_R$  and  $k_O$  are temperature and pressure dependent. In addition,  $k_R$  and  $k_O$  are also dependent on the potential difference between the electrode and solution. The manipulation of  $\phi_M$  and  $\phi_S$  alters the energy level of the oxidised and reduced species (A and B in the generic reaction above), triggering a reduction or oxidation reaction which is more thermodynamically favorable. Consequently, the dependence of  $k_R$  and  $k_O$  on potential can be expressed in the Arrhenius form below, with the potential difference ( $\phi_M - \phi_S$ ) expressed in  $(E - E^{0'})$ , as discussed in section 2.1.1.

$$k_R = k_R^0 \exp\left(\frac{-\alpha F(E - E^{0'})}{RT}\right) \quad (2.23)$$

$$k_o = k_o^0 \exp\left(\frac{(1-\alpha)F(E-E^{0'})}{RT}\right) \quad (2.24)$$

with  $\alpha$  being the electron transfer coefficient.

For a dynamic equilibrium, reductive and oxidative currents balance each other and  $k_R^0 = k_O^0 = k^0$ , with  $k^0$  being the standard electrochemical rate constant. Replacing  $k^0$  in the rate constant equations above we obtain:

$$k_R = k^0 \exp\left(\frac{-\alpha F(E-E^{0'})}{RT}\right) \quad (2.25)$$

$$k_O = k^0 \exp\left(\frac{(1-\alpha)F(E-E^{0'})}{RT}\right) \quad (2.26)$$

and the net current can be written as:

$$I = nFA_{elec}k^0 \left[ [B]_0 e^{\left(\frac{-\alpha nF(E-E^{0'})}{RT}\right)} - [A]_0 e^{\left(\frac{(1-\alpha) nF(E-E^{0'})}{RT}\right)} \right] \quad (2.27)$$

This is known as the Butler-Volmer equation.

The standard electrochemical rate constant is an important parameter to evaluate the reversibility of electrochemical reactions. Reactions with high values of  $k^0$  display fast electrode kinetics, are said to be reversible and will obey the Nernst equation described in section 2.1.1. Reactions with low values of  $k^0$  are said to be irreversible because of their slow electrode kinetics. However, high and low values are relative words, which in this context are with reference to the mass transfer coefficient introduced in section 2.1.3.

### 2.1.6 Electrochemical reversibility

The concept of reversibility in chemistry in very simple terms can be thought as a reaction that can proceed in both the forward and the backward direction, with stable products in both directions. In electrochemistry, a reaction can be said to be reversible whenever the electrode kinetics are fast enough so that a Nernstian equilibrium is attained.

Sections 2.1.3 and 2.1.5, showed that the net flux of species towards the electrode is determined by both how fast the species approach the electrode (mass transport), and how fast they react (kinetics). These two variables can be summarised into the mass transport coefficient ( $m_T$ , section 2.1.3) and the standard electrochemical rate constant ( $k^0$ , section 2.1.5). The thermodynamic reversibility of electrochemical reactions is based on the relationship between the values of  $k^0$  and  $m_T$ . The reaction is said reversible if:

$$k^0 \gg m_T \quad (2.28)$$

And so, the active species promptly react at the electrode surface, and the reaction will obey the Nernst equation. In thermodynamics, a process is reversible if infinitesimal changes in one of the variables of the system causes the process to reverse direction. In electrochemical reactions, potential is a variable in the system that can be altered and, under Nernstian equilibrium, modify the concentration of oxidising and reducing species. For such reactions, these changes can be predicted by the Nernst Equation.

Reactions are said to be electrochemically irreversible if

$$k^0 \ll m_T \quad (2.29)$$

and consequently, the electron transfer reaction is very slow, and more extreme potentials (than those predicted by the Nernst equation) need to be applied to observe a modification in the system.

### 2.1.7 Battery cells

Batteries are formed by a combination of electrochemical cells, which consists of a positive and a negative electrode separated by an electrolyte within a separator material (glassfibre for example). During usage and discharge of a battery, the electrochemical cells operate as a galvanic cell, in which chemical energy is converted into electric energy. In a galvanic cell, the positive electrode is the cathode, at which reduction reactions take place, whilst the negative electrode is the anode, at which oxidation reactions occur. Unlike galvanic cells,

## Chapter 2

an electrolytic cell converts electrical energy into chemical energy. Moreover, the cathode and anode nomenclature changes, and the reduction reactions occurs at the negative electrode (anode in galvanostatic mode, cathode in the electrolytic mode), whilst oxidation reactions occur in the positive electrode (cathode in galvanostatic mode and anode in electrolytic mode).

Batteries can be classified in primary or secondary batteries. Primary batteries are composed only of galvanic cells. In other words, they cannot be recharged. The electrochemical cells in secondary batteries can operate either as a galvanic cell, or as an electrolytic cell, allowing the battery to be rechargeable.

Besides the electrodes and electrolyte, the electrochemical cells also include current collectors adjacent to the electrodes, and in the case of liquid electrolytes it also includes a separator (a membrane soaked with the electrolyte). The cell is placed within a casing, which can be made into different shapes to accommodate the cell format. The most common geometries of cells include cylindrical, coin, and prismatic.

There are a few parameters that characterise battery cells, including cell voltage and cell capacity. The theoretical cell voltage is simply the difference in potential between the positive and the negative electrodes. When not in use, the cell has an open circuit voltage (ocv) which is usually close in value to the cell theoretical voltage. During discharge the cell voltage decreases up to a cut-off limit, likewise, the voltage increases during charge. The average voltage during discharge is often described as the battery's nominal voltage by the manufacturer.

Cell capacity is the total charge available in a specific period when the battery is discharged at a certain rate. In practice, it is the product of the time it takes to discharge a battery cell by the current density at which the battery is discharged. Usually, the faster the discharge rate, the lower the capacity.

Energy and power are other parameters typically used to describe electrochemical cells. The energy of an electrochemical cell is defined as the

amount of useful work the cell can execute until reaching the cut-off limit. The energy can be calculated as the product of the cell voltage and capacity of the cell at a certain time. The rate at which the cell energy can be delivered is the cell power.

The specific energy of a cell is the cell energy per weight unit. This is at times reported with relation to the weight of the active materials (electrodes) or the weight of the non-active materials as well (current collectors, separator, casing, etc). As the name says, the volumetric energy is the cell energy per unit of volume, and similar to specific energy can be described with relation to active or non-active materials.

Analysis methods typically used to study battery cells include galvanostatic cycling to understand the performance of the electrochemical cells and cyclic voltammetry to obtain information about the different electrode-electrolyte reactions. Electrochemical impedance spectroscopy is also a commonly used technique to study electrode reactions, the state of the cell and degradation processes.

## 2.2. Electrochemical Techniques

### 2.2.1 Cyclic voltammetry

Cyclic voltammetry is the most used voltammetric technique to study electrochemical reactions. A three-electrode electrochemical cell (see section 2.1.2) is the usual set up for this technique. In cyclic voltammetry, the potential of the working electrode is scanned within an upper and a lower limit, at a certain scan rate, with reference to the RE. The current response is recorded and displayed as function of the applied potential and this is shown in a plot called cyclic voltammogram (CV). During cyclic voltammetry, an initial potential  $E_1$ , at which (usually) no redox event takes place, is scanned towards a limit potential  $E_2$ , followed by a switch in the scanning direction, scanning from  $E_2$  towards  $E_3$ ,

which may or may not be equal to  $E_1$ , as displayed in Figure 2.4a. For a typical reversible redox couple, the current response is shown in Figure 2.4b.

Considering a generic reaction as an example:



Section 2.1.1 introduced that the Fermi level of electrodes may be manipulated by the voltage applied by a potentiostat. Assuming Figure 2.4b is the correspondent CV for the generic reaction above, when the potential is scanned from  $E_1$  to  $E_2$ , the fermi level of the electrode is elevated. It then becomes favourable for the electrode to transfer this electron to the empty orbital of A, which will then be reduced to B. When the potential is scanned from  $E_2$  back to  $E_1$ , the Fermi level of the electrode is lowered and is favourable for B to transfer electrons back to the electrode, forming A again.

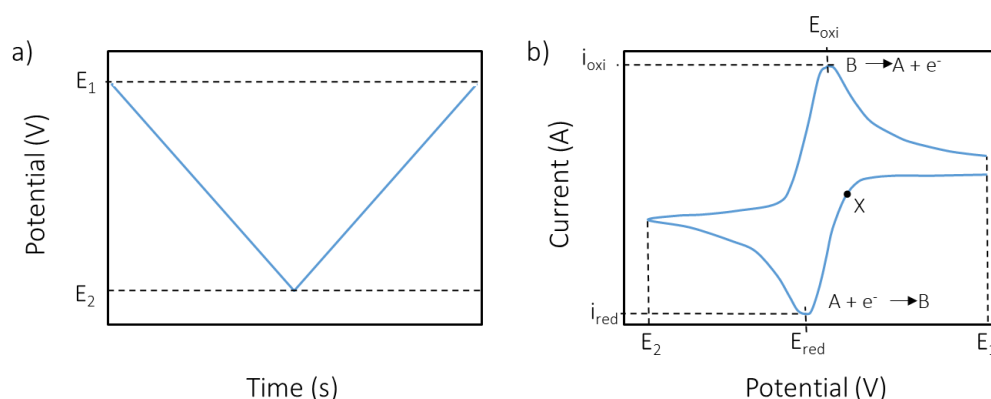


**Figure 2.4.** Cyclic voltammetry: a) Potential cycle applied to a generic electrochemical cell; b) Resulting voltammogram of potential cycle displayed in (a): As the potential is scanned from  $E_1$  to  $E_2$ , a generic reduction from A to B takes place at the reduction potential  $E_{red}$  resulting in a current response  $i_{red}$ . Species B are oxidised to A when the potential is scanned from  $E_2$  to  $E_1$ , with a current response  $i_{oxi}$ .

For each electrochemical process taking place in Figure 2.4b as the potential is scanned from  $E_1$  to  $E_2$  and back to  $E_1$ , a corresponding current response is developed. As the potential is scanned from  $E_1$  towards  $E_2$ , we observe an increase in the current response to a maximum point at  $E_{red}$ , followed by a decrease to a level close to the current at the start of the experiment. As

the potential is scanned towards  $E_2$ , at point X for example, some A has been reduced forming B, but the applied potential is not reductive enough to promote a significant reduction of A yet. As the potential approaches  $E_{red}$ , it is negative enough for large quantities of A to be reduced, thus the cathodic current reaches a maximum. However, as the potential continues to be scanned towards  $E_2$  and A is consumed, the concentration gradient of A drops. Thus, despite the favourable electrode kinetics, the flux of A towards the electrode decreases, causing a decrease in the current response. When the potential is reversed and scanned towards  $E_1$ , B formed at the forward scan is then oxidised at the electrode surface. The anodic current reaches a maximum at  $E_{oxi}$ , followed by a decrease in the current response due to a decrease in the flux of reactant B to the electrode.

Figure 2.5 shows a typical CV for a thermodynamic irreversible redox process. The sluggish electrode kinetics mean that very large overpotentials need to be applied to promote a reduction/oxidation, hence the large peak separation.

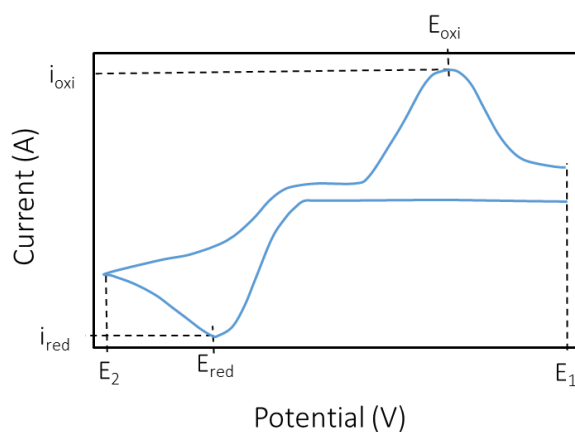


**Figure 2.5.** Typical voltammogram of an electrochemically irreversible redox couple

### 2.2.2 Voltammetry using microelectrodes

Microelectrodes are electrodes with at least one dimension in the order of microns. In a microdisc electrode this dimension is the radius of the disc. Several parameters change when moving from macroelectrodes to

microelectrodes. In large electrodes, the mass transport is predominantly one-dimensional, considering the large flux of species normal to the electrode compared to the flux of species at the edge of the electrode (see illustration in Figure 2.6a). Given the smaller dimension of microdisc electrodes, the flux of species towards the edges of the disc cannot be neglected. Thus, because of the significant contribution of flux of species at the edges of the electrode, mass transport in microdisc electrodes can be said to be three-dimensional (Figure 2.6b).

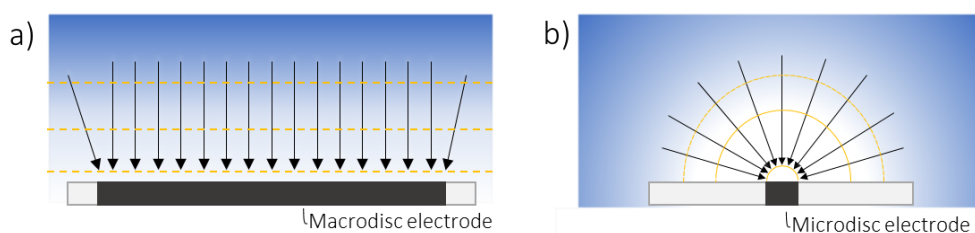


**Figure 2.6.** Side view of mass transport towards macrodisc electrodes (a) and microdisc electrode (b). Arrows show direction of mass transport towards the electrode and yellow dashed lines show changes on the diffusion layer over time.

In the previous section, it was described that as the electrochemical reaction is made kinetically favoured by increasing the overpotential, reducing species are consumed to the extent that the concentration gradient established between electrode and bulk solution decreases. This is accompanied by a decrease in current response, hence a peak in a CV. When using a microdisc electrode, the rate at which the reducing species are consumed is slower than in a macroelectrode, given the small dimension of the microelectrode. Thus, no significant changes can be observed in the concentration gradient in the time scale of the vast majority of the experiments. Consequently, the current response does not decrease, but instead reaches a steady-state current. The steady-state current achieved during voltammetry in a microdisc electrode is described by the following equation, where  $r$  is the radius of the microdisc:

$$i_{ss} = 4nFDcr \quad (2.31)$$

### 2.2.3 Chronoamperometry

Chronoamperometry is a potential step technique, in which the current response is plotted against time. The potential is stepped from a value at which no redox event take place with the active species in solution, to a potential at which a reduction or oxidation reaction occurs, as demonstrated in Figure 2.7.

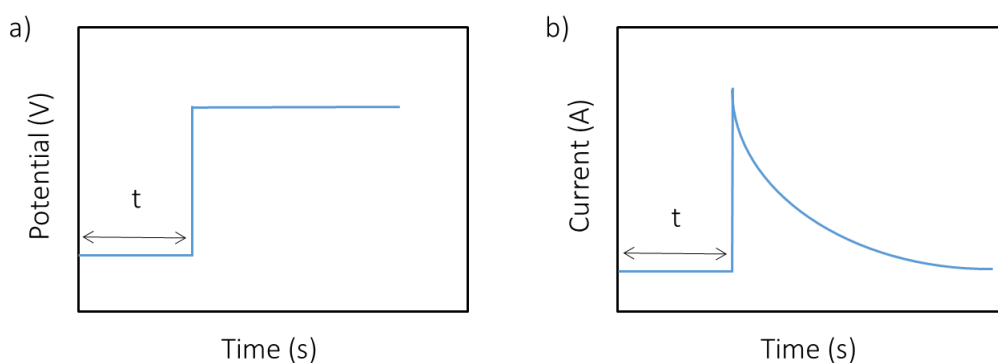


**Figure 2.7.** Potential and current response in chronoamperometry showing the potential step at time  $t$  (a) and the current response to the potential step, from a region where no redox events take place ( $\text{time} < t$ ) to an electroactive region.

For electrochemical reactions under diffusion control the current observed can be defined by the Cottrell equation, presented in section 2.1.3. The Cottrell equation introduced in section 2.1.3 describes the changes in current for a planar electrode, in which the diffusion of species can be considered one-dimensional. This is the case for chronoamperometry in macroelectrodes. In microdisc electrodes, mass transport is three-dimensional, and the current response can display different regimes with time. In a very short period of time the dimension of the diffusion layer is small compared to the radius of the disc. In this short period, the three-dimensional mass transport is still not as significant, and the current response can be described by the Cottrell equation. However, as time passes and the dimension of the diffusion layer becomes comparable to the radius of the disc, the current response in microelectrodes differs to the current predicted by the Cottrell equation. Shoup and Szabo developed an equation that describes the variation of current as a function of time for potential steps at microdisc electrodes:

$$I = -4nFDCr f(\tau) \quad (2.32)$$

where

$$f(\tau) = 0.7854 + 0.8863 \tau^{-0.5} + 0.2146 e^{(-0.7823 \tau^{-0.5})}$$

and

$$\tau = \frac{4Dt}{r^2}$$

The empirical relationship of current and time described by Shoup and Szabo allow the simultaneous determination of diffusion and solubility of the electroactive species of interest.

#### 2.2.4 Hydrodynamic techniques: rotating disc electrode and rotating ring-disc electrode

In hydrodynamic techniques, the mass transport of active species to the electrode surface takes place not only by diffusion, but also by forced convection. Typically, a rotating disc electrode (RDE) is composed of a disc of the material of interest surrounded by a cylinder made of an insulating material. The electrical connection is made by a set of carbon/silver brushes at the top of the cylinder.

The RDE is mechanically rotated in solution, making it act as a pump, pulling fresh electrolyte towards the electrode. The electrolyte flows upwards towards the electrode, spins around the electrode surface and is thrown outwards, as shown in Figure 2.8a. This movement is critical for the mass transport in these experiments, as fresh active species are constantly being delivered to the electrode through forced convection. The diffusion layer in RDE under well stirred solutions is considerably smaller than for stationary electrodes. Therefore, if the electrode potential is set to a certain value to induce electrochemical reactions with rate limited by mass transport, the current response will reach a steady state current, contrary to the peak shape seen with

stationary electrodes. The mass transport limiting current is described by the Levich equation below:

$$i_{lim} = 0.620nFAD^{2/3}\nu^{-1/6}[A]_{bulk}\omega^{1/2} \quad (2.33)$$

where  $i_{lim}$  is the current at which the rate of electron transfer is determined by mass transport to the electrode;  $\nu$  is the kinematic viscosity of the electrolyte in  $\text{cm}^2/\text{s}$  and  $\omega$  is the rotation speed of the RDE, in  $\text{rad}/\text{s}$ .

A rotating ring disc electrode (RRDE) follows the same principle as a RDE, however it has a ring second WE2 around the disc electrode (WE), separated by an insulating material (see inset in Figure 2.8b). RRDE experiments can, for example, give information about the product formed at the WE, reducing or oxidising it as it is moved outwards the disc electrode. Figure 2.8b, shows a typical example of a RRDE in operation, where the oxidation of  $[\text{Fe}(\text{CN})_6]^{4-}$  can be observed by the disc current, whereas the reduction of  $[\text{Fe}(\text{CN})_6]^{3-}$  can be observed by the ring current.

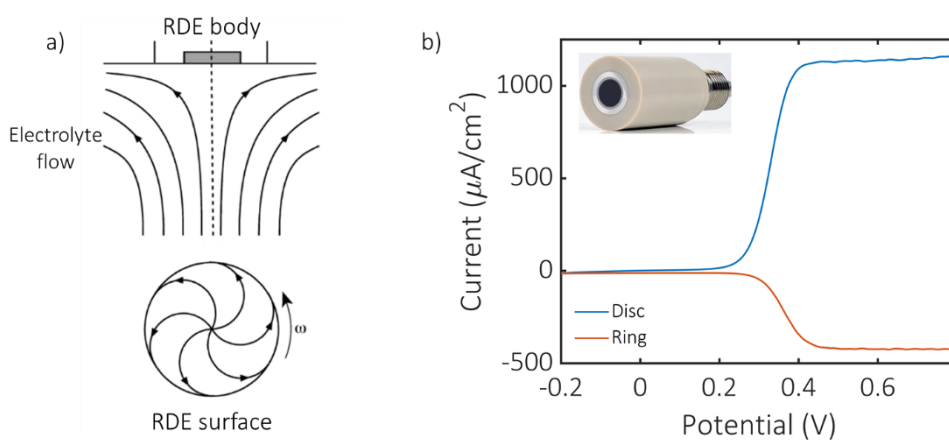


**Figure 2.8.** a) Mass transport in the RDE showing electrolyte flow pattern towards the RDE caused by rotation (top) and electrolyte flow pattern at the electrode surface, viewed from below (bottom).<sup>59</sup> Typical linear sweep voltammetry of 5mM  $[\text{Fe}(\text{CN})_6]^{4-}$  in 1 M KCl aqueous solution using RRDE; Disc current in blue referent to  $[\text{Fe}(\text{CN})_6]^{4-}$  oxidation and ring current in orange referent to  $[\text{Fe}(\text{CN})_6]^{3-}$  reduction. WE=GC disc, WE2=Pt ring, CE = Pt coil and RE = Ag wire qRE; inset: a GC disc and Pt ring RRDE.

### 2.2.5 Electrochemical impedance spectroscopy

In an electrochemical impedance spectroscopy (EIS) experiment, an oscillating potential bias with a small amplitude is applied to the electrochemical cell. Consequently, an oscillating current response develops in the cell, which is phase shifted with relation to the applied voltage. The sinusoidal potential and the sinusoidal current response are represented by:

$$E = E^0 \sin(\omega t) \quad (2.34)$$

$$i = i^0 \sin(\omega t + \varphi) \quad (2.35)$$

in which  $\omega$  is the frequency of the oscillating potential, and  $\varphi$  is the phase shift.

Similar to resistance in an ideal resistor, impedance is the ability of a circuit to resist the flow of electrical current, however, it is not limited by the properties of an ideal resistor. Therefore, the impedance ( $Z$ ) of the electrochemical cell upon application of the sinusoidal potential is described as:

$$Z(\omega) = \frac{E}{i} \quad (2.36)$$

$$Z(\omega) = Z^0 \exp(\sqrt{-1}\varphi) \quad (2.37)$$

And from Euler's relation we obtain:

$$Z(\omega) = Z^0 (\cos\varphi - \sin\varphi) \quad (2.38)$$

As shown in the equations above, the impedance as a function of the frequency can be described by an imaginary part and a real part. These parts can be plotted in a Nyquist plot, in which the imaginary impedance (y axis) is plotted as a function of the real impedance (x axis). A typical Nyquist plot is shown in Figure 2.9a.

An electrochemical cell can be seen as an electric circuit, in which capacitors may represent non-faradaic processes and resistors may represent the resistance to charge transfer at the electrode. Thus, different regions in the Nyquist plot represent different processes during the passage of current in the cell. The Nyquist plot shown in Figure 2.9a can be represented by the typical

Randles equivalent circuit shown in Figure 2.9b. At very high frequencies of potential oscillation, the only resistance in the cell is due to the electrolyte resistance ( $R_{\text{electrolyte}}$ ), which is read from the real impedance axis (x axis). As the oscillation frequency decreases (in the middle of the semi-circle), a more capacitive response is obtained, associated with the non-faradaic processes in the electrochemical cell as the double layer formation (represented by  $C_{dl}$ ). Finally, at low frequencies, at the end of the semi-circle, the electrons may flow to and from the electrodes, and the charge transfer resistance ( $R_{ct}$ ) can be read from the real impedance axis (x axis). Nyquist plots often display a tail at low frequencies, which is associated with diffusion limited electrochemical processes ( $D_{\text{process}}$ ). This is typically represented by the Warburg impedance (W) in the equivalent circuits.

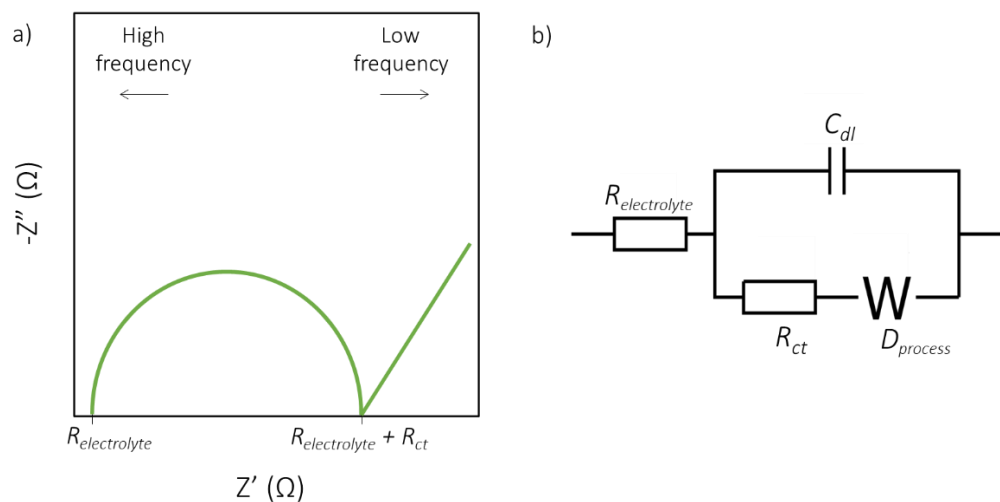


**Figure 2.9.** Typical Nyquist plot obtained in an EIS experiment, showing the electrolyte resistance at high frequencies and the charge transfer resistance at lower frequencies (a), and the Randles equivalent circuit for the Nyquist plot (b).

EIS can be used in a vast range of analyses, including determining the conductivity of electrolytes, changes at the electrode surfaces by monitoring  $R_{ct}$ , and to determine the internal state of battery cells. The charge transfer resistance is a particularly insightful parameter to study solid-electrolyte interphase formation. EIS measurements overtime during resting and cell cycling

can reveal the resistive or conductive character of the SEI, aiding comprehension of cell performance.

### 2.2.6 Galvanostatic cycling

Galvanostatic cycling is based on the application of a constant current density and measurement of the voltage developed across the cell over time. Voltage profiles are the output of a galvanostatic experiment, which show the changes in the electrochemical cell performance during discharge and charge procedures. A typical discharge and charge voltage profile is shown in Figure 2.10. It is one of the most commonly used methods to evaluate battery cells, both at new material discovery level, and advanced long-term degradation studies.

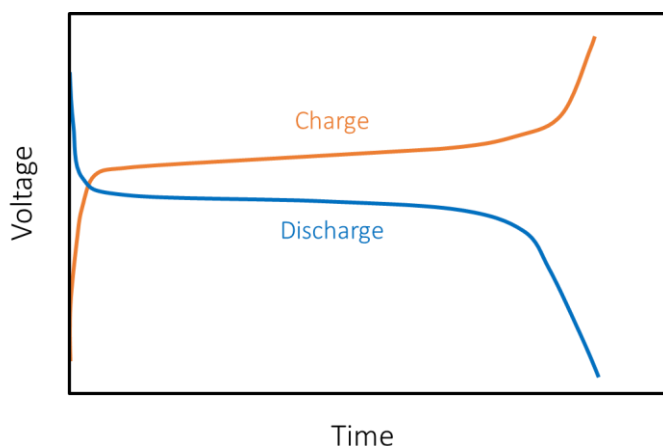


**Figure 2.10.** Voltage profiles from galvanostatic cycling, showing discharge profile in blue, and charge profile in orange.

A two-electrode cell setup can be used in galvanostatic cycling experiments, which is either a full cell or a half cell. A half cell is typically used in early research and development states, thus one electrode can be studied at a time.<sup>60</sup> A half cell is composed of the electrode to be studied and an electrode with a well-known potential as the counter electrode. Full cells as the name suggests, are composed of both battery electrodes. Whilst half cell cycling gives explicit information about the reactions and performance of each individual electrode, full cells shows how these two electrodes and reactions perform in

conjunction.<sup>60</sup> Furthermore, galvanostatic cycling can be used in symmetrical cells, which are commonly used to study plating and stripping reactions in metallic electrodes.

### 2.3. Secondary-ion mass spectrometry

Secondary-ion mass spectrometry (SIMS) is a technique based on the bombardment of a primary ion beam on the sample, and the detection of the secondary ions formed during the sputtering process. The impact of the highly energetic primary ion beam (in the order of keV) leads to sputtering of the sample surface and emission of sample fragments (secondary fragments). The fragmentation occurs as a consequence of the cascade of collisions triggered by the bombardment of the primary ions on the sample, when direct (primary ion collides with atoms of the sample surface causing atomic motion) and non-direct (collision between atoms in motion) collisions take place. Molecular ions and part of the emitted fragments become ionised and are directed by an electric field into a mass analyser.

In depth profile mode, extended sputtering caused by continuous primary ion bombardment erodes the sample and information from deeper layers into the sample is obtained. Thus, sputter time is an indirect measure of depth of analysis, as shown in Figure 2.11. Figure 2.11 displays schematics of a depth profile analysis of a generic sample that is structured in clearly separated layers, and the respective depth profiles and mass spectra for the analysis. In the depth profile mode, the final mass spectrum is an accumulation of the spectra acquired throughout the whole sputter time, and each assignment has a respective intensity profile over time, which is shown in the depth profile plots (see the schemes shown in Figure 2.11 on the right).

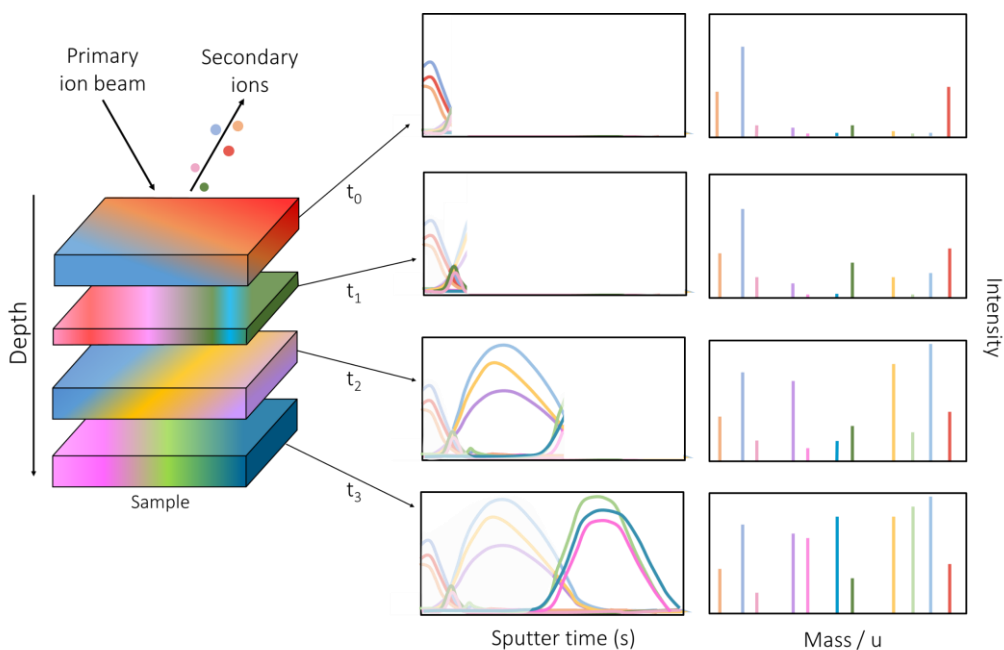


**Figure 2.11.** Schematics of SIMS in depth profile mode showing: on the left, a generic layered sample being continuously sputtered over a time  $t$  (in which  $t_0$  is at the beginning of the sputter time and  $t_3$  is at the end of the sputter time); on the left, the respective depth profile plot and mass spectra. Note the relation between depth of analysis and sputter time, and how the intensity varies in both mass spectra and depth profile plot over time (the colour scheme in each layer of the generic sample on the left is only for intuitive representation of the assignments shown in the mass spectra and depth profile on the right).

The extent of the secondary ionisation is conditional to the sputter yield and the ionisation probability of each sample fragment. The sputtering yield is the ratio between the atoms removed from the sample (sputtered) and the atoms bombarded onto the sample (primary ion beam). The sputtering of sample material is highly dependent on the intensity of the primary ion beam as well as the sample material properties such as the binding energy of the atoms, lattice energy and crystal orientation. Typically, the higher the energy of the primary ion beam, the higher the sputtering yield and the greater the degree of fragmentation. Whilst this may increase the sensitivity of the analysis, higher fragmentation means that information pertaining to larger molecules is compromised. In addition to the energy of the primary ion beam, there are other aspects that influence fragmentation, such as ion size and the ion source. For

example, the use of ion clusters causes less fragmentation and penetration through the sample due to lower energy/ion ratio.<sup>61</sup> The individual ions separate and disperse over the surface when the cluster hits the sample, thus the energy carried by the cluster spreads through each individual ion. With respect to ionisation, the source of primary ion beam may increase the ionisation yield. Oxygen and caesium are primary ion sources known to increase positive and negative secondary ion yield, respectively.

Thus, considering that only a small portion of the fragments are ionised (up to 10%), high sputtering yield does not directly translate into high ionisation. Consequently, direct correlation of ion (or molecule, or fragment) intensity with element abundance in the sample can be problematic, as an element may be more likely to ionise than another, thus a greater quantity of ions is detected. However, a sensible analysis strategy may include comparison of the same assignment across multiple samples of the same matrix, as a particular assignment will display very similar ion yield across samples of the same matrix. Other strategies for correct interpretation of SIMS depth profile data include normalisation to the total ion counts, or normalisation to common ions. This excludes any differences across samples due to surface roughness or length of the experiment.

### 2.3.1 The Orbitrap™ detector

The most commonly used mass analyser in SIMS is time-of-flight (tof). ToF analysers separates the ions according to the time the ions take to travel from the acceleration zone, through a flight tube of known length to the detector. Ions of same charge display the same kinetic energy, thus the velocity of ions with same charge depends on the mass of the ion. Likewise, the overall velocity of the ions depends on the mass-to-charge ( $m/z$ ) ratio. Despite being a powerful technique, SIMS using tof mass analyser have limited mass accuracy and mass resolving power.<sup>61</sup> This makes particularly challenging to deconvolute data from organic samples with complex chemistry.

The Orbitrap™ detector is the newest addition to the mass analysers employed in SIMS.<sup>61</sup> The latest SIMS technology, the 3D OrbiSIMS, uses a hybrid mass analyser comprising an Orbitrap™ and a tof analyser as fully described by Passerili *et al.*<sup>61</sup> This considerably improves the mass measurement accuracy of SIMS, given the superior mass resolution of the Orbitrap™. The hybrid system allows nine different mode of operations, with different choices of primary ion beam, as well as a choice of mass analyser.

Like tof, the Orbitrap™ is also based on the ion motion in an electrostatic field, but the ions follow a complex trajectory which is summarised as follows. The Orbitrap™ is composed of an inner and an outer electrode as shown in Figure 2.12, which create an electrical field in the cavity between them. This electrical field causes ion motion and rotation around the inner electrode. In addition to this rotation, there is also movement along the axis of the inner electrode, with the ions going back and forward along the axis. The frequency of the ion motion along of the inner electrode axis is dictated by the  $m/z$  of the ions.<sup>62</sup>

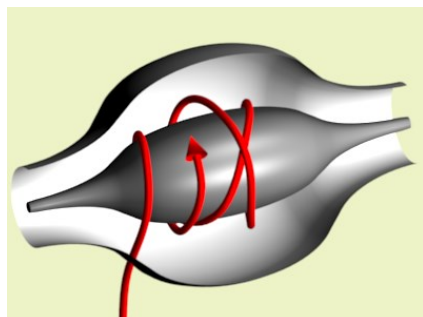


**Figure 2.12.** Schematics of the Orbitrap™ mass analyser showing the ion movement (in red) within the inner and outer electrode of the Orbitrap™.<sup>62</sup>

To ensure a stable ion trajectory inside the Orbitrap™, the kinetic energy carried by the ions when entering the Orbitrap™ must be such that it is not too low so that the ions are sucked in by the inner electrode, neither too high where the ions might collide with the outer electrode. To stabilise the kinetic energy of the ions before entering the Orbitrap™, the ions are “cooled down” in a

damping trap, the C-trap. Thus, the C-trap injects ions by pulses with controlled kinetic energy into the Orbitrap™, as shown in Figure 2.13.

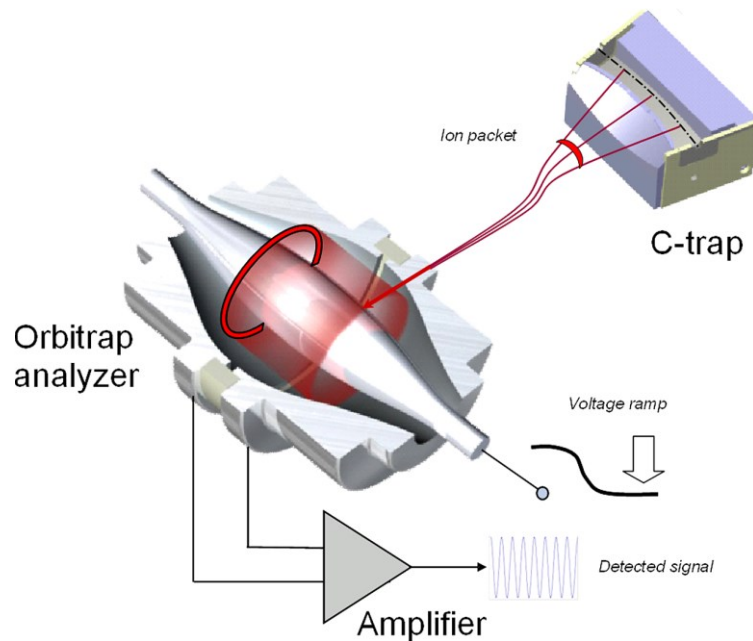


**Figure 2.13.** Schematics of the Orbitrap™ mass analyser showing a cross section of the c-trap.<sup>62</sup>

One of the factors responsible for the improved sensitivity of the Orbitrap™ analyser is the amount of information processed by this mass analyser in comparison to tof analyser in depth profiling studies. In a typical SIMS depth profiling analysis with tof mass analyser, data is extracted at discrete times, whilst information during sputtering is discarded, as shown in Figure 2.14a. However, depth profiling analysis using the Orbitrap™ mass analyser means there is no loss of information, as all sputtered ions are analysed by the Orbitrap™ as shown in Figure 2.14b.<sup>61</sup> This substantially increases the sensitivity of the Orbitrap™ in comparison to tof analyser. Furthermore, by using Ar clusters as the sputtering and analysis beam, large molecules can be detected more intact. This is due to the softer sputtering process provided by ion clusters, which causes less sample fragmentation from the high energy collisions and removes ambiguity in assigning peak identities.

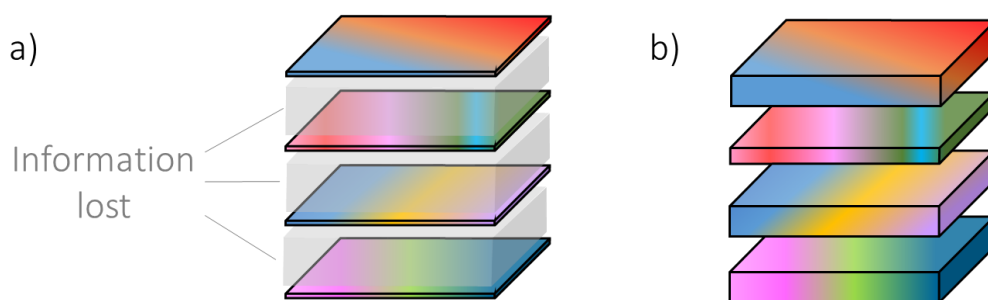


**Figure 2.14.** a) Data obtained with tof-sims analysis (colourful layers) and information lost during sputtering (in grey) in comparison to information obtained with OrbiSIMS (b) of the entire depth of the layers.

## 2.4. Multivariate analysis and the rationale for the process adopted for analysis of 3D OrbiSIMS dataset

Multivariate analysis (MVA) are a series of methods for statistical analysis of complex datasets with multiple variables, which can be correlated to one another by a shared characteristic. In the SIMS community, MVA has become a very popular tool for a large range of applications, from surface imaging to depth profiling.<sup>63</sup>

SIMS data was analysed using non-negative matrix factorisation (NMF), a type of a multivariate curve resolution technique (MCR). This analysis aims to resolve mixture problems, by grouping the constituents into endmembers that represent 'pure' compounds. It is a methodology vastly used in chromatography studies by de Juan, Tauler and co-workers, and has been previously reviewed.<sup>64</sup> NMF simplifies the complex data into a simpler model of pure contributions from the original data matrix. It is a bilinear fit that results in a compressed version of the original data set. The outputs of NMF analysis on SIMS data are the intensity plot of the endmembers and the characteristic spectra. Schematics of an NMF analysis of a generic example is demonstrated in Figure 2.15.

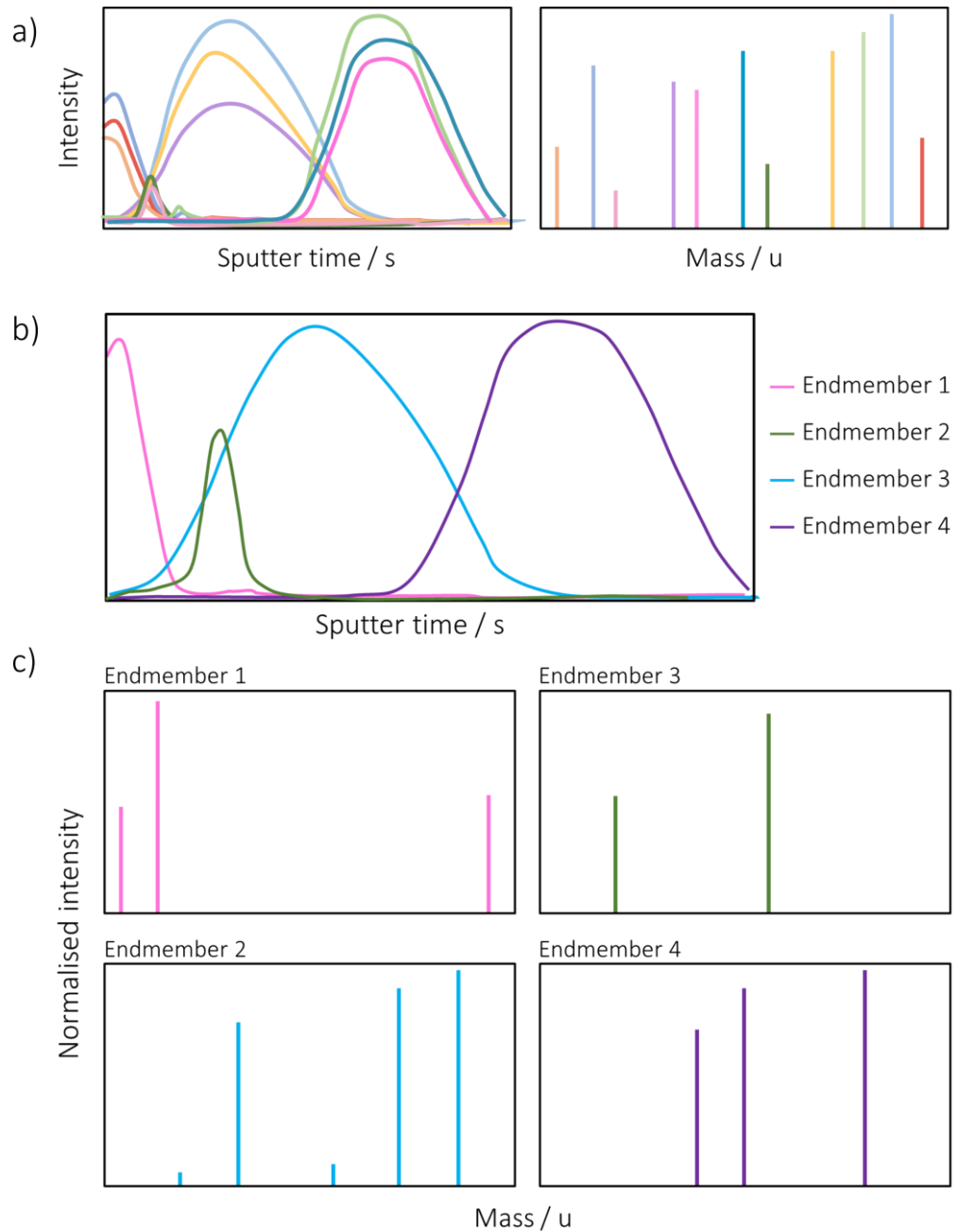


**Figure 2.15.** Schematics showing NMF analysis for the generic example from Figure 2.11: a) depth profile (left) and mass spectrum (right) of a generic example; b) intensity plot of endmembers; c) characteristic spectra of each endmember.

In NMF, each endmember is a meaningful representation of a ‘pure’ compound, or a ‘pure intensity profile’ in this case of SIMS depth profile dataset. Figure 2.15b shows the intensity plot of the endmembers which is a very intuitive representation of the data in Figure 2.15a. Each one of these endmembers is formed by a combination of assignments that display similar

intensity profiles. These assignments may be visualised in the characteristic spectra output of NMF, which is shown in Figure 2.15c. The NMF characteristic spectra of each endmember, as the name suggests, is a representation of the mass spectra showing only the assignments that are part of that endmember. In other words, it is the mass spectrum of assignments with depth profiles that display features represented by that endmember in the NMF intensity plot. The higher the intensity of an assignment in the characteristic spectra, the greater the contribution of that assignment to the endmember. Finally, a comparison of the original generic data (Figure 2.15a) with the NMF results (Figure 2.15b and c), shows that NMF is a powerful exploratory tool, that facilitates data interpretation, and helps to organise and visualise the data in a much clearer manner.

It is important to bear in mind that NMF is a representation, a bilinear fit of complex data and therefore, does not have a definitive solution. In fact, to perform a NMF the user must input the expected number of endmembers and the number of iterations, in other words, the number of times the algorithm runs until it reaches convergence. The 'accuracy' of the NMF representation, and the number of iterations that actually have an impact on the analysis output can be visualised by the lack-of fit plot, shown in Figure 2.16. Regarding the user inputs, the number of iterations is easily determined by trial and error and analysis of the lack-of-fit plot, however the number of expected endmembers is more challenging to determine. For a simple dataset such as the example shown in Figure 2.15a, it is relatively simple to determine the presence of four main intensity profiles, however for large SIMS datasets this is not as straightforward. Indeed, the lack-of-fit plot may be an indication of the number of endmembers that best represents the dataset. However, the lack-of-fit plot should be carefully interpreted, as a large number of endmembers may display very low lack of fit and yet not be a realistic approximation of the different intensity profiles in the sample, as demonstrated in the comparison shown in Figure 2.16.

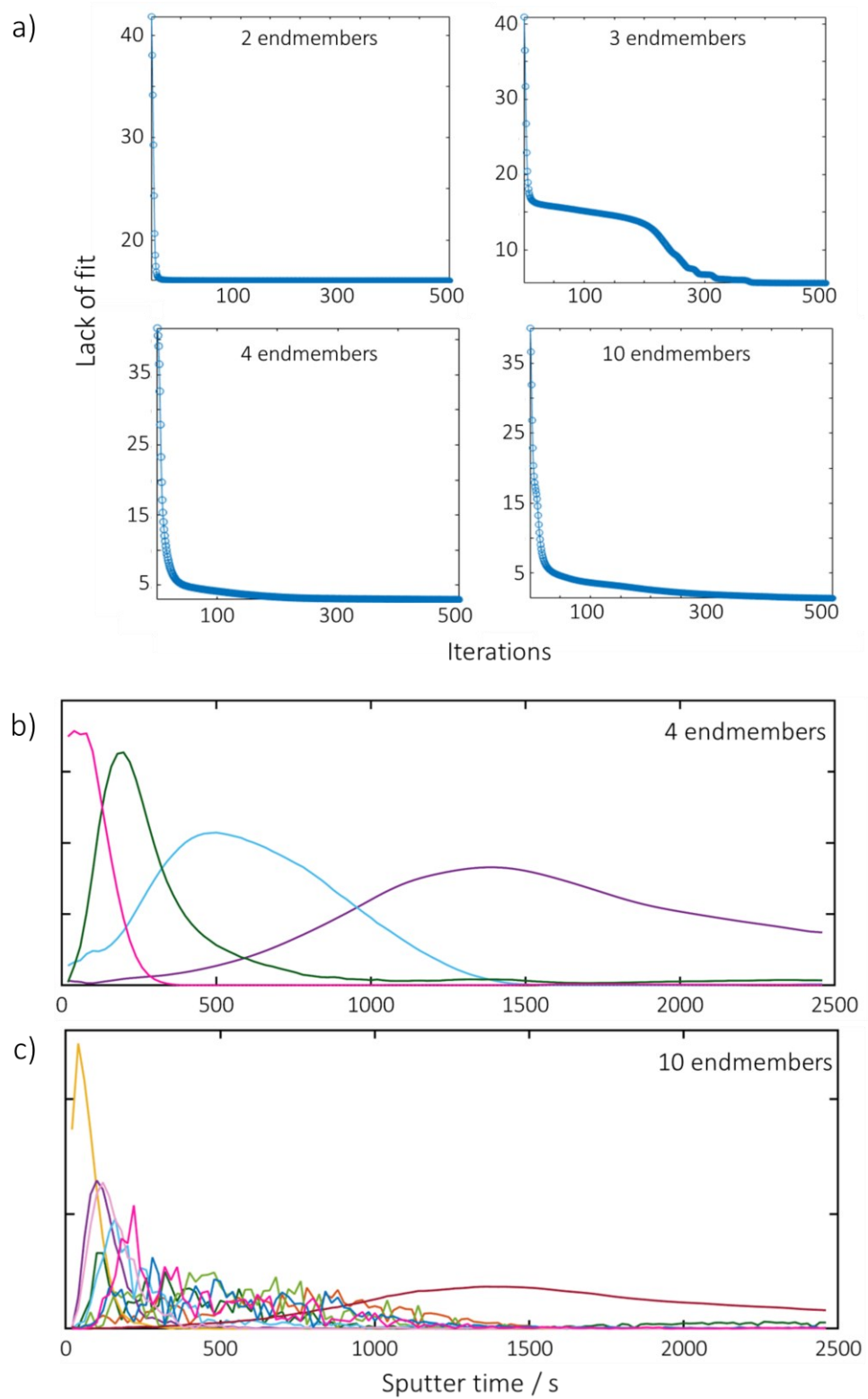


**Figure 2.16.** NMF analysis for  $\text{Na}[\text{N}_{C_1, C_1, C_2, C_4}][\text{NTf}_2]$  interphase demonstrating variations in the lack of fit for a range of expected endmembers, maintaining a fixed number of iterations (a), and intensity plot of NMF analysis with four (b) and ten (c) endmembers.

## Chapter 2

Another approach to determine the number of expected endmembers, is by performing principal component analysis (PCA). PCA is a method of reducing the dimension of a dataset by focusing on the variability of the dataset, grouping strong variation patterns into PCs. Thus, each PC is not representing a feature (an intensity profile) of the data as the endmembers in NMF does, but instead each component represents specific variations within the data. A very common variation in a depth profile plot is an increase in intensity for some assignments and decrease in intensity of others. Figure 2.17a demonstrates a few potential regions of variance represented by PCs.

Unlike NMF, PCA has an exact solution, hence, there is a certain number of components (commonly named PC1, PC2, ..., PCn) that fully represent the variance in the sample. The first few components explain the most relevant information of the dataset, and typically for SIMS datasets only a few components are sufficient to represent over 95% of the variance within the sample. The other components are often related to inherent noise present in the analysis.

PCA gives positive and negative scores to variances within the dataset by grouping the data by its variance. The scores plot over time (Figure 2.17b) might display features that resemble the original intensity plot. However, because PCA is an analysis of variance, with positive and negative scoring, the scores plot does not seem an intuitive method of summarising and understanding surface layers and composition. Nevertheless, PCA is still a very helpful tool to start grouping and understanding SIMS data. The assignments responsible for the main variances within the data are displayed in the loading plot of each PC. When performing PCA of SIMS data, the loading plot of a PC resembles a mass spectrum but showing only the assignments that are part of that PC, as shown in Figure 2.17c-e, similar to the NMF characteristic spectrum described above. The loading plot shows how strongly each assignment influences that PC, thus the higher the loading (either positive or negative) of an assignment, the more relevant this assignment is for that PC.

Whenever PCA aims to categorise the sample by the types of assignments, or size of SIMS fragments, the loadings plot is a very useful tool. However, when PCA is used to determine the number of endmembers for NMF, the loadings plot can be used to obtain information about the most relevant assignments for each PC. By looking at the depth profile of the main assignments of each PC, it becomes easier to visualise how many different intensity profiles there might be within the sample. This is demonstrated in Figure 2.17f-h.

Interpretation of the PCA results (Figure 2.17) of a generic example (from Figure 2.11) for determination of the number of endmembers for NMF is described as follows. The depth profile of the most relevant assignments of PC1 (Figure 2.17f), shows two very distinct intensity profiles, with two very distinct maxima, thus two endmembers for NMF. Depth profile of the main assignments of PC2 also shows two very distinct intensity profiles, however one profile is 'already represented' by PC1, so 3 endmembers can be expected for NMF from analysis of the depth profile of PC1 and 2. Finally, PC3 demonstrates small variations that represent another distinct intensity profile, and it is concluded that NMF analysis should be performed with four expected endmembers. This analysis could be carried on for all the components found by PCA (not shown in this example in Figure 4.24), but as mentioned previously, usually a few components are sufficient to explain most of the variation within a sample. In fact, analysis of the remaining PCs (PC4, PC5, etc) for the SIMS datasets in this chapter found that the remaining PCs describe other small variances of the dataset, but not necessarily a variance that represents a new intensity profile.

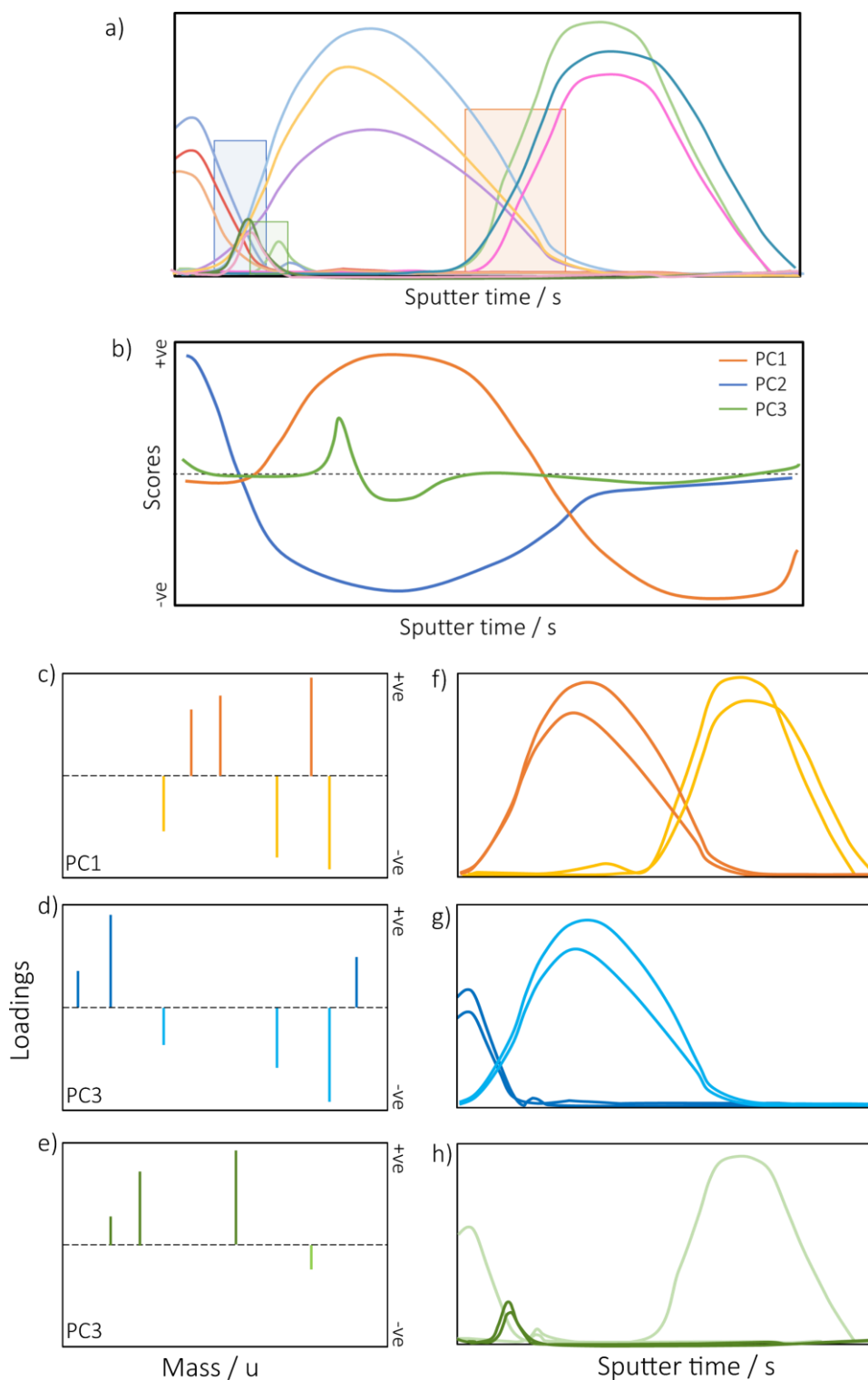


**Figure 2.17.** Schematics showing principal component analysis (PCA) of example from Figure 2.11: a) depth profile plot with shaded areas demonstrating regions of variance that can be represented by principal components (PCs); PCA outputs: b) scores plot of PCA showing three PCs; c-e) loadings plot for PC 1, 2 and 3 respectively; f-h) depth profile of main constituents (assignments) described by PC1, 2 and 3 respectively.

## 2.5. Characterisation techniques of ionic liquid properties

### 2.5.1 Viscosity

In a nutshell, viscosity is the resistance of a fluid to flow. It can be classified into dynamic viscosity and kinematic viscosity. The dynamic viscosity is a measure of the forces that a fluid must overcome to flow, for example, the friction between the fluid and the internal walls of a tube. The kinematic viscosity measures the rate of the flow, how quickly the fluid can get from point A to point B in a tube. In practical terms, the kinematic viscosity can be determined by dividing the dynamic viscosity by the density of the fluid.

On a molecular level, a liquid flows when the molecules in the liquid move past one another, and the lower the resistance the molecules must overcome to move, the lower the viscosity of the liquid. Consequently, intermolecular forces, the structure, and the size of the molecules, are factors that affect the viscosity of molecular liquids. The Hole Theory has been the most widely accepted theory to describe viscosity in ionic liquids (ILs).<sup>65</sup> In summary, it assumes that at any point in time a fluid will have a given distribution of voids, and the ions/molecules are able to move if those cavities have a size compatible with the molecule allowing the movement. Thus, the distribution of hole size determines the likelihood of movement. Typically, the higher the temperature, the larger the hole size, and so with an increase in temperature, the probability of finding larger holes is higher and consequently a decrease in viscosity is observed. The high viscosity of room temperature ionic liquids (RTILs) can be explained by the low probability of finding holes of the right size to allow movement of the large ions present in ILs at low temperatures (room temperature).

### 2.5.2 Donor Number

Donor number (DN) is an approach to express the basicity of solvents. In other words, a measure of the tendency of solvents to donate electron density to acceptors. It was originally determined by measuring the interaction of the solvent with  $\text{SbCl}_5$ . In this method, the experiment was performed calorimetrically, and the DN was determined as the change of enthalpy was attributed to the solvent interaction with the  $\text{SbCl}_5$  probe, with values varying from 0 to 38.8 kcal/mol. Another method was proposed by Popov and Erlich, which linearly correlates the  $^{23}\text{Na}$  NMR shifts of the  $\text{NaClO}_4$  probe with the DN of the solvents. Schmeisser *et al* has used the  $^{23}\text{Na}$  NMR method to determine the donor number of imidazolium-based ILs. <sup>66</sup>

## 2.6. Materials

N,N-dimethylethylamine (Merck, >99%), N-methylpyrrolidine (Acros Organics, >99%), 2-bromo-1,1-dimethoxy ethane (Alfa Aesar, 97%) and 2-bromoethyl methyl ether (Acros Organics, 95%), 1-bromo-butane (Sigma, >99%) were distilled before use. Lithium trifluoroacetate (Fisher scientific, >97%), sodium dicyanamide (Acros Organics, >97%), sodium trifluoroacetate (Alfa Aesar, >98%) and sodium perchlorate (Acros Organics 99%) were dried under vacuum ( $\leq 10^{-3}$  mbar) at 100 °C before use. Lithium bis(trifluoromethanesulfonyl)imide (3M, battery grade) and sodium bis(trifluoromethanesulfonyl)imide (Strem Chemicals, >97%) were also recrystallised from 1,4-Dioxane and dried under vacuum ( $\leq 10^{-3}$  mbar) at 120 °C before use. Amberlite ion exchange resin IRA-402(OH) (Alfa Aesar) was washed with methanol three times before use. 2,2,3,3,3-Pentafluoropropionic acid (Sigma Aldrich, >97%), were used as received. Oxygen was passed through a drying column before bubbled into electrolytes (BOC, 99.95%). All solvents used in the synthesis were anhydrous, and ultrapure water is miliQ 18.2 Mohm/cm.

## 2.7. Synthesis and characterisation of ionic liquids

All ILs were synthesised by modified procedures from literature<sup>67-69</sup>, with the exception of [C<sub>1</sub>C<sub>4</sub>Pyrr][DCA] (Iolitec, >98%). All synthesised ILs were characterised by <sup>1</sup>H, <sup>13</sup>C, <sup>19</sup>F NMR Spectroscopy (recorded at room temperature on a Bruker DPX-400 Spectrometer), ESI-MS (Bruker Micro TOF Spectrometer) and CHN Elemental microanalysis (Exeter CE-440 Elemental Analyser). For syntheses which involved anion metathesis, the complete exchange was confirmed via ion chromatography (Dionex ICS-3000 machine fitted with AS20 analytical column and AG20 guard column).

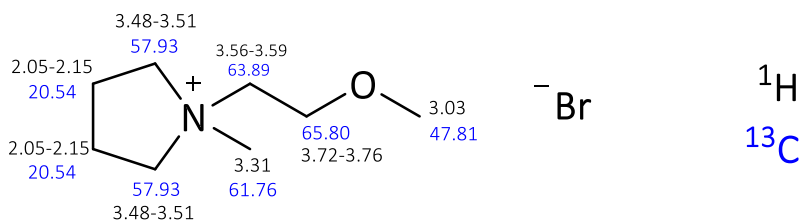
The viscosity and density of the ionic liquids was measured with a stabinger viscometer (Anton Paar, SVM 3000) from 15 to 45 °C. The ILs were dried before the analysis and kept in a sealed flask. The viscometer injection and analysis tubing were fluxed with Argon prior to the analysis and kept sealed during the measurements to avoid moisture uptake. The Arrhenius plots of viscosity can be found in Appendix A.1, and the values at 25 °C are displayed for each individual RTIL in the synthesis description.

The DN of ILs was determined according to methods described previously.<sup>66</sup> NaClO<sub>4</sub> was dissolved in the ILs as the DN probe, and the <sup>23</sup>Na chemical shift was measured. A D<sub>2</sub>O solution of NaCl was used as the reference in a coaxial insert. The calibration line used to determine the DN in the ILs was obtained with solvents of known DN using the same methodology described above. The calibration line can be found in Appendix A.1, and the DN values for the RTILs are displayed in the synthesis description.

### 2.7.1 Synthesis of [C<sub>1</sub>(C<sub>2</sub>OC<sub>1</sub>)Pyrr]Br

In a typical procedure, 2-Bromoethyl methyl ether (14.88 g, 107.07 mmol) was slowly added to a stirring mixture of N-methylpyrrolidine (7.60 g, 89.23 mmol) and ethyl acetate (30 mL). The resulting mixture was heated to 60 °C and left to react for three to four days. The dark solid raw product was filtered and

recrystallised from acetonitrile/ethyl acetate 2-3 times. The resulting solid was filtered, further washed with ethyl acetate and dried at 60 °C under vacuum ( $\leq 10^{-3}$  mbar) yielding a pale yellow solid (18.23 g, 91% yield).



$^1\text{H}$  NMR (400 MHz,  $(\text{CD}_3)_2\text{SO}$ ):  $\delta$  ppm 2.05 – 2.15 (m, 4H), 3.03 (s, 3H), 3.31 (s, 1H), 3.48 – 3.51 (m, 4H), 3.56 – 3.59 (m, 2H), 3.72 – 3.76 (m, 2H);

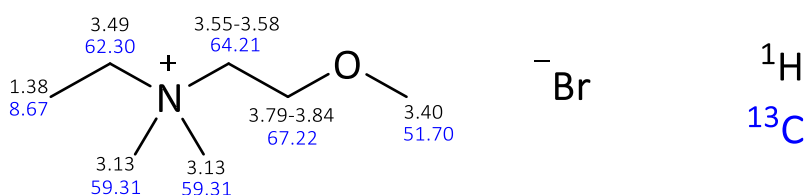
$^{13}\text{C}$  NMR (101 MHz,  $(\text{CD}_3)_2\text{SO}$ ):  $\delta$  ppm 20.54, 47.81, 57.93, 61.76, 63.89, 65.80;

ESI-MS (+ve) for  $[\text{C}_8\text{H}_{18}\text{NO}]^+$ : calcd 144.14, found 144.1392;

Elemental Analysis: calcd  $[(\text{C}_{12}\text{O}_1\text{Pyrr})\text{Br}\cdot\text{H}_2\text{O}]$  C 39.68, H 8.33, N 5.78, found C 39.79, H 8.46, N 5.70.

## 2.7.2 Synthesis of $[\text{N}_{\text{C}_1,\text{C}_1,\text{C}_2,(\text{C}_2\text{OC}_1)]\text{Br}$

In a typical procedure, N,N-dimethyl-N-ethyl-amine (6.90 g, 94.28 mmol) was slowly added to a stirring mixture of 2-Bromoethyl methyl ether (15.73 g, 113.14 mmol) and acetonitrile (30 mL). The resultant mixture was raised in temperature to 35 °C and left to react for five days. The solvent was evaporated, and the crude product, a yellow solid, was recrystallised from acetonitrile/ethyl acetate 2-3 times. The solid product was filtered and dried at 60 °C under vacuum ( $\leq 10^{-3}$  mbar) yielding a white solid (18.56 g, 92.8% yield).



$^1\text{H}$  NMR (400 MHz,  $\text{CD}_3\text{OD}$ ):  $\delta$  ppm 1.38 (tt,  $J=7.28$ , 2.13 Hz, 3 H), 3.13 (s, 6 H), 3.40 (s, 3 H), 3.49 (q,  $J=7.28$  Hz, 2 H), 3.55 - 3.58 (m, 2 H), 3.79 - 3.84 (m, 2 H);

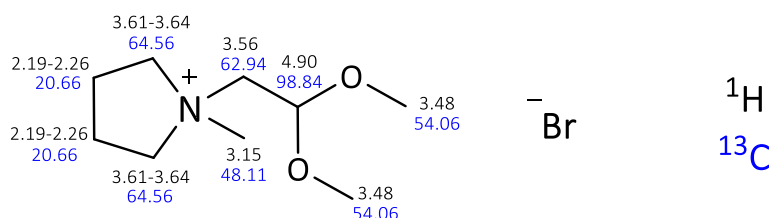
$^{13}\text{C}$  NMR (101 MHz,  $\text{CD}_3\text{OD}$ ):  $\delta$  ppm 8.67, 51.70 (s, 2 C), 59.31 (s, 1 C), 62.30 (s, 1 C), 64.21 (s, 1 C), 67.22 (s, 1 C);

ESI-MS (+ve) for  $[\text{C}_7\text{H}_{18}\text{NO}]^+$ : calcd. 132.14, found 132.1391;

**Elemental Analysis:** calcd. C 39.63, H 8.55, N 6.60, found C 42.12, H 9.15, N 7.20. (GC-MS confirmed impurity to be acetonitrile, drying time and temperature to adjusted for next synthesis).

### 2.7.3 Synthesis of $[\text{C}_1\text{C}_{\text{dma}}\text{Pyrr}]\text{Br}$

In a typical procedure, N-methyl-pyrrolidine (14.88 g, 174.69 mmol) was slowly added to a stirring mixture of 2-Bromo-1,1-dimethylacetate (24.60 g, 145.57 mmol) and acetonitrile (50 mL). The resultant mixture was heated to 40 °C and left to react for three to four days. The solvent was evaporated, and the crude product, a yellow solid, was recrystallised from acetonitrile/ethyl acetate. The solid product was filtered and dried at 60 °C under vacuum (pressure  $\leq 10^{-3}$  mbar) yielding a white solid (28.34 g, 76% yield).



$^1\text{H}$  NMR (400 MHz,  $\text{CD}_3\text{OD}$ ):  $\delta$  ppm 2.19 – 2.26 (m, 4 H), 3.15 (s, 3 H), 3.48 (s, 6 H), 3.56 (d,  $J=5.02$  Hz, 2 H), 3.61 – 3.64 (m, 4 H), 4.90 (t,  $J=5.02$  Hz, 1 H);

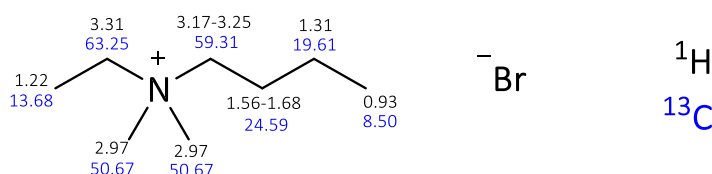
$^{13}\text{C}$  NMR (101 MHz,  $(\text{CD}_3)_2\text{SO}$ ):  $\delta$  ppm 20.66, 48.11, 54.06, 62.94, 64.56, 98.84;

ESI-MS (+ve) for  $[\text{C}_7\text{H}_{18}\text{NO}]^+$ : calcd. 174.15, found 174.1491;

**Elemental Analysis:** calcd. C 42.53, H 7.93, N 5.51, found C 42.63, H 8.04, N 5.50.

### 2.7.4 Synthesis of $[N_{C_1,C_1,C_2,C_4}]Br$

In a typical procedure, N,N-dimethyl-N-ethyl-amine (6.96 g, 95.17 mmol) was slowly added to a stirring mixture of 1-bromobutane (15.6475 g, 114.20 mmol) and acetonitrile (40 mL). The resultant mixture was heated to 35 °C and left to react for five days. The solvent was evaporated, and the crude product, a yellow solid, was recrystallised from acetonitrile/ethyl acetate 2-3 times. The solid product was filtered and dried at 60 °C under vacuum ( $\leq 10^{-3}$  mbar) yielding a white solid (19.3 g, 96.5% yield).



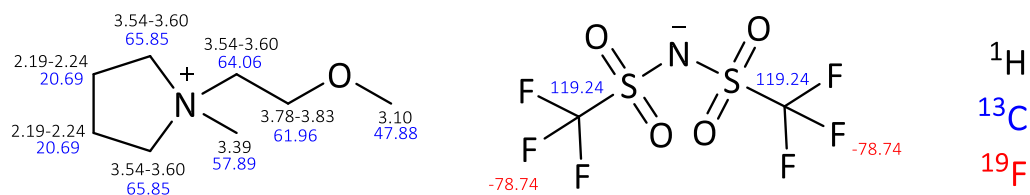
$^1H$  NMR (400 MHz,  $(CD_3)_2SO$ ):  $\delta$  ppm 0.93 (t,  $J=7.34$  Hz, 3 H), 1.22 (tt,  $J=7.30$ , 1.90 Hz, 3 H), 1.31 (sxt,  $J=7.34$  Hz, 2 H), 1.56 - 1.68 (m, 2 H) 2.97 (s, 6 H) 3.17 - 3.25 (m, 2 H) 3.31 (q,  $J=7.30$  Hz, 2 H)

$^{13}C$  NMR (101 MHz,  $CCl_3D$ ):  $\delta$  ppm 8.50, 13.68, 19.61, 24.59, 50.67, 59.31, 63.25.

ESI-MS (+ve) for  $[C_8H_{20}NO]^+$ : calcd. 130.16, found 130.1579;

### 2.7.5 Synthesis of $[C_1(C_2OC_1)Pyrr][NTf_2]$

$Li[NTf_2]$  (12.18 g, 42.42 mmol) was dissolved in ultrapure water (20 mL) and added to a stirring solution of  $[C_1C_{201}Pyrr]Br$  (6.35 g, 35.35 mmol) and ultrapure water (10 mL). The mixture was left to react overnight. The resultant biphasic solution was separated and the aqueous phase was washed with dichloromethane (3 x 10 mL) to extract the remaining  $[C_1C_{201}Pyrr][NTf_2]$ . The combined organic phases were washed with ultra-pure water (10 x 5 mL). Solvent was evaporated and the resulting IL was dried under vacuum (pressure  $\leq 10^{-3}$  mbar) at 60 °C, yielding a yellow liquid (12.20 g, 81.33 % yield).



$^1\text{H}$  NMR (400 MHz,  $\text{CD}_3\text{OD}$ ):  $\delta$  ppm 2.19 - 2.24 (m, 4 H), 3.10 (s, 3 H), 3.39 (s, 3 H), 3.54 - 3.60 (m, 6 H), 3.78 - 3.83 (m, 2 H);

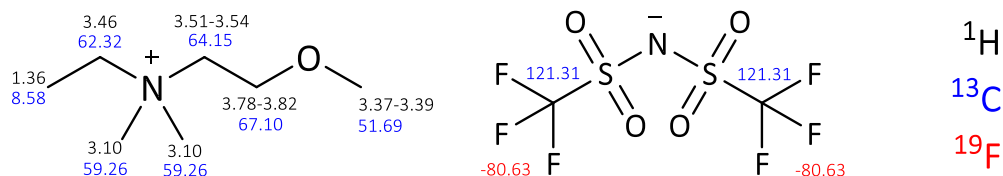
$^{13}\text{C}$  NMR (101 MHz,  $(\text{CD}_3)_2\text{SO}$ ):  $\delta$  ppm 20.69, 47.88, 57.89, 61.96, 64.06, 65.85, 119.24 (q,  $J_{\text{C-F}} = 320$  Hz).

$^{19}\text{F}$  NMR (377 MHz,  $(\text{CD}_3)_2\text{SO}$ ):  $\delta$  ppm -78.74

DN: 10.2

## 2.7.6 Synthesis of $[\text{N}_{\text{C}_1, \text{C}_1, \text{C}_2, (\text{C}_2\text{OC}_1)}][\text{NTf}_2]$

$\text{Li}[\text{NTf}_2]$  (16.71 g, 58.2 mmol) was dissolved in ultrapure water (20 mL) and added to a stirring solution of  $[\text{N}_{\text{C}_1, \text{C}_1, \text{C}_2, (\text{C}_2\text{OC}_1)}]\text{Br}$  (10.29 g, 48.5 mmol) and ultrapure water (10 mL). The mixture was left stirring overnight. The resultant biphasic solution was separated and the aqueous phase was washed with dichloromethane (3 x 10 mL) to extract the remaining  $[\text{N}_{\text{C}_1, \text{C}_1, \text{C}_2, (\text{C}_2\text{OC}_1)}][\text{NTf}_2]$  in water. The combined organic phases were washed with ultra-pure water (10 x 5 mL). Solvent was evaporated and the resulting IL was dried under vacuum ( $\leq 10^{-3}$  mbar) at 60 °C yielding a yellow liquid (17.2 g, 86.0 % yield).



$^1\text{H}$  NMR (400 MHz,  $\text{CD}_3\text{OD}$ ):  $\delta$  ppm 1.36 (tt,  $J = 7.28$ , 2.01 Hz, 3 H), 3.10 (s, 6 H) 3.37 - 3.39 (m, 3 H), 3.46 (q,  $J = 7.28$  Hz, 2 H), 3.51 - 3.54 (m, 2 H), 3.78 - 3.82 (m, 2 H)

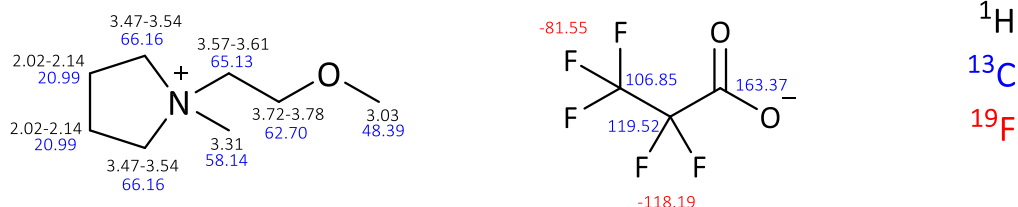
$^{13}\text{C}$  NMR (101 MHz,  $\text{CD}_3\text{OD}$ ):  $\delta$  ppm 8.58, 51.69, 59.26, 62.32, 64.15, 67.10, 121.31 (q,  $J_{\text{C-F}}=300.77$  Hz)

$^{19}\text{F}$  NMR (376 MHz,  $\text{CD}_3\text{OD}$ ):  $\delta$  ppm -80.63;

DN: 9.1

### 2.7.7 Synthesis of $[\text{C}_1(\text{C}_2\text{OC}_1)\text{Pyrr}][\text{C}_2\text{F}_5\text{COO}]$

$[\text{C}_1(\text{C}_2\text{OC}_1)\text{Pyrr}][\text{C}_2\text{F}_5\text{COO}]$  was synthesised via acid-base reaction of  $[\text{C}_1(\text{C}_2\text{OC}_1)\text{Pyrr}][\text{OH}]$  and pentafluoropropionic acid. A solution of  $[\text{C}_1(\text{C}_2\text{OC}_1)\text{Pyrr}]\text{Br}$  (4.46 g, 30.92 mmol) in methanol (10 mL) was eluted through a column of Amberlite ion exchange resin IRA-402(OH) (190 g), at a drop rate of one drop every three seconds into a solution of pentafluoropropionic acid (3.25 mL, 30.92 mmol) in methanol. At the end of the  $[\text{C}_1(\text{C}_2\text{OC}_1)\text{Pyrr}]\text{Br}$  elution, the column was flushed with methanol. The solvent in the resulting  $[\text{C}_1(\text{C}_2\text{OC}_1)\text{Pyrr}][\text{C}_2\text{F}_5\text{COO}]$  solution was evaporated and the product was dried under vacuum for several days (approximately 10 days for water content below 50 ppm), resulting in yellow-brown liquid (8.9 g, 93.7% yield)



$^1\text{H}$  NMR (400 MHz,  $(\text{CD}_3)_2\text{SO}$ ):  $\delta$  ppm 2.02 - 2.14 (m, 1 H), 3.03 (s, 3 H) 3.29 - 3.34 (m, 3 H), 3.47 - 3.54 (m, 4 H), 3.54 - 3.61 (m, 2 H), 3.72-3.78 (m, 2 H);

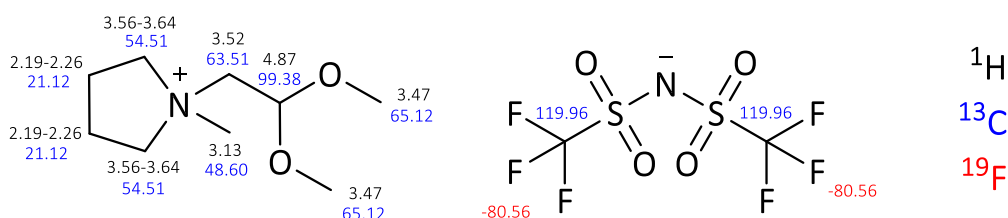
$^{13}\text{C}$  NMR (101 MHz,  $\text{D}_2\text{O}$ ):  $\delta$  ppm 20.99, 48.39, 58.14, 62.69, 65.13, 66.16, 106.85, 119.52, 163.37

$^{19}\text{F}$  NMR (376 MHz,  $(\text{CD}_3)_2\text{SO}$ ):  $\delta$  ppm -118.19, -81.55;

DN: 23.5

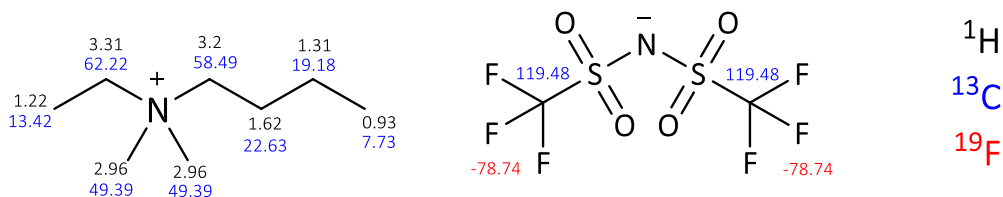
2.7.8 Synthesis of [C<sub>1</sub>C<sub>dma</sub>Pyrr][NTf<sub>2</sub>]

Li[NTf<sub>2</sub>] (13.9 g, 48.42 mmol) was dissolved in water (20 mL) and added to a stirring solution of [C<sub>1</sub>C<sub>dma</sub>Pyrr]Br (11.19 g, 44.01 mmol) and water (15 mL). The mixture was left to react overnight. The resultant biphasic solution was separated and the aqueous phase was washed with dichloromethane (3 x 15 mL) to extract the remaining [C<sub>1</sub>C<sub>dma</sub>Pyrr][NTf<sub>2</sub>] in water. The combined organic phases were washed with ultra-pure water (10 x 5 mL). Solvent was evaporated and the resulting IL was dried under vacuum ( $\leq 10^{-3}$  mbar) at 60 °C yielding a yellow liquid (17.6 g, 88.0 % yield).

2.7.9 Synthesis of [N<sub>C<sub>1</sub>,C<sub>1</sub>,C<sub>2</sub>,C<sub>4</sub></sub>][NTf<sub>2</sub>]

Li[NTf<sub>2</sub>] (23.04 g, 80.25 mmol) was dissolved in water (30 mL) and added to a stirring solution of [N<sub>C<sub>1</sub>,C<sub>1</sub>,C<sub>2</sub>,C<sub>4</sub></sub>]Br (15.33 g, 72.95 mmol) and water (10 mL). The mixture was left stirring overnight. The resulting biphasic solution was separated and the aqueous phase was washed with dichloromethane (3 x 20 mL) to extract the remaining [N<sub>C<sub>1</sub>,C<sub>1</sub>,C<sub>2</sub>,C<sub>4</sub></sub>][NTf<sub>2</sub>] in water. The combined organic phases were washed with ultra-pure water (10 x 5 mL). Solvent was evaporated and the

resulting IL was dried under vacuum ( $\leq 10^{-3}$  mbar) at 60 °C yielding a yellow liquid (28.1 g, 93.7% yield).



$^1\text{H}$  NMR (400MHz,  $\text{CD}_3\text{OD}$ ):  $\delta$  ppm 0.93 (t,  $J=7.40$  Hz, 3 H), 1.22 (t,  $J=7.22$  Hz, 3 H), 1.31 (sxt,  $J=7.40$  Hz, 2H), 1.57 - 1.67 (m, 2 H), 2.96 (s, 6 H), 3.17 - 3.24 (m, 2 H), 3.30 (q,  $J=7.22$  Hz, 2 H);

$^{13}\text{C}$  NMR (101 MHz,  $(\text{CD}_3)_2\text{SO}$ ):  $\delta$  ppm 7.73, 13.42, 19.18, 22.63, 43.39, 58.49, 62.22, 119.48(q,  $J_{\text{C-F}} = 325$  Hz);

$^{19}\text{F}$  NMR (377 MHz,  $(\text{CD}_3)_2\text{SO}$ ):  $\delta$  ppm -78.74

DN: 7.4

## 2.8. References

- Noviandri, I.; Brown, K. N.; Fleming, D. S.; Gulyas, P. T.; Lay, P. A.; Masters, A. F.; Phillips, L., The Decamethylferrocenium/Decamethylferrocene Redox Couple: A Superior Redox Standard to the Ferrocenium/Ferrocene Redox Couple for Studying Solvent Effects on the Thermodynamics of Electron Transfer. *J. Phys. Chem. B* **1999**, *103* (32), 6713-6722.
- Compton, R. G.; Craig, E. B., Hydrodynamic Electrodes. In *Understanding Voltammetry*, World Scientific: 2010; pp 291-346.
- Berg, H., The electrochemical cell. In *Batteries for Electric Vehicles: Materials and Electrochemistry*, Berg, H., Ed. Cambridge University Press: Cambridge, 2015; pp 7-46.
- Passarelli, M. K.; Pirkl, A.; Moellers, R.; Grinfeld, D.; Kollmer, F.; Havelund, R.; Newman, C. F.; Marshall, P. S.; Arlinghaus, H.; Alexander, M. R.; West, A.; Horning, S.; Niehuis, E.; Makarov, A.; Dollery, C. T.; Gilmore, I. S., The 3D OrbiSIMS—label-free metabolic imaging with subcellular lateral resolution and high mass-resolving power. *Nat. Methods* **2017**, *14* (12), 1175-1183.
- Zubarev, R. A.; Makarov, A., Orbitrap mass spectrometry. *Anal. Chem.* **2013**, *85* (11), 5288-96.
- Graham, D. J.; Castner, D. G., Multivariate analysis of ToF-SIMS data from multicomponent systems: the why, when, and how. *Biointerphases* **2012**, *7* (1-4), 49.
- de Juan, A.; Jaumot, J.; Tauler, R., Multivariate Curve Resolution (MCR). Solving the mixture analysis problem. *Anal. Methods* **2014**, *6* (14), 4964-4976.

8. Abbott, A. P., Application of hole theory to the viscosity of ionic and molecular liquids. *Chemphyschem* **2004**, *5* (8), 1242-1246.
9. Schmeisser, M.; P., I.; Puchta, R.; Zahl, A.; van Eldik, R., Gutmann donor and acceptor numbers for ionic liquids. *Chem. - Eur. J.* **2012**, *18*, 10969-10982.
10. Blundell, R. K.; Licence, P., Quaternary ammonium and phosphonium based ionic liquids: a comparison of common anions. *Phys Chem Chem Phys* **2014**, *16* (29), 15278-88.
11. Dinarès, I.; Garcia de Miguel, C.; Ibáñez, A.; Mesquida, N.; Alcalde, E., Imidazolium ionic liquids: A simple anion exchange protocol. *Green Chemistry* **2009**, *11* (10), 1507.
12. Moreno, M.; Montanino, M.; Carewska, M.; Appetecchi, G. B.; Jeremias, S.; Passerini, S., Water-soluble, triflate-based, pyrrolidinium ionic liquids. *Electrochimica Acta* **2013**, *99*, 108-116.

# 3. Electrochemical performance and stability of Na metal electrode with IL-based electrolytes

## 3.1. Introduction

Li-ion batteries have revolutionised the electronics and transportation sector, and although development dates back to the 1990s, they are still the leading commercially available electrochemical storage technology in terms of life cycle, specific energy and energy density.<sup>3, 70</sup> However, Li-ion batteries are not predicted to meet the future demands of energy storage, particularly to enable the widespread electrification of transport. Current Li-ion battery cells primarily use graphite sheets as the negative electrode, a variety of metal oxides as the positive electrode (LiCoO<sub>4</sub>, LiFePO<sub>4</sub>, etc), and its high cyclability relies upon the intercalation of Li cations into the electrodes. The specific energy of these materials is typically below 400 mAh/g for graphite and 200 mAh/g for LiNi<sub>0.8</sub>Co<sub>0.15</sub>Al<sub>0.05</sub>O<sub>2</sub> (NCA), which is one of the positive electrodes with the highest capacity. This leads to the belief that the cathode side is the limiting factor in current battery capacity, encouraging the development of very distinctive battery concepts, such as Li-O<sub>2</sub><sup>29</sup> and Li-S.<sup>71</sup> However, Albertus *et al* clearly discussed the impact on cell capacity of replacing graphite electrodes with lithium metal, and demonstrated that actually the weight and volume of graphite imposes the upper limit in Li-ion energy metrics<sup>3</sup>. Li metal batteries are estimated to have nearly twice the specific energy and three times the energy density of Li-ion batteries, as shown in Figure 3.1.<sup>3</sup> Hence Li metal is often regarded as the “*holy grail*” of battery negative electrodes, as it would not only

revolutionise “*beyond Li-ion*” batteries, such as Li-S or Li-O<sub>2</sub>, but also much improve the capacity of current technologies.

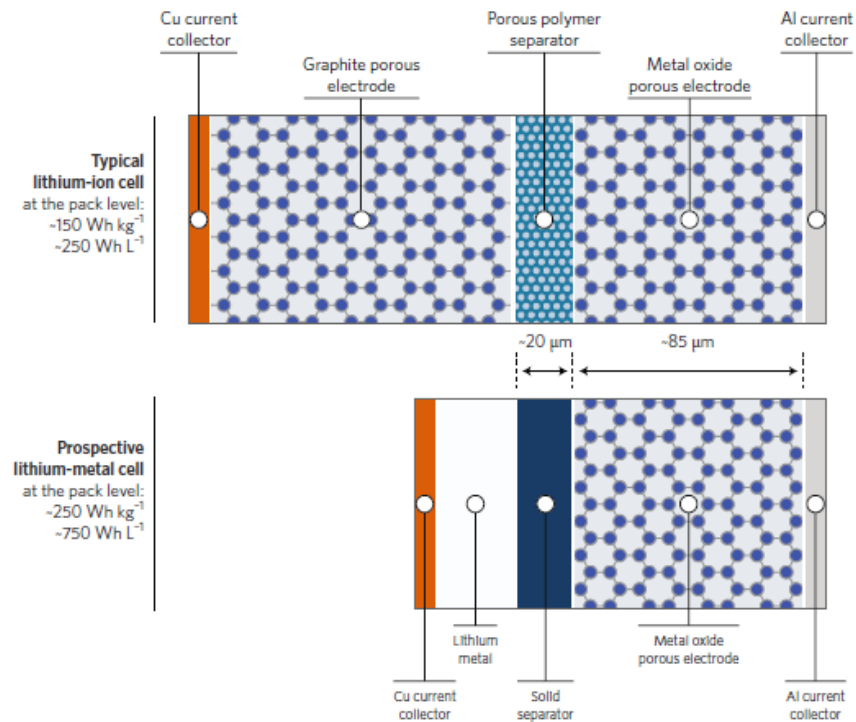


**Figure 3.1.** Typical Li-ion cell (top) and projected Li-metal cell (bottom), demonstrating differences in volume and weight by replacing graphite anode with Li metal.<sup>3</sup>

Na based batteries promise to be a more sustainable long-term energy storage alternative, due to higher Na natural abundance compared to Li, and its geographic distribution throughout the globe.<sup>6, 57, 72-74</sup> Similar to Li, Na is the negative electrode of choice of several Na based batteries,<sup>8, 21</sup> such as Na-O<sub>2</sub>, Na-S, and Na-ion. However, several challenges still prevent the use of alkali metal electrodes in any of the battery technologies mentioned above, such as low coulombic efficiency and safety concerns due to dendrite growth.<sup>3</sup> In fact, dendrite formation is the main failure mechanism of Li metal. Lack of uniformity at the electrode surfaces is the greatest trigger for dendrite formation and growth.<sup>9</sup> This non-uniformity can be intrinsic to the electrode material itself, due to cell assembly/preparation process<sup>9</sup> and/or due to a non-stable and non-protective solid electrolyte interphase (SEI) layer, which will be discussed in the following paragraphs. During the charge process, plating occurs with Li<sup>+</sup> or Na<sup>+</sup>

being reduced at the electrode surface. The lack of homogeneity mentioned above causes non-uniform current density across the electrode, and consequently, a non-uniform plating process. This is the first step towards the formation of dendrites, which due to the constant surface modification during cycling (plating/stripping process) are likely to grow.<sup>8</sup> The dendrites can disconnect from the electrode and move through the electrolyte, causing significant loss of active material.<sup>13</sup> Dendrites may also continue to grow, crossing the separator and causing short circuit by contacting the opposite electrode. Short circuits are one of the main triggers for thermal runaways which are likely to be disastrous, especially for large battery packs with highly flammable electrolytes.<sup>9</sup> Hence research towards developing alkali metal electrodes is crucial to safely advance several battery technologies, from more complex alternatives involving S and O<sub>2</sub> to more common ion-based batteries.

Methods of stabilising the highly active surface of alkali metal electrodes have been studied and revised previously,<sup>7, 8, 15, 17</sup> including mechanical treatment used to strategically control dendrite development, use of protective layers, and design of electrolytes to promote the formation of a stable SEI. SEI is a layer formed at the electrode surface by electrolyte decomposition products.<sup>8, 21, 75</sup> The formation of SEI is crucial for the performance of lithium ion batteries and, in fact, finding electrolytes that would form a stable SEI on graphite electrodes strongly supported the breakthrough of li-ion cells in the 1990s.<sup>9</sup> In Li-ion cells, the potential of the graphite electrode during lithiation lies outside of the electrochemical stability window (ESW) of most electrolytes. Consequently, during the first cell cycle, the electrolyte decomposes, forming a SEI layer at the electrode.<sup>76, 77</sup> Stable SEIs form across the entire graphite electrode, protecting it from further react with the electrolyte, allowing stable cell cycling.<sup>76</sup>

When using alkali metal electrodes, such as Li and Na, the same SEI formation pathway may be observed, as Li and Na plating/stripping reaction occurs at potentials more negative than the cathodic limit of the ESW of the electrolytes. In addition, the strong reducing characteristic of alkali metals leads

to electrolyte breakdown even during open cell potential and SEI can be formed simply by having the alkali metal in contact with the electrolyte. Similar to Li-ion cells, a stable SEI layer is beneficial to the cell by protecting the bare metal from further reacting with the electrolyte.<sup>8</sup> The SEI formation mechanism, growth and composition have significant impact on cell performance.<sup>11, 12, 78, 79</sup> Unstable SEIs can lead to metal and electrolyte overconsumption and depletion in the long term.<sup>33</sup> An unstable SEI may also crack during cell cycling, exposing bare metal, leading to formation of dendrites.<sup>8, 11</sup> Therefore, deep understanding of SEI layers is crucial in advancing the use of alkali metal electrodes. Ideally, an SEI should display high ion conductivity to allow uniform diffusion of Li or Na cations through the layer. In addition, the SEI layer should have a homogeneous surface and conductivity, to allow uniform ion flux and prevent the formation of “hot spots” for dendrite growth. The SEI should also be stable in the presence of the electrolyte, to inhibit further reaction over time. Battery electrodes are also constantly facing significant volume changes because of the plating/stripping reactions. For this reason, the SEI should be mechanically stable to support such volume changes without rupturing.

Several studies have correlated cycling performance with SEI properties and composition.<sup>12, 33, 35, 39, 77-83</sup> SEI in Li electrodes have been extensively studied in literature and reviewed in a number of papers, and many Li SEI findings can be translated into Na systems.<sup>3, 72, 75, 84</sup> However, critical physical and electrochemical parameters between the two elements may lead to different trends in Li and Na cells.<sup>16, 80</sup> In 2009, Aubarch *et al* thoroughly studied surface reactions at Li electrodes in electrolytes based on 1-3 dioxolane (DOL) and Li[NiF<sub>2</sub>], Li[NO<sub>3</sub>] and Li<sub>2</sub>S<sub>6</sub>. Based on a combination of FTIR and XPS data, as well as electrochemical observations, the authors suggested the reduction of DOL in the presence of Li metal led to the formation of radical fragments, which could undergo radical oligomerisation. The authors also found that the presence of Li[NO<sub>3</sub>] additives in the electrolyte resulted in a more controlled and protective layer on the Li anode, diminishing side reactions of Li metal and polysulfide in Li-S batteries.<sup>85</sup> Another study<sup>81</sup> used XPS to investigate SEI composition on Na

metal suggested that the use of polysulfides as an additive resulted in a stable and protective SEI layer, and the opposite effect was observed when  $\text{NaNO}_3$  was included. The electrolyte composition containing sodium polysulfide increased the long-term stability of Na symmetrical cells.<sup>81</sup> Despite these reports, certain trends have been agreed across literature, including the positive effect of the presence of fluoride in SEI composition,<sup>12, 33-35</sup> the possibility of radical induced oligomerisation,<sup>33, 85-87</sup> and the improved cell performance when a stable SEI layer is obtained.<sup>33, 35, 57</sup>

Ionic liquids (ILs) are particularly interesting electrolyte options from a safety perspective because of their nonflammability, and negligible volatility.<sup>88</sup> Additionally, the high tunability of ILs mean specific properties may be enhanced, including their electrochemical stability window, which can minimise electrolyte decomposition during cell cycling. A recent study<sup>87</sup> also introduced the idea of '*cationic SEI-former*' ILs and evaluated the effect of a range of features in IL cations on their reduction ability. The authors calculated the reduction potential of the modified cations, their thermodynamic stability and carried out reaction pathway calculations to predict the composition of an SEI layer formed in those ILs. The study suggested that addition of certain features, such as vinyl or allyl side groups, to the IL cation would enhance the radical polymerisability of ILs and would contribute to the formation a protective layer onto the standard SEI.<sup>87</sup> [FSI]-based ILs have demonstrated better stability and reversibility in Na plating and stripping in comparison to its equivalent ILs with  $[\text{NTf}_2]^-$  anions.<sup>57</sup> XPS results over certain etching times, suggested that although displaying very similar SEI composition,  $[\text{NTf}_2]^-$  forms a thicker SEI layer. This was also observed with electrochemical impedance spectroscopy (EIS).<sup>57</sup> Similar results have been observed by Forsyth *et al*, using [DCA]-based ILs with a range of Na salts.<sup>35</sup> In addition, chloroaluminate IL based electrolytes have shown high cyclability combined with improved safety in Na metal batteries.<sup>39</sup> Recently, Forsyth and co-workers<sup>56</sup> have studied the effect of salt concentration in IL electrolytes using atomic force microscopy and molecular dynamics. The study successfully demonstrated that the improved cycling performance with

concentrated electrolytes (50 mol % salt) was due to the interphase structure formed, which contained salt aggregates within the innermost layers and IL cations within the outermost layer.

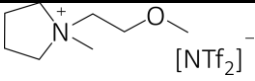
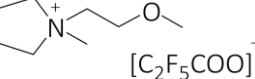
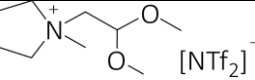
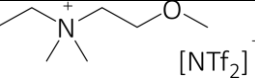
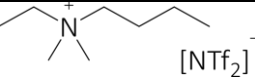
In conclusion, several studies have explored the use of certain additives, or the choice of salt and type of liquid in the electrolyte design to improve metal electrode performance. In our study, we aim to explore one of the most remarkable properties in ILs, their tunability. We propose that even simple changes in the IL structure may significantly impact the performance and stability of Na electrodes. To investigate this, we carried out a comprehensive study on Na<sup>+</sup> plating/stripping with symmetrical cell galvanostatic cycling, electrode surface resistance over (resting and cycling) time with electrochemical impedance spectroscopy, and a novel investigation of SEI structure and composition with 3D Orbitrap<sup>TM</sup> secondary ion mass spectrometry (3D OrbiSIMS). The unique sensitivity and mass resolution of 3D OrbiSIMS,<sup>61</sup> allowed us to obtain vast and detailed information of the SEI in these IL-based electrolytes, leading to much greater accuracy in designing high performing stable electrolytes for use in Na-electrode cells. Finally, a comparison between composition and structure of the SEI was also performed using Na[PF<sub>6</sub>] as an additive, to thoroughly evaluate the effect of composition and structure on cell performance. This comprehensive study builds upon the conclusions of previous work covering a wide range of fields including Li metal mechanisms and IL interface and degradation, to advance the understanding of high performing stable electrolytes for application in alternative battery chemistries.

## 3.2. Experimental

### 3.2.1 Electrolyte preparation

A summary of the ILs studied in this chapter are displayed in Table 3.1, which were synthesised as described in Chapter 2. Section 3.3.1 shows the rationale for the choice of anions and cations.

Table 3.1. Summary of ILs used in electrolytes studied in this chapter

IL structure	IL abbreviation
	[C <sub>1</sub> (C <sub>2</sub> OC <sub>1</sub> )Pyrr][NTf <sub>2</sub> ]
	[C <sub>1</sub> (C <sub>2</sub> OC <sub>1</sub> )Pyrr][C <sub>2</sub> F <sub>5</sub> COO]
	[C <sub>1</sub> C <sub>dma</sub> Pyrr][NTf <sub>2</sub> ]
	[N <sub>C<sub>1</sub>,C<sub>1</sub>,C<sub>2</sub>,C<sub>2</sub>OC<sub>1</sub>}] [NTf<sub>2</sub>]</sub>
	[N <sub>C<sub>1</sub>,C<sub>1</sub>,C<sub>2</sub>,C<sub>4</sub>}] [NTf<sub>2</sub>]</sub>

Prior to electrolyte preparation, ILs were dried under vacuum ( $\leq 10^{-3}$  mbar) in a Schlenk line at 50 °C until their water content was below 40 ppm (measured by Karl Fisher titration). Na<sup>+</sup> salts were dried under vacuum ( $\leq 10^{-3}$  mbar) at 110 °C for 24 h. All electrolytes were prepared within a glovebox, and unless stated, Na<sup>+</sup> salts with the equivalent anion in the IL were used (e.g. [NTf<sub>2</sub>]<sup>-</sup> IL electrolyte prepared with Na[NTf<sub>2</sub>] salt). Na[PF<sub>6</sub>] was used as an additive in selected electrolytes, and was previously dried under vacuum for 48 h at 50 °C under vacuum ( $\leq 10^{-3}$  mbar). The salt concentration in the electrolytes was kept at 0.5 M as the upper limit due to saturation being reached in some ILs.

### 3.2.2 Cyclic voltammetry

Na redox reactions in the electrolytes described in Section 3.2.1. were studied using cyclic voltammetry (Autolab PGSTAT302, EcoChemie, Netherlands) in a three-electrode cell. For a set of experiments, glassy carbon (GC, 3 mm) was used as the working electrode (WE) and a platinum coil (Pt coil) was used as the counter electrode (CE). Prior to use, GC electrode was polished with alumina suspension in ultrapure water, thoroughly rinsed with ultrapure water, and acetone. A Na flag reference electrode (RE) was freshly prepared for

each electrolyte before each set of experiments as follows. Within a glovebox (Braun, Argon filled), two layers of Na were cut from a clean Na metal cube, the oxidised parts were removed and disposed, and the layers were flattened into two thin sheets (thickness < 1 mm). Polished Cu wires were placed in between the metal sheets, and this Na-Cu-Na pack was further compressed to ensure good contact between the metals. The flags were cut out and used as RE for cyclic voltammetry experiments. Another set of experiments used Na metal as the WE, CE and RE, prepared as described above. iR compensation was used in all experiments.

### **3.2.3 Electrochemical impedance spectroscopy and symmetrical cell plating/stripping experiments**

Symmetrical Na cells were built using Swagelok fittings and used for both electrochemical impedance spectroscopy (EIS) and plating/stripping experiments. Schematics of the cells are shown in Figure 3.2. The Swagelok cells were composed of stainless steel (SS)  $\frac{1}{2}$  in nuts and  $\frac{1}{2}$  in body, and the SS rod ( $\varnothing = \frac{1}{2}$  in) was fitted with PTFE front and back ferrules. The potentiostat connection was made with 1 mm banana plugs through a hole on the outer side of the SS rod. Na electrodes were prepared by cutting the oxidised parts from a clean Na cube and flattening the cube into a thin Na sheet (< 1 mm thickness) within a glovebox. Discs (12 mm diameter) were cut out and used as working and counter/reference electrodes. The Na electrodes were placed in contact with the SS, which act as the current collectors. Glass fibre discs (12.8 mm diameter, 0.26 mm thickness, 1.6  $\mu\text{m}$  pore size) were previously dried under vacuum at 330 °C and used as the separator. The separators were placed in between the electrodes and wet with 105  $\mu\text{L}$  of electrolyte. A PTFE film (50  $\mu\text{m}$  thickness) was placed on the internal walls of the Swagelok body to prevent short-circuit.

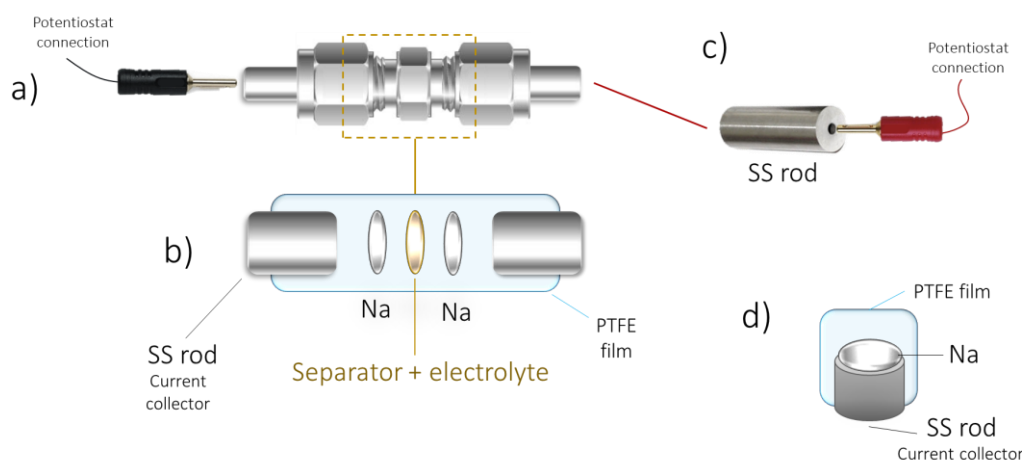


**Figure 3.2.** Symmetrical Swagelok cells used in EIS and Na cycling studies: a) Assembled cell showing potentiostat connection on the left with 1 mm banana plugs, SS rod current collector ( $\varnothing = \frac{1}{2}$  in), Swagelok nuts and body ( $\frac{1}{2}$  in parts); b) exploded view of internal cell components within PTFE insulating film: SS rod current collector, Na electrode (12 mm disc), glass fibre separator ( $\varnothing = \frac{1}{2}$  in) embedded with 105  $\mu\text{L}$  electrolyte, and Na electrode; c) SS rod showing 1 mm banana plug connection to potentiostat; d) Na electrode adhered to SS rod current collector. Cells assembled within an Ar glovebox ( $\text{H}_2\text{O}$  and  $\text{O}_2 < 1$  ppm).

EIS was used to estimate changes in cell resistance during open cell potential. A 0.01 V potential bias was applied to the cell, with frequencies varying from  $1 \times 10^5$  Hz to 0.1 Hz. Two cells of the same electrolyte were assembled each time, and the cell impedance was measured periodically for up to 4 days. Plating and stripping experiments were carried out for 30 min polarization time, with  $\pm 2$  V cut off potential limit.

### 3.2.4 SEI composition study with 3D OrbiSIMS

Cryo 3D OrbiSIMS was used to investigate the composition of the SEI of Na and IL based electrolytes. The cryo 3D OrbiSIMS (Hybrid SIMS, IONTOF GmbH, Germany) is equipped with a fully proportional–integral–derivative temperature controller which controls resistive heating and a direct liquid  $\text{N}_2$  closed loop circulation cooling stage, allowing sample temperature control within the load lock and main chamber. Being installed with cryogenic storage

tanks, liquid N<sub>2</sub> was pumped for circulating the cooling medium through vacuum feedthroughs to a cooling finger below the sample, allowing fast cooling to -180 °C with a stability of  $\pm 1-2$  °C for at least seven days. This system allows for full sample movement in x, y, z, rotate and tilt directions whilst under cryogenic conditions.

Before the measurement, the samples were prepared as half cells described as follows. Within a glovebox, separators discs (6 mm diameter, dried as described in 3.2.3) were placed in individual dry aluminium containers, and wet with 20  $\mu$ L of electrolyte. Na metal electrodes (6 mm diameter discs) were prepared according to section 3.2.3, and stuck onto gold planchets. The planchets were placed on the wet separators described above, having Na in contact with the electrolyte. Prior the experiment, the planchets were placed on a sample holder and stage, and immersed in liquid N<sub>2</sub>, to keep an inert atmosphere during transfer from the glovebox to the cryo-manipulation station, Leica EM VCM (Leica, Germany), from where they are transferred to the cryo-OrbiSIMS using a shuttle chamber Leica EM VCT500 (Leica, Germany) (a detailed description is given in the supporting protocol of reference <sup>89</sup>). All experiments were run 73 h after sample preparation and the analyses were conducted at <-175 °C. The data obtained from the 3D OrbiSIMS had mass calibration of the Q Exactive instrument performed using silver cluster ions. Electrons with an energy of 21 eV (current approximately 10  $\mu$ A) and Ar gas flooding were used for charge compensation. The 3D OrbiSIMS used in this work has previously been described<sup>61</sup> (mode 4 single beam, 20 keV Ar<sub>3000</sub><sup>+</sup>, Orbitrap MS). The orbitrap analyser was operated in positive-ion mode at the 240,000 at m/z 200 mass-resolution setting (512 ms transient time). For depth profiling and spectra, a 284.8  $\times$  284.8  $\mu$ m<sup>2</sup> region (analyse in the central 200  $\times$  200  $\mu$ m<sup>2</sup> region) of sample was sputtered using defocused 20 keV Ar<sub>3000</sub><sup>+</sup> beam for 2.0 s per cycle. The gas cluster ion beam (GCIB) target current was 0.23 nA. The total ion dose was 1.17-1.27 $\times 10^{17}$  ions/cm<sup>2</sup>. Peak assignment was performed with aid of the data analysis software, SurfaceLab from Iontof. Although no mechanism is proposed for each assignment, they represent clusters of atoms/molecules sputtered

from the Na surface, based on reactions proposed in literature for SEI formation, and based on fundamental principles of radical-initiated reactions.<sup>87, 90-92</sup>

### 3.2.5 Multivariate analysis

Multivariate analysis of 3D OrbiSIMS dataset was carried out using a MATLAB software extension developed by Dr. Gustavo Trindade, the *simsMVA*.<sup>93</sup>

Principal component analysis (PCA) and non-negative matrix factorisation (NMF) were performed using the profiles mode in the software. The dataset was mean-centred prior calculation of the PCs, and the algorithm used in PCA was singular value decomposition. The number of NMF endmembers was obtained with PCA (see Chapter 2 for details), and multiplicative update was the algorithm used to calculate NMF, with random initial conditions and 500 iterations.

## 3.3. Electrochemical studies of electrolyte effect on $\text{Na}^0/\text{Na}^+$ redox reactions

### 3.3.1 Rationale for IL selection

It was discussed that the SEI in alkali metal electrodes can be formed simply via chemical reactions when the highly reactive metal is in contact with the electrolyte. With this in mind and taking advantage of the high tunability property of ILs, the electrolytes chosen for this study were carefully designed. Ideally, electrolytes should have a wide electrochemical stability window, whilst displaying high conductivity, hence low viscosity and promote a stable SEI formation.

Despite the relatively low viscosity of imidazolium based ILs, which is attractive for electrochemical applications, imidazolium ILs display much narrower ESW compared to other equivalent IL systems.<sup>88</sup> Quaternary

ammonium based ILs, in turn, are known for having large cathodic limit, and consequently wider ESW than equivalent imidazolium ILs. For this reason, all ILs studied in this chapter are based on pyrrolidinium and quaternary ammonium cations. The greater electrochemical stability of the ILs chosen for this study comes at the cost of higher viscosity, as shown in Table 3.2. Table 3.2 shows a summary of the viscosities of the neat ILs studied, and of [EMIM][NTf<sub>2</sub>] and tetraethyleneglycol dimethylether (a typically used organic solvent in battery applications) for comparison. Ether side chains (-C<sub>2</sub>OC<sub>1</sub>) were introduced to decrease the viscosity of the ILs, however, they may also shorten the ESW, so hydrocarbon side chains (-C<sub>4</sub>) were also investigated for comparison.

**Table 3.2.** Summary of dynamic viscosities ( $\eta$ ) of IL studied in this chapter at 20°C, [EMIM][NTf<sub>2</sub>]<sup>94</sup> and tetraethyleneglycol dimethylether (TEGDME)<sup>95</sup>

IL	$\eta$ (mPa.s)
[C <sub>1</sub> (C <sub>2</sub> OC <sub>1</sub> )Pyrr][NTf <sub>2</sub> ]	74.0
[C <sub>1</sub> (C <sub>2</sub> OC <sub>1</sub> )Pyrr][C <sub>2</sub> F <sub>5</sub> COO]	103.7
[C <sub>1</sub> C <sub>dma</sub> Pyrr][NTf <sub>2</sub> ]	120.2
[N <sub>C<sub>1</sub>,C<sub>1</sub>,C<sub>2</sub>,C<sub>2</sub>OC<sub>1</sub></sub> ][NTf <sub>2</sub> ]	64.4
[N <sub>C<sub>1</sub>,C<sub>1</sub>,C<sub>2</sub>,C<sub>4</sub></sub> ][NTf <sub>2</sub> ]	115.1
[EMIM][NTf <sub>2</sub> ]	38.6
TEGDME	4.1

Finally, structural variations were introduced to the IL to examine changes within the IL cation-anion interactions, as well as solvent-solute interactions. For example, ILs based on acetate anions ([Ac]<sup>-</sup>) have higher H-bond ability than [NTf<sub>2</sub>]<sup>-</sup> anions, as demonstrated by their Kamlet-Taft parameter hydrogen bond acceptor ability ( $\beta$ ) 0.95 for [EMIM][Ac] and 0.28 for [EMIM][NTf<sub>2</sub>].<sup>96</sup> This means that acetate-based ILs are more likely to disrupt certain intermolecular interactions as H-bonding and to solvate electron deficient molecules/ions, compared to [NTf<sub>2</sub>]-based ILs. This has long been observed for example, in the superior dissolution of polysaccharides in acetate-

based ILs compared to [NTf<sub>2</sub>]-ILs.<sup>97</sup> Nevertheless, acetate-based ILs are hydrophilic, challenging to a certain extent its application in electrochemical devices. For this reason, pentafluoropropionate was the anion of choice to synthesise high DN ILs, as it has the  $-\text{[COO]}^-$  unit but the fluoride content makes it less hydrophilic.

### 3.3.2 Cyclic voltammetry of Na<sup>+</sup> containing ILs

Cyclic voltammetry was used to evaluate Na<sup>0</sup>/Na<sup>+</sup> redox reaction in the electrolytes based on the ILs shown on Table 3.1. The cyclic voltammograms (CVs) are shown in Figure 3.3.

Figure 3.3 shows the CVs of the IL electrolytes containing 0.5 M Na<sup>+</sup> salt, (salt counter ion accordingly to the IL anion) whereas the grey dotted lines are related to Na<sup>+</sup> salt free ILs. All experiments were set to start at +0.5 V vs Na<sup>0</sup>/Na<sup>+</sup> and scanning direction towards negative potentials (cathodic scan), as indicated by the arrows in Figure 3.3. The peaks shown by the blue lines during the cathodic scan are attributed to Na<sup>+</sup> reduction (plating). Overall, Na<sup>+</sup> reduction occurred at considerably lower potential (between -0.25 and -0.50 V vs Na<sup>0</sup>/Na<sup>+</sup>) than expected, and this could be attributed to slow Na<sup>+</sup> diffusion, consequence of the high viscosity of the electrolytes. To evaluate this more clearly, the onset potential for Na<sup>+</sup> reduction is displayed on Table 3.3.

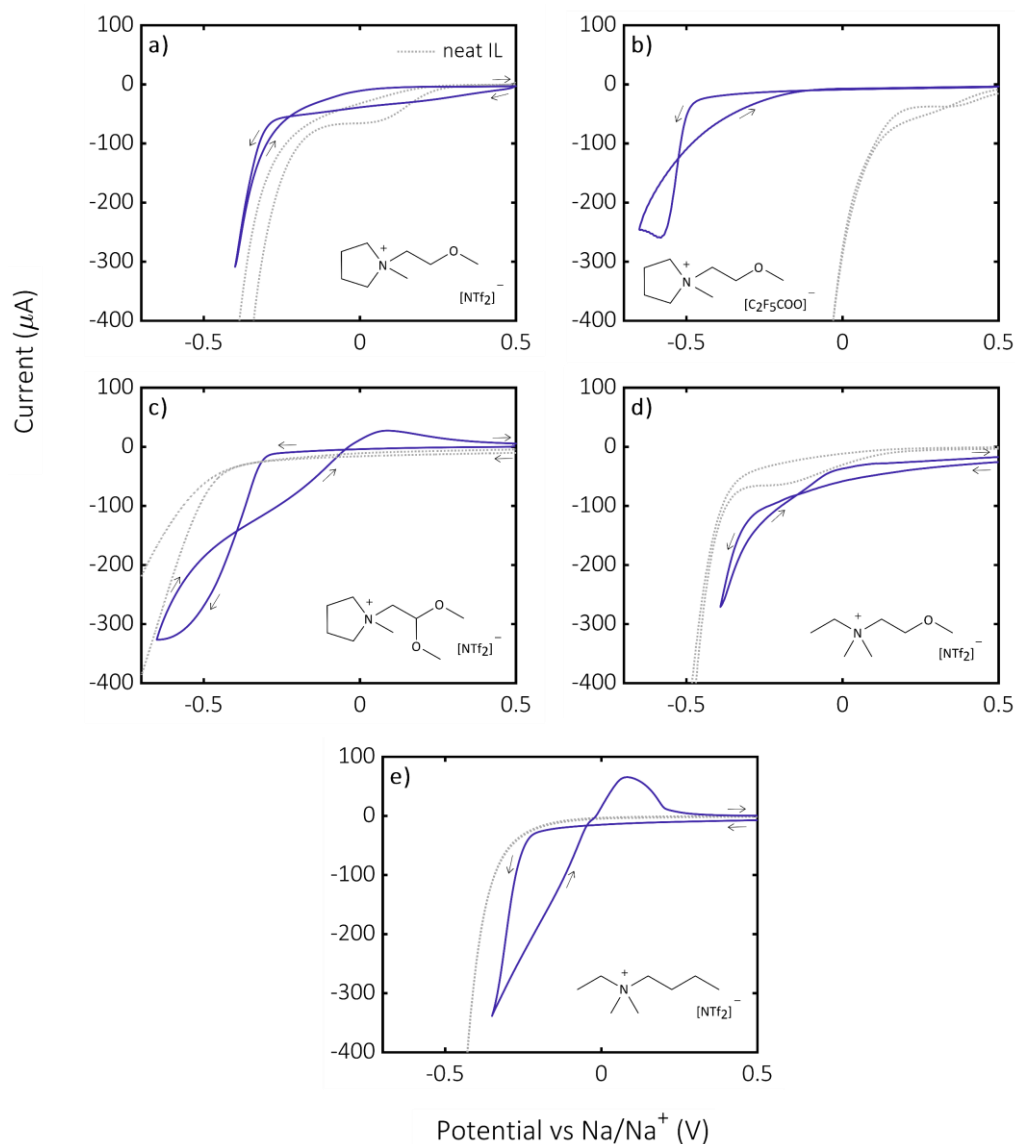


**Figure 3.3.** CVs of 0.5 M Na<sup>+</sup> in the IL based electrolytes showing Na<sup>+</sup> reduction in the cathodic scan, at 100 mV.s<sup>-1</sup> using glassy carbon working electrode, Pt coil counter electrode and Na flag reference electrode. Arrows show scanning direction and grey dotted line shows CVs of Na<sup>+</sup>-free ILs. **a)** [C<sub>1</sub>(C<sub>2</sub>OC<sub>1</sub>)Pyrr][NTf<sub>2</sub>], **b)** [C<sub>1</sub>(C<sub>2</sub>OC<sub>1</sub>)Pyrr][C<sub>2</sub>F<sub>5</sub>COO], **c)** [C<sub>1</sub>C<sub>dma</sub>Pyrr][NTf<sub>2</sub>], **d)** [N<sub>C<sub>1</sub>,C<sub>1</sub>,C<sub>2</sub>,C<sub>2</sub>OC<sub>1</sub>}] [NTf<sub>2</sub>], and **e)** [N<sub>C<sub>1</sub>,C<sub>1</sub>,C<sub>2</sub>,C<sub>4</sub>}] [NTf<sub>2</sub>] IL-based electrolytes. Note the differences in Na<sup>+</sup> reduction onset potential (also shown in **Table 3.3**) with variation in the IL structure, the absence of a Na<sup>0</sup> stripping peak in some electrolytes, and that Na<sup>+</sup> reduction lays outside the ESW (in grey) of [C<sub>1</sub>(C<sub>2</sub>OC<sub>1</sub>)Pyrr][NTf<sub>2</sub>] and [C<sub>1</sub>(C<sub>2</sub>OC<sub>1</sub>)Pyrr][C<sub>2</sub>F<sub>5</sub>COO].</sub></sub>

Diffusion of active species towards the electrode surface is known to affect the shape of cyclic voltammograms.<sup>98, 99</sup> Although diffusion may be related to an overall more negative reduction potential in all ILs, data shown in Table 3.2 and Table 3.3 shows that there is no clear correlation between onset potential and viscosity of the neat ionic liquids studied. However, the addition of Na<sup>+</sup> salts is likely to increase considerably the viscosity of the electrolytes,<sup>100, 101</sup> and this increase may be more or less significant to each individual electrolyte depending on the interactions among Na<sup>+</sup> and IL ions.<sup>102</sup> The ILs used in this study have differences in their structure, and consequently different ‘electron donating abilities’ as reflected by the Gutmann donor numbers (DNs) shown in Table 3.3. The Gutmann DN is an empirical measure of the tendency of a solvent to donate electrons to electron-deficient solutes.<sup>66</sup> Table 3.3 shows a subtle correlation between DN and reduction potential onset was found, which is a result of a stronger solvation of Na<sup>+</sup> by the higher DN ILs, hence slower Na<sup>+</sup> diffusion and more negative reduction potential onset. This is clearly evident by comparing the data of [C<sub>1</sub>(C<sub>2</sub>OC<sub>1</sub>)Pyrr][NTf<sub>2</sub>] and [C<sub>1</sub>(C<sub>2</sub>OC<sub>1</sub>)Pyrr][C<sub>2</sub>F<sub>5</sub>COO], as the DN doubles in value, the E<sub>onset,red</sub> becomes considerably more negative.

**Table 3.3.** Onset potential for Na<sup>+</sup> reduction (E<sub>onset,red</sub>) for each IL-based electrolyte (0.5 M Na<sup>+</sup> salt in IL), compared to the donor number (DN) of ILs. Note the slight correlation between E<sub>onset,red</sub> and DN.

IL	E <sub>onset,red</sub> (V)	DN
[C <sub>1</sub> (C <sub>2</sub> OC <sub>1</sub> )Pyrr][NTf <sub>2</sub> ]	-0.32	10.2
[C <sub>1</sub> (C <sub>2</sub> OC <sub>1</sub> )Pyrr][C <sub>2</sub> F <sub>5</sub> COO]	-0.49	23.5
[C <sub>1</sub> C <sub>dma</sub> Pyrr][NTf <sub>2</sub> ]	-0.31	8.0
[N <sub>C<sub>1</sub>,C<sub>1</sub>,C<sub>2</sub>,C<sub>2</sub>OC<sub>1</sub></sub> ][NTf <sub>2</sub> ]	-0.32	9.1
[N <sub>C<sub>1</sub>,C<sub>1</sub>,C<sub>2</sub>,C<sub>4</sub></sub> ][NTf <sub>2</sub> ]	-0.25	7.4

Figure 3.3a and b show that Na<sup>+</sup> reduction potential lies outside the ESW of [C<sub>1</sub>(C<sub>2</sub>OC<sub>1</sub>)Pyrr][NTf<sub>2</sub>] and [C<sub>1</sub>(C<sub>2</sub>OC<sub>1</sub>)Pyrr][C<sub>2</sub>F<sub>5</sub>COO], differently from the other ILs. As discussed previously, this means that the SEI formed on Na anodes

with these electrolytes will occur via chemical and electrochemical pathways. Another feature in common to electrolytes based on  $[C_1(C_2OC_1)Pyrr][NTf_2]$ ,  $[C_1(C_2OC_1)Pyrr][C_2F_5COO]$  (Figure 3.3a and b) is the absence of an oxidation peak (stripping process) on the anodic scan. This irreversible behaviour may be a consequence of rapid SEI formation in those liquids, meaning that as soon as  $Na^+$  is reduced to  $Na^0$  at the electrode surface, it promptly reacts with the electrolyte and consequently no  $Na^0$  remains to be oxidised back to  $Na^+$ . Na stripping is observed in the  $[N_{C_1,C_1,C_2,(C_2OC_1)}][NTf_2]$ ,  $[C_1C_{dma}Pyrr][NTf_2]$  and  $[N_{C_1,C_1,C_2,C_4}][NTf_2]$  electrolytes (Figure 3.3c, d and e) despite the low coulombic efficiency indicated in the CVs, which can also be related to Na loss for SEI formation. The next section uses EIS to study SEI formation of metallic Na and IL-based electrolytes.

### 3.4. Solid-electrolyte interphase studies with electrochemical impedance spectroscopy

To further study IL and metallic Na reactions, and formation of the SEI on Na metal, symmetrical Na|Na cells using the IL electrolytes described above were evaluated with EIS. EIS is typically used for battery ageing monitoring, often installed in battery packs of electric vehicles for diagnosis of the internal state of the cells.<sup>103</sup> EIS spectra typically displays a semicircle in a Nyquist plot of imaginary ( $Z''$ ) versus real ( $Z'$ ) impedances, as described more thoroughly in Chapter 2. In summary, as shown in Figure 3.4, the semicircle rises from the left-hand side, at high frequencies. In this region, the intercept of the real impedance axis refers to the bulk electrolyte resistance ( $R_{electrolyte}$ ). On the right-hand side of the semicircle at lower frequencies, the intercept of the real impedance axis is associated to charge transfer resistance at the electrodes ( $R_{ct}$ ) and finally the tail at lower frequencies is related to diffusion controlled electrochemical process.<sup>60</sup> Over time, side reactions, material degradation processes and changes at the structure of electrodes affect cell resistance. An increase in the size of the semicircle as demonstrated by the green line in Figure 3.4 reflects an increase of the electrode surface resistance ( $R_{surface}$ ).<sup>103</sup> SEI reactions modify the

surface of the electrode altering its resistance, which can be observed by changes in the semi-circle of the Nyquist plot.<sup>9</sup>

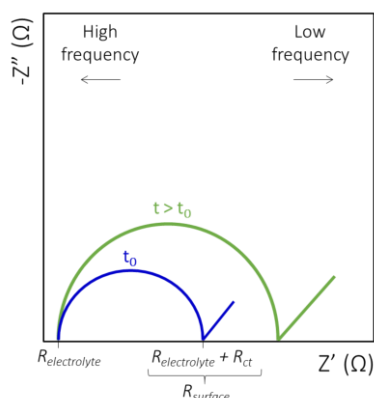


**Figure 3.4.** Nyquist plot of EIS showing initial impedance (blue line) and impedance after a time  $t$  (green line).  $R_{\text{electrolyte}}$  refers to the resistance related to the bulk electrolyte resistance,  $R_{\text{ct}}$  is the charge transfer resistance at the electrode and  $R_{\text{surface}}$  is assumed the overall electrode surface resistance.

SEI growth over time was studied with EIS during open-circuit conditions, meaning that any changes observed in the semi-circles are caused only by reactions between electrode and electrolyte in the absence of any applied current. Figure 3.5 shows the Nyquist plots for Na|Na symmetrical cells with the IL based electrolytes studied in this chapter and the inserts show pictures of one of the Na electrodes post-analysis. Repeats of the impedance tests can be found in Appendix 1.A.2.

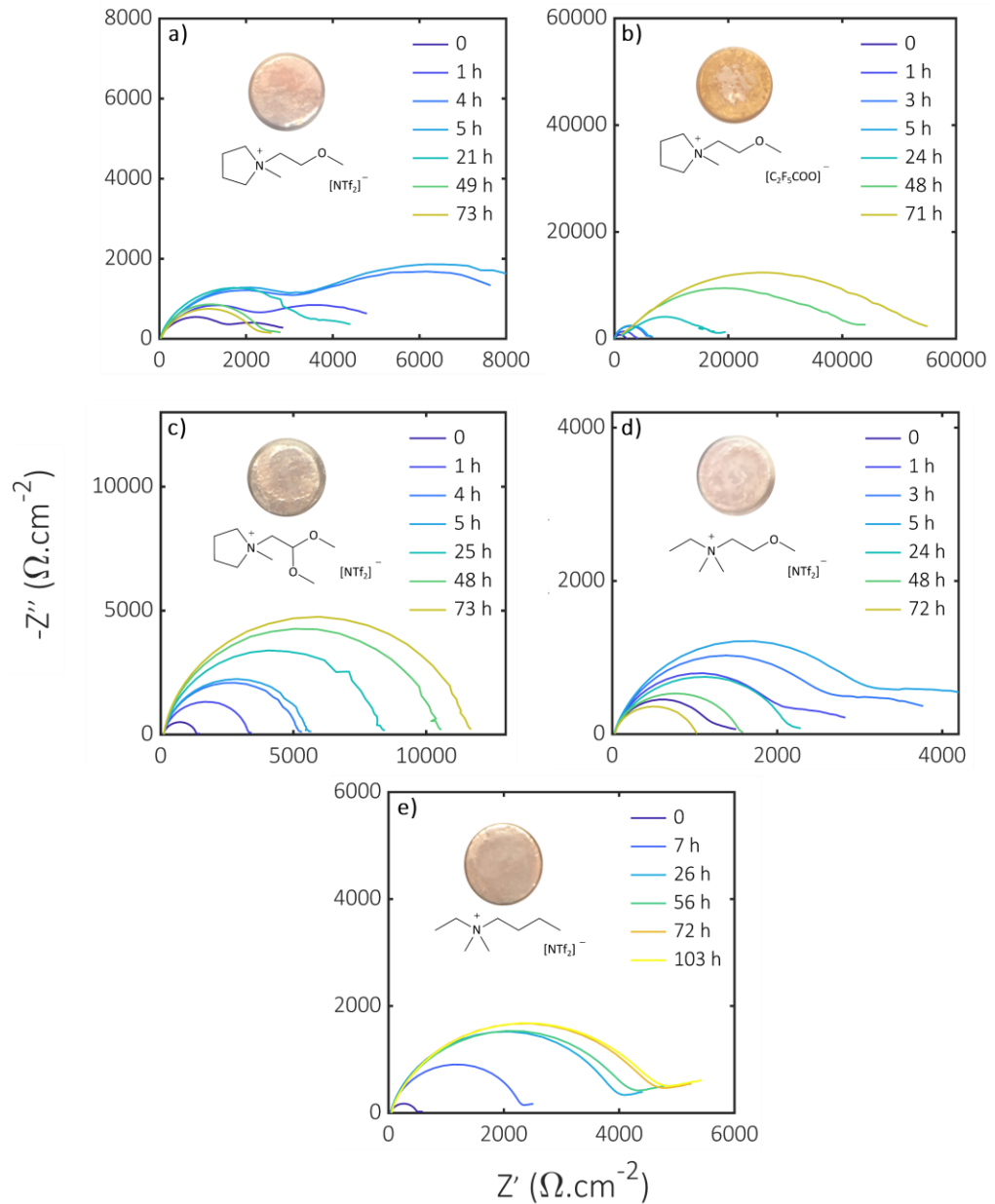
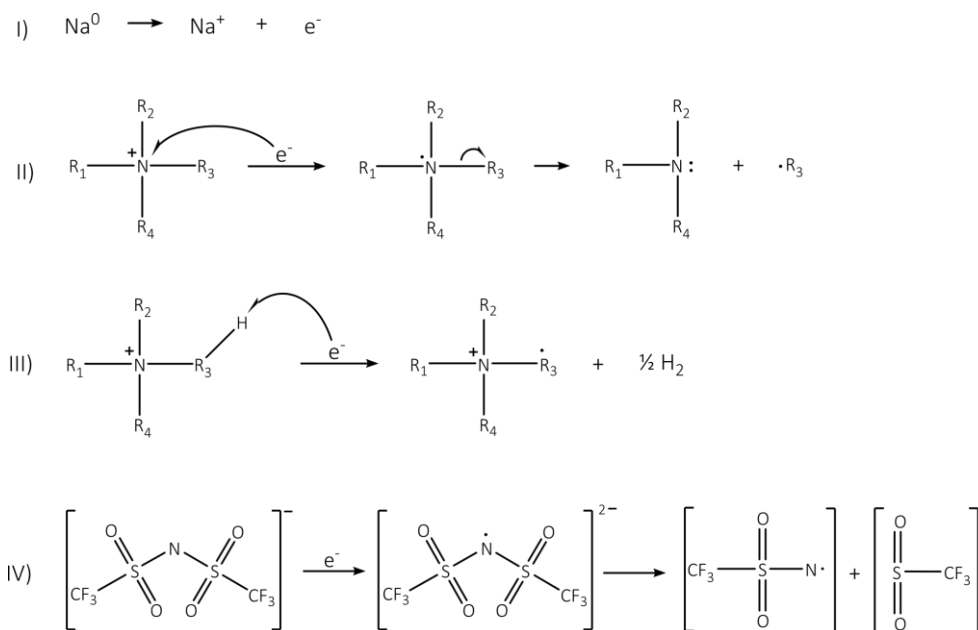


**Figure 3.5.** Nyquist plots of EIS of Na|Na symmetrical cells during open circuit conditions for over 70 h, using the various IL electrolytes (0.5 M Na<sup>+</sup>, with counter ion accordingly to IL anion) Note the increase in  $R_{\text{surface}}$  followed by a decrease over time in  $[\text{C}_1(\text{C}_2\text{OC}_1)\text{Pyrr}][\text{NTf}_2]$  **(a)** and  $[\text{N}_{\text{C}_1, \text{C}_1, \text{C}_2, (\text{C}_2\text{OC}_1)}][\text{NTf}_2]$  **(d)**, the constant increase in  $R_{\text{surface}}$  over time for  $[\text{C}_1\text{C}_{\text{dma}}\text{Pyrr}][\text{NTf}_2]$  **(c)** and  $[\text{C}_1(\text{C}_2\text{OC}_1)\text{Pyrr}][\text{C}_2\text{F}_5\text{COO}]$  **(b)**, and the increase and stabilisation of  $R_{\text{surface}}$  for  $[\text{N}_{\text{C}_1, \text{C}_1, \text{C}_2, \text{C}_4}][\text{NTf}_2]$  **(e)**. Inserts show pictures of one of Na electrodes post analysis (cell disassembled within a glovebox). Repeats shown in Figure A 5 in Appendix 1.A.2.

Overall, very large resistances are observed at low frequencies (surface resistance) for all electrolyte systems, which have also been shown previously for other ILs.<sup>35, 104</sup> This confirms what has been mentioned previously, that alkali metal electrodes promptly form an SEI when in contact with the electrolyte, as a consequence of alkali metals being good reducing agents. Metallic sodium readily oxidises and releases electrons (see Scheme 3.1 I), which trigger a series of other reactions with the electrolyte. Electron transfer to the IL cation leads to radical formation, as shown in Scheme 3.1, scheme II in which  $R_3$  represents the most stable radical, thus the most likely to be formed. Radical formation may also happen via proton abstraction as shown in reaction III (Scheme 3.1). Electron transfer to the  $[NTf_2]^-$  anion has been reviewed<sup>90</sup> and it is suggested that electron transfer is followed by heterolytic cleavage of the N-S bond (see scheme IV in Scheme 3.1). All reaction products shown in Scheme 3.1 can then be involved in countless reaction possibilities, including further electron transfer, radical propagation and/or termination and reactions involving  $Na^+$ .

Figure 3.5 also shows that IL-based electrolytes display considerably different impedance behaviour over time. To aid understanding of the changes over time for each IL system, a percentual analysis of the surface resistance overtime is demonstrated in Figure 3.6 and described as follows. Figure 3.6a shows the percentual changes of the surface resistance overtime with respect to the initial ( $t_0$ ) resistance ( $Change/R(t_0)$ ). Figure 3.6b displays the sequential percentual change of the surface resistance with respect to the resistance of the immediately preceding measurement (Sequential change). Whilst the plot of percentual change with respect to the initial resistance (Figure 3.6a) suggests an overall trend of the surface resistance over time, the sequential change plot (Figure 3.6b) assists the visualisation of any critical times for surface modification.



**Scheme 3.1** Schematics of possible reactions taking place at the Na-IL interphase: **I)** metallic sodium oxidation; **II)** electron transfer and radical formation at the cation; **III)** proton abstraction and radical formation at the cation; **IV)** electron transfer at the  $[\text{NTf}_2]^-$  anion.<sup>90</sup>

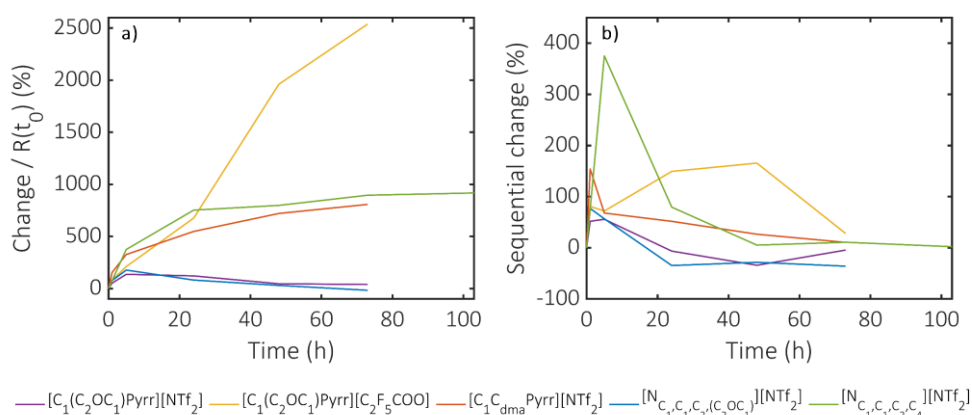
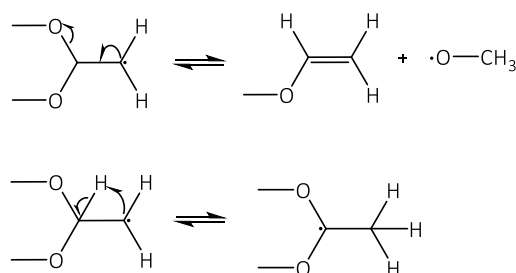


**Figure 3.6.** Analysis of EIS of Na|Na symmetrical cells using IL-based electrolytes (0.5 M  $\text{Na}^+$  salts in the ILs displayed in the figure legend), demonstrating the variations of  $R_{\text{surface}}$  over time in the different ILs. Note the greatest increase in  $[\text{NTf}_2]$ -based ILs during the first 24 h and the constant increase in  $R_{\text{surface}}$  of  $[\text{C}_1(\text{C}_2\text{OC}_1)\text{Pyrr}][\text{C}_2\text{F}_5\text{COO}]$ . **a)** Change/ $R(t_0)$ : Percentual change of surface resistance over time with respect to the resistance at the initial time ( $t_0$ ); **b)** Sequential change: Percentual change of surface resistance over time with respect to the resistance of the immediately preceding measurement. Analysis of repeats shown in Figure A 6 in Appendix A.2.

Regarding the individual behaviour displayed by each IL electrolyte,  $[\text{C}_1(\text{C}_2\text{OC}_1)\text{Pyrr}][\text{C}_2\text{F}_5\text{COO}]$  (Figure 3.5b) seems to yield a very unstable SEI formation, suggested by the very broad lines in the Nyquist plot, the corroded electrode shown in the insert picture, and the trends shown in Figure 3.6. In fact, a close inspection of Figure 3.5b shows that the surface resistance not only increased, but the shape of the Nyquist semi-circle considerably changed, which indicates severe modification of the electrode surface. The sharp curve shown in Figure 3.6a implies a highly reactive electrode surface, with rapid resistance increase over time. The high basicity of this IL (see DN values, on Table 3.3) may increase its reactivity towards SEI reactions, which may be the reason for the extent of electrode surface modification within this IL. In addition, thermal degradation studies with acetate-based ILs have suggested IL decomposition via nucleophilic attack of acetate anion to a cation side chain and/or via Hofmann elimination by abstraction of a proton from the cation side chain and subsequent formation of carboxylic acid and alkene. These reactions observed in those thermal degradation studies perhaps become feasible in the presence of  $\text{Na}^+$ ,  $\text{e}^-$  and radicals (Scheme 3.1), which would explain the high reactivity demonstrated by this IL electrolyte. Less likely (yet possible), the high reactivity may be originated from a vestige of acid from the synthetic procedure (see Chapter 2 for details on the synthesis), despite great effort to eliminate any starting materials from the final product.

$\text{Na}|\text{Na}$  symmetrical cell with  $[\text{C}_1\text{C}_{\text{dma}}\text{Pyrr}][\text{NTf}_2]$  based electrolyte also shows continuous surface resistance increase as shown in Figure 3.5c. In contrast to  $[\text{C}_1(\text{C}_2\text{OC}_1)\text{Pyrr}][\text{C}_2\text{F}_5\text{COO}]$ , the electrode in  $[\text{C}_1\text{C}_{\text{dma}}\text{Pyrr}][\text{NTf}_2]$  is not visually corroded (compare inserts in Figure 3.5b and c), and the surface resistance seems to grow at a slower rate than  $[\text{C}_1(\text{C}_2\text{OC}_1)\text{Pyrr}][\text{C}_2\text{F}_5\text{COO}]$ , as shown in Figure 3.6a. Interestingly, sequential resistance change plots (Figure 3.6b) suggests that the highest surface resistance increase for  $[\text{C}_1\text{C}_{\text{dma}}\text{Pyrr}][\text{NTf}_2]$  occurs within the first hour of resting period, whilst for  $[\text{C}_1(\text{C}_2\text{OC}_1)\text{Pyrr}][\text{C}_2\text{F}_5\text{COO}]$  it occurs during the first 24 hours, indicating the diversity of chemical reactions and reaction kinetics that may take place during SEI formation in different

liquids. The constant increase in surface resistance suggests the continuous formation of an unstable SEI, as no protective layer is formed to prevent further electrode-electrolyte reaction. Considering the more complex structure of this IL cation compared to the others, there is a wider range of reactions that can proceed from the initial reactions shown in Scheme 3.1. In fact, even the formation of the radical can lead to different structures, as suggested in the Scheme 3.2. Other reactions may also involve the decomposition of the acetal group.



**Scheme 3.2.** Possible radical rearrangement exemplifying the great range of reactions that can occur in the  $[\text{C}_1\text{C}_{\text{dma}}\text{Pyrr}][\text{NTf}_2]$  electrolyte: formation of new radicals via homolytic cleavage of C-O bond (top), and intramolecular rearrangement (bottom).

Another electrolyte that displays increase in surface resistance over time is  $[\text{N}_{\text{C}_1, \text{C}_1, \text{C}_2, \text{C}_4}][\text{NTf}_2]$  (see Figure 3.5e). Differently from the ILs discussed above ( $[\text{C}_1\text{C}_{\text{dma}}\text{Pyrr}][\text{NTf}_2]$  and  $[\text{C}_1(\text{C}_2\text{OC}_1)\text{Pyrr}][\text{C}_2\text{F}_5\text{COO}]$ ), the surface resistance for the  $[\text{N}_{\text{C}_1, \text{C}_1, \text{C}_2, \text{C}_4}][\text{NTf}_2]$  system sharply increases within the first 5 hours, as suggested by Figure 3.6b. However, the surface resistance seems to stabilise after 24 hours, especially shown by the curves in the Nyquist plot for 72 and 103 h. The impedance data for this IL indicates formation of a stable SEI layer. Despite the development of a high surface resistance during the first hours, it appears to reach a plateau within 73 h, after which it is likely that no further (or limited) reactions continue to proceed. In addition, the electrode in  $[\text{N}_{\text{C}_1, \text{C}_1, \text{C}_2, \text{C}_4}][\text{NTf}_2]$  does not seem corroded as in the  $[\text{C}_1(\text{C}_2\text{OC}_1)\text{Pyrr}][\text{C}_2\text{F}_5\text{COO}]$  IL.

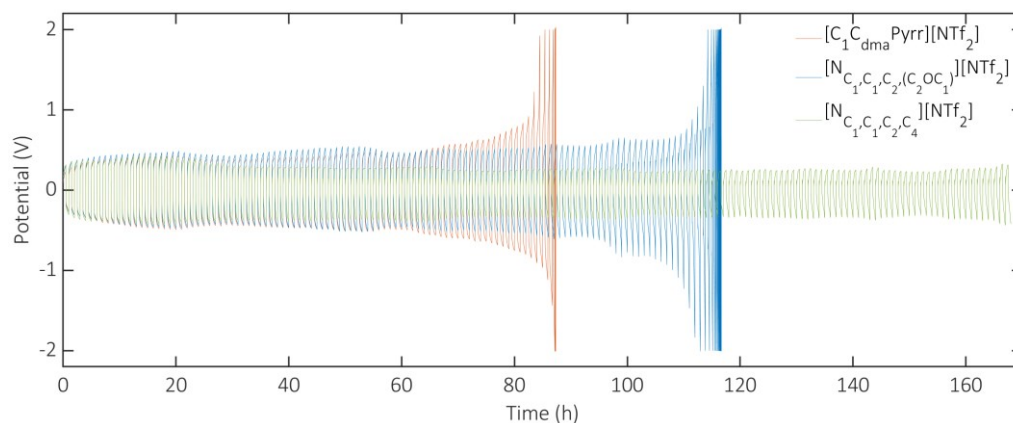
The Nyquist plots for Na|Na cells with electrolytes based on  $[\text{C}_1(\text{C}_2\text{OC}_1)\text{Pyrr}][\text{NTf}_2]$  and  $[\text{N}_{\text{C}_1, \text{C}_1, \text{C}_2, (\text{C}_2\text{OC}_1)}][\text{NTf}_2]$  show a very distinct behaviour than the other ILs discussed so far. Both  $[\text{C}_1(\text{C}_2\text{OC}_1)\text{Pyrr}][\text{NTf}_2]$  and

$[N_{C_1,C_1,C_2,(C_2OC_1)}][NTf_2]$  show a decrease in the surface resistance after 24 hours, clearly seen in Figure 3.5a and d, as well as in the percentual change analysis shown in Figure 3.6. Previous studies have shown effective  $Na^+$  plating/stripping for certain electrolyte systems that showed a decrease in surface resistance over time.<sup>33</sup> With the aid of EIS and XPS studies, the authors suggested that the decrease in surface resistance indicate formation of a stable SEI layer, which is crucial for continuous Na|Na cell cycling. Despite the decrease in surface resistance appears to be beneficial (considering the literature), the data displayed herein for  $[C_1(C_2OC_1)Pyrr][NTf_2]$  and  $[N_{C_1,C_1,C_2,(C_2OC_1)}][NTf_2]$  is not sufficient to explain this trend. In fact, further studies are needed to explore the different behaviours observed in this section and their impact on Na anodes.

Next sections show studies of Na|Na symmetrical cell cycling followed by studies on composition of the SEI formed by Na and electrolytes based on  $[C_1C_{dma}Pyrr][NTf_2]$ ,  $[N_{C_1,C_1,C_2,(C_2OC_1)}][NTf_2]$  and  $[N_{C_1,C_1,C_2,C_4}][NTf_2]$ . Considering the highly reactive behaviour displayed by  $[C_1(C_2OC_1)Pyrr][C_2F_5COO]$  and the very similar behaviour of  $[C_1(C_2OC_1)Pyrr][NTf_2]$  and  $[N_{C_1,C_1,C_2,(C_2OC_1)}][NTf_2]$ , these pyrrolidinium ILs are not included in the next sections.

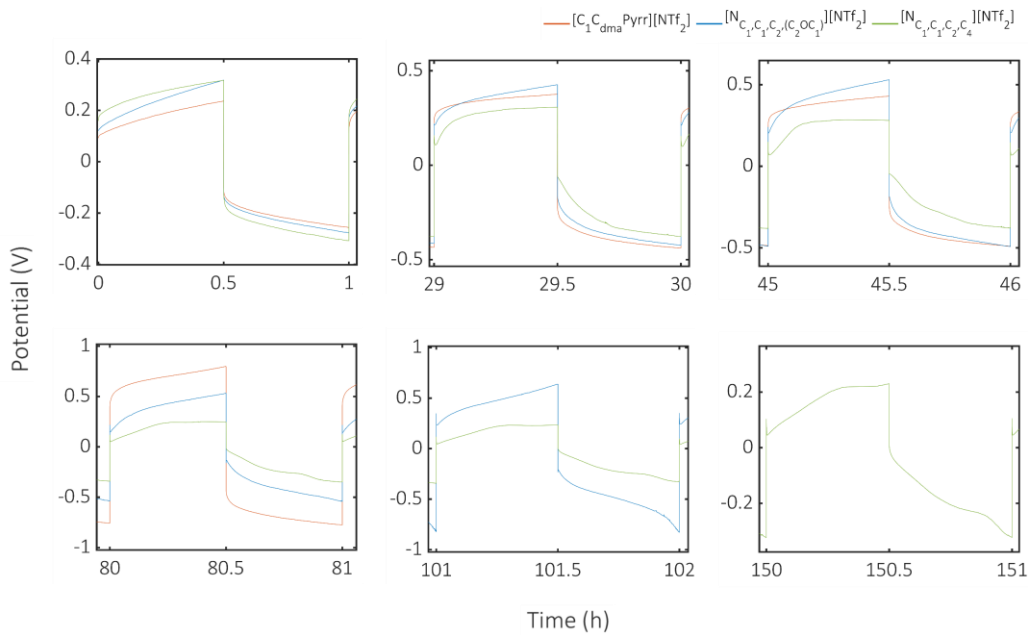
### 3.5. Na|Na symmetrical cell cycling using selected IL-based electrolytes

Stable, highly efficient and long-term cyclability are crucial parameters that alkali metal electrodes need to meet to be used in full battery cells.<sup>3, 8, 16, 33</sup> To evaluate the effect of IL-based electrolytes on Na electrode cyclability, Na|Na symmetrical cells using selected ILs from previous section ( $[C_1C_{dma}Pyrr][NTf_2]$ ,  $[N_{C_1,C_1,C_2,(C_2OC_1)}][NTf_2]$  and  $[N_{C_1,C_1,C_2,C_4}][NTf_2]$ ) were studied using galvanostatic cycling. Figure 3.7 shows the voltage profiles of Na|Na symmetrical cells during galvanostatic cycling, with cut-off limits at  $\pm 2$  V.



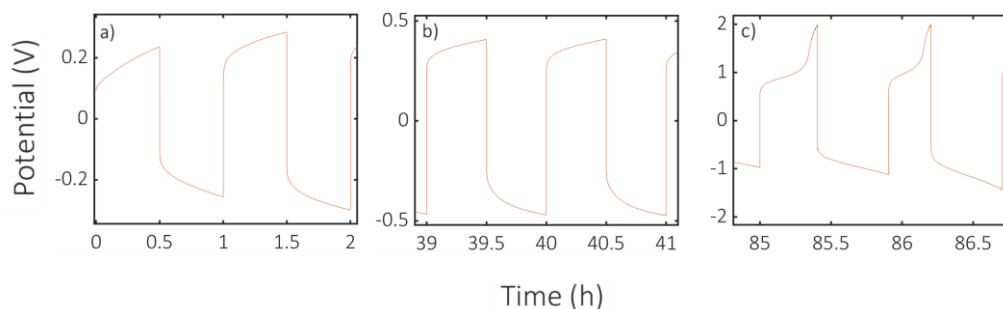
**Figure 3.7.** Galvanostatic cycling of Na|Na symmetrical cell cycled at  $0.1 \text{ mA}\cdot\text{cm}^{-2}$ , with 30 minutes polarisation time and  $105 \mu\text{L}$  of electrolyte ( $0.5 \text{ M Na}[\text{NTf}_2]$ ) in each IL): —  $[\text{C}_1\text{C}_{\text{dma}}\text{Pyrr}][\text{NTf}_2]$ , —  $[\text{N}_{\text{C}_1,\text{C}_1,\text{C}_2,(\text{C}_2\text{OC}_1)}][\text{NTf}_2]$  and —  $[\text{N}_{\text{C}_1,\text{C}_1,\text{C}_2,\text{C}_4}][\text{NTf}_2]$ , showing that cells with  $[\text{C}_1\text{C}_{\text{dma}}\text{Pyrr}][\text{NTf}_2]$  and  $[\text{N}_{\text{C}_1,\text{C}_1,\text{C}_2,(\text{C}_2\text{OC}_1)}][\text{NTf}_2]$  reach the cut-off limits ( $\pm 2 \text{ V}$ ) after 84 and 115 cycles, and cell with  $[\text{N}_{\text{C}_1,\text{C}_1,\text{C}_2,\text{C}_4}][\text{NTf}_2]$  displays low overpotential over 160 cycles.

Figure 3.7 clearly shows that the choice of electrolyte affects how long cells can be cycled before reaching the cut-off potential. In addition, the magnified traces in Figure 3.8 reveal very distinct voltage profiles among the electrolytes. Despite the similar shape (though differences in overpotential) at the first cycles, by 29 h of cycling  $[\text{N}_{\text{C}_1,\text{C}_1,\text{C}_2,(\text{C}_2\text{OC}_1)}][\text{NTf}_2]$  and  $[\text{N}_{\text{C}_1,\text{C}_1,\text{C}_2,\text{C}_4}][\text{NTf}_2]$  seem to display comparable profiles, whilst voltage traces for  $[\text{C}_1\text{C}_{\text{dma}}\text{Pyrr}][\text{NTf}_2]$  remains the same through the whole length of the experiment.



**Figure 3.8.** Selected times of galvanostatic cycling of Na | Na symmetrical cell from Figure 3.7, showing different voltage profiles depending on the IL used. Cell cycled at  $0.1 \text{ mA}\cdot\text{cm}^{-2}$ , 30 minutes polarisation time and  $105 \mu\text{L}$  electrolyte ( $0.5 \text{ M Na}[\text{NTf}_2]$ ) based on —  $[\text{C}_1\text{C}_{\text{dma}}\text{Pyrr}][\text{NTf}_2]$ , —  $[\text{N}_{\text{C}_1,\text{C}_1,\text{C}_2,(\text{C}_2\text{OC}_1)}][\text{NTf}_2]$  and —  $[\text{N}_{\text{C}_1,\text{C}_1,\text{C}_2,\text{C}_4}][\text{NTf}_2]$ . Note the differences in potential (y-axis) scale across the magnified figures.

Firstly focusing on  $[\text{C}_1\text{C}_{\text{dma}}\text{Pyrr}][\text{NTf}_2]$ , Figure 3.9 shows selected cycles demonstrating the voltage profile evolution of the cell assembled with the  $[\text{C}_1\text{C}_{\text{dma}}\text{Pyrr}][\text{NTf}_2]$ -based electrolyte. An arc shaped profile dominates throughout cycling, with increasing overpotential over cycling time. Similar arc shaped profiles have been observed by Chen *et al* (2017)<sup>14</sup> in symmetrical Li | Li cells after several cycles. The authors associated such behaviour to accumulation of “dead Li” (dendrites that lose connection with electrode over cycling, see schemes D and F in Figure 3.12), at the electrode surface and the tortuous path imposed by this layer of inactive material. Consequently, the effective diffusion of  $\text{Li}^+$  across this “dead Li” layer is significantly lower than across the electrolyte, and high overpotential are needed to maintain mass transport of  $\text{Li}^+$  across the cell.



**Figure 3.9.** Selected times of galvanostatic cycling of Na | Na symmetrical cell from Figure 3.7, with focus on  $[C_1C_{dma}Pyrr][NTf_2]$  electrolyte (105  $\mu\text{L}$  of 0.5 M  $\text{Na}[NTf_2]$  solution) showing arc voltage profile from the start of cycling (**a**) and across the whole cycling time (**b**) until it approaches the cut-off limits (**c**). Cell cycled at  $0.1 \text{ mA}\cdot\text{cm}^{-2}$ , 30 minutes polarisation time. Note the differences in potential (y-axis) scale across the magnified figures.

The  $[C_1C_{dma}Pyrr][NTf_2]$  system shows the arc profile since the first cycle and throughout the whole length of the experiment, hence it is unlikely that the arc profile is caused by accumulation of dendrites. Figure 3.5 and Figure 3.6 also show that  $[C_1C_{dma}Pyrr][NTf_2]$  electrolyte displays highly reactive SEI formation, with considerable increase in surface resistance over time. Therefore, the arc shaped voltage profile might be caused by deficient mass transport across the cell, however, it originates from a highly resistive and tortuous SEI rather than a “dead Li” layer. The continuous increase in overpotential throughout cycling suggests that mass transport diminishes over time, and larger potentials are needed to promote  $\text{Na}^+$  transport. This is likely to be caused by continuous SEI growth, suggesting that the resistive SEI is also highly reactive, so electrolyte is constantly consumed by taking part of SEI formation reactions.<sup>105</sup> In order to evaluate whether electrolyte consumption can be associated with increase of overpotential, symmetrical cells assembled with lower electrolyte volume (80  $\mu\text{L}$  instead of 105  $\mu\text{L}$ ) were studied.

Figure 3.10 shows that decreasing electrolyte volume by 23% caused the cell to reach the potential cut-off limits approximately 50% faster. This supports the idea of a reactive SEI that continuously grow over cycling, depleting electrolyte, and limiting mass transport. Another reason for an early cycling

termination (voltage reaches the cut-off potentials) could be poor wetting of the separator. However, if wettability of the separator was the main cause for reaching the cut-off limits earlier, an increased overpotential would be expected already in the very first few cycles, which is not observed in Figure 3.10. Overall, these observations indicate that the arc shaped voltage profile of cells with  $[C_1C_{dma}Pyrr][NTf_2]$  are associated to mass transport limitations that lead to continuous increase of overpotential. This is caused by a non-stable and non-protective SEI formed with the  $[C_1C_{dma}Pyrr][NTf_2]$  electrolyte.

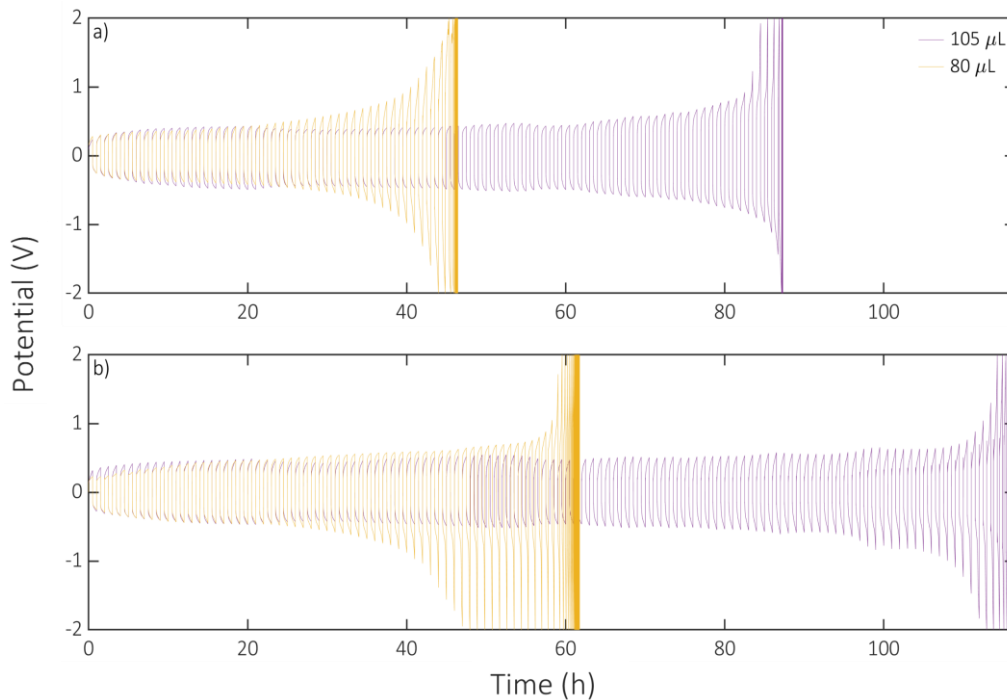


**Figure 3.10.** Galvanostatic cycling of Na|Na symmetrical cells comparing effect of electrolyte volume (—) 105  $\mu\text{L}$  and (—) 80  $\mu\text{L}$ , using electrolytes (0.5 M Na[NTf<sub>2</sub>]) based on **a)**  $[C_1C_{dma}Pyrr][NTf_2]$ , and **b)**  $[N_{C_1,C_1,C_2,(C_2OC_1)}][NTf_2]$ . Note the earlier termination (E reaches  $\pm 2$  v) of cells assembled with lower electrolyte volume despite the similar overpotential at the beginning of the experiment. Cells cycled at 0.1 mA.cm<sup>-2</sup> and 30 minutes polarisation time.

Looking back at Figure 3.8, we observe that though Na|Na cells with  $[N_{C_1,C_1,C_2,(C_2OC_1)}][NTf_2]$  and  $[N_{C_1,C_1,C_2,C_4}][NTf_2]$ -based electrolytes share some similarities in their voltage profile, the cell with  $[N_{C_1,C_1,C_2,(C_2OC_1)}][NTf_2]$  reaches

the cut-off voltage limit, whilst the cell with  $[N_{C_1,C_1,C_2,C_4}][NTf_2]$  does not display a significant increase in overpotential throughout the length of the experiment.

Figure 3.8 shows that  $[N_{C_1,C_1,C_2,(C_2OC_1)}][NTf_2]$  and  $[N_{C_1,C_1,C_2,C_4}][NTf_2]$  display an arc shaped profile at the first cycles, but changes after a few hours of cycling to a more “peaking”-type profile, differently from the voltage profiles shown by the cell with  $[C_1C_{dma}Pyrr][NTf_2]$ . Peaking profile has been associated to a combination of charge transfer processes taking place at the electrode, each one with a particular rate constant and area of action which determines the dominant process.<sup>11, 105,13</sup> These processes will be further discussed later in this section (see discussion for Figure 3.12).

The arc shaped voltage profile is determined by mass transport limitation due to SEI formation, as discussed for  $[C_1C_{dma}Pyrr][NTf_2]$  cells. The substantial change in the potential profiles at later cycling times indicate that there must be a shift in the processes dictating the voltage response for  $[N_{C_1,C_1,C_2,(C_2OC_1)}][NTf_2]$  and  $[N_{C_1,C_1,C_2,C_4}][NTf_2]$  cells. Reasoning for different shapes of voltage profile have been suggested in literature,<sup>11, 13, 14, 105</sup> though trends observed in this chapter are somewhat unique.

Chapter 2 introduced that the current-voltage relationship is defined by a combination of charge transfer rate and mass transfer rate. Both rates determine the concentration of reagents and products at the electrode at a certain time, either by how promptly the reagents react (charge transfer) or how quickly fresh reagents are supplied to the electrode (mass transfer). Thus, the rate of an electrochemical process is a combination of both charge transfer and mass transfer rates, and the slowest rate determines the overall rate of the process. In fact, the Butler-Volmer equation shown below demonstrates that the effect of the reaction rate constant ( $k_0$ ), the gradient of the electroactive species ( $C_{Na^+}(0,t)/C_{Na^+}^*$ ) and the overpotential ( $\eta_E$ ) play a role in the net current at the electrode:

$$i = nFAk_0 \left[ \frac{C_{Na^+}(0,t)}{C_{Na^+}^*} \exp\left(\frac{-\alpha nF}{RT} \eta_E\right) - \frac{C_{Na}(0,t)}{C_{Na}^*} \exp\left(\frac{(1-\alpha)nF}{RT} \eta_E\right) \right]$$

Based on the observations described in this section so far, the arc shaped profile displayed at the first galvanostatic cycles of  $[N_{C_1,C_1,C_2,(C_2OC_1)}][NTf_2]$  and  $[N_{C_1,C_1,C_2,C_4}][NTf_2]$  cells are related to mass transport limitations due to SEI formation, as discussed above for  $[C_1C_{dma}Pyrr][NTf_2]$ . However, the appearance of peaking profile at later cycles, presumably related to the kinetics of the processes happening at the electrode surface, indicates formation of a more stable and less resistive SEI throughout the first cycles. A less tortuous and resistive SEI is likely to have less impact on the effective diffusion of  $Na^+$ . Consequently, the overall electrode process is no longer determined by mass transfer limitations, hence the shift in the voltage profiles. If this is true, then the surface resistance observed in EIS is expected to decrease over cycling. EIS measurements were carried out at different times throughout cell cycling and are shown in Figure 3.11. The first column of Figure 3.11 shows selected cycles of  $[N_{C_1,C_1,C_2,(C_2OC_1)}][NTf_2]$  (blue traces) and  $[N_{C_1,C_1,C_2,C_4}][NTf_2]$  (green traces), second column shows impedance data for  $[N_{C_1,C_1,C_2,C_4}][NTf_2]$  and third column shows impedance data for  $[N_{C_1,C_1,C_2,(C_2OC_1)}][NTf_2]$ .

The plot on Figure 3.11a shows an arc shaped profile, which is accompanied by an increase on the surface resistance after the first cycle, attributed to SEI formation (see plots on Figure 3.11b and c). At later cycling times, as discussed in the paragraphs above, the arc shape starts to shift to a more peaking shape. In fact, at around 24 hours of cycling, peaking profile starts to develop as can be seen in the magnified region on Figure 3.11d. The cell with  $[N_{C_1,C_1,C_2,C_4}][NTf_2]$  electrolyte also features a significant decrease in surface resistance (Figure 3.11e) after 24 cycles. This decrease in surface resistance suggests that a stable and less resistive SEI has developed at the electrode in contact with the  $[N_{C_1,C_1,C_2,C_4}][NTf_2]$  electrolyte. Consequently, mass transport is likely to be less affected and the voltage profile starts to be determined by the kinetics of the processes taking place at the electrode surface. Impedance data for the cell with  $[N_{C_1,C_1,C_2,(C_2OC_1)}][NTf_2]$  (Figure 3.11f) still shows an increase in surface resistance after 24 h, suggesting that SEI reactions might be still taking

place at the electrode. Perhaps for this reason the initial peak at 23 h of cycling for  $[\text{N}_{\text{C}_1, \text{C}_1, \text{C}_2, \text{C}_4}][\text{NTf}_2]$  is more evident than for  $[\text{N}_{\text{C}_1, \text{C}_1, \text{C}_2, (\text{C}_2\text{OC}_1)}][\text{NTf}_2]$  (compare green and blue traces in the magnified region of Figure 3.11d).

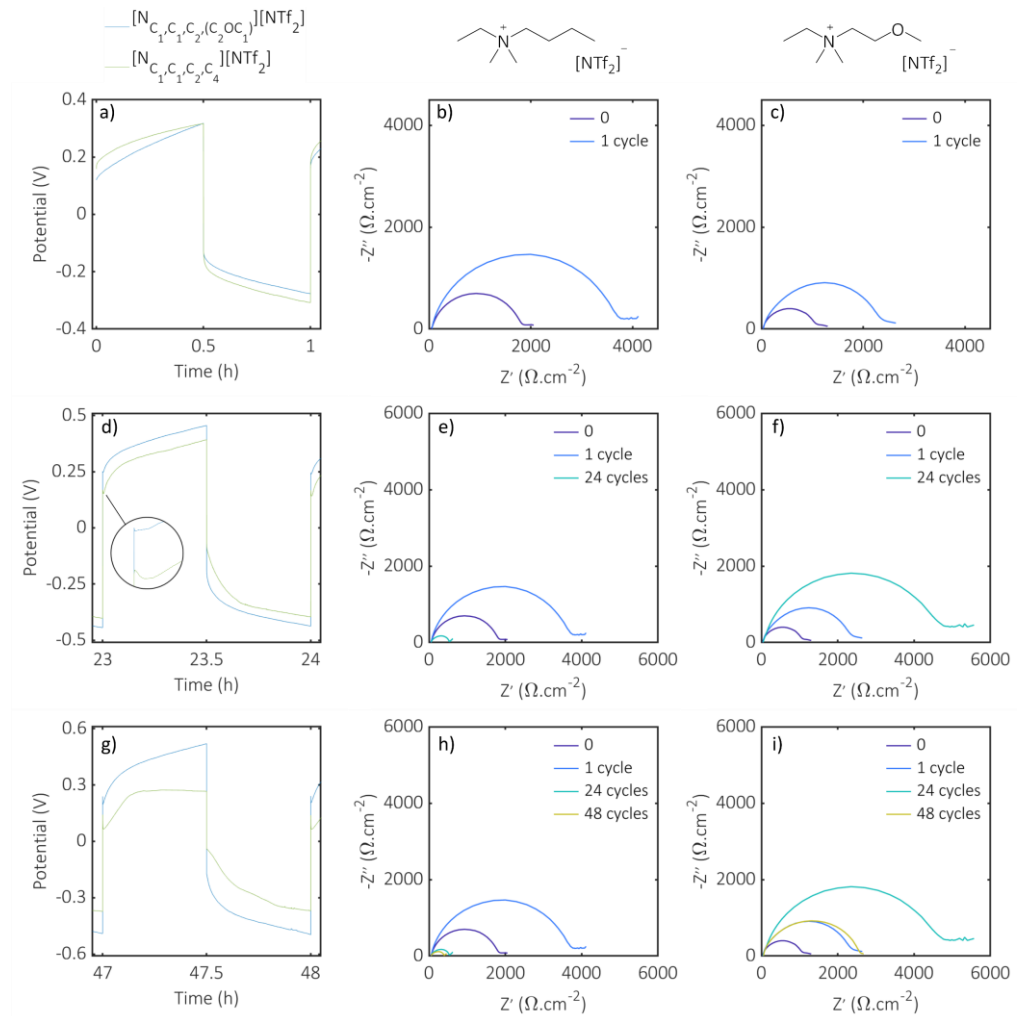


**Figure 3.11.** Selected times of galvanostatic cycling and EIS demonstrating correlation between peaking profile, cell overpotential and  $R_{\text{surface}}$ . First column shows Na|Na symmetrical cells from Figure 3.7 ( $0.1 \text{ mA}\cdot\text{cm}^{-2}$ , 30 min polarisation time), with focus on  $[\text{N}_{\text{C}_1, \text{C}_1, \text{C}_2, \text{C}_4}][\text{NTf}_2]$  (—) and  $[\text{N}_{\text{C}_1, \text{C}_1, \text{C}_2, (\text{C}_2\text{OC}_1)}][\text{NTf}_2]$  (—): **a)** From the start to 1 h of cycling, **d)** From 23 to 24 h cycling and **g)** From 47 to 48 h of cycling. EIS analysis of Na|Na symmetrical cell during cycling for  $[\text{N}_{\text{C}_1, \text{C}_1, \text{C}_2, \text{C}_4}][\text{NTf}_2]$  (second column: **b, e, h**) and  $[\text{N}_{\text{C}_1, \text{C}_1, \text{C}_2, (\text{C}_2\text{OC}_1)}][\text{NTf}_2]$  (third column: **c, f, i**), at the start (—), after 1 cycle (—), 24 cycles (—), and 48 cycles (—). Note the differences in potential (y-axis) scale across the figures.

With 48 hours of cycling the cell assembled with  $[N_{C_1,C_1,C_2,C_4}][NTf_2]$  seems to display a small increase in voltage followed by a plateau after the initial peak (see Figure 3.11g), suggesting stable mass transport is achieved in the cell without the need of larger overpotential to promote it. Therefore, it is likely that by 48 hours of cycling, mass transport limitation by a resistive SEI is no longer the main factor determining the voltage profiles, which is corroborated by the low surface resistance (Figure 3.11h) of the  $[N_{C_1,C_1,C_2,C_4}][NTf_2]$  system.

The surface resistance decreases for the cell with  $[N_{C_1,C_1,C_2,(C_2OC_1)}][NTf_2]$  after 48 hours of cycling, as shown in Figure 3.11i. Despite the peaking behaviour being slightly more evident after 48 hours, the  $[N_{C_1,C_1,C_2,(C_2OC_1)}][NTf_2]$  system still features the arc shape profile accompanied by larger overpotential (note different scales on the y-axis on Figure 3.11d and g). The considerably higher surface resistance shown by the cell with  $[N_{C_1,C_1,C_2,(C_2OC_1)}][NTf_2]$  compared to the cell with  $[N_{C_1,C_1,C_2,C_4}][NTf_2]$  (see Figure 3.11h and i) indicates that a more resistive SEI is formed. This is also suggested by the difference in overpotential observed between  $[N_{C_1,C_1,C_2,C_4}][NTf_2]$  and  $[N_{C_1,C_1,C_2,(C_2OC_1)}][NTf_2]$  voltage traces (Figure 3.11g). Consequently, even though the peaking at the start of the half cycles may be related to the kinetics of the processes at the electrode, mass transport seems to play a role in the  $[N_{C_1,C_1,C_2,(C_2OC_1)}][NTf_2]$  voltage profile throughout the whole cycling experiment.

The differences in the voltage profiles of  $[N_{C_1,C_1,C_2,C_4}][NTf_2]$  and  $[N_{C_1,C_1,C_2,(C_2OC_1)}][NTf_2]$  cells have been attributed to mass transport limitations and rate of processes taking place at the electrode surface. These processes are described as follows and the schematics of the processes are shown in Figure 3.12.

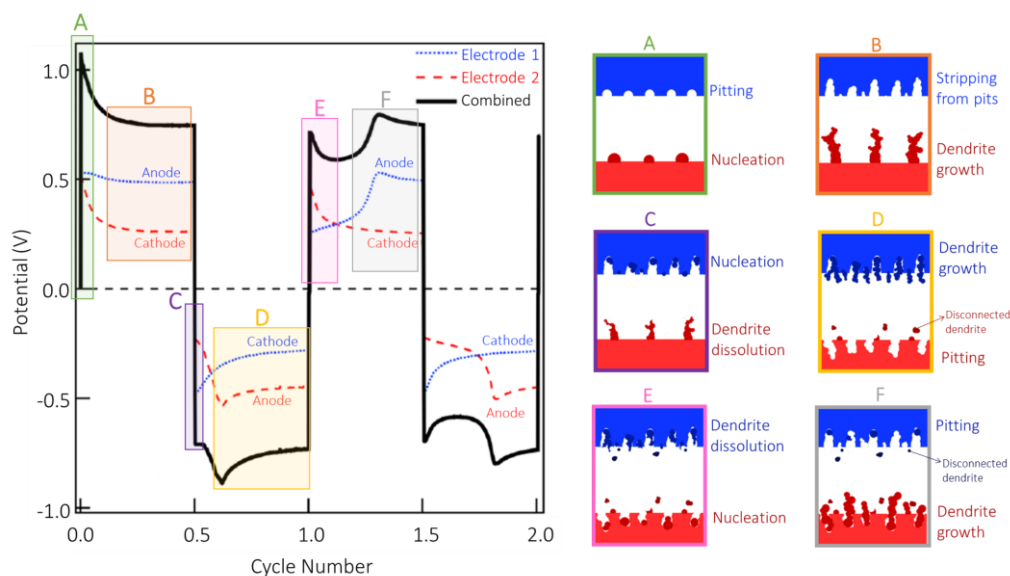


**Figure 3.12.** Voltage profile displaying contribution from each electrode in a symmetrical cell (**left**): measurements taken using a three-electrode cell at  $1 \text{ mA}\cdot\text{cm}^{-2}$ . Schematic representation of processes taking place at electrodes 1 (blue) and 2 (red) during different stages (A-F) of cycling (**right**). Adapted from reference <sup>11</sup>.

During plating and stripping reactions, several processes take place at the electrode. Wood *et al* thoroughly investigate these processes using operando video microscopy, three-electrode measurements, and modelling. <sup>11</sup> These processes were also investigated by Deng *et al* with operando optical microscopy.<sup>13</sup> In summary, each process at the electrode have a different rate constant, which can be directly related to Gibbs energy of the process by the equation below:

$$k_p^0 = A_p \exp\left(-\Delta G_p/RT\right)$$

where  $k_p^0$  is the rate constant for a particular process  $p$ ,  $A_p$  is the Arrhenius constant for the process  $p$  and  $-\Delta G_p$  is the energy barrier of the process  $p$ , and the effective rate constant ( $k_{eff}^0$ ) shown in the Butler-Volmer equation earlier is a combination of the rates of all processes taking place at the electrode. The difference in the rates of these processes originates from the distinct energy barriers for each process, which can be related to an unequal surface at the “areas of action” of each process.

During the first half-cycle of kinetically limited cells (negligible mass transport limitations), a sharp increase in the overpotential is observed, as shown in the shaded area A (light green) Figure 3.12. Similar sharp increase is observed at the cathode traces (shown in red), and is attributed to the nucleation of new dendrites (see scheme A in Figure 3.12). A slight increase though less pronounced at the anode (blue trace), is attributed to the formation of pits where the electrode has been oxidised. Then a drop in the overpotential is observed (shaded area B, in orange), and is attributed to dendrite growth at the spots already nucleated, rather than nucleating new areas. The SEI at the freshly plated metal (at the nuclei) is thinner than at the bulk Li, thus less resistant to charge transfer. Equally, stripping continuous at the pits, rather than new locations at the anode. When the polarity is reversed, an increase in the overpotential is observed in the purple shaded region C, and the same increase is observed at the cathode traces (in blue). However, the overpotential is not as high as on the previous nucleation process (shaded region A), because the surface of the cathode has already been modified (during stripping in the precedent half cycle). The anode trace shows low over potential at the beginning of the half cycle because stripping is occurring from the dendrites, rather than from the bulk electrode. The beginning of the yellow shaded region D in Figure 3.12 features an increase in the overpotential, attributed to an increase in the overpotential at the anode. At this point, stripping starts on the bulk electrode (see scheme D, in Figure 3.12), where a thicker SEI layer (compared to the dendrite SEI) has been established. The decrease in overpotential that follows is associated to continuous stripping from the pits, rather than new sites at the bulk electrode. At the same time at the cathode, plating occurs at the already nucleated spots, accompanied by a decrease in the overpotential. The subsequent half cycles follow the same process: high overpotential with nucleation and pitting at the beginning of the half cycle (pink shaded region E), followed by decrease in overpotential during dendrite growth and stripping from pits until an increase in overpotential (grey shaded region F) is caused by stripping of bulk electrode.

Based on the summary above, the peaking at the beginning of the half cycles of  $[N_{C_1, C_1, C_2, (C_2OC_1)}][NTf_2]$  and  $[N_{C_1, C_1, C_2, C_4}][NTf_2]$  cells is likely to be associated to the nucleation of Na electrodes. The persistent arc shaped profile of the  $[N_{C_1, C_1, C_2, (C_2OC_1)}][NTf_2]$  cell after the initial peak may be explained as follows. Nucleation occurs at the beginning of the half cycle consuming  $Na^+$  at the vicinity of the electrode, thus there is no significant mass transport restriction at that point. However, as plating continues, concentration of  $Na^+$  at the vicinity of the electrode drops, and higher overpotentials are needed to promote mass transfer. At later cycling times, as shown in Figure 3.13c, the overpotential considerably increases, approaching the cut-off limits of  $\pm 2$  V. In fact, the voltage profile seems to have changed slightly at these late cycling times, featuring a peak towards the end of the half cycle. This can be related to critically limited mass transport, perhaps caused by an accumulation of disconnected dendrites,<sup>14</sup> or most likely due to mass transport limitations associated to the SEI. Though significant decrease in surface potential is shown in Figure 3.11i, the tests with lower volume of electrolyte (see Figure 3.10) display the electrolyte consumption trends already discussed above for  $[C_1C_{dma}Pyrr][NTf_2]$ . In addition, this high overpotential of the half cycles could also be a combination of mass transport limitations and pitting of the bulk electrode. Schemes D and F in Figure 3.12, show an increase in the overpotential when stripping occurs preferentially from the bulk electrode over the dendrites. Also, it has been demonstrated that this second peak can appear at the different cycling stages depending on the electrolyte,<sup>11</sup> so perhaps this transition of the stripping process only occurs at the end of the half cycles in the  $[N_{C_1, C_1, C_2, (C_2OC_1)}][NTf_2]$ -system.

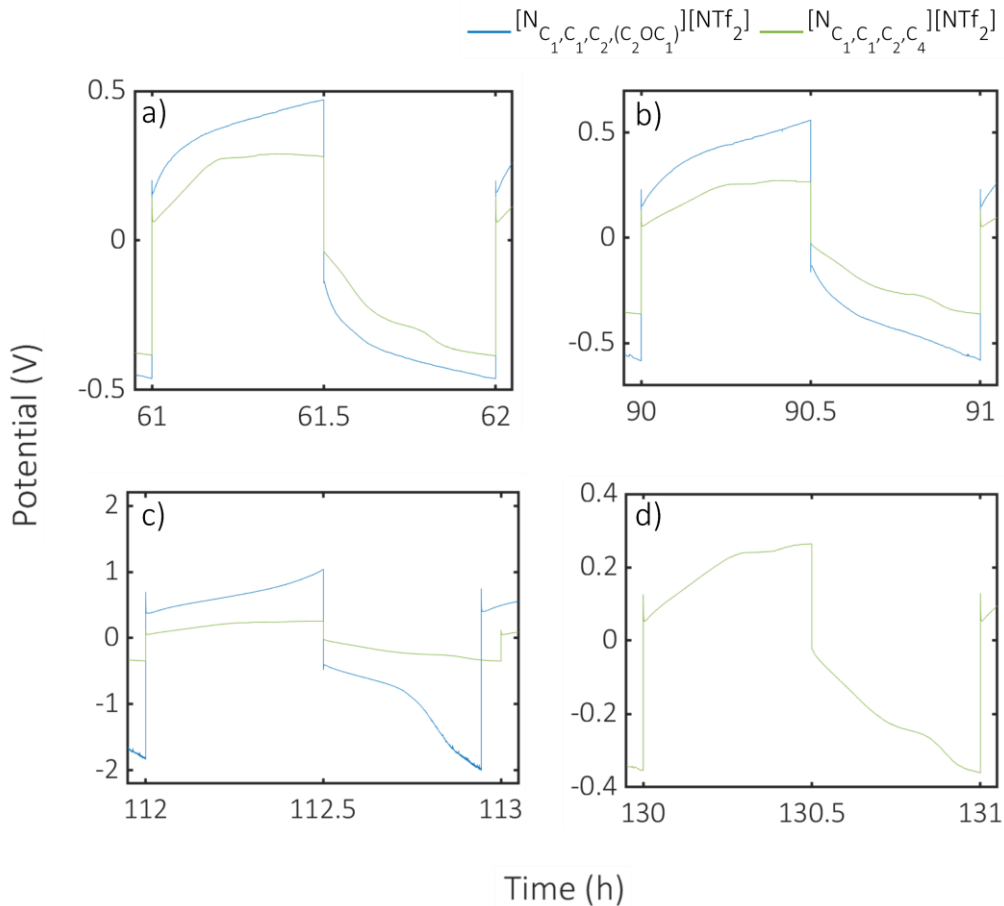


**Figure 3.13.** Selected times of galvanostatic cycling ( $0.1 \text{ mA}\cdot\text{cm}^{-2}$ , 30 min polarisation time) of Na|Na symmetrical cells shown in Figure 3.7, with focus on  $[\text{N}_{\text{C}_1,\text{C}_1,\text{C}_2,\text{C}_4}][\text{NTf}_2]$  ( $\text{—}$ ) and  $[\text{N}_{\text{C}_1,\text{C}_1,\text{C}_2,(\text{C}_2\text{OC}_1)}][\text{NTf}_2]$  ( $\text{—}$ ), showing that when  $[\text{N}_{\text{C}_1,\text{C}_1,\text{C}_2,(\text{C}_2\text{OC}_1)}][\text{NTf}_2]$  reaches the cut-off potentials  $[\text{N}_{\text{C}_1,\text{C}_1,\text{C}_2,\text{C}_4}][\text{NTf}_2]$  still displays low overpotentials. a) From 61 to 62 h of cycling, b) From 90 to 91 h cycling and c) From 112 to 113 h of cycling and d) From 130 to 131 h of cycling. Note the differences in potential (y-axis) scale across the magnified figures.

After the initial peak, related to nucleation of new dendrites and pitting during stripping at the anode, the cell with  $[\text{N}_{\text{C}_1,\text{C}_1,\text{C}_2,\text{C}_4}][\text{NTf}_2]$  electrolyte shows a linear increase in overpotential. For the positive potential traces, the overpotential stabilises with very few changes from at least 47 (Figure 3.11g) to over 130 (Figure 3.13d) hours of cycling. This suggests that after the initial nucleation, there is some mass transport limitation, but it seems to reach a steady state with just a modest increase in overpotential. Towards the end of the half cycle, there is a small increase in the overpotential, for both the positive

and the negative voltage traces. As discussed above for the  $[N_{C_1, C_1, C_2, (C_2OC_1)}][NTf_2]$  system and described by the schemes D and F in Figure 3.12, this is likely to be caused by dissolution of bulk Na, rather than dendrites during the stripping process.

Surprisingly for a symmetrical cell, positive and negative voltage traces for the cycling of  $[N_{C_1, C_1, C_2, C_4}][NTf_2]$  cell display differences in overpotential. During negative polarisation, the cell seems to develop higher overpotential throughout the half cycle. As discussed previously, an increase in overpotential during the half cycle can be either associated to a mass transport limitation and to increase in overpotential at the anode (see Figure 3.12 and shaded regions D and F). To understand this observation, it is important to look at the processes occurring at each individual electrode during the positive and negative polarisations.

The experimental set up for the galvanostatic cycling of the Na|Na cells starts by applying positive currents to one of the electrodes. Accordingly, in Figure 3.12 this electrode would be the blue electrode (electrode 1) and the opposite electrode would be the red electrode (electrode 2). The three-electrode experiment carried out by Wood *et al* (2016),<sup>11</sup> shows that the overpotential associated with nucleation is higher than the overpotential associated with pitting (see Figure 3.12, shaded regions A, C and E), thus the nucleation process has a higher energy barrier to overcome than the pitting process.<sup>11</sup> Hence it is fair to expect a higher number of pits to be formed at the anode, compared to the number of nuclei at the cathode, particularly on the first half cycle (shaded region A). In addition, schemes C and E in Figure 3.12, show that on subsequent half cycles nucleation is more likely to take place at the pits and stripping to occur on the dendrites formed in the previous half cycle. Consequently, the blue electrode is more likely to have higher number of nucleus sites than the red electrode, because the blue electrode has had higher number of pits formed in the very first half cycle. Thus, at the red electrode the area of bulk metal covered by dendrites is presumably smaller than at the blue electrode, so stripping from the bulk metal (and consequently increase in

overpotential) is more likely to occur at the red electrode than the blue electrode. This may explain the increase in overpotential to be more significant at the negative voltage traces because the red electrode behaves as the anode at negative potentials. In addition, the absence of a nucleation peak during negative polarisation may be associated to lower energy barrier for nucleation at the cathode (blue electrode). This is because the formation of pits in the previous half cycle (positive polarisation) facilitates the nucleation process on the subsequent cycle (negative polarisation).

This section has shown that it is possible to cycle Na symmetrical cells with  $[N_{C_1, C_1, C_2, C_4}][NTf_2]$  based electrolyte at  $0.1 \text{ mA/cm}^2$ , with 30 min polarisation time ( $0.1 \text{ mAh/cm}^2$  for each complete plating/stripping cycle) with overpotentials less than  $0.8 \text{ V}$ , for at least 160 cycles. To put in context of recent studies, it has been demonstrated that Na symmetrical cells containing  $[C_3C_1\text{Pyrr}][FSI]$  based electrolyte (with 50 mol% NaFSI) can be cycled for at least at  $1.0 \text{ mA/cm}^2$  with polarisation time of 6 minutes for at least 700 cycles with overpotentials less than  $0.15 \text{ V}$ , for cells with a polarisation preconditioning.<sup>56</sup> Furthermore, Howlett and co-workers also found that Na symmetrical cells containing  $[C_3C_1\text{Pyrr}][DCA]$  and 19 mol% of Na[FSI], can be cycled at  $0.1 \text{ mA/cm}^2$  and polarisation time of 1 h for 100 cycles at  $0.1 \text{ mA/cm}^2$  with overpotentials less than  $1.5 \text{ V}$ .<sup>35</sup> More recent studies on IL application in Na batteries has been recently reviewed by Hagiwara and co-workers.<sup>106</sup>

### 3.6. Na-IL solid-electrolyte interphase studies with depth profiling 3D OrbiSIMS

The structure and composition of Na-IL interphase was studied with secondary ion mass spectroscopy (SIMS), using depth profile mode. The high sensitivity of SIMS technique is a strong advantage, however, it makes data analysis very challenging. This can be seen in the raw data plots in Appendix 1.A.2.3, which shows the depth profile for the all Na-IL interphase samples. A

thoroughly interpretation of the results shown in Appendix 1.A.2.3 is difficult due to the volume and complexity of the dataset. For this reason, selected assignments of each sample are plotted separately to visualise the data more clearly, and the depth profile plots are shown in Figure 3.15, Figure 3.16 and Figure 3.14 for  $[C_1C_{dma}Pyrr][NTf_2]$ ,  $[N_{C_1,C_1,C_2,(C_2OC_1)}][NTf_2]$  and  $[N_{C_1,C_1,C_2,C_4}][NTf_2]$ -Na interphase, respectively.

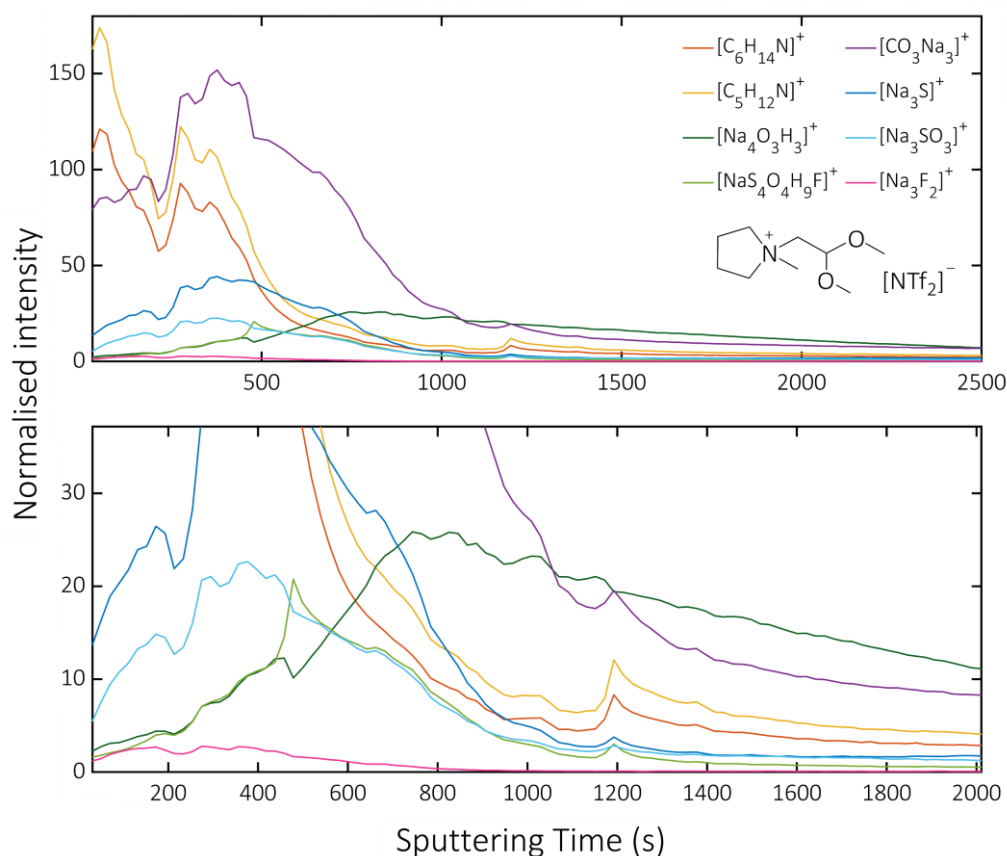


**Figure 3.14.** Positive ion depth profiles of Na- $[C_1C_{dma}Pyrr][NTf_2]$  (with 0.5 M Na $[NTf_2]$ ) SEI showing highly overlapped intensity profiles, the presence of small cation-related fragments, and anion-based and inorganic fragments. Analysis performed using 20 keV  $Ar_{3000}^+$  for sputtering and analysis at  $-175$  °C. Bottom image shows magnified lower intensity region (bottom).

The assignments were selected with the aim of displaying the variety of fragments detected in the SEI with these IL-based electrolytes, including more

‘cation-related’ ( $C_mH_nN_zO_k$ ) , ‘anion-based’ ( $S_mO_nF_zN_k$  etc) , small inorganic fragments ( $Na_nX_m$ ), and ‘native layer’ ( $Na_mO_nH_k$ ) type of assignments.

Interestingly,  $[N_{C_1,C_1,C_2,(C_2OC_1)}][NTf_2]$  and  $[N_{C_1,C_1,C_2,C_4}][NTf_2]$  (see Figure 3.15 and Figure 3.16 below, and Figure A 11 and Figure A 9 from Appendix 1.A.2) show cation-related assignments which are larger and/or more diverse than the IL cation itself ( $[C_7H_{18}NO]^+$  for  $[N_{C_1,C_1,C_2,(C_2OC_1)}][NTf_2]$  and  $[C_8H_{20}N]^+$  for  $[N_{C_1,C_1,C_2,C_4}][NTf_2]$ ). This suggests that a combination of radicals formed in the reactions shown in Scheme 3.1 occurred during SEI formation. However, this is not observed to the same extent for  $[C_1C_{dma}Pyrr][NTf_2]$  (see Figure 3.14 Figure A 10 from Appendix A.2).

In Section 3.4 (impedance studies of SEI), the discussion regarding Na- $[C_1C_{dma}Pyrr][NTf_2]$  cells suggested that the complex structure the  $[C_1C_{dma}Pyrr]^+$  cation may lead to substantial fragmentation and formation of a vast range of radicals. This may be corroborated by the considerable amount of small ‘cation-related’ assignments in the Na- $[C_1C_{dma}Pyrr][NTf_2]$  SIMS data.

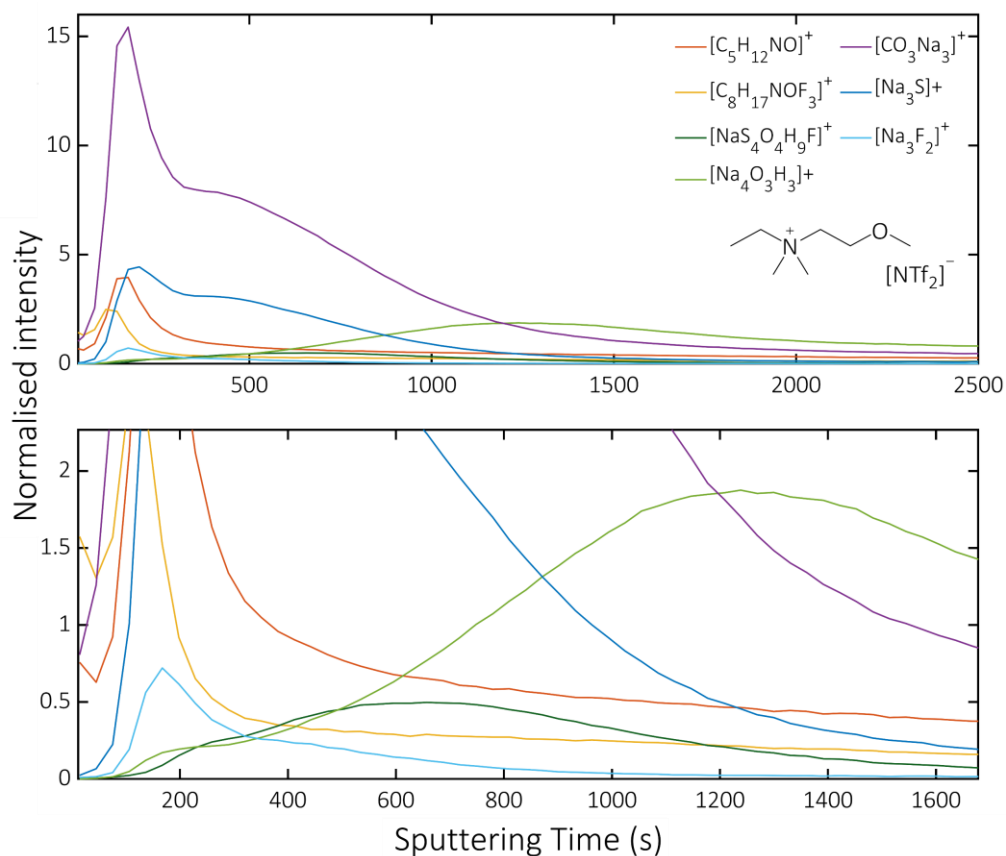


**Figure 3.15.** Positive ion depth profiles of  $\text{Na}[\text{N}_{\text{C}_1,\text{C}_1,\text{C}_2,(\text{C}_2\text{OC}_1)}][\text{NTf}_2]$  (with 0.5 M  $\text{Na}[\text{NTf}_2]$ ) SEI showing presence of potential cation-anion reaction product  $[\text{C}_8\text{H}_{17}\text{NOF}_3]^+$  and other cation and anion-related assignments. Analysis performed using 20 keV  $\text{Ar}_{3000}^+$  for sputtering and analysis at  $-175^\circ\text{C}$ . Bottom image shows magnified lower intensity region (bottom).

Another aspect that may be noticed by analysing Figure 3.15, Figure 3.16 and Figure 3.14 is the diversity in the shape of the intensity profiles.  $\text{Na}[\text{C}_1\text{C}_{\text{dma}}\text{Pyrr}][\text{NTf}_2]$  intensity profiles appear more overlapped than in  $\text{Na}[\text{N}_{\text{C}_1,\text{C}_1,\text{C}_2,\text{C}_4}][\text{NTf}_2]$ , for example. In addition, the ‘cation-related’ fragments in  $[\text{N}_{\text{C}_1,\text{C}_1,\text{C}_2,\text{C}_4}][\text{NTf}_2]$  seem to have a considerable decrease in intensity upon sputtering time, whereas for  $[\text{N}_{\text{C}_1,\text{C}_1,\text{C}_2,(\text{C}_2\text{OC}_1)}][\text{NTf}_2]$ , for example, the intensity does not seem to decrease to the same extent (see orange and yellow intensity profiles in Figure 3.15).

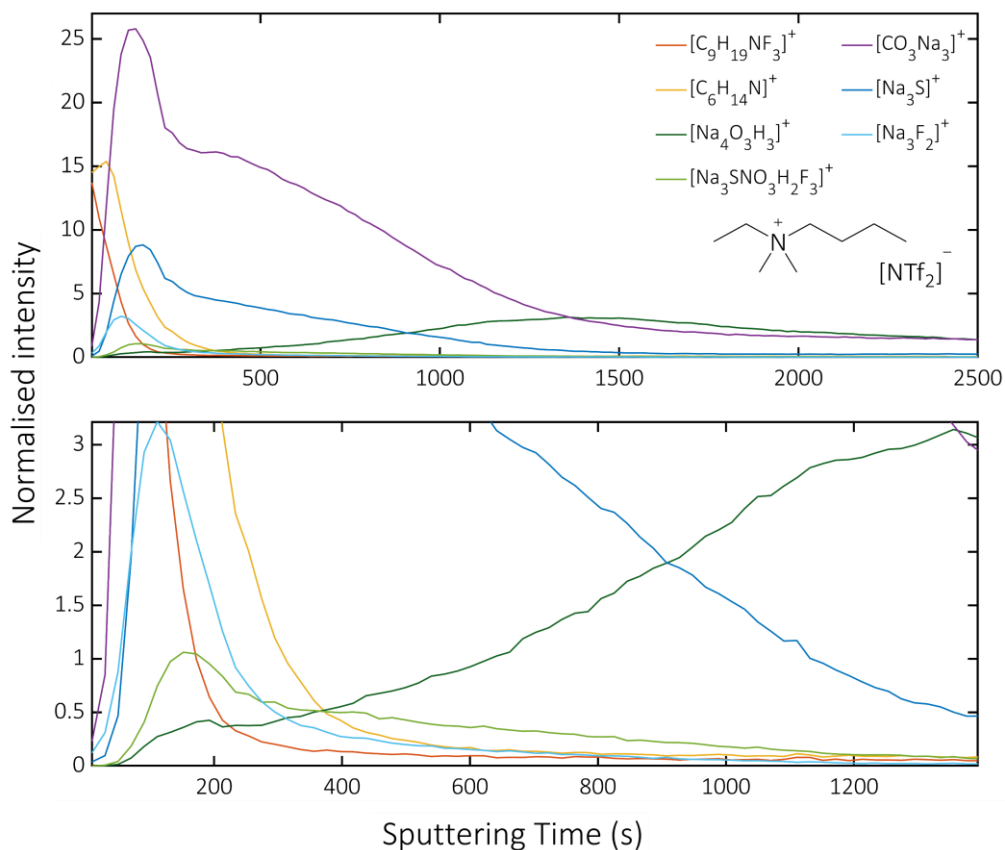


**Figure 3.16.** Positive ion depth profile of Na-[N<sub>C<sub>1</sub>,C<sub>1</sub>,C<sub>2</sub>,C<sub>4</sub></sub>][NTf<sub>2</sub>] (with 0.5 M Na[NTf<sub>2</sub>]) SEI showing the presence of cation-related assignments at the outermost layer, with potential cation-anion reaction product [C<sub>9</sub>H<sub>19</sub>NF<sub>3</sub>]<sup>+</sup>. Analysis performed using 20 keV Ar<sub>3000</sub><sup>+</sup> for sputtering and analysis at -175 °C. Bottom image shows magnified lower intensity region (bottom).

Analysis of these selected assignments shown in Figure 3.14, Figure 3.15 Figure 3.16 has led to a few pertinent observations. However, this is just a small reflection of the data, considering the size of the SIMS dataset obtained in these interphase studies. In addition, although these peaks selected show some of the most prominent intensity profiles in the depth profile plots, it is important to remember that intensity does not necessarily mean concentration in SIMS analysis. Thus, many other assignments with lower intensity, which perhaps might even have a higher abundance in the SEI, have not been analysed carefully. To overcome the challenge of analysing the voluminous and complex SIMS dataset, multivariate analysis was used to gain a better picture of the Na-IL interphase structure and composition.

### 3.6.1 Multivariate analysis of 3D OrbiSIMS depth profile of Na-IL interphase

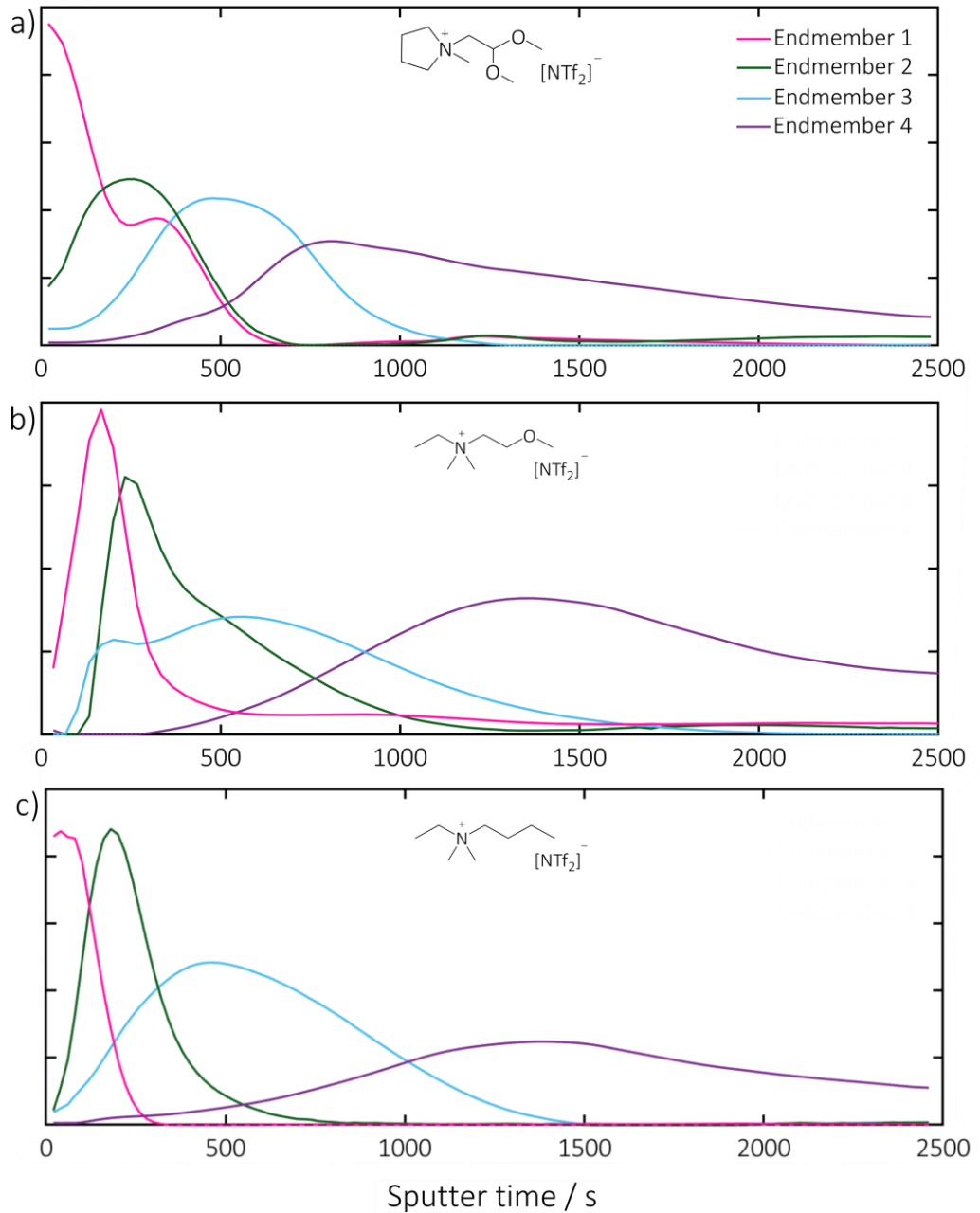
Multivariate analysis of SIMS data for the Na-IL SEI studies was performed as described in Chapter 2. For a full rationale of the process followed to obtain the results present herein, refer to Section 2.4, in Chapter 2. In summary, Non-negative Matrix Factorisation (NMF), a type of a Multi Curve Resolution (MCR) was adopted. In simple terms, NMF organises complex dataset by grouping the constituents that display similar features into endmembers. Thus, each endmember is a fit, a representation of all the constituents in the dataset that display a certain feature. When performing NMF of depth profiling SIMS dataset, the endmembers are displayed in an intensities plot, which represents the depth profile plots in SIMS. The constituents of the endmembers are displayed in a characteristic plot. A characteristic plot is a mass spectrum of the constituents of that endmember, with the intensity of the constituents normalised to how much each constituent is described by that endmember.

The number of expected endmembers (a user input when performing NMF) was estimated with principal component analysis (PCA), as described in Section 2.4. The PCA of each dataset is shown in Appendix 1.A.2.3. Appendix 1.A.2.3 also shows NMF results for SIMS dataset excluding the assignments with the largest area (and consequently high intensity in the depth profile plots), as  $[\text{CO}_3\text{Na}_3]^+$  for example. The very intense profile of these assignments may hinder the intensity profile of other assignments, limiting the scope of the MVA. Thus, this has been done to be sure that any conclusions made with the aid of MVA accounts for the intensity profile of the vast majority of the assignments.

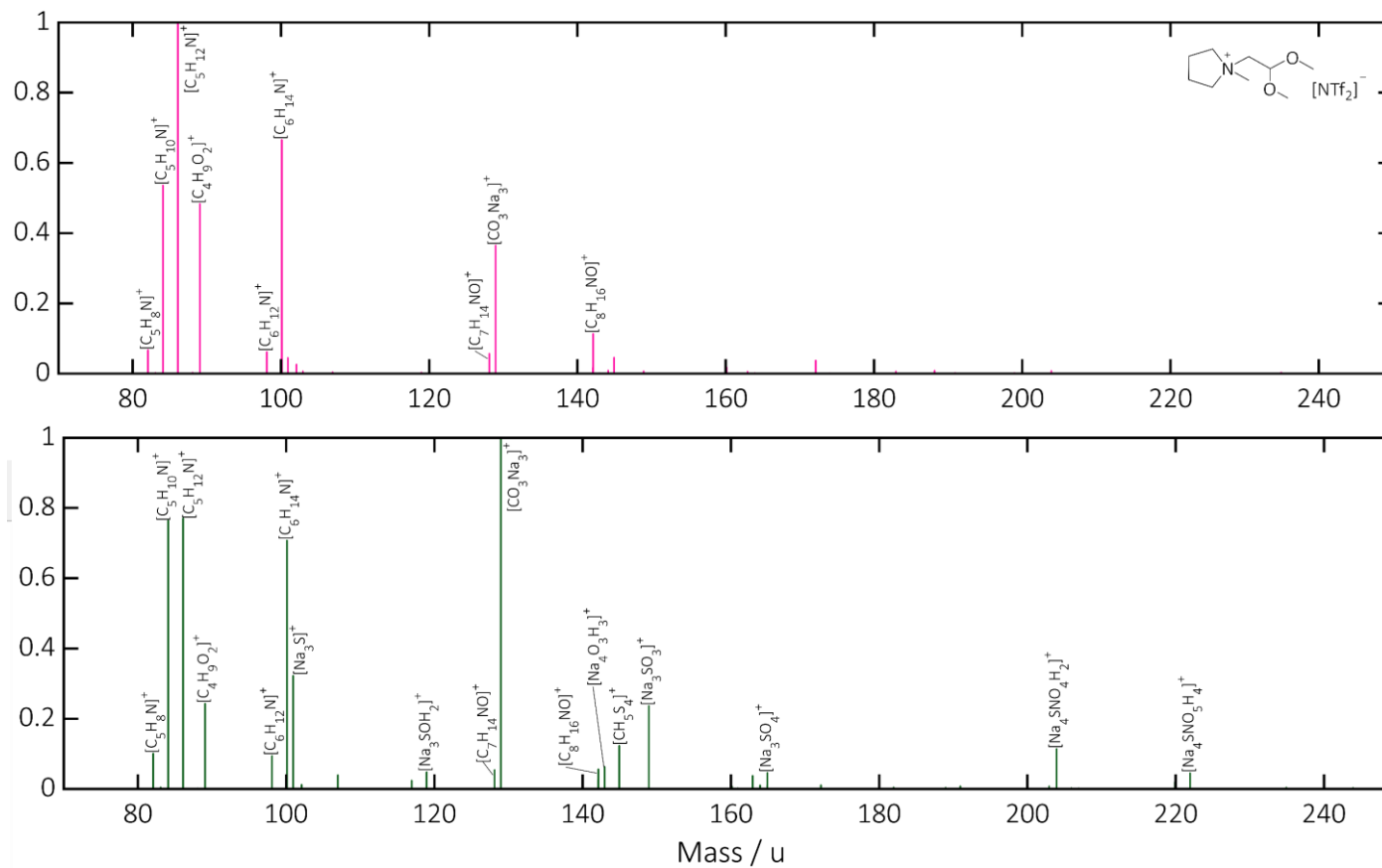
Figure 3.17 shows the NMF intensity plot for the three Na-IL samples, and Figure 3.18, Figure 3.19 and Figure 3.20 show the characteristic spectra of each endmember for  $[\text{C}_1\text{C}_{\text{dma}}\text{Pyrr}][\text{NTf}_2]$ ,  $[\text{N}_{\text{C}_1,\text{C}_1,\text{C}_2,(\text{C}_2\text{OC}_1)}][\text{NTf}_2]$  and  $[\text{N}_{\text{C}_1,\text{C}_1,\text{C}_2,\text{C}_4}][\text{NTf}_2]$ -Na interphase, respectively.

Figure 3.17 shows that the SEI for all the ILs studied herein can be summarised into four main intensity profiles (NMF endmembers). All intensity profiles show that the constituents described by endmember 1 (pink traces) are

largely concentrated within the outermost layer (at very early sputter times), whilst assignments described by endmembers 2 and 3 are mostly concentrated in the inner layers. Finally, the deepest layer, thought to be at the vicinity of the Na electrode, is where most of the assignments represented by endmember 4 are concentrated. Regarding the SEI with  $[C_1C_{dma}Pyrr][NTf_2]$ -based electrolyte, Figure 3.17a shows that endmember 1 also shows significant presence within the inner layers. In fact, endmember 1 displays a local maximum at approximately 300 s sputter time. This suggests that the SEI with  $[C_1C_{dma}Pyrr][NTf_2]$  is not as clearly layered as the SEI with  $[N_{C_1,C_1,C_2,(C_2OC_1)}][NTf_2]$  and  $[N_{C_1,C_1,C_2,C_4}][NTf_2]$  seems to be, considering the overlap of the endmembers as evidently shown in Figure 3.17a.



**Figure 3.17.** NMF intensity plot of SIMS dataset for SEI of a) Na-[C<sub>1</sub>C<sub>dma</sub>Pyrr][NTf<sub>2</sub>], b) N-[N<sub>C<sub>1</sub>,C<sub>1</sub>,C<sub>2</sub>,C<sub>2</sub>OC<sub>1</sub>][NTf<sub>2</sub>] and c) Na-[N<sub>C<sub>1</sub>,C<sub>1</sub>,C<sub>2</sub>,C<sub>4</sub>][NTf<sub>2</sub>], showing four NMF endmembers (representation of all the constituents in the dataset that display similar feature, intensity profiles in this case). Note how the overlap of NMF endmembers decreases in the order [C<sub>1</sub>C<sub>dma</sub>Pyrr][NTf<sub>2</sub>] – [N<sub>C<sub>1</sub>,C<sub>1</sub>,C<sub>2</sub>,C<sub>2</sub>OC<sub>1</sub>][NTf<sub>2</sub>] – [N<sub>C<sub>1</sub>,C<sub>1</sub>,C<sub>2</sub>,C<sub>4</sub>][NTf<sub>2</sub>].</sub></sub></sub></sub>



**Figure 3.18-Part I.** NMF characteristic spectra of Na-[C<sub>1</sub>C<sub>dma</sub>Pyrr][NTf<sub>2</sub>] (0.5 M Na[NTf<sub>2</sub>]) SEI showing endmembers 1 (pink) and 2 (green), with endmember 1 mainly composed of cation-related compounds and endmember 2 composed of a mixture of cation and anion-related assignments.

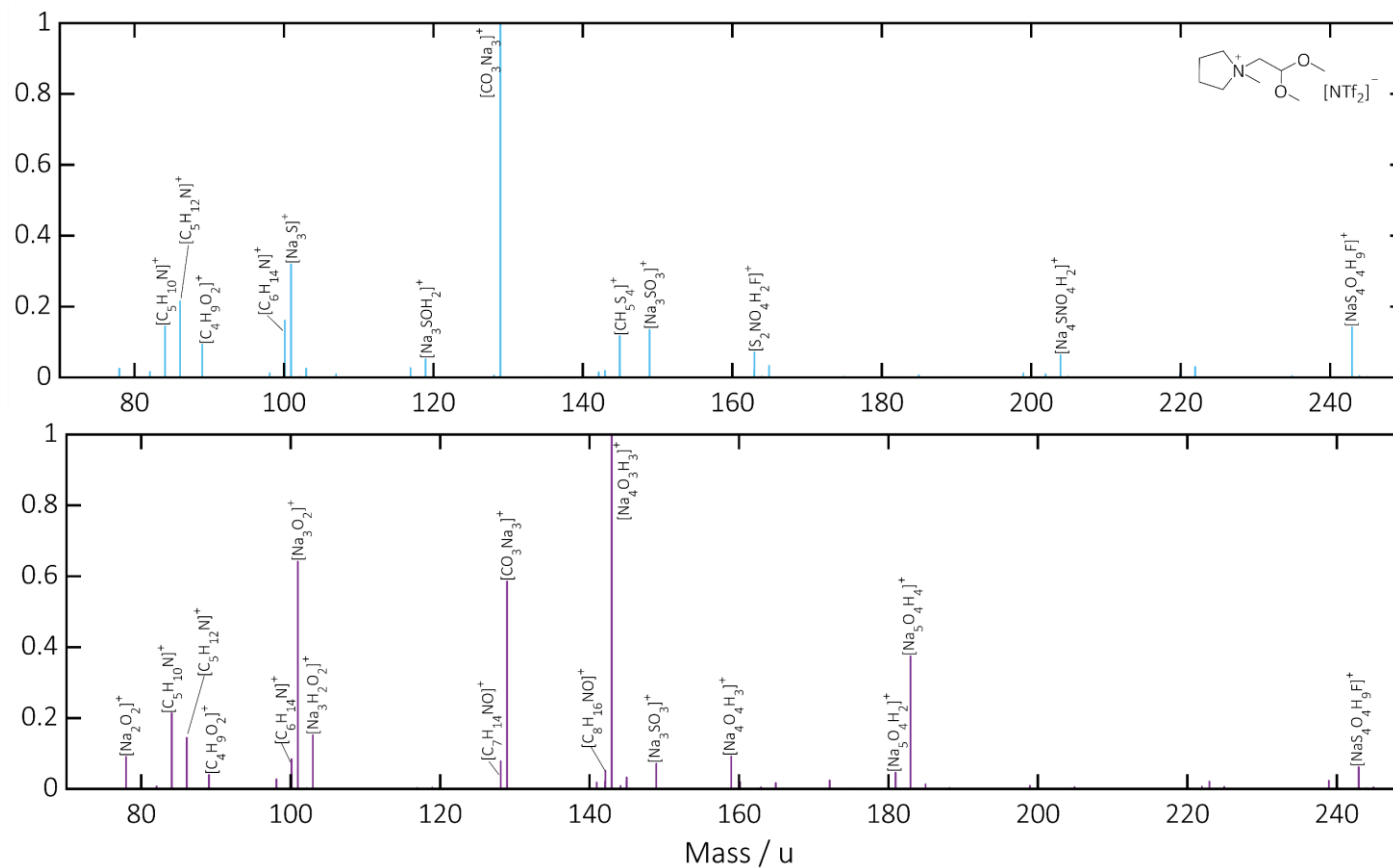


**Figure 3.18-Part II.** NMF characteristic spectra of Na-[C<sub>1</sub>C<sub>dma</sub>Pyrr][NTf<sub>2</sub>] (0.5 M Na[NTf<sub>2</sub>]) SEI showing endmembers 3 (blue) and 4 (purple). Note the presence of oxides and hydroxides as well as cation-related assignments even at the innermost profile depth represented by endmember 4.



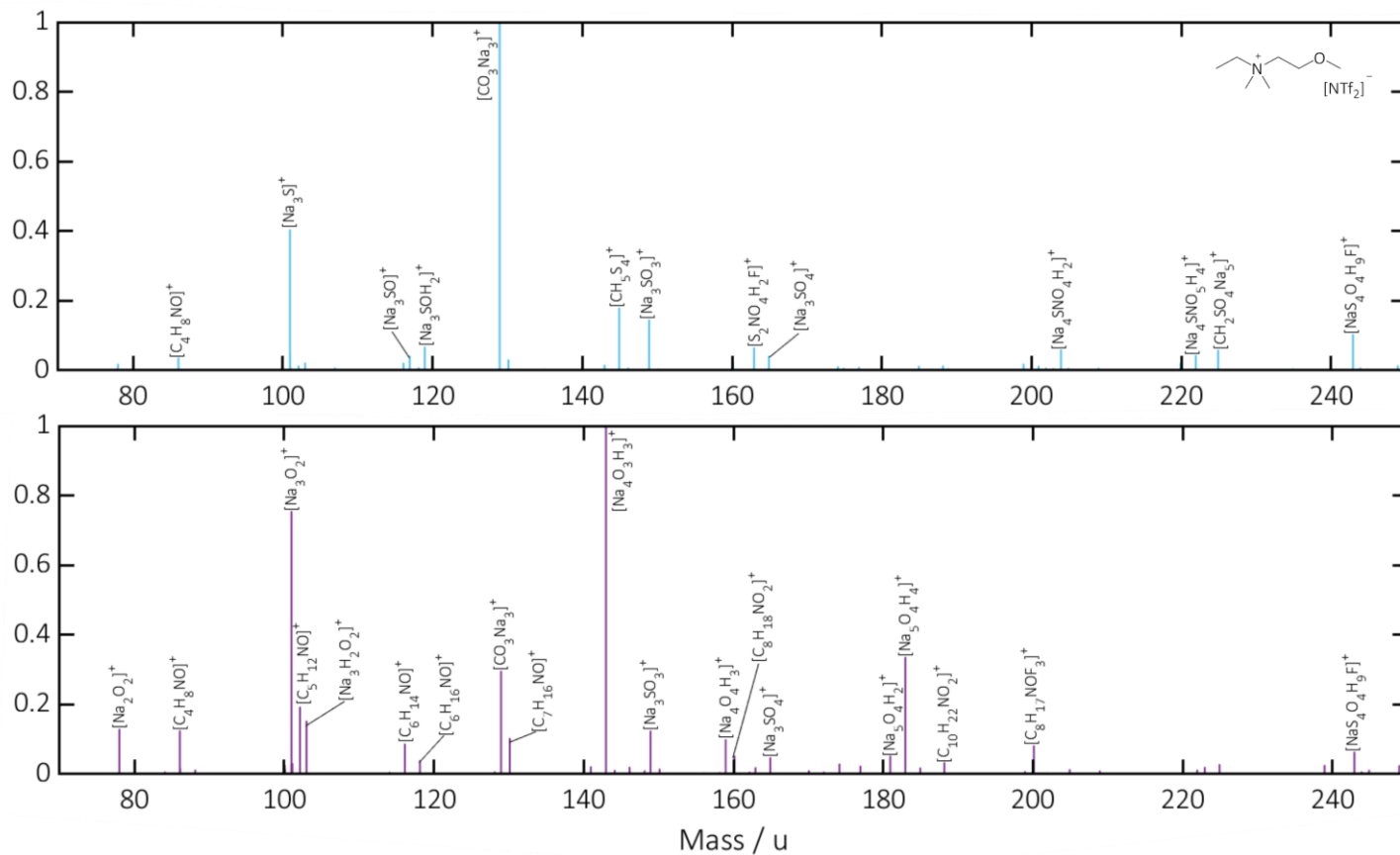


**Figure 3.19-Part II.** NMF characteristic spectra of Na-[N<sub>C<sub>1</sub>,C<sub>1</sub>,C<sub>2</sub>,(C<sub>2</sub>OC<sub>1</sub>)</sub>][NTf<sub>2</sub>] (0.5 M Na[NTf<sub>2</sub>]) interphase showing endmembers 3 (blue) and 4 (purple), with endmember 3 mostly composed of anion-related compounds, and endmember 4 showing [Na<sub>x</sub>O<sub>y</sub>H<sub>v</sub>]<sup>+</sup> and cation-related compounds.

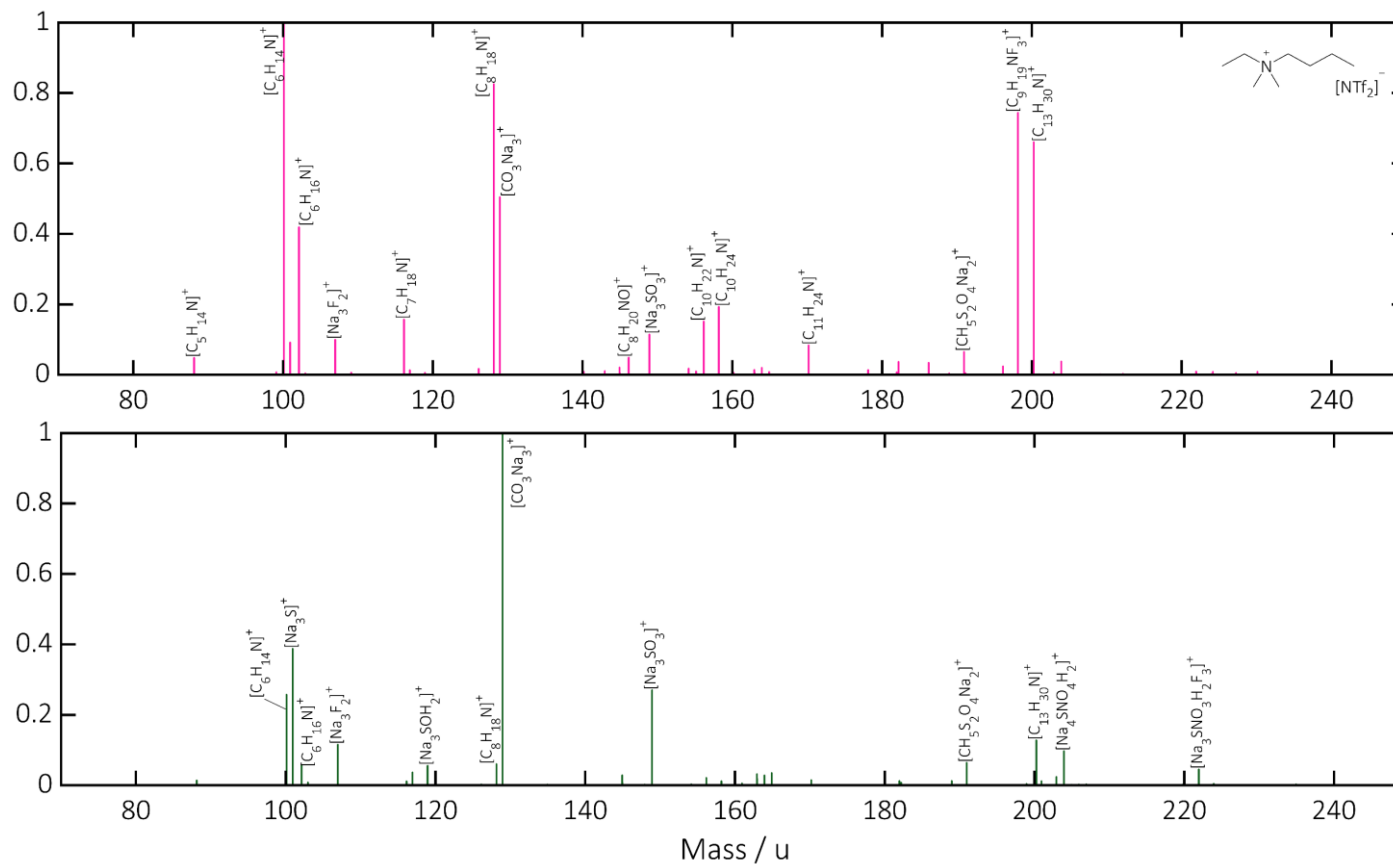


**Figure 3.20-Part I.** NMF characteristic spectra of Na-[N<sub>C<sub>1</sub>,C<sub>1</sub>,C<sub>2</sub>,C<sub>4</sub>][NTf<sub>2</sub>] (0.5 M Na[NTf<sub>2</sub>]) interphase showing endmembers 1 (pink) and 2 (green). Note the relatively large cation-related compounds [C<sub>9</sub>H<sub>19</sub>NF<sub>3</sub>]<sup>+</sup> and [C<sub>13</sub>H<sub>30</sub>N]<sup>+</sup> in endmember 1.</sub>

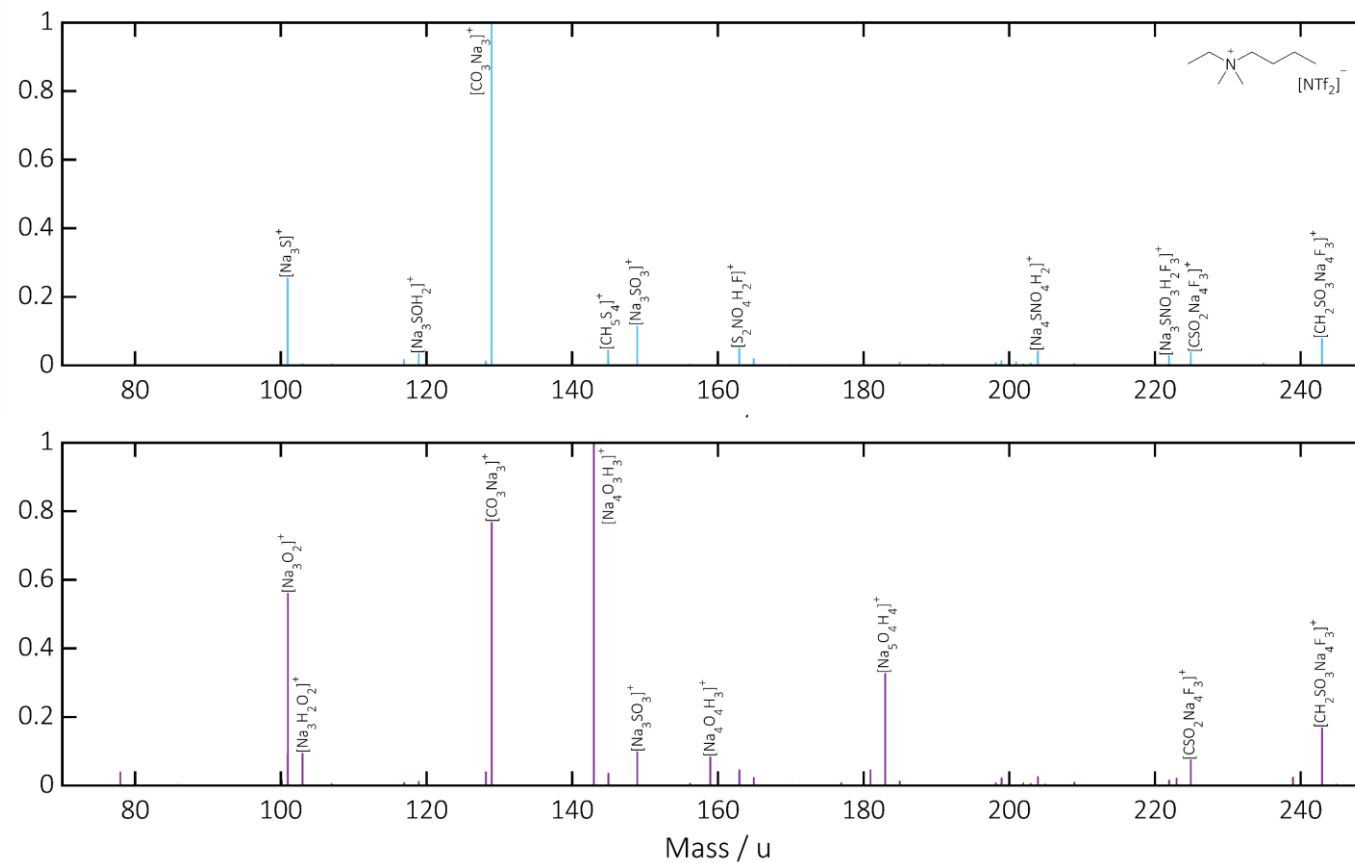


**Figure 3.20-Part II.** NMF characteristic spectra of Na-[N<sub>C<sub>1</sub>,C<sub>1</sub>,C<sub>2</sub>,C<sub>4</sub></sub>][NTf<sub>2</sub>] (0.5 M Na[NTf<sub>2</sub>]) interphase showing endmembers 3 (blue) and 4 (purple) with anion-related and [Na<sub>x</sub>O<sub>y</sub>H<sub>y</sub>]<sup>+</sup> compounds, and absence of significant cation-related assignments.

Figure 3.18-Part I shows that the endmember 1 is mainly composed of small organic fragments, with  $[\text{C}_5\text{H}_{12}\text{N}]^+$  being the most significant assignment. These small fragments may be product of the sputter process of any remaining IL, and/or a radical fragmentation during electron transfer reactions (see scheme in Scheme 3.1).

As sputtering continues, endmember 2 (green traces, Figure 3.17a) shows maximum intensity at approximately 250 s, followed by endmember 3 with maximum intensity at approximately 500 s (blue traces, Figure 3.17a). Endmembers 2 and 3 represent a diverse range of assignments (see Figure 3.18-Part I), from small organic and cation-related fragments, to small and larger inorganic fragments.  $[\text{C}_5\text{H}_{12}\text{N}]^+$  is still one of the most significant assignments of this endmember, which could be expected considering the overlap between endmembers 1 and 2 shown in Figure 3.17a. Inorganic fragments such as  $[\text{Na}_3\text{S}]^+$ ,  $[\text{Na}_3\text{SO}_3]^+$  and  $[\text{Na}_4\text{SNO}_4\text{H}_2]^+$ , strongly suggests that electron transfer reactions involving Na and  $[\text{NTf}_2]^-$  took place during SEI formation.

Finally, endmember 4 is concentrated predominantly within the innermost layer of the interphase (Figure 3.17a, purple traces), likely to be at the vicinity of the Na electrode. The main components of this endmember are sodium oxides and hydroxides (see  $[\text{Na}_3\text{O}_2]^+$ ,  $[\text{Na}_4\text{O}_4\text{H}_3]^+$  and  $[\text{Na}_5\text{O}_4\text{H}_4]^+$  assignments in Figure 3.18-Part II, in purple), which may be part of the metallic sodium native layer, as described previously.<sup>107, 108</sup> Alternatively, it may be product of a reaction between metallic Na with and any moisture present in the electrolyte. Due to the high reactivity of Na metal and water, any moisture in the electrolyte is likely to be promptly consumed, thus being at the vicinity of the electrode. Note that despite the outermost layer have the largest concentration of cation-related fragments, these fragments are still part of the endmember 4, which is found mainly within the innermost layer. This supports the poor layer separation suggested in the previous paragraphs and demonstrated in Figure 3.17a.

The NMF intensity plot for the Na-[N<sub>C<sub>1</sub>,C<sub>1</sub>,C<sub>2</sub>,C<sub>2</sub>OC<sub>1</sub></sub>][NTf<sub>2</sub>] interphase is shown in Figure 3.17b, and the characteristic spectra are displayed in Figure 3.19. Endmember 1 (in pink) is mostly composed by cation-related fragments, similar to the Na-[C<sub>1</sub>C<sub>dma</sub>Pyrr][NTf<sub>2</sub>] interphase. However fragments larger than the [N<sub>C<sub>1</sub>,C<sub>1</sub>,C<sub>2</sub>,C<sub>2</sub>OC<sub>1</sub></sub>]<sup>+</sup> cation are also observed, such as [C<sub>10</sub>H<sub>22</sub>NO<sub>2</sub>]<sup>+</sup> and [C<sub>9</sub>H<sub>20</sub>NO<sub>2</sub>]<sup>+</sup>.

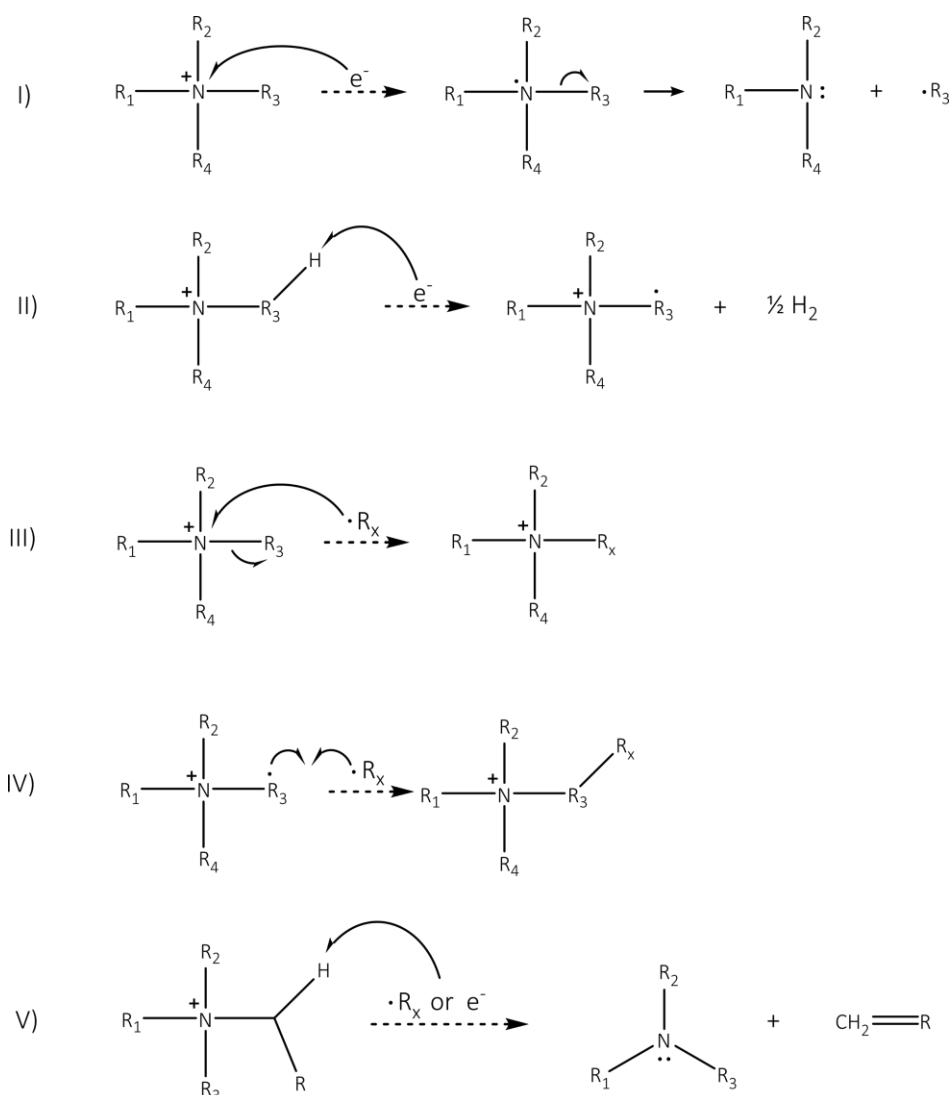
Endmember 1 of Na-[N<sub>C<sub>1</sub>,C<sub>1</sub>,C<sub>2</sub>,C<sub>4</sub></sub>][NTf<sub>2</sub>] interphase (see Figure 3.17c for NMF intensity plot and Figure 3.20 for characteristic spectra) is also rich in organic fragments, with assignments as large as [C<sub>13</sub>H<sub>30</sub>N]<sup>+</sup>, analogous to the trends shown by Na-[N<sub>C<sub>1</sub>,C<sub>1</sub>,C<sub>2</sub>,C<sub>2</sub>OC<sub>1</sub></sub>][NTf<sub>2</sub>]. These observations suggest that radicals formed in SEI reactions (Scheme 3.1) are more likely to recombine forming larger structures in these IL electrolytes than in [C<sub>1</sub>C<sub>dma</sub>Pyrr][NTf<sub>2</sub>]. In addition, quaternary ammonium ILs are also prone to chain shuffling, reversible Menshutkin and elimination reactions at elevated temperatures.<sup>109, 110</sup> However, these reactions may happen independently of the presence of Na, being intrinsic to the IL and not a SEI reaction. To investigate whether these assignments are inherent to the IL or formed during an SEI reaction, 3D OrbiSIMS was also performed on pure IL samples. If the neat ILs also show similar composition to the Na-IL interphase samples, then the large molecules are thought to be formed by means other than a SEI reaction. Table 3.4 shows the relative areas of these large fragments and also smaller fragments for comparison, in both the neat IL and the Na-IL interphase for [N<sub>C<sub>1</sub>,C<sub>1</sub>,C<sub>2</sub>,C<sub>2</sub>OC<sub>1</sub></sub>][NTf<sub>2</sub>] and [N<sub>C<sub>1</sub>,C<sub>1</sub>,C<sub>2</sub>,C<sub>4</sub></sub>][NTf<sub>2</sub>]. To account for differences in acquisition time, topology and sample ionization, all m/z peaks were normalised to the most intense peak in common to both samples, their respective IL cation.

Table 3.4 shows that both neat ILs (no Na salt added) share the same peaks as their respective Na-IL SEI, but significant differences in their relative peak areas can be noticed. A comparison of peak areas in this instance is acceptable because it is between the same assignments across samples of highly similar matrix, thus same ionisation yield.

**Table 3.4.** Comparison of peak areas ( $10^{-3}$  a.u.) of selected assignments in neat IL and Na-IL interphase for  $[\text{N}_{\text{C}_1, \text{C}_1, \text{C}_2, (\text{C}_2\text{OC}_1)}][\text{NTf}_2]$  and  $[\text{N}_{\text{C}_1, \text{C}_1, \text{C}_2, \text{C}_4}][\text{NTf}_2]$ . Peak areas normalised to the IL cation.

$[\text{N}_{\text{C}_1, \text{C}_1, \text{C}_2, \text{C}_4}][\text{NTf}_2]$			$[\text{N}_{\text{C}_1, \text{C}_1, \text{C}_2, (\text{C}_2\text{OC}_1)}][\text{NTf}_2]$		
Assignment	Neat IL	Na-IL SEI	Assignment	Neat IL	Na-IL SEI
$[\text{C}_{13}\text{H}_{30}\text{N}]^+$	0.0012	9.71	$[\text{C}_{10}\text{H}_{22}\text{NO}_2]^+$	0.25	5.46
$[\text{C}_{11}\text{H}_{24}\text{N}]^+$	0.21	1.51	$[\text{C}_9\text{H}_{20}\text{NO}_2]^+$	0.28	4.18
$[\text{C}_{10}\text{H}_{24}\text{N}]^+$	2.04	2.36	$[\text{C}_8\text{H}_{18}\text{NO}_2]^+$	0.38	7.07
$[\text{C}_{10}\text{H}_{22}\text{N}]^+$	0.50	2.56	$[\text{C}_7\text{H}_{16}\text{NO}]^+$	3.00	10.6
$[\text{C}_8\text{H}_{18}\text{N}]^+$	7.88	13.2	$[\text{C}_6\text{H}_{14}\text{N}]^+$	2.74	0.95
$[\text{C}_7\text{H}_{18}\text{N}]^+$	0.94	1.96	$[\text{C}_5\text{H}_{14}\text{NO}]^+$	3.90	6.65
$[\text{C}_6\text{H}_{16}\text{N}]^+$	3.42	5.54	$[\text{C}_5\text{H}_{12}\text{NO}]^+$	1.41	23.5
$[\text{C}_5\text{H}_{14}\text{N}]^+$	0.17	0.90	$[\text{C}_4\text{H}_8\text{NO}]^+$	1.11	10.4

The peak areas of the vast majority of the large fragments (first entries on Table 3.4) in the Na-IL SEI samples are considerably larger than in the neat IL samples. The fact that some large fragments are present in the neat samples, despite the lower peak area of most assignments, suggests that rearrangement reactions such as chain shuffling and reverse Menshutkin may have occurred in the neat liquids. However, the greater area of these assignments in the Na-IL SEI samples indicates that either the presence of metallic Na promotes further rearrangement, and/or these large assignments are formed in SEI-related reactions, such as electron transfer and radical reactions. In addition to the reactions already shown in Scheme 3.1, other reactions are suggested as possible routes for the formation of large fragments, and are shown in Scheme 3.3. These may include a radical assisted chain shuffling, large radical combination, and elimination reactions as proposed by the reactions III, IV and V in Scheme 3.3. The reactions suggested in Scheme 3.3 have also been proposed previously as degradation pathways of ILs,<sup>90, 109, 110</sup> and other radical related oligomer formation has also been described by other studies as potential SEI-related reactions.<sup>33, 87</sup>



**Scheme 3.3.** Schematics of reactions possibly occurring during SEI formation involving quaternary ammonium cations considering the assignments displayed in Table 3.4

In the  $[N_{C_1, C_1, C_2, C_4}][NTf_2]$  system (Table 3.4 columns on the left), the smaller fragments display somewhat similar peak area in both neat and SEI samples. This suggests that part of these smaller fragments is likely to be inherent to the IL and associated to fragmentation and ionization of any remaining IL in the SEI sample, whilst part might be small radicals formed in SEI-related reactions. This is not entirely the case for the  $[N_{C_1, C_1, C_2, (C_2OC_1)}][NTf_2]$  system (see Table 3.4, columns on the right). With exception of  $[C_6H_{12}N]^+$  and  $[C_5H_{14}NO]^+$ , the smaller fragments in the Na-IL SEI sample display remarkably larger peak areas than in the neat IL sample. Perhaps, the lower viscosity of the  $[N_{C_1, C_1, C_2, (C_2OC_1)}][NTf_2]$  IL, compared to  $[N_{C_1, C_1, C_2, C_4}][NTf_2]$ , allows these fragments

to diffuse away, avoiding further reaction and/or radical combination to form larger fragments.

The more prominent difference between SEI peak areas and neat IL peak areas in  $[N_{C_1,C_1,C_2,(C_2OC_1)}][NTf_2]$  than  $[N_{C_1,C_1,C_2,C_4}][NTf_2]$  is discussed as follows. A potential reason could simply be that formation of small fragments via SEI reactions is more likely in the  $[N_{C_1,C_1,C_2,(C_2OC_1)}][NTf_2]$  system than in the  $[N_{C_1,C_1,C_2,C_4}][NTf_2]$  system. Another explanation for this difference may be related to the extent that small fragments, formed via SEI reactions, undergo further reactions to form larger molecules. Perhaps, SEI reactions in the  $[N_{C_1,C_1,C_2,(C_2OC_1)}][NTf_2]$  system are indeed more likely to yield small fragments, which even with further reactions, remain as small fragments. However, in the SEI formation of  $[N_{C_1,C_1,C_2,C_4}][NTf_2]$ , the small fragments might be more likely to combine forming larger molecules, thus similar peak areas of small molecules, and considerable higher peak areas of large molecules in the SEI compared to the neat sample (see areas for  $[C_{13}H_{30}N]^+$  for example). Note that this reasoning is a comparison of the differences in peak areas (between neat and Na-IL interphase), not a comparison of the areas themselves.

Returning the attention to the NMF characteristic spectra of endmember 1 for the Na- $[N_{C_1,C_1,C_2,(C_2OC_1)}][NTf_2]$  (Figure 3.19-Part I) and Na- $[N_{C_1,C_1,C_2,C_4}][NTf_2]$  (Figure 3.20-Part II) interphases, another distinct feature is the presence of assignments such as  $[C_8H_{17}NOF_3]^+$  and  $[C_9H_{19}NF_3]^+$ . Detection of these molecules demonstrates that SEI-related reactions also involves a mixture of fragments from the IL cation and the IL anion ( $CF_3$ ).

Another aspect regarding the NMF characteristic spectra of endmember 1 (Figure 3.19-Part I) is that  $[CO_3Na_3]^+$  is the most significant assignment in  $[N_{C_1,C_1,C_2,(C_2OC_1)}][NTf_2]$ , being a lot more relevant than any of the organic fragments. However, the characteristic spectra of endmember 1 in the Na- $[N_{C_1,C_1,C_2,C_4}][NTf_2]$  interphase shows that  $[C_6H_{14}N]^+$ ,  $[C_8H_{18}N]^+$ ,  $[C_9H_{19}NF_3]^+$  and  $[C_{13}H_{30}N]^+$  are the main assignments for this endmember.

NMF characteristic spectra of endmembers 2, 3 and 4 in the  $[N_{C_1,C_1,C_2,(C_2OC_1)}][NTf_2]$  system (Figure 3.19-Part I and II) display similar characteristics already discussed for the  $[C_1C_{dma}Pyrr][NTf_2]$  system (Figure 3.18-Part I and II). Endmembers 2 and 3 display a range of small and large inorganic fragments and some organic fragments as well, and finally endmember 4 shows a larger concentration of oxides and hydroxides. It is important to note that in both  $[N_{C_1,C_1,C_2,(C_2OC_1)}][NTf_2]$  and  $[C_1C_{dma}Pyrr][NTf_2]$  organic fragments are detected even in the deepest layers of the interphase as demonstrated by the vast presence of these fragments in the characteristic spectra of endmember 4, which shows maximum intensity at late sputter times.

Whilst NMF characteristic spectra of endmembers 2 and 3 for the Na- $[N_{C_1,C_1,C_2,C_4}][NTf_2]$  interphase display similar range of assignments to  $[N_{C_1,C_1,C_2,(C_2OC_1)}][NTf_2]$  and  $[C_1C_{dma}Pyrr][NTf_2]$ , the presence of organic fragments significantly decreases in endmember 2, and is not significant in endmembers 3 and 4. Because endmembers 3 and 4 have maxima in the deeper interphase layers (see Figure 3.17c), it is likely that the vast majority of organic fragments in the Na- $[N_{C_1,C_1,C_2,C_4}][NTf_2]$  SEI are concentrated at the outermost layer, with very little presence in the inner layers.

### 3.6.2 MVA study remarks, correlation to other analysis and to the original dataset.

Overall, the Na- $[N_{C_1,C_1,C_2,C_4}][NTf_2]$  interphase seems more structured, with more defined separation of endmembers, which can be observed by analysis of the intensity plot (Figure 3.17c) and the discussion above regarding composition of endmembers. Several surface studies have been performed on ILs<sup>111</sup> which can aid understanding of this 'more structured' interphase with  $[N_{C_1,C_1,C_2,C_4}][NTf_2]$ . XPS studies have shown that ILs with long aliphatic hydrocarbon side chains structure themselves in such a way that the hydrocarbon chains are stacked by van der Waals forces. However, PEG-ILs contain one or multiple O atoms in the side chain, which disrupts the Van der

Waals forces that were keeping the organised structure in the hydrocarbon-side chain IL. Therefore, these XPS studies may aid reasoning of the greater concentration of  $[N_{C_1,C_1,C_2,C_4}]^+$  derived fragments within the same location, at the outermost SEI layer. In addition, the high concentration of these species within the same location can make it more likely that radicals meet and combine forming larger molecules.

Another factor to be considered to understand the differences in the interphase structure and composition between the ILs is the reactivity of the side chains in the  $[C_1C_{dma}Pyrr][NTf_2]$ ,  $[N_{C_1,C_1,C_2,(C_2OC_1)}][NTf_2]$  and  $[N_{C_1,C_1,C_2,C_4}][NTf_2]$  ILs. The lone pair of electrons on the oxygen atom, and electronegativity difference are factors that contribute to the higher reactivity of ether ( $-C_2OC_1$ ) and dimethylacetal ( $-C_{dma}$ ) side chains compared to a purely hydrocarbon side chain. In fact, a previous study highlighted the lower thermal and electrochemical stability of ether side chains.<sup>112</sup> Thus, in addition to the lack of van der Waals stacking stabilisation, the oxygen-containing chains are also more prone to undergo SEI-related reactions. This has been clearly observed in the impedance studies of Na|Na symmetrical cells with these ILs, in which the cell with  $[C_1C_{dma}Pyrr][NTf_2]$  demonstrated highly reactive SEI, with significant increase of surface resistance over time (see Section 3.4, and Figure 3.5, Figure 3.6 and Scheme 3.2). Moreover, the lack of large organic fragments, and abundance of small fragments, are also an indication of the degree of reactivity of the  $[C_1C_{dma}Pyrr][NTf_2]$  IL. Finally, the lack of stability of the interphase with this IL can be associated to poor cycling performance of Na|Na symmetrical cells. Section 3.5 has shown that Na|Na cells with  $[C_1C_{dma}Pyrr][NTf_2]$ -based electrolyte display high overpotentials, reaching the cut-off limits considerably earlier than the cells with the other ILs (see Figure 3.7).

This increase in surface resistance was not observed for the Na|Na cells with  $[N_{C_1,C_1,C_2,(C_2OC_1)}][NTf_2]$ , in fact this system actually displayed a decrease in surface resistance after 24 hours of resting time (see Figure 3.5 Figure 3.6). A possible explanation for the decrease in the surface resistance in the

$[\text{N}_{\text{C}_1, \text{C}_1, \text{C}_2, (\text{C}_2\text{OC}_1)}][\text{NTf}_2]$  system can be associated to solubility and/or diffusion of the SEI reaction products, and is described as follows. In the first 24 hours, extensive SEI reaction takes place at the electrode surface, leading to an increase in surface resistance. The SEI reaction products perhaps display a certain degree of solubility in this IL and diffuse away from the layer adjacent to the electrode. As this occurs, IL molecules replace the SEI products at the vicinity of the Na electrode, leading to a change in the surface area and a decrease in resistance. This would also explain the presence of  $[\text{N}_{\text{C}_1, \text{C}_1, \text{C}_2, (\text{C}_2\text{OC}_1)}]^+$ -related fragments at deeper layers observed in the NMF studies of the SIMS data. In addition,  $[\text{N}_{\text{C}_1, \text{C}_1, \text{C}_2, (\text{C}_2\text{OC}_1)}][\text{NTf}_2]$  displays the lowest viscosity among the three ILs studied in this section (see Table 3.2), which can perhaps facilitate the diffusion of SEI reaction products.

Regarding the impedance studies of Na|Na cells with  $[\text{N}_{\text{C}_1, \text{C}_1, \text{C}_2, \text{C}_4}][\text{NTf}_2]$ , it was described that the surface resistance seems to reach a plateau from which no significant increase in resistance is observed. It is possible that once a significant amount of large organic fragments are formed at the outermost interphase layer, these fragments act as ‘barrier’ suppressing the SEI reactions to the molecules in the inner interphase layers, and preventing further reaction with the bulk IL. Furthermore, the SEI reaction products might also display low solubility in this organic fragment layer, which diminishes the movement of these products away from the Na electrode. The presence of this ‘barrier’ may explain the remarkable performance of Na|Na symmetrical cells with this IL, that displayed the lowest overpotential (see Figure 3.10) of the cells studied in Section 3.5.

These findings are similar to what has been reported previously by Howlett and co-workers.<sup>113</sup> In their study, the authors suggest that the SEI formed between Li metal and a phosphonium bis(fluorosulfonyl)imide ionic liquid has an inner layer formed mostly of inorganic and anion-related products, whilst the outermost layer was formed by cation-related products.

Finally, it is imperative to look back to the original SIMS dataset in Figure 3.14, Figure 3.15 and Figure 3.16 and compare these observations to the original depth profile plots. The overlap of the different assignments in the  $[C_1C_{dma}Pyrr][NTf_2]$  interphase is evident in Figure 3.14, as well as the presence of small organic fragments across the majority of the interphase (see orange and yellow traces in Figure 3.14).

The original  $[N_{C_1,C_1,C_2,(C_2OC_1)}][NTf_2]$  depth profile also shows, to a certain extent, overlay of assignments of different nature, as demonstrated by the traces of  $[CO_3Na_3]^+$ ,  $[C_5H_{12}NO]^+$ ,  $[C_8H_{17}NOF_3]^+$  and  $[Na_3S]^+$ . In addition, the intensity of  $[C_5H_{12}NO]^+$ ,  $[C_8H_{17}NOF_3]^+$  does not reach zero, indicating presence of these fragments across the whole interphase.

The  $[N_{C_1,C_1,C_2,C_4}][NTf_2]$  original dataset (Figure 3.16) shows the presence of  $[C_9H_{19}NF_3]^+$  and  $[C_6H_{14}N]^+$  at the outermost layer, which rapidly decreases with sputter time. The intensity profile maxima also occur at similar time for fragments of similar 'type', with organic, cation-related fragments first, followed by more inorganic, anion-related fragments and finally hydroxide at latest sputter times, thus corroborating the 'more structured' interphase formed in this IL.

In conclusion, it is suggested that  $[N_{C_1,C_1,C_2,C_4}][NTf_2]$ -based electrolyte may afford formation of a stable SEI layer, due to the formation of a large organic fragments 'barrier' at the outermost layer of the Na-IL interphase. The benefits of this stable SEI, can be observed in the galvanostatic cycling of Na|Na symmetrical cells using this electrolyte, which display low overpotential over several hours of plating and stripping.

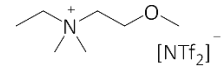
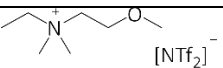
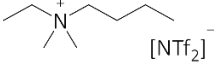
An important future study is to carry OrbiSIMS analysis out after a certain number of cycles, giving the fact that the SEI changes considerably with cycling. Nevertheless, despite the OrbiSIMS analysis have been performed without cell cycling, the analysis of the cell impedance whilst cycling shown in Figure 3.11, gives an insight on the changes in the SEI resistance with  $[N_{C_1,C_1,C_2,(C_2OC_1)}][NTf_2]$  and  $[N_{C_1,C_1,C_2,C_4}][NTf_2]$  ILs. Figure 3.11 showed that  $[N_{C_1,C_1,C_2,C_4}][NTf_2]$  displays much

lower SEI resistance after 48 h of cycling compared to  $[N_{C_1,C_1,C_2,(C_2OC_1)}][NTf_2]$ , which resulted in much more stable cycling, as shown in section 3.2.3.

### 3.7. Evaluating the role of $Na[PF_6]$ as an additive in IL-based electrolytes: electrochemical and 3D OrbiSIMS studies

This section, evaluates the use of small quantities of  $Na[PF_6]$  as an additive in the IL-based electrolytes, as  $Na[PF_6]$  have been described to be beneficial do form a stable SEI layer due to the NaF content in the SEI.<sup>7, 33, 35</sup> To do so, of the 0.5 M of  $Na^+$  salts added to prepare the IL electrolytes, 50 % were the usual  $Na[NTf_2]$  and 50 % were  $Na[PF_6]$ . This electrolyte will often be referred to as the '*mixed salt electrolyte*' in the text, to differentiate to  $[N_{C_1,C_1,C_2,(C_2OC_1)}][NTf_2]$  with  $Na[NTf_2]$  only. This is clarified in Table 3.5.  $[N_{C_1,C_1,C_2,(C_2OC_1)}][NTf_2]$  was the IL chosen for this study, as an improvement in cell performance with this electrolyte would be interesting considering it has the lowest viscosity among the ILs studied herein. In addition, despite not displaying the best results in the previous sections,  $[N_{C_1,C_1,C_2,(C_2OC_1)}][NTf_2]$  is not as reactive and unstable as  $[C_1C_{dma}Pyrr][NTf_2]$ .

**Table 3.5.** Description of electrolytes mentioned throughout this section. Note all electrolytes contain 0.5 M  $Na^+$  salt with composition described below

Nomenclature throughout the text	Salt composition	Electrolyte schematics
'Mixed salt electrolyte' or $[N_{C_1,C_1,C_2,(C_2OC_1)}][NTf_2]$ with $Na[PF_6]$ and $Na[NTf_2]$	50 % $Na[PF_6]$ and 50 % $NaNTf_2$	 50 % $Na[NTf_2]$ : 50 % $Na[PF_6]$
$[N_{C_1,C_1,C_2,(C_2OC_1)}][NTf_2]$ electrolyte	$Na[NTf_2]$ only	 $Na[NTf_2]$
$[N_{C_1,C_1,C_2,C_4}][NTf_2]$ electrolyte	$Na[NTf_2]$ only	 $Na[NTf_2]$

The instability of  $[\text{PF}_6]^-$  anion has conflicted the traditional postulation that ILs are green solvents, and previous studies on  $[\text{PF}_6]$ -containing ILs have highlighted their low instability and susceptibility to hydrolysis, especially at higher temperatures.<sup>114, 115</sup> To a certain extent, the instability and prospect of releasing fluoride of the  $[\text{PF}_6]^-$  anion can be used as an advantage in battery research. Many reports have demonstrated improved cell performance with increased fluoride content in the SEI,<sup>75, 116</sup> often associated with the presence of NaF in the SEI.<sup>33-35, 57</sup> Interestingly, many studies have also found poor stability and electrochemical performance of cells with electrolytes containing  $[\text{NTf}_2]^-$  anion.<sup>33, 35, 57</sup>

In the previous sections, stability and cell performance were found to be associated to SEI structure and distribution of SEI reaction products across the SEI layers. Therefore, in this section the effect of using  $[\text{PF}_6]^-$  anion, as an additive and potential fluoride source will be compared against the formation of a structured SEI, as described above. This section will display and discuss the results obtained with the mixed electrolyte, however, for ease of comparison with results previously displayed, some figures presented in the previous sections are reprinted here.

As a starting point, cyclic voltammetry was used to evaluate how the  $\text{Na}^+/\text{Na}^0$  redox reactions compare in the electrolyte containing Na $[\text{PF}_6]$  additive. The CVs are shown in Figure 3.21.

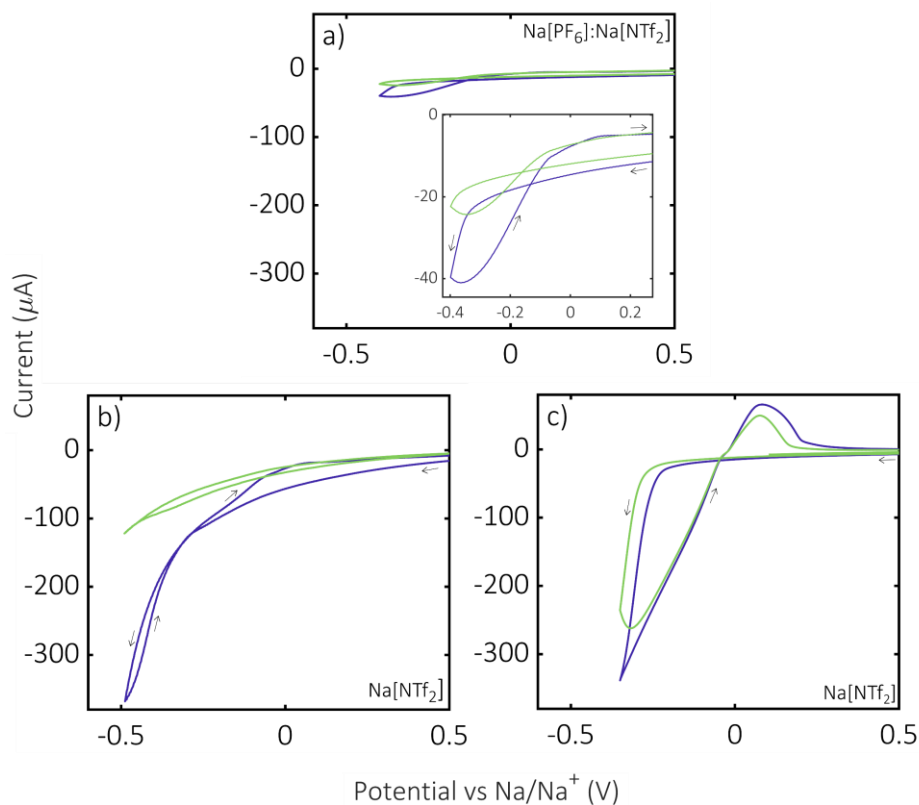


**Figure 3.21.** Cyclic voltammograms (CVs) of 0.5 M Na<sup>+</sup> salts in the IL based electrolytes, at 100 mV.s<sup>-1</sup> using Glassy carbon working electrode, Pt coil counter electrode and Na flag reference electrode. (—) Blue lines show first scan and (—) green lines second scan; arrows show scanning direction. a) [N<sub>C<sub>1</sub>,C<sub>1</sub>,C<sub>2</sub>,C<sub>2</sub>OC<sub>1</sub></sub>][NTf<sub>2</sub>] with with 50 % Na[PF<sub>6</sub>] and 50 % Na[NTf<sub>2</sub>], b) [N<sub>C<sub>1</sub>,C<sub>1</sub>,C<sub>2</sub>,C<sub>2</sub>OC<sub>1</sub></sub>][NTf<sub>2</sub>] with Na[NTf<sub>2</sub>] only, and c) [N<sub>C<sub>1</sub>,C<sub>1</sub>,C<sub>2</sub>,C<sub>4</sub></sub>][NTf<sub>2</sub>] with Na[NTf<sub>2</sub>] only.

Figure 3.21 shows that there is no significant difference in the onset potential for Na<sup>+</sup> reduction in [N<sub>C<sub>1</sub>,C<sub>1</sub>,C<sub>2</sub>,C<sub>2</sub>OC<sub>1</sub></sub>][NTf<sub>2</sub>] with Na[NTf<sub>2</sub>] (-0.32 V, Figure 3.21b) and [N<sub>C<sub>1</sub>,C<sub>1</sub>,C<sub>2</sub>,C<sub>2</sub>OC<sub>1</sub></sub>][NTf<sub>2</sub>] with Na[PF<sub>6</sub>] and Na[NTf<sub>2</sub>] (-0.34 V, Figure 3.21a). Despite the current density being considerably lower in the system with Na[PF<sub>6</sub>] (Figure 3.21a), the second scan (green lines) does not display a passive behaviour as demonstrated by [N<sub>C<sub>1</sub>,C<sub>1</sub>,C<sub>2</sub>,C<sub>2</sub>OC<sub>1</sub></sub>][NTf<sub>2</sub>] with Na[NTf<sub>2</sub>] only. Following the discussion in Section 3.3, this indicates that differences in SEI formation/stability and in plating/stripping reactions may be expected. These will be further studied in the following sections.

### 3.7.1 Effect of Na[PF<sub>6</sub>] additive on the solid electrolyte interphase evaluated by electrochemical impedance spectroscopy

EIS was used to evaluate the SEI formation in the  $[N_{C_1,C_1,C_2,(C_2OC_1)}][NTf_2]$  electrolyte containing Na[PF<sub>6</sub>] and Na[NTf<sub>2</sub>]. The use of EIS to study battery cells and SEIs has been described earlier in Section 3.4. Nyquist plot for the symmetrical cell containing the mixed Na[PF<sub>6</sub>] and Na[NTf<sub>2</sub>] in  $[N_{C_1,C_1,C_2,(C_2OC_1)}][NTf_2]$  electrolyte is shown in Figure 3.22a. Impedance data for  $[N_{C_1,C_1,C_2,(C_2OC_1)}][NTf_2]$  and  $[N_{C_1,C_1,C_2,C_4}][NTf_2]$  with Na[NTf<sub>2</sub>] is also shown in Figure 3.22 for comparison. The percentual change of the surface resistance over time with respect to the initial ( $t_0$ ) resistance (Change/ $R(t_0)$ ) and the sequential percentual change of the surface resistance with respect to the resistance of the immediately preceding measurement (Sequential change) are shown in Figure 3.23a and b respectively.

Interestingly, within the first hour of resting time the cell with the electrolyte containing Na[PF<sub>6</sub>] and Na[NTf<sub>2</sub>] shows a substantial increase in surface resistance, as shown in Figure 3.22 and expressed by the percentual change in Figure 3.23b. The steeper increase within the first hour shown by the Na[PF<sub>6</sub>]:Na[NTf<sub>2</sub>]  $[N_{C_1,C_1,C_2,(C_2OC_1)}][NTf_2]$  sample compared to the equivalent sample containing only Na[NTf<sub>2</sub>] (compare Figure 3.22a and b, and red and blue traces in Figure 3.23) might be associated to the higher reactivity of the [PF<sub>6</sub>]<sup>-</sup> anion. Perhaps, because [PF<sub>6</sub>]<sup>-</sup> releases fluoride more easily than [NTf<sub>2</sub>]<sup>-</sup>, some SEI reactions might be facilitated, and consequently the surface resistance increases more rapidly.

Of further interest, after 20 hours of resting time the surface resistance seems to reach a plateau and no significant increase is observed, similar to what has been observed for  $[N_{C_1,C_1,C_2,C_4}][NTf_2]$  (compare Figure 3.22a and c, and red and green traces in Figure 3.23). This has been previously attributed to the formation of a stable SEI, in which no further reactions significantly affect the surface resistance.

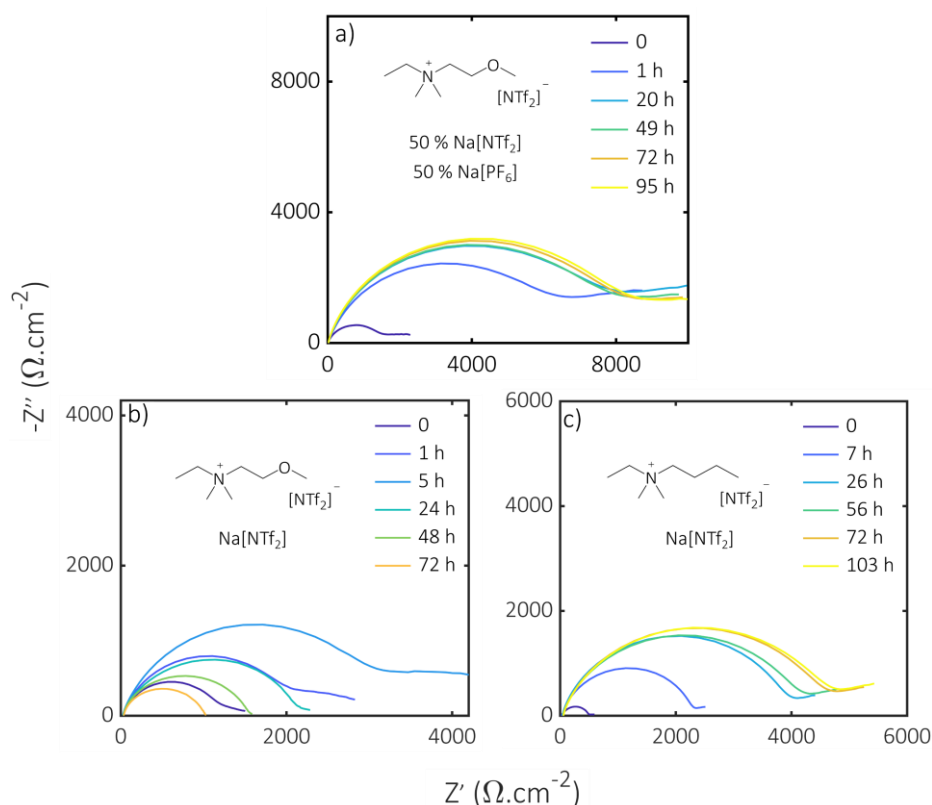


**Figure 3.22.** Nyquist plots of electrochemical impedance spectroscopy (EIS) of Na|Na symmetrical cells during open circuit conditions for over 70 h, using the IL-based electrolytes with 0.5 M Na<sup>+</sup> salts. Note that the cell with 50% Na[PF<sub>6</sub>] and 50% Na[NTf<sub>2</sub>] in [N<sub>C<sub>1</sub>,C<sub>1</sub>,C<sub>2</sub>,C<sub>2</sub>OC<sub>1</sub>][NTf<sub>2</sub>] **(a)**  $R_{\text{surface}}$  stabilises after 49 h, showing behaviour more alike the cell with [N<sub>C<sub>1</sub>,C<sub>1</sub>,C<sub>2</sub>,C<sub>4</sub>][NTf<sub>2</sub>] electrolyte **(c)** than the cell with [N<sub>C<sub>1</sub>,C<sub>1</sub>,C<sub>2</sub>,C<sub>2</sub>OC<sub>1</sub>][NTf<sub>2</sub>] **(b)**, both with Na[NTf<sub>2</sub>] only.</sub></sub></sub>

Overall, cells with the mixed salt electrolyte ([N<sub>C<sub>1</sub>,C<sub>1</sub>,C<sub>2</sub>,C<sub>2</sub>OC<sub>1</sub>][NTf<sub>2</sub>] with Na[PF<sub>6</sub>] and Na[NTf<sub>2</sub>]) seem to form a stable, although relatively highly resistant (see impedance on the right hand side, at high frequencies in Figure 4.31a) Na-IL interphase.</sub>

The next section evaluates how this mixed salt electrolyte affects Na plating and stripping in Na|Na symmetrical cell galvanostatic cycling.

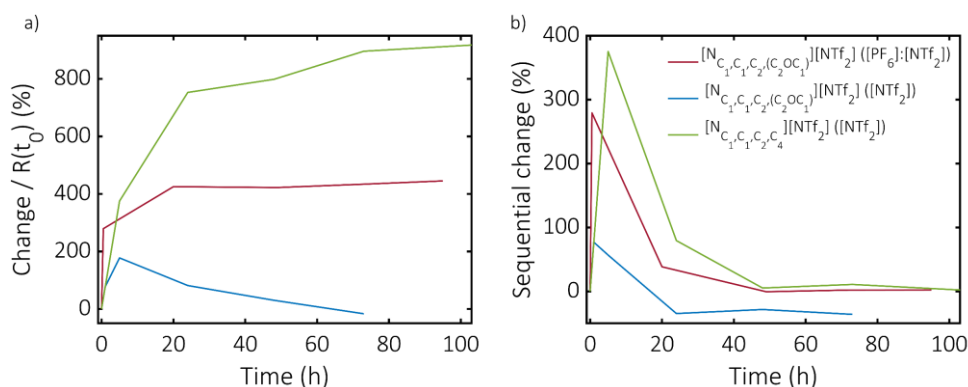


**Figure 3.23.** Analysis of electrochemical impedance data (EIS) of Na|Na symmetrical cells, demonstrating negligible change in the  $R_{\text{surface}}$  of the cell with the mixed electrolyte after 40 h of resting. **a)** Change/ $R(t_0)$ : Percentual change of surface resistance over time with respect to the resistance at the initial time ( $t_0$ ); **b)** Sequential change: Percentual change of surface resistance over time with respect to the resistance of the immediately preceding measurement. IL electrolytes containing 0.5 M  $Na^+$ : — 50%  $Na[PF_6]$  and 50 %  $Na[NTf_2]$  in  $[N_{C_1,C_1,C_2,(C_2OC_1)}][NTf_2]$ , —  $Na[NTf_2]$  in  $[N_{C_1,C_1,C_2,(C_2OC_1)}][NTf_2]$  and —  $Na[NTf_2]$  in  $[N_{C_1,C_1,C_2,C_4}][NTf_2]$ .

### 3.7.2 Effect of $Na[PF_6]$ additive on Na|Na symmetrical cell galvanostatic cycling

Voltage traces of Na|Na symmetrical cell with  $[N_{C_1,C_1,C_2,(C_2OC_1)}][NTf_2]$ -based electrolyte containing  $Na[PF_6]$  and  $Na[NTf_2]$  during galvanostatic cycling is shown in Figure 3.24 in red. Cycling data for  $[N_{C_1,C_1,C_2,(C_2OC_1)}][NTf_2]$  and  $[N_{C_1,C_1,C_2,C_4}][NTf_2]$  containing  $Na[NTf_2]$  only are also shown for comparison purposes. In addition, selected magnified traces are shown in Figure 3.25.

The cell assembled with the mixed salt electrolyte (red traces) reaches the voltage cut-off limits at later cycling times than  $[N_{C_1,C_1,C_2,(C_2OC_1)}][NTf_2]$  with  $Na[NTf_2]$  only (blue traces), as clearly shown in Figure 3.24. This is even more evident in the cycling data shown in the repeats shown in Figure A 8.

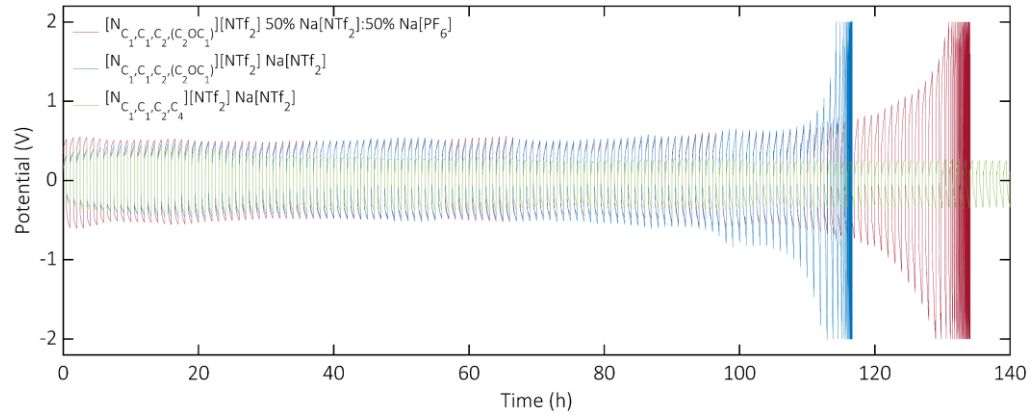


**Figure 3.24.** Galvanostatic cycling of Na|Na symmetrical cells with the cell with mixed electrolyte (—) showing higher overpotential at the start and longer cycling time than the equivalent electrolyte with Na[NTf<sub>2</sub>] only (—). Cells cycled at 0.1 mA.cm<sup>-2</sup>, with 30 minutes polarisation time and 105 μL of electrolyte containing 0.5 M Na<sup>+</sup> salts: — 50 % Na[PF<sub>6</sub>] and 50 % Na[NTf<sub>2</sub>] in [N<sub>C<sub>1</sub>,C<sub>1</sub>,C<sub>2</sub>,C<sub>2</sub>OC<sub>1</sub></sub>][NTf<sub>2</sub>], — Na[NTf<sub>2</sub>] in [N<sub>C<sub>1</sub>,C<sub>1</sub>,C<sub>2</sub>,C<sub>2</sub>OC<sub>1</sub></sub>][NTf<sub>2</sub>] and — Na[NTf<sub>2</sub>] in [N<sub>C<sub>1</sub>,C<sub>1</sub>,C<sub>2</sub>,C<sub>4</sub></sub>][NTf<sub>2</sub>].

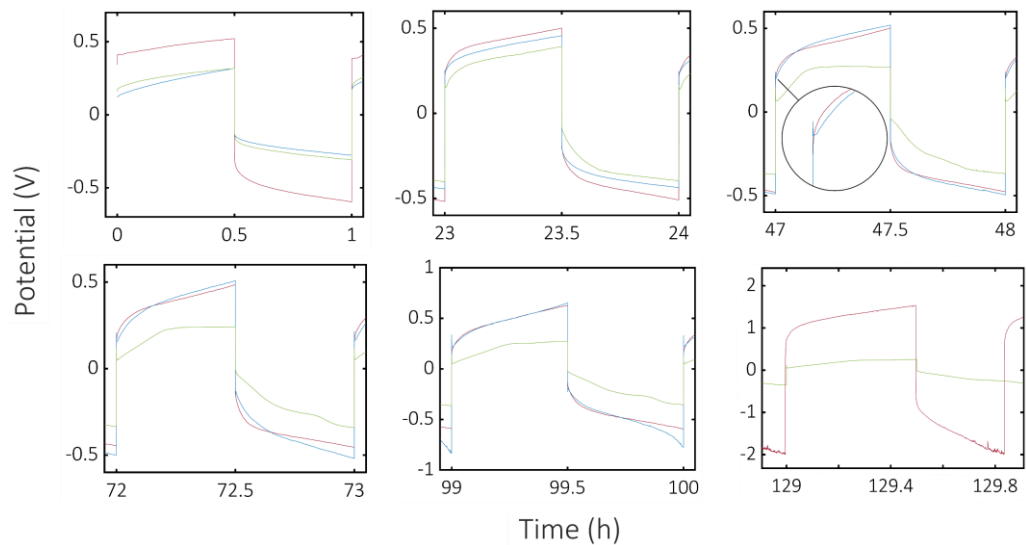


**Figure 3.25.** Selected times of galvanostatic cycling of Na|Na symmetrical cell shown in Figure 3.24. Note the arc shaped voltage profile of the cell with mixed electrolyte across the entire cycling time. Cells cycled at 0.1 mA.cm<sup>-2</sup>, 30 minutes polarisation time and 105 μL electrolyte containing 0.5 M Na<sup>+</sup> salts: — 50 % Na[PF<sub>6</sub>] and 50 % Na[NTf<sub>2</sub>] in [N<sub>C<sub>1</sub>,C<sub>1</sub>,C<sub>2</sub>,C<sub>2</sub>OC<sub>1</sub></sub>][NTf<sub>2</sub>], — Na[NTf<sub>2</sub>] in [N<sub>C<sub>1</sub>,C<sub>1</sub>,C<sub>2</sub>,C<sub>2</sub>OC<sub>1</sub></sub>][NTf<sub>2</sub>] and — Na[NTf<sub>2</sub>] in [N<sub>C<sub>1</sub>,C<sub>1</sub>,C<sub>2</sub>,C<sub>4</sub></sub>][NTf<sub>2</sub>].

The magnified regions in Figure 3.25 show that the voltage profile at early cycling times is an arc shaped profile. Arc shaped voltage profiles at early cycling stages have been associated to formation of tortuous and resistive SEI. In addition, the cell with the mixed salt electrolyte (red traces) displays high overpotential in the first few cycles. This agrees with the surface resistance at  $t_0$  which is approximately  $1760 \Omega$  for  $[\text{N}_{\text{C}_1, \text{C}_1, \text{C}_2, (\text{C}_2\text{OC}_1)}][\text{NTf}_2]$  with  $\text{Na}[\text{PF}_6]$  and  $\text{Na}[\text{NTf}_2]$ , compared to  $1198 \Omega$  for  $[\text{N}_{\text{C}_1, \text{C}_1, \text{C}_2, (\text{C}_2\text{OC}_1)}][\text{NTf}_2]$  with  $\text{Na}[\text{NTf}_2]$  only (determined by fit of the data in Figure 3.22).

The voltage profile of  $[\text{N}_{\text{C}_1, \text{C}_1, \text{C}_2, (\text{C}_2\text{OC}_1)}][\text{NTf}_2]$  electrolyte with  $\text{Na}[\text{PF}_6]$  and  $\text{Na}[\text{NTf}_2]$  keeps the arc shape throughout cycling, without a shift from arc to peak shape as described previously. Thus, for this mixed salt electrolyte, mass transport is the determining factor for the voltage profile throughout the whole cycling time. In fact, even the peak observed at the end of the half cycles at later cycling times (see peak at approximately 100 h in Figure 3.25, blue trace) for  $[\text{N}_{\text{C}_1, \text{C}_1, \text{C}_2, (\text{C}_2\text{OC}_1)}][\text{NTf}_2]$ , which has been associated to a combination of severe mass transport limitation and pitting from the bulk electrode, is not observed for the mixed salt electrolyte. Instead, at late cycling times (approaching voltage cut-off, see voltage traces around 129 h of cycling in Figure 3.25), the cell with the mixed salt electrolyte shows a noisy feature previously associated to soft internal short circuits.<sup>117</sup> However, without *in-situ* studies or meticulously designed time-intervalled cycling with periodic *ex-situ* analysis it is challenging to confirm either hypothesis.

Overall it has been demonstrated that  $\text{Na}^+$  can be plated and stripped in the cell with the mixed salt electrolyte for approximately 40 cycles more than in the cell with  $[\text{N}_{\text{C}_1, \text{C}_1, \text{C}_2, (\text{C}_2\text{OC}_1)}][\text{NTf}_2]$  containing  $\text{Na}[\text{NTf}_2]$  only. To try to understand this behaviour, the SEI of  $\text{Na}-[\text{N}_{\text{C}_1, \text{C}_1, \text{C}_2, (\text{C}_2\text{OC}_1)}][\text{NTf}_2]$  containing  $\text{Na}[\text{PF}_6]$  and  $\text{Na}[\text{NTf}_2]$  is studied with depth profile 3D OrbiSIMS and discussed in the next section.

### 3.7.3 3D OrbiSIMS and MVA study of effect of Na[PF<sub>6</sub>] additive on the Na-IL electrolyte interphase

In section 3.6, depth profiling with 3D OrbiSIMS has been thoroughly described, as well as the process used to perform a multivariate analysis (MVA) in the SIMS dataset. The same process has been applied to the dataset of the sample containing Na[PF<sub>6</sub>] additive, and the complete depth profile plot is shown in Figure A 25 in Appendix 1.A.2. Figure 3.26 shows the depth profile of selected assignments of the Na-[N<sub>C<sub>1</sub>,C<sub>1</sub>,C<sub>2</sub>,C<sub>2</sub>OC<sub>1</sub>][NTf<sub>2</sub>] with Na[PF<sub>6</sub>] and Na[NTf<sub>2</sub>] interphase data.</sub>

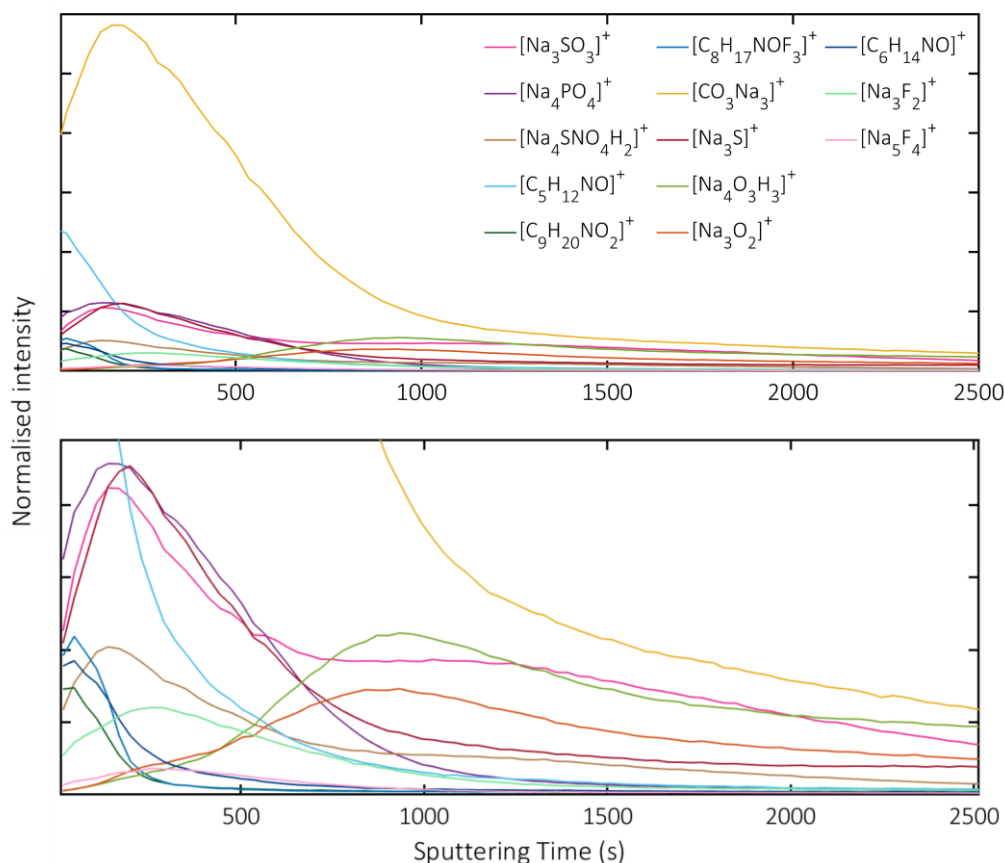


**Figure 3.26.** Positive ion depth of SEI of Na-[N<sub>C<sub>1</sub>,C<sub>1</sub>,C<sub>2</sub>,C<sub>2</sub>OC<sub>1</sub>][NTf<sub>2</sub>] containing 0.5 M of Na<sup>+</sup> salts (50% Na[PF<sub>6</sub>], 50% Na[NTf<sub>2</sub>]) using eV Ar for sputtering and analysis, showing selected assignments (top) and a zoom of the lower intensity region (bottom).</sub>

Figure 3.26 shows the presence of the assignment [Na<sub>4</sub>PO<sub>4</sub>]<sup>+</sup>, product of [PF<sub>6</sub>]<sup>-</sup> anion decomposition during SEI formation. Previous studies<sup>90</sup> have

detected  $[\text{PO}_4]^-$  during acid catalysed hydrolysis of  $[\text{PF}_6]$ -based ILs, and others have found that acid or heat assisted hydrolysis of  $[\text{PF}_6]^-$  leads to formation of  $[\text{PO}_2\text{F}_2]^-$ . Other aspects regarding the different intensity profiles displayed by this Na-IL SEI, the structure, and more details on the SEI composition are further explored with multivariate analysis, as described in the previous sections.

With aid of PCA, it was found that four endmembers are a good representation of the main intensity profiles for the dataset with  $\text{Na}[\text{PF}_6]$  additive. The PCA results and depth profile plot of main assignments, and NMF lack of fit are shown in 1.A.2. NMF intensity plot is shown in Figure 3.27.

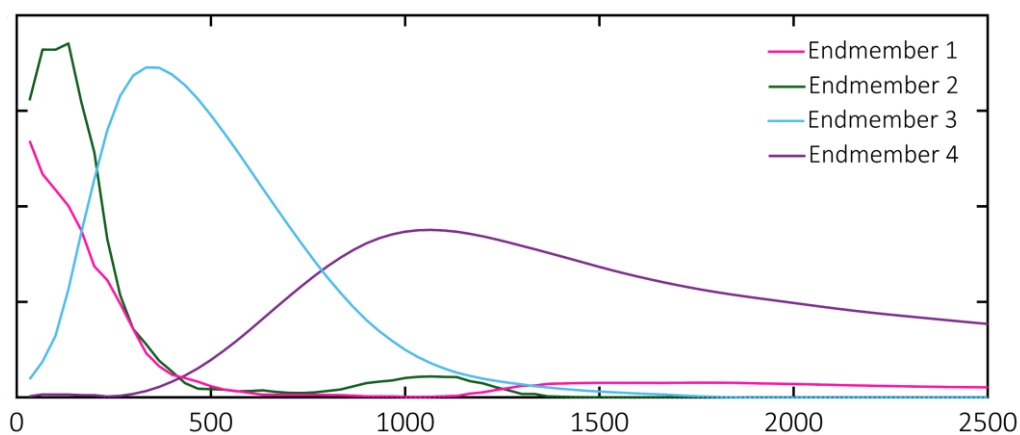


**Figure 3.27.** NMF intensity plot of SIMS dataset for interphase of  $\text{Na}-[\text{N}_{\text{C}_1,\text{C}_1,\text{C}_2,(\text{C}_2\text{OC}_1)}][\text{NTf}_2]$  containing 0.5 M of 50:50  $\text{Na}[\text{PF}_6]$  and  $\text{Na}[\text{NTf}_2]$ . Note overlap of endmembers 1 and 2, and the separation of endmembers 3 and 4.

Figure 3.27 shows that endmember 1 is mostly concentrated within the outermost SEI layer, but its intensity rapidly drops so that it is not present as much in the inner phases. Endmember 2 is highly concentrated just below the outermost layer, and sharply decreases in concentration approximately at the same time as endmember 3 reaches its maximum intensity. Finally, at around 1000 s sputter time, endmember 4 displays maximum intensity, concomitantly to a small increase in intensity of endmember 3, and later of endmember 1, showing that these endmembers are also present at later sputter times. Despite this, and the overlap of endmembers 1 and 2, the intensity profiles are relatively separated, especially endmembers 3 and 4.

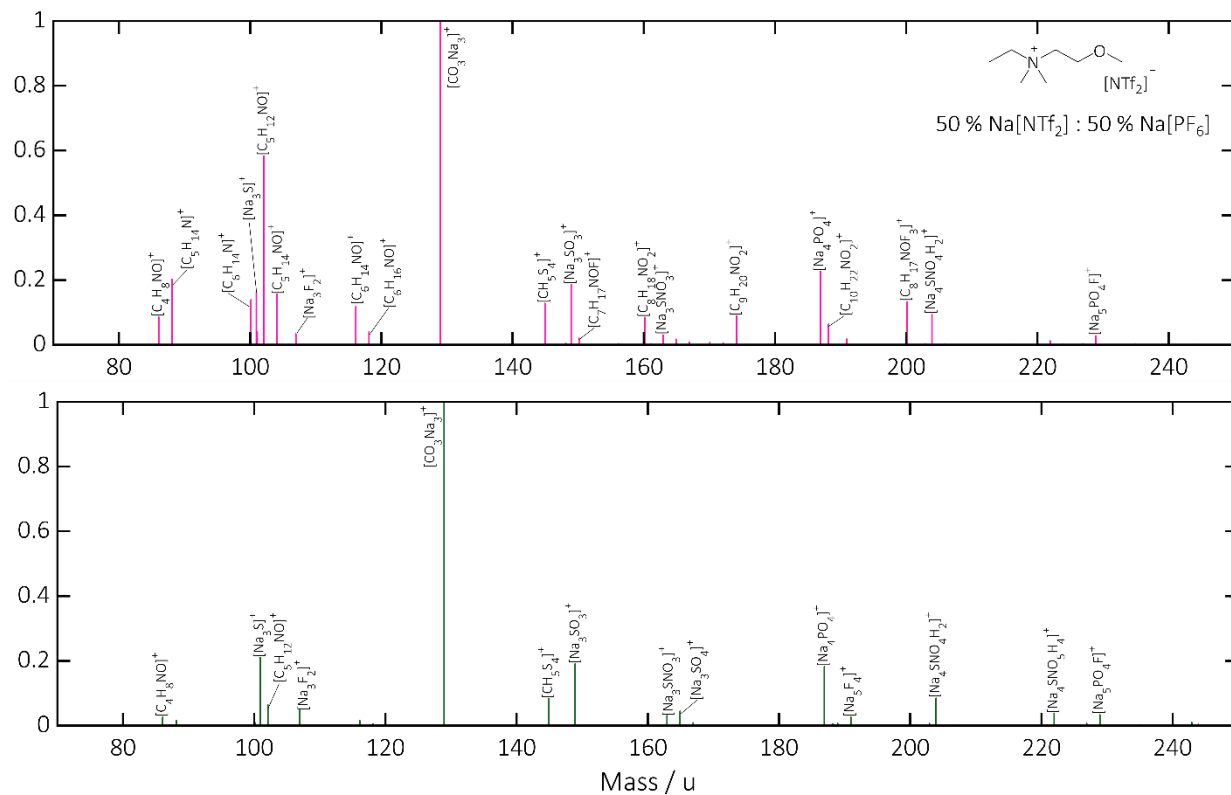


**Figure 3.28-Part I.** NMF characteristic spectra of Na-[N<sub>C<sub>1</sub>,C<sub>1</sub>,C<sub>2</sub>,C<sub>2</sub>OC<sub>1</sub>][NTf<sub>2</sub>] (0.5 M 50% Na[PF<sub>6</sub>], 50% Na[NTf<sub>2</sub>]) SEI showing endmembers 1 (pink) and 2 (green). Note the presence of [Na<sub>4</sub>PO<sub>4</sub>]<sup>+</sup> and [Na<sub>3</sub>F<sub>2</sub>]<sup>+</sup> in both endmembers, with endmember 1 mostly composed of cation-related fragments, and 2 anion-related fragments.</sub>

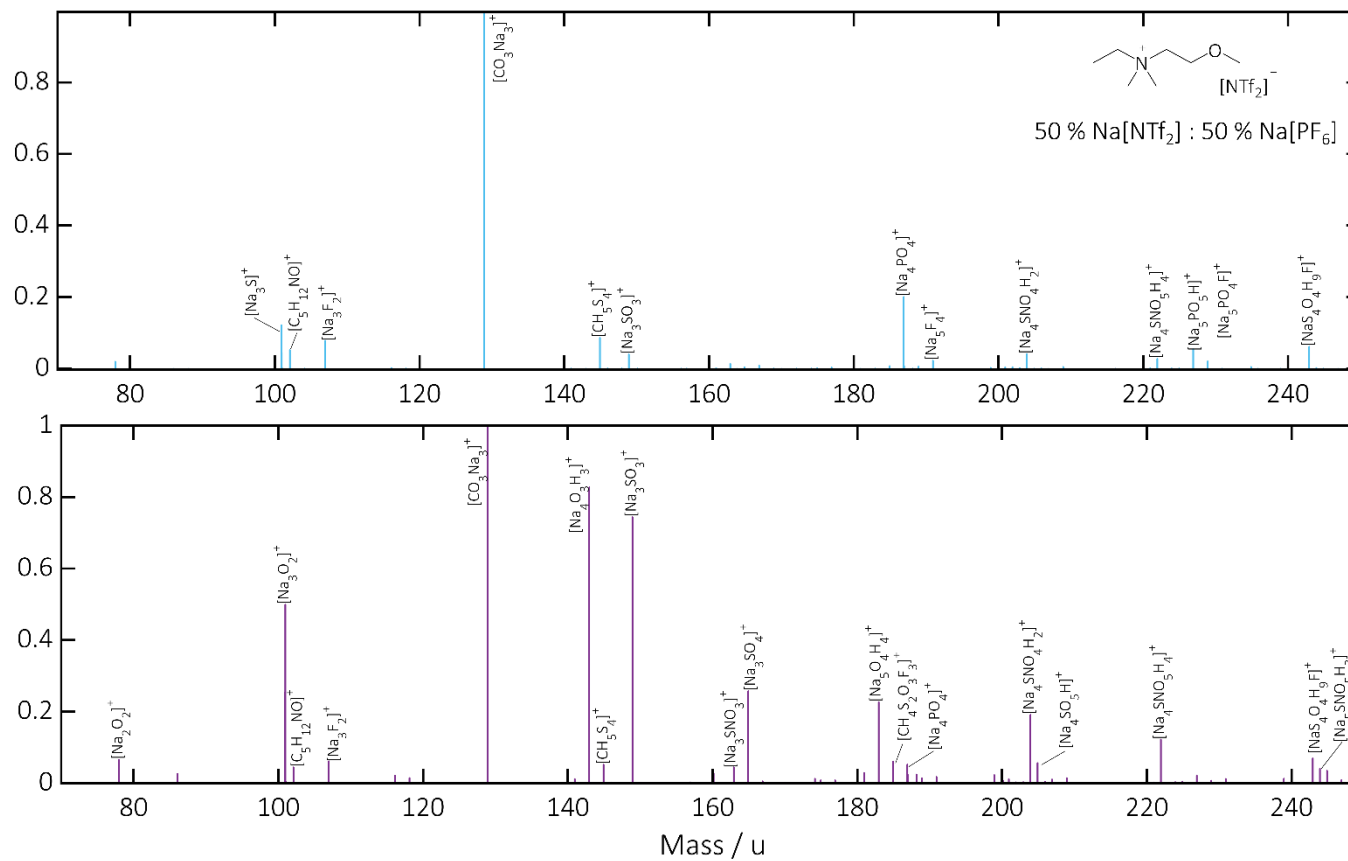


**Figure 3.28-Part II.** NMF characteristic spectra of Na-[N<sub>C<sub>1</sub>,C<sub>1</sub>,C<sub>2</sub>,(C<sub>2</sub>)OC<sub>1</sub></sub>][NTf<sub>2</sub>] (0.5 M 50% Na[PF<sub>6</sub>], 50% Na[NTf<sub>2</sub>]) interphase showing endmembers 3 (blue) and 4 (purple). Note the little presence of cation-related assignments in both endmembers.

Regarding the composition of the endmembers,  $[\text{CO}_3\text{Na}_3]^+$  is the main assignment in all endmembers, which is understandable considering the high intensity of this fragment displayed in the original depth profile plot (see Figure 3.26, yellow trace). To be sure that the high intensity of  $[\text{CO}_3\text{Na}_3]^+$  and other assignments do not limit the scope of NMF analysis, NMF results for dataset without these large fragments is shown in Appendix 1.A.2. Besides  $[\text{CO}_3\text{Na}_3]^+$ ,  $[\text{C}_5\text{H}_{12}\text{NO}]^+$  is also a relevant assignment for endmember 1, which is mostly formed of cation-related fragments, some being larger than the IL cation. Endmember 1 also displays other fragments derived from the  $[\text{NTf}_2]^-$  anion, and  $[\text{NaPO}_4]^+$ .  $[\text{Na}_4\text{PO}_4]^+$  is present in all four endmembers, indicating that products of  $[\text{PF}_6]^-$  anion decomposition have extended through the whole depth of this SEI. Endmembers 2 and 3 are composed mainly of anion-derived fragments, from both  $[\text{PF}_6]^-$  and  $[\text{NTf}_2]^-$ .  $[\text{Na}_4\text{O}_3\text{H}_3]^+$  is one of the most relevant assignments in endmember 4, which also shows a mix of other hydroxide and oxide-based, organic, and anion-based fragments.

A comparison of NMF analysis of the SEI of  $\text{Na}-[\text{N}_{\text{C}_1,\text{C}_1,\text{C}_2,(\text{C}_2\text{OC}_1)}][\text{NTf}_2]$  containing  $\text{Na}[\text{NTf}_2]$  and  $\text{Na}[\text{PF}_6]$  (Figure 3.28), with its equivalent  $\text{Na}-[\text{N}_{\text{C}_1,\text{C}_1,\text{C}_2,(\text{C}_2\text{OC}_1)}][\text{NTf}_2]$  ( $\text{Na}[\text{NTf}_2]$  only) (Figure 3.19) shows a few differences discussed as follows. Firstly, the presence of  $[\text{Na}_4\text{PO}_4]^+$  indicates degradation of  $[\text{PF}_6]^-$ , thus a higher amount of fluoride is expected to be present in the SEI with the mixed salt electrolyte than in  $[\text{N}_{\text{C}_1,\text{C}_1,\text{C}_2,(\text{C}_2\text{OC}_1)}][\text{NTf}_2]$  with  $\text{Na}[\text{NTf}_2]$  only. This can be observed by the greater presence of  $[\text{Na}_x\text{F}_y]^+$  fragments in Figure 3.28 than in Figure 3.19. The normalised peak areas for these assignments are shown in Table 3.6. The SEI with the mixed salt electrolyte indeed shows the greatest amount of  $[\text{Na}_x\text{F}_y]^+$ , as expected by the presence of the  $[\text{PF}_6]^-$  anion. Therefore, a direct and simple comparison between the two  $[\text{N}_{\text{C}_1,\text{C}_1,\text{C}_2,(\text{C}_2\text{OC}_1)}][\text{NTf}_2]$  systems ( $\text{Na}[\text{NTf}_2]$  only and  $\text{Na}[\text{PF}_6]:\text{Na}[\text{NTf}_2]$ ) shows that the system with the highest fluoride content displayed the better cycling performance (see Figure 3.24) agreeing with previous studies in literature. However,  $\text{Na}-[\text{C}_1\text{C}_{\text{dma}}\text{Pyrr}][\text{NTf}_2]$  SEI also shows high quantities of  $[\text{Na}_x\text{F}_y]^+$ , and the  $\text{Na}|\text{Na}$  cell with this electrolyte was the first system to reach the cut-off voltages (Figure 3.7). In addition it also

displayed highly resistive and unstable SEI (see Figure 3.5 and Figure 3.6). Thus, there must be other key aspects besides SEI fluoride content that affect Na cell cycling and stability in these electrolyte systems.

**Table 3.6.** Comparison of normalised peak areas ( $10^{-3}$  a.u.) across different electrolytes. Peak areas normalised to the IL cation. Note that  $[\text{Na}_x\text{F}_y]^+$  represent large clusters of ions sputtered during the analysis, for example, large ionised NaF, not single species.

Electrolyte	Normalised peak area per assignment	
	$[\text{Na}_5\text{F}_4]^+$	$[\text{Na}_3\text{F}_2]^+$
$[\text{N}_{\text{C}_1,\text{C}_1,\text{C}_2,(\text{C}_2\text{OC}_1)}][\text{NTf}_2]$ with Na[PF <sub>6</sub> ] and Na[NTf <sub>2</sub> ]	5.13	15.36
$[\text{N}_{\text{C}_1,\text{C}_1,\text{C}_2,(\text{C}_2\text{OC}_1)}][\text{NTf}_2]$ with Na[NTf <sub>2</sub> ]	0.80	2.91
$[\text{N}_{\text{C}_1,\text{C}_1,\text{C}_2,\text{C}_4}][\text{NTf}_2]$ with Na[NTf <sub>2</sub> ]	2.33	3.74
$[\text{C}_1\text{C}_{\text{dma}}\text{Pyrr}][\text{NTf}_2]$ with Na[NTf <sub>2</sub> ]	3.26	12.15

NMF characteristic spectra for the mixed salt electrolyte system show that organic-related assignments are found mostly in endmember 1. In fact NMF characteristic spectrum for endmember 4 shows significantly fewer cation-related assignments than endmember 4 for the  $[\text{N}_{\text{C}_1,\text{C}_1,\text{C}_2,(\text{C}_2\text{OC}_1)}][\text{NTf}_2]$  electrolyte with Na[NTf<sub>2</sub>] only (Figure 3.19-Part II, in purple). These differences can also be clearly observed in the NMF analysis of the dataset without the most intense assignments shown in Appendix 1.A.2. This suggests that, similar to  $[\text{N}_{\text{C}_1,\text{C}_1,\text{C}_2,\text{C}_4}][\text{NTf}_2]$ , the mixed salt electrolyte displays a more structured interphase with organic fragments within the outermost layer, and [PF<sub>6</sub>]<sup>-</sup> and [NTf<sub>2</sub>]<sup>-</sup> related fragments within the inner layers, similar to what has been described for  $[\text{N}_{\text{C}_1,\text{C}_1,\text{C}_2,\text{C}_4}][\text{NTf}_2]$  in the previous section. This may be corroborated by the impedance studies displayed in Figure 3.22a and Figure 3.23. After 49 hours of resting time, no significant increase in surface resistance

is observed for the Na|Na cell with the mixed salt electrolyte. The same trends have been demonstrated by the  $[N_{C_1,C_1,C_2,C_4}][NTf_2]$  system.

To evaluate this structural hypothesis, it is important to correlate these NMF findings to the original dataset. The magnified region in Figure 3.26 shows that the intensity of the assignments  $[C_8H_{17}NOF_3]^+$ ,  $[C_9H_{20}NO_2]^+$  and  $[C_6H_{14}NO]^+$  rapidly decreases to zero, and do not display significant presence in the inner layers of the SEI. The intensity of  $[C_5H_{12}NO]^+$ , however, reaches zero only at later sputter times, overlapping with assignments such as  $[Na_4O_3H_3]^+$  and  $[Na_3O_2]^+$ , likely to be at the vicinity of the sodium electrode. This thoroughly agrees with the NMF results, as  $[C_5H_{12}NO]^+$  is present in all endmembers, including endmember 4 that is mostly concentrated at the innermost SEI layer.

The formation of a stable organic fragment barrier within the outermost layer of the SEI, promoted by van der Waals interactions of the long IL side chains was the rationale proposed to be behind the structural interphase displayed by the  $[N_{C_1,C_1,C_2,C_4}][NTf_2]$  system. However, this is unlikely to be the case for the  $[N_{C_1,C_1,C_2,(C_2OC_1)}][NTf_2]$  system with Na[PF<sub>6</sub>] and Na[NTf<sub>2</sub>]. Therefore, this structure may be caused by the following. It is possible that the SEI products have lower solubility/diffusion in the mixed salt electrolyte, thus their diffusion towards the bulk is limited. Consequently, the SEI products accumulate closer to the electrode resulting in coverage of the sodium electrode, hence limiting contact of bulk electrolyte with metallic sodium.

The structural SEI interphase formed with  $[N_{C_1,C_1,C_2,(C_2OC_1)}][NTf_2]$  containing Na[PF<sub>6</sub>] and Na[NTf<sub>2</sub>] is more stable, however it also seems to be more resistive (Figure 3.22a) and perhaps more tortuous, limiting Na<sup>+</sup> mass transport. This had a major effect on Na|Na cell cycling, as higher overpotentials were needed to promote Na<sup>+</sup> transport, to the extent of reaching the cut-off voltages.

### 3.8. Conclusions and future work

The effect of simple changes in the IL structure on Na<sup>+</sup> plating and stripping and on solid electrolyte interphase stability, structure and composition has been demonstrated in this chapter. The choice of IL has caused small variations in the onset potential for Na<sup>+</sup> reduction, likely to be associated to solvation of Na<sup>+</sup> in the ILs. In addition, it has been described that the stability of metallic sodium surface in symmetrical cells with IL-based electrolytes is affected by both anion and cation choice, as shown by the reactivity of [C<sub>1</sub>(C<sub>2</sub>OC<sub>1</sub>)Pyrr][C<sub>2</sub>F<sub>5</sub>COO] towards metallic sodium and the constant increase of surface resistance the cells with [C<sub>1</sub>C<sub>dma</sub>Pyrr][NTf<sub>2</sub>]. The reactivity of the latter has been associated to the numerous reaction possibilities involving the more complex [C<sub>1</sub>C<sub>dma</sub>Pyrr]<sup>+</sup> cation structure.

The voltage profiles of galvanostatic cycling of Na|Na symmetrical cells using selected IL electrolytes have also been affected by the electrolyte choice. In addition, the shape of the voltage traces also changes dramatically depending on the choice of IL. Early cut-off voltages have been linked to unstable SEI causing major electrolyte consumption, and Na<sup>+</sup> transport limitations. This has been observed for the [C<sub>1</sub>C<sub>dma</sub>Pyrr][NTf<sub>2</sub>] system, which has displayed a continuous increase of surface resistance in impedance studies and has also been the cell to reach the voltage cut-off limits the earliest during cycling. A switch in the shape of the voltage profiles from ‘arc’ to ‘peaking’ has been associated to a change from mass transport limitation to a kinetic limitation of the voltage response, respectively. Stabilisation of the SEI has been suggested to be one of the key factors related to the switch from arc to peaking profiles, and this has been demonstrated by the [N<sub>C<sub>1</sub>,C<sub>1</sub>,C<sub>2</sub>,C<sub>4</sub></sub>][NTf<sub>2</sub>] system, which has shown stable and low overpotential across several hours of cycling.

3D OrbiSIMS studies of Na-IL interphase in conjunction with multivariate analysis have revealed the effect of IL design on SEI structures. The [N<sub>C<sub>1</sub>,C<sub>1</sub>,C<sub>2</sub>,C<sub>4</sub></sub>][NTf<sub>2</sub>] system has not only displayed more separated intensity profiles, but has also shown that the organic fragments, including large

assignments such as  $[C_{13}H_{30}N]^+$ , are mostly concentrated within the outermost SEI layer, with negligible presence within the innermost layer. These fragments have been proposed to form a protective 'barrier', insulating the inner SEI layers from the bulk IL, and promoting formation of a stable SEI. The effect of this protective 'barrier' has been noticed in the remarkable cycling performance and stable surface resistance of the cells with  $[N_{C_1, C_1, C_2, C_4}][NTf_2]$  electrolyte. To the best of our knowledge, this has been the first time a SEI has been studied with SIMS using an Orbitrap<sup>TM</sup> detector and an Ar cluster primary source. The combination of the high mass resolution and sensitivity of the Orbitrap<sup>TM</sup> and the Ar cluster softer sputtering process has provided unique and detailed information about SEI structure and composition.

Finally, a study comparing composition and structure of SEI has found that the presence of Na[PF<sub>6</sub>] additive not only increases the amount of  $[Na_xF_y]^+$  assignments, but also promotes the formation of a more structured SEI. This has been accompanied by a more stable surface resistance and longer cycling times until reaching cut-off voltages.

All the 3D OrbiSIMS analyses have been performed after metallic Na and IL have been in contact for three days. An insightful future work will be performing SIMS analysis at different resting times. This will give information regarding the timeframe of the SEI reactions. More importantly, will also perform OrbiSIMS analysis during cycling, which is when most SEI changes occur.

Further studies to verify the assignments suggested in this chapter will be an insightful future work. Previous studies have estimated the composition of SEI products by analysing the electrode surface with XPS, for instance, which would be an interesting complementary tool for this work.<sup>75, 86, 113</sup> In addition, calculations similar to those done by Jankowski et al, are another valuable complementary analysis to verify the assignments proposed in this chapter.<sup>87</sup>

Finally, giving the novelty of the 3D OrbiSIMS method to investigate SEI composition, a brief study using this technique to evaluate the SEI formed in extensively studied electrolytes such as  $[C_1C_4Pyrr][FSI]$  or  $[C_1C_3Pyrr][FSI]$ , would

be an important piece of future work to further validate the 3D OrbiSIMS methodology.

This chapter has demonstrated that electrolytes capable of forming a protective barrier on the SEI are beneficial for cell cycling. Thus, regarding future design of IL based electrolytes, features such as double bonds or other polymerisable sites may be implemented in the IL structure, as also suggested previously via simulations,<sup>87</sup> as these may enhance the protective barrier formation. In addition, despite the very satisfactory results displayed by  $[\text{N}_{\text{C}_1, \text{C}_1, \text{C}_2, \text{C}_4}][\text{NTf}_2]$ , the viscosity of this IL might be too high for certain applications. Thus, electrolyte mixtures with the major component being  $[\text{N}_{\text{C}_1, \text{C}_1, \text{C}_2, \text{C}_4}][\text{NTf}_2]$  are worth investigating to try and reduce the viscosity of  $[\text{N}_{\text{C}_1, \text{C}_1, \text{C}_2, \text{C}_4}][\text{NTf}_2]$  without losing its excellent SEI formation and Na cycling abilities.

### 3.9. References

1. Albertus, P.; Babinec, S.; Litzelman, S.; Newman, A., Status and challenges in enabling the lithium metal electrode for high-energy and low-cost rechargeable batteries. *Nat. Energy* **2017**, *3* (1), 16-21.
2. Schmidt, O.; Hawkes, A.; Gambhir, A.; Staffell, I., The future cost of electrical energy storage based on experience rates. *Nat. Energy* **2017**, *2* (8), 17110.
3. Balaish, M.; Kraytsberg, A.; Ein-Eli, Y., A critical review on lithium-air battery electrolytes. *Phys. Chem. Chem. Phys.* **2014**, *16* (7), 2801-22.
4. Zhao, H.; Deng, N.; Yan, J.; Kang, W.; Ju, J.; Ruan, Y.; Wang, X.; Zhuang, X.; Li, Q.; Cheng, B., A review on anode for lithium-sulfur batteries: Progress and prospects. *Chem. Eng. J. (Amsterdam, Neth.)* **2018**, *347*, 343-365.
5. Sapunkov, O.; Pande, V.; Khetan, A.; Choomwattana, C.; Viswanathan, V., Quantifying the promise of 'beyond' Li-ion batteries. *Transl. Mater. Res.* **2015**, *2* (4), 045002.
6. Wang, Y. R.; Chen, R. P.; Chen, T.; Lv, H. L.; Zhu, G. Y.; Ma, L. B.; Wang, C. X.; Jin, Z.; Liu, J., Emerging non-lithium ion batteries. *Energy Stor. Mater.* **2016**, *4*, 103-129.
7. Yabuuchi, N.; Kubota, K.; Dahbi, M.; Komaba, S., Research Development on Sodium-Ion Batteries. *Chem. Rev.* **2014**, *114* (23), 11636-11682.
8. Palomares, V.; Serras, P.; Villalunga, I.; Hueso, K. B.; Carretero-González, J.; Rojo, T., Na-ion batteries, recent advances and present challenges

- to become low cost energy storage systems. *Energy Environ. Sci.* **2012**, *5* (3), 5884-5901.
9. Bruce, P. G.; Freunberger, S. A.; Hardwick, L. J.; Tarascon, J., Li–O<sub>2</sub> and Li–S batteries with high energy storage. *Nat. Mat.* **2012**, *11* (1), 19-29.
  10. Zheng, X.; Bommier, C.; Luo, W.; Jiang, L.; Hao, Y.; Huang, Y., Sodium metal anodes for room-temperature sodium-ion batteries: Applications, challenges and solutions. *Energy Stor. Mater.* **2019**, *16*, 6-23.
  11. Berg, H., Lithium battery materials. In *Batteries for Electric Vehicles: Materials and Electrochemistry*, Cambridge University Press: Cambridge, 2015; pp 83-125.
  12. Deng, Y.; Zheng, J.; Warren, A.; Yin, J.; Choudhury, S.; Biswal, P.; Zhang, D.; Archer, L. A., On the Reversibility and Fragility of Sodium Metal Electrodes. *Adv. Energy Mater.* **2019**, *9* (39).
  13. Lee, B.; Paek, E.; Mitlin, D.; Lee, S. W., Sodium Metal Anodes: Emerging Solutions to Dendrite Growth. *Chem. Rev.* **2019**, *119* (8), 5416-5460.
  14. Matios, E.; Wang, H.; Wang, C.; Li, W., Enabling Safe Sodium Metal Batteries by Solid Electrolyte Interphase Engineering: A Review. *Ind. Eng. Chem. Res.* **2019**, *58* (23), 9758-9780.
  15. Wang, Y.; Wang, Y.; Wang, Y.; Feng, X.; Chen, W.; Ai, X.; Yang, H.; Cao, Y., Developments and Perspectives on Emerging High-Energy-Density Sodium-Metal Batteries. *Chem* **2019**, *5* (10), 2547-2570.
  16. Cheng, X. B.; Zhang, R.; Zhao, C. Z.; Wei, F.; Zhang, J. G.; Zhang, Q., A Review of Solid Electrolyte Interphases on Lithium Metal Anode. *Adv. Sci. (Weinheim, Ger.)* **2016**, *3* (3), 1500213.
  17. Goodenough, J. B.; Kim, Y., Challenges for Rechargeable Li Batteries. *Chem. Mater.* **2010**, *22* (3), 587-603.
  18. Wang, A.; Kadam, S.; Li, H.; Shi, S.; Qi, Y., Review on modeling of the anode solid electrolyte interphase (SEI) for lithium-ion batteries. *npj Comput. Mater.* **2018**, *4* (1).
  19. Rodriguez, R.; Loeffler, K. E.; Nathan, S. S.; Sheavly, J. K.; Dolocan, A.; Heller, A.; Mullins, C. B., In Situ Optical Imaging of Sodium Electrodeposition: Effects of Fluoroethylene Carbonate. *ACS Energy Lett.* **2017**, *2* (9), 2051-2057.
  20. Wood, K. N.; Kazyak, E.; Chadwick, A. F.; Chen, K.-H.; Zhang, J.-G.; Thornton, K.; Dasgupta, N. P., Dendrites and Pits: Untangling the Complex Behavior of Lithium Metal Anodes through Operando Video Microscopy. *ACS Cent. Sci.* **2016**, *2* (11), 790-801.
  21. Markevich, E.; Salitra, G.; Chesneau, F.; Schmidt, M.; Aurbach, D., Very Stable Lithium Metal Stripping–Plating at a High Rate and High Areal Capacity in Fluoroethylene Carbonate-Based Organic Electrolyte Solution. *ACS Energy Lett.* **2017**, *2* (6), 1321-1326.
  22. Brown, Z. L.; Jung, S.; Nguyen, C. C.; Lucht, B. L., Effect of Fluoroethylene Carbonate Electrolytes on the Nanostructure of the Solid Electrolyte Interphase and Performance of Lithium Metal Anodes. *ACS Appl. Energy Mater.* **2018**, *1* (7), 3057-3062.
  23. Lutz, L.; Alves Dalla Corte, D.; Tang, M.; Salager, E.; Deschamps, M.; Grimaud, A.; Johnson, L.; Bruce, P. G.; Tarascon, J.-M., Role of Electrolyte Anions in the Na–O<sub>2</sub> Battery: Implications for NaO<sub>2</sub> Solvation and the Stability of the

Sodium Solid Electrolyte Interphase in Glyme Ethers. *Chem. Mater.* **2017**, *29* (14), 6066-6075.

24. Iermakova, D. I.; Dugas, R.; Palacín, M. R.; Ponrouch, A., On the Comparative Stability of Li and Na Metal Anode Interfaces in Conventional Alkyl Carbonate Electrolytes. *J. Electrochem. Soc.* **2015**, *162* (13), A7060-A7066.

25. Wang, H.; Wang, C.; Matios, E.; Li, W., Facile Stabilization of the Sodium Metal Anode with Additives: Unexpected Key Role of Sodium Polysulfide and Adverse Effect of Sodium Nitrate. *Angew. Chem., Int. Ed. Engl.* **2018**, *57* (26), 7734-7737.

26. Yu, J.; Gao, N.; Peng, J.; Ma, N.; Liu, X.; Shen, C.; Xie, K.; Fang, Z., Concentrated LiODFB Electrolyte for Lithium Metal Batteries. *Front. Chem.* **2019**, *7* (494).

27. Schafzahl, L.; Ehmann, H.; Kriechbaum, M.; Sattelkow, J.; Ganner, T.; Plank, H.; Wilkening, M.; Freunberger, S. A., Long-Chain Li and Na Alkyl Carbonates as Solid Electrolyte Interphase Components: Structure, Ion Transport, and Mechanical Properties. *Chem. Mater.* **2018**, *30* (10), 3338-3345.

28. Sun, H.; Zhu, G.; Xu, X.; Liao, M.; Li, Y.; Angell, M.; Gu, M.; Zhu, Y.; Hung, W.; Li, J.; Kuang, Y.; Meng, Y.; Lin, M.; Peng, H.; Dai, H., A safe and non-flammable sodium metal battery based on an ionic liquid electrolyte. *Nat. Commun.* **2019**, *10* (1), 3302.

29. Forsyth, M.; Hilder, M.; Zhang, Y.; Chen, F.; Carre, L.; Rakov, D. A.; Armand, M.; Macfarlane, D. R.; Pozo-Gonzalo, C.; Howlett, P. C., Tuning Sodium Interfacial Chemistry with Mixed-Anion Ionic Liquid Electrolytes. *ACS Appl. Mater. Interfaces* **2019**, *11* (46), 43093-43106.

30. Wang, H.; Liu, Y.; Li, Y.; Cui, Y., Lithium Metal Anode Materials Design: Interphase and Host. *Electrochem. Energy Rev.* **2019**, *2* (4), 509-517.

31. Wang, H.; Yu, D.; Kuang, C.; Cheng, L.; Li, W.; Feng, X.; Zhang, Z.; Zhang, X.; Zhang, Y., Alkali Metal Anodes for Rechargeable Batteries. *Chem* **2019**, *5* (2), 313-338.

32. Aurbach, D.; Pollak, E.; Elazari, R.; Salitra, G.; Kelley, C. S.; Affinito, J., On the Surface Chemical Aspects of Very High Energy Density, Rechargeable Li-Sulfur Batteries. *J. Electrochem. Soc.* **2009**, *156* (8), A694.

33. Seh, Z. W.; Sun, J.; Sun, Y.; Cui, Y., A Highly Reversible Room-Temperature Sodium Metal Anode. *ACS Cent. Sci.* **2015**, *1* (8), 449-55.

34. Fiedler, C.; Luerssen, B.; Rohnke, M.; Sann, J.; Janek, J., XPS and SIMS Analysis of Solid Electrolyte Interphases on Lithium Formed by Ether-Based Electrolytes. *J. Electrochem. Soc.* **2017**, *164* (14), A3742-A3749.

35. Jankowski, P.; Wiczorek, W.; Johansson, P., Functional ionic liquids: Cationic SEI-formers for lithium batteries. *Energy Stor. Mater.* **2019**, *20*, 108-117.

36. Hosokawa, T.; Matsumoto, K.; Nohira, T.; Hagiwara, R.; Fukunaga, A.; Sakai, S.; Nitta, K., Stability of Ionic Liquids against Sodium Metal: A Comparative Study of 1-Ethyl-3-methylimidazolium Ionic Liquids with Bis(fluorosulfonyl)amide and Bis(trifluoromethylsulfonyl)amide. *J. Phys. Chem. C* **2016**, *120* (18), 9628-9636.

37. Watanabe, M.; Thomas, M. L.; Zhang, S.; Ueno, K.; Yasuda, T.; Dokko, K., Application of Ionic Liquids to Energy Storage and Conversion Materials and Devices. *Chem. Rev.* **2017**.
38. Rakov, D. A.; Chen, F.; Ferdousi, S. A.; Li, H.; Pathirana, T.; Simonov, A. N.; Howlett, P. C.; Atkin, R.; Forsyth, M., Engineering high-energy-density sodium battery anodes for improved cycling with superconcentrated ionic-liquid electrolytes. *Nat. Mater.* **2020**.
39. Passarelli, M. K.; Pirkl, A.; Moellers, R.; Grinfeld, D.; Kollmer, F.; Havelund, R.; Newman, C. F.; Marshall, P. S.; Arlinghaus, H.; Alexander, M. R.; West, A.; Horning, S.; Niehuis, E.; Makarov, A.; Dollery, C. T.; Gilmore, I. S., The 3D OrbiSIMS—label-free metabolic imaging with subcellular lateral resolution and high mass-resolving power. *Nat. Methods* **2017**, *14* (12), 1175-1183.
40. Zhang, J.; Brown, J.; Scurr, D. J.; Bullen, A.; MacLellan-Gibson, K.; Williams, P.; Alexander, M. R.; Hardie, K. R.; Gilmore, I. S.; Rakowska, P. D., Cryo-OrbiSIMS for 3D Molecular Imaging of a Bacterial Biofilm in Its Native State. *Anal. Chem.* **2020**, *92* (13), 9008-9015.
41. Trindade, G. F.; Abel, M.-L.; Watts, J. F., simsMVA: A tool for multivariate analysis of ToF-SIMS datasets. *Chemom. Intell. Lab. Syst.* **2018**, *182*, 180-187.
42. Fröba, A. P.; Kremer, H.; Leipertz, A., Density, Refractive Index, Interfacial Tension, and Viscosity of Ionic Liquids [EMIM][EtSO<sub>4</sub>], [EMIM][NTf<sub>2</sub>], [EMIM][N(CN)<sub>2</sub>], and [OMA][NTf<sub>2</sub>] in Dependence on Temperature at Atmospheric Pressure. *J. Phys. Chem. B* **2008**, *112* (39), 12420-12430.
43. Rinaldi, A.; Wang, Y.; Tan, K. S.; Wijaya, O.; Yazami, R., Lithium-air batteries for medium- and large-scale energy storage. In *Advances in Batteries for Medium and Large-Scale Energy Storage*, Menictas, C.; Skyllas-Kazacos, M.; Lim, T. M., Eds. Woodhead Publishing: 2015; pp 387-440.
44. Zhang, S.; Qi, X.; Ma, X.; Lu, L.; Deng, Y., Hydroxyl Ionic Liquids: The Differentiating Effect of Hydroxyl on Polarity due to Ionic Hydrogen Bonds between Hydroxyl and Anions. *J. Phys. Chem. B* **2010**, *114* (11), 3912-3920.
45. Isik, M.; Sardon, H.; Mecerreyes, D., Ionic Liquids and Cellulose: Dissolution, Chemical Modification and Preparation of New Cellulosic Materials. *Int. J. Mol. Sci.* **2014**, *15*, 11922-11940.
46. Richard G Compton, C. E. B., Diffusion. In *Understanding Voltammetry*, WORLD SCIENTIFIC: 2007; pp 77-106.
47. Richard G Compton, C. E. B., Cyclic Voltammetry at Macroelectrodes. In *Understanding Voltammetry*, WORLD SCIENTIFIC: 2007; pp 107-151.
48. Rosol, Z. P.; German, N. J.; Gross, S. M., Solubility, ionic conductivity and viscosity of lithium salts in room temperature ionic liquids. *Green Chem.* **2009**, *11* (9).
49. Tong, J.; Wu, S.; von Solms, N.; Liang, X.; Huo, F.; Zhou, Q.; He, H.; Zhang, S., The Effect of Concentration of Lithium Salt on the Structural and Transport Properties of Ionic Liquid-Based Electrolytes. *Front. Chem.* **2019**, *7*, 945.
50. Bonhôte, P.; Dias, A.-P.; Papageorgiou, N.; Kalyanasundaram, K.; Grätzel, M., Hydrophobic, Highly Conductive Ambient-Temperature Molten Salts. *Inorg. Chem.* **1996**, *35* (5), 1168-1178.

51. Schmeisser, M.; P., I.; Puchta, R.; Zahl, A.; van Eldik, R., Gutmann donor and acceptor numbers for ionic liquids. *Chem. - Eur. J.* **2012**, *18*, 10969-10982.
52. Berg, H., Battery usage and degradation. In *Batteries for Electric Vehicles: Materials and Electrochemistry*, Berg, H., Ed. Cambridge University Press: Cambridge, 2015; pp 194-229.
53. Berg, H., The electrochemical cell. In *Batteries for Electric Vehicles: Materials and Electrochemistry*, Berg, H., Ed. Cambridge University Press: Cambridge, 2015; pp 7-46.
54. Zheng, J.; Gu, M.; Chen, H.; Meduri, P.; Engelhard, M. H.; Zhang, J.-G.; Liu, J.; Xiao, J., Ionic liquid-enhanced solid state electrolyte interface (SEI) for lithium-sulfur batteries. *J. Mater. Chem. A* **2013**, *1* (29).
55. De Vos, N.; Maton, C.; Stevens, C. V., Electrochemical Stability of Ionic Liquids: General Influences and Degradation Mechanisms. *ChemElectroChem* **2014**, *1* (8), 1258-1270.
56. Chen, K.-H.; Wood, K. N.; Kazyak, E.; LePage, W. S.; Davis, A. L.; Sanchez, A. J.; Dasgupta, N. P., Dead lithium: mass transport effects on voltage, capacity, and failure of lithium metal anodes. *J. Mater. Chem. A* **2017**, *5* (23), 11671-11681.
57. Bieker, G.; Winter, M.; Bieker, P., Electrochemical in situ investigations of SEI and dendrite formation on the lithium metal anode. *Phys. Chem. Chem. Phys.* **2015**, *17* (14), 8670-9.
58. Kanamura, K.; Tamura, H.; Takehara, Z.-i., XPS analysis of a lithium surface immersed in propylene carbonate solution containing various salts. *J. Electroanal. Chem.* **1992**, *333* (1), 127-142.
59. Bessette, S.; Hovington, P.; Demers, H.; Golozar, M.; Bouchard, P.; Gauvin, R.; Zaghbi, K., In-Situ Characterization of Lithium Native Passivation Layer in A High Vacuum Scanning Electron Microscope. *Microsc. Microanal.* **2019**, *25* (4), 866-873.
60. Clough, M. T.; Geyer, K.; Hunt, P. A.; Mertes, J.; Welton, T., Thermal decomposition of carboxylate ionic liquids: trends and mechanisms. *Phys. Chem. Chem. Phys.* **2013**, *15* (47), 20480-95.
61. Prasad, M. R. R.; Krishnan, K.; Ninan, K. N.; Krishnamurthy, V. N., Thermal decomposition of tetraalkyl ammonium tetrafluoroborates. *Thermochim. Acta* **1997**, *297* (1), 207-210.
62. Steinruck, H. P., Recent developments in the study of ionic liquid interfaces using X-ray photoelectron spectroscopy and potential future directions. *Phys. Chem. Chem. Phys.* **2012**, *14* (15), 5010-29.
63. Zhou, Z. B.; Matsumoto, H.; Tatsumi, K., Cyclic quaternary ammonium ionic liquids with perfluoroalkyltrifluoroborates: synthesis, characterization, and properties. *Chem. - Eur. J.* **2006**, *12* (8), 2196-212.
64. Freire, M. G.; Neves, C. M. S. S.; Marrucho, I. M.; Coutinho, J. A. P.; Fernandes, A. M., Hydrolysis of Tetrafluoroborate and Hexafluorophosphate Counter Ions in Imidazolium-Based Ionic Liquids. *J. Phys. Chem. A* **2010**, *114* (11), 3744-3749.
65. Wang, B.; Qin, L.; Mu, T.; Xue, Z.; Gao, G., Are Ionic Liquids Chemically Stable? *Chem. Rev.* **2017**, *117* (10), 7113-7131.

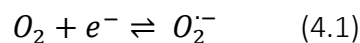
66. Wu, F.; Maier, J.; Yu, Y., Guidelines and trends for next-generation rechargeable lithium and lithium-ion batteries. *Chem. Soc. Rev.* **2020**, *49* (5), 1569-1614.
67. Kong, L.; Xing, Y.; Pecht, M. G., *In-Situ* Observations of Lithium Dendrite Growth. *IEEE Access* **2018**, *6*, 8387-8393.



## 4. Fundamental studies on the oxygen reduction reaction in ionic liquids

### 4.1. Introduction

The oxygen reduction reaction (ORR) is one of the electrochemical reactions with one of the most diverse range of applications. The superoxide ion, which can be generated during ORR according to the equation



is present in biological applications,<sup>118</sup> destruction of hazardous compounds,<sup>119, 120</sup> and synthesis of organic compounds,<sup>119, 121</sup> to cite a few. A recent publication has reviewed the different roles the superoxide ion can assume in organic synthesis.<sup>121</sup> In addition, ORR is also employed in amperometric sensors,<sup>122, 123</sup> fuel cells and next generation batteries.<sup>44, 119, 122</sup>

The widespread use of renewable sources of energy, and the electrification of transport, has promoted research into alternative methods of energy generation and storage. Thus, great attention has recently been given to the study of the electroreduction of  $O_2$ ,<sup>44</sup> considering the application of ORR in fuel cells and metal- $O_2$  batteries.

The stability of electrolytes in the presence of the superoxide ion, is one of the major challenges related to metal- $O_2$  batteries. The electrolyte must not only offer a stable environment for the metallic electrode (as thoroughly described in Chapter 3), it also must be stable against superoxide attack, and display high  $O_2$  diffusion. In addition, breathable cells may experience considerable solvent evaporation over time,<sup>124</sup> thus an electrolyte with low volatility is desired.

Ionic liquids (ILs) display negligible volatility and flammability, demonstrating much improved safety aspects compared to typical organic battery electrolytes. The stability of ILs against the superoxide ion has generated contrasting reports in literature.<sup>5</sup> Some studies have reported poor long-term stability of [C<sub>1</sub>C<sub>4</sub>Pyrr][NTf<sub>2</sub>], and other pyrrolidinium-based ILs.<sup>125, 126</sup> Furthermore, the instability of imidazolium cations, due to the more acidic proton at the C2 position in the imidazolium ring, has been long established.<sup>127</sup> However, several other reports have successfully used IL-based electrolytes as electrolytes in Li<sup>+</sup>/Na<sup>+</sup> and O<sub>2</sub> systems.<sup>43, 44, 46, 52, 55, 128</sup> Other reports have highlighted concerns regarding the viscosity of ILs, the low O<sub>2</sub> diffusion coefficient, and the electrode kinetics when using IL-based electrolytes.<sup>5</sup> Therefore, key parameters associated with the O<sub>2</sub> reaction must be determined and fundamental studies must be performed prior to application of IL electrolytes in full metal-O<sub>2</sub> cells.

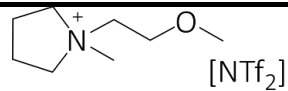
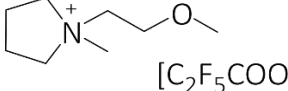
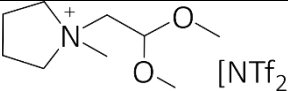
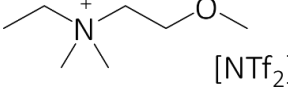
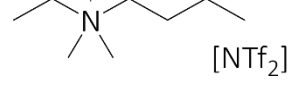
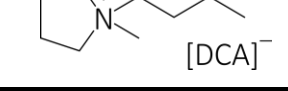
This chapter aims to evaluate the ORR in a selection of pyrrolidinium and quaternary ammonium ILs varying the cation side chain and anion structure to examine how physical and electrochemical parameters are affected in these O<sub>2</sub>-IL systems. To do so, a combination of voltammetric studies using macroelectrodes, microelectrodes and rotating disc electrodes were used to investigate O<sub>2</sub>-saturated IL systems. The solubility and diffusion coefficients of O<sub>2</sub> are also determined for each IL, which are verified using different methodologies. Moreover, the electrode kinetics during ORR are determined in selected ILs, as well as the effect of small structural changes in the IL on the electrode kinetics and charge transfer coefficients.

## 4.2. Experimental

## 4.2.1 Electrolyte preparation

The ILs studied in this chapter were synthesised as described in Chapter 2, and their structure and nomenclature are displayed in Table 4.1, with the exception of [C<sub>1</sub>C<sub>4</sub>Pyrr][DCA], which was purchased from Iolitec.

**Table 4.1.** Summary of ILs studied in this chapter

IL structure	IL abbreviation
	[C <sub>1</sub> (C <sub>2</sub> OC <sub>1</sub> )Pyrr][NTf <sub>2</sub> ]
	[C <sub>1</sub> (C <sub>2</sub> OC <sub>1</sub> )Pyrr][C <sub>2</sub> F <sub>5</sub> COO]
	[C <sub>1</sub> C <sub>dma</sub> Pyrr][NTf <sub>2</sub> ]
	[N <sub>C<sub>1</sub>,C<sub>1</sub>,C<sub>2</sub>,C<sub>2</sub>OC<sub>1</sub>}] [NTf<sub>2</sub>]</sub>
	[N <sub>C<sub>1</sub>,C<sub>1</sub>,C<sub>2</sub>,C<sub>4</sub>}] [NTf<sub>2</sub>]</sub>
	[C <sub>1</sub> C <sub>4</sub> Pyrr][DCA]

Prior to use, all ILs were dried under high vacuum at 65 °C, until their water content was below 40 ppm, confirmed by Karl-Fischer titration. Before carrying out the experiments, dry O<sub>2</sub> (purity ≥ 99.5%) was bubbled in the ILs for 20 minutes to ensure saturation, and for an additional five minutes between measurements. After drying, all ILs were handled within a glovebox (H<sub>2</sub>O < 1 ppm).

### 4.2.2 Cyclic voltammetry and chronoamperometry

O<sub>2</sub> redox reactions were initially studied with cyclic voltammetry, in an air-tight five-necked heart-shaped cell (Figure 4.1). Glassy carbon (GC, 3 mm diameter) was used as the working electrode (WE) and a platinum coil (Pt coil) was used as the counter electrode (CE). Prior to use, GC electrode was polished with an alumina suspension in ultrapure water (miliQ 18.2 Mohm/cm), then thoroughly rinsed with acetone and ultrapure water. Ag wire was used as the quasi reference electrode (qRE). The separation of Ag wire from the bulk electrolyte by a glass frit was attempted, however no electrochemical contact could be achieved as the IL did not diffuse through the glass frit, even by heating the IL to higher temperatures. Therefore, no attempt to compare potentials will be discussed in this chapter. All experiments were performed within a glovebox and iR-compensation was used in all measurements.

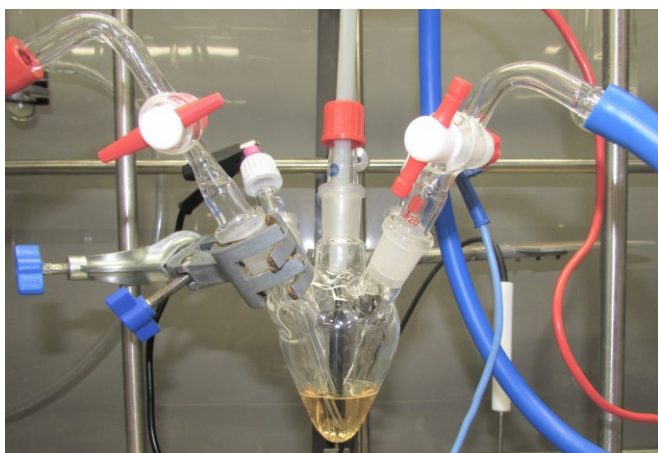


**Figure 4.1.** Five-necked cell showing gas inlet (left) and outlet (right) at the front, the CE and RE necks at the back and the neck for the WE in the centre.

Cyclic voltammetry was also evaluated using gold microdisc electrodes ( $\mu$ WE). The experimental setup adopted was identical to the one described above, except for the  $\mu$ WE, which was made as follows. A short length of the 25- $\mu$ m diameter gold wire was sealed into a thin borosilicate glass tube, by flame melting the glass. A polished piece of Cu wire was connected to the Au wire with Ag epoxy, via the open end of the glass for the electrical contact with the potentiostat. The Au microdisc was exposed by grinding and polishing the sealed

end of the glass tube, and the disc shape was confirmed using optical microscopy. Prior to use the  $\mu$ WE, polished with alumina suspension in ultrapure water and thoroughly rinsed with ultrapure water and acetone, was systematically checked for any cracks or deformation of the disc using optical microscopy. Pt coil and Ag wire were used as the CE and qRE, respectively. The same air-tight five neck heart shaped cell from the previous section was used, and all experiments were carried out within a glovebox. Potentiostep chronoamperometry was also evaluated using the same cell preparation and electrode setup described for the cyclic voltammetry with Au microdisc electrode. The potential step applied to each IL is described throughout the text in the results section.

#### 4.2.3 Hydrodynamic voltammetry

A GC disc (5 mm diameter) was used as the rotating disc working electrode (RDE), and Pt coil and Ag wire were used as the CE and qRE, respectively. Prior to the start of the experiments,  $O_2$  was bubbled into the IL for 20 min, and for another three minutes in between measurements. During the measurements, an  $O_2$  flow was maintained in the cell headspace, forming an “ $O_2$  blanket” above the solution to avoid any change in  $O_2$  concentration throughout the experiment. iR-compensation was used and the experiments were carried out in a five-necked cell with a large central neck (Figure 4.2) within a glovebox.



**Figure 4.2.** Five-necked cell with large central neck for RDE experiments, showing from left to right gas inlet tap, Pt coil electrode and cell with Ag wire electrode.

## 4.3. Results and discussion

### 4.3.1 Key properties of the ILs studied in this chapter

The ILs studied in this chapter and shown in Table 4.1, were chosen for several reasons. Firstly, despite the low viscosity of imidazolium-based ILs being an attractive feature for electrochemical applications, the acidic H in the C2 position in the imidazolium ring is prone to abstraction in the presence of superoxide anions.<sup>129</sup> Thus, other IL alternatives not involving imidazolium cations must be found. Previous studies have already been performed in pyrrolidinium and quaternary ammonium ILs<sup>44, 129, 130</sup> and these ILs appear to be stable against superoxide. Thus, these families of ILs are further explored herein. The incorporation of ether side chains decreases the viscosity of ILs because of increased mobility of the ether chains, compared to their hydrocarbon equivalents, and the disruption of van-der-Waals stacking displayed by the latter. Therefore, ILs with this functionalisation were chosen for this study.  $[N_{C_1, C_1, C_2, C_4}][NTf_2]$  was also synthesised to directly compare the effect of the ether side chain, and/or higher viscosity on the in the O<sub>2</sub> related electrochemical reactions. Table 4.2 shows the viscosity of these ILs. Moreover,

[C<sub>1</sub>C<sub>dma</sub>Pyrr][NTf<sub>2</sub>] was synthesised with the aim of having a reduced cation-anion interaction due to the bulkier side chain in the IL cation, however, this feature comes at the cost of higher viscosity displayed by this IL, which is shown in Table 4.2.

**Table 4.2.** IL properties at 20 °C: dynamic viscosity, kinematic viscosity, and density.

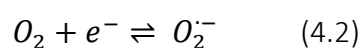
\* [C<sub>1</sub>C<sub>4</sub>Pyrr][DCA] data provided by the supplier.

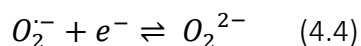
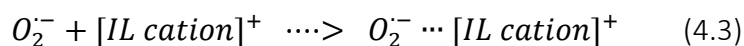
IL	Dynamic viscosity (in mPa.s)	Kinematic viscosity (cm <sup>2</sup> /s)	Density (g/cm <sup>3</sup> )
[C <sub>1</sub> (C <sub>2</sub> OC <sub>1</sub> )Pyrr][NTf <sub>2</sub> ]	74	61	1.46
[C <sub>1</sub> (C <sub>2</sub> OC <sub>1</sub> )Pyrr][C <sub>2</sub> F <sub>5</sub> COO]	107	83	1.32
[C <sub>1</sub> C <sub>dma</sub> Pyrr][NTf <sub>2</sub> ]	120	98	1.45
[N <sub>C<sub>1</sub>,C<sub>1</sub>,C<sub>2</sub>,C<sub>2</sub>,C<sub>2</sub>OC<sub>1</sub></sub> ][NTf <sub>2</sub> ]	63	53	1.43
[N <sub>C<sub>1</sub>,C<sub>1</sub>,C<sub>2</sub>,C<sub>4</sub></sub> ][NTf <sub>2</sub> ]	115	95	1.37
[C <sub>1</sub> C <sub>4</sub> Pyrr][DCA]*	46	45	1.02

In addition, [C<sub>1</sub>C<sub>4</sub>Pyrr][DCA] and [C<sub>1</sub>(C<sub>2</sub>OC<sub>1</sub>)Pyrr][C<sub>2</sub>F<sub>5</sub>COO] IL were designed to compare the effect of a strong donating anion.<sup>66</sup> However, carboxylate ILs are very hydrophilic, and high water contents are found in ILs of this type. In addition, high O<sub>2</sub> solubility has been found in ILs with high fluoride content.<sup>48</sup> Hence, the pentafluoropropionate anion was chosen as the fluoride chain helps to reduce the hydrophilicity of the IL and is likely to aid O<sub>2</sub> solubility.

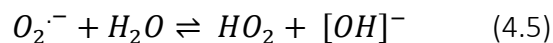
### 4.3.2 Oxygen reduction reaction in ILs

The ORR mechanism and reversibility are highly dependent on several factors, one of them being the electrolyte. In ILs, it is widely accepted<sup>44, 45</sup> that oxygen is reduced, forming O<sub>2</sub><sup>-</sup> (Eq 4.2), which may be stabilised by the ionic liquid cation (Eq 4.3),<sup>131</sup> or it may also be further reduced to peroxide at more negative potentials (Eq 4.4):





The superoxide anion may also promptly establish the following equilibrium with protic impurities or any residual water in the electrolytes:<sup>44</sup>



ORR in the synthesised ILs was firstly studied with cyclic voltammetry. The cyclic voltammograms (CVs) of the O<sub>2</sub>-saturated ILs are shown in Figure 4.3, and key parameters obtained from the CVs is displayed in Table 4.3. The CVs shown in Figure 4.3 display one reduction peak (peak i) in the cathodic scan and one oxidation peak (peak ii) in the anodic scan. The reduction peak i is attributed to a one-electron reduction, forming the superoxide anion, whilst peak ii is attributed to a one-electron oxidation, according to equation 4.2.

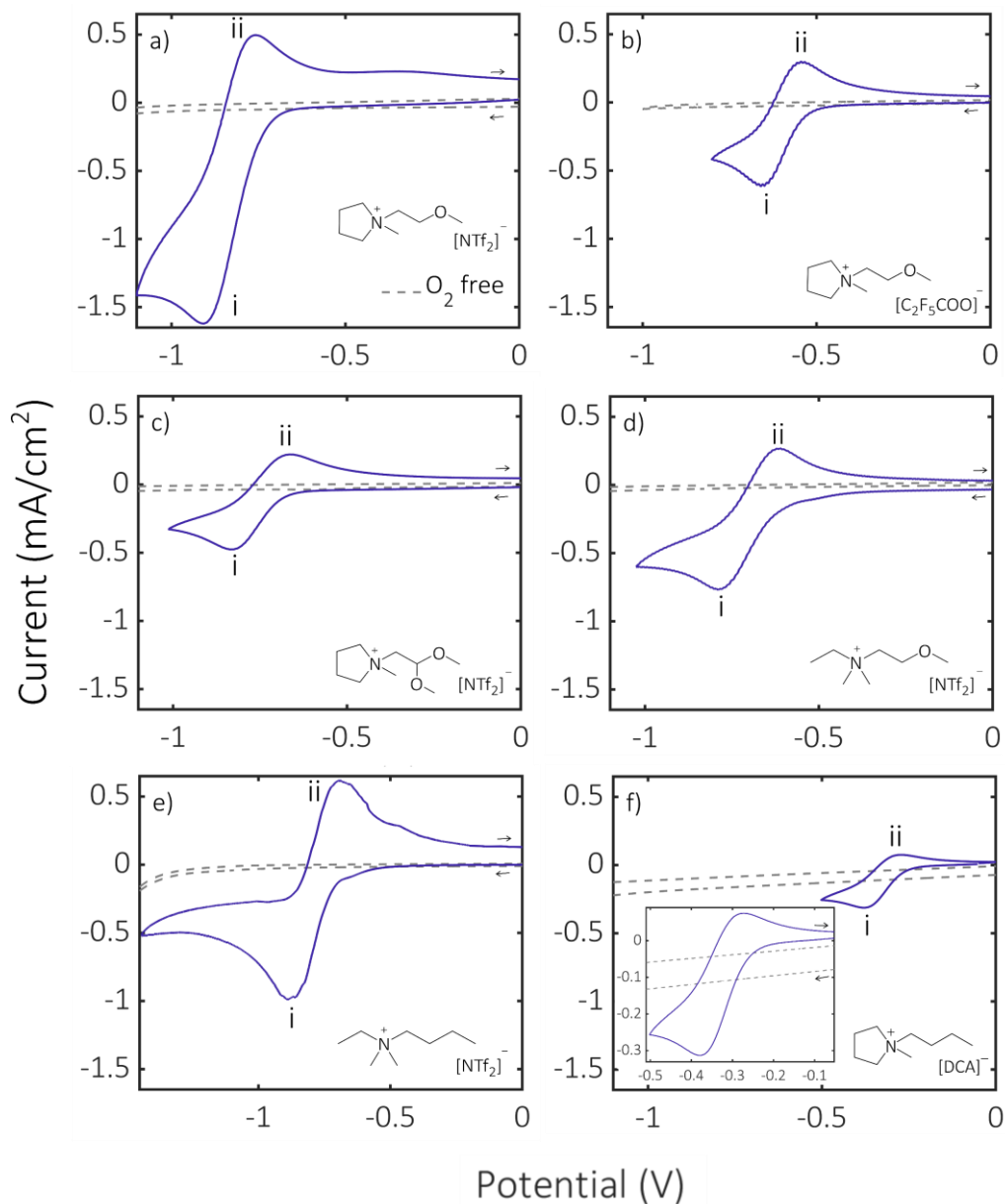


**Figure 4.3.** CVs showing  $1e^-$   $O_2/O_2^-$  redox couple with varying degrees of electrochemical reversibility and  $i_{oxi}/i_{red}$  ratios in several  $O_2$ -saturated ILs, at 100 mV/s using glassy carbon working electrode, Pt coil counter electrode and Ag wire quasi-reference electrode. Arrows show scan direction and grey dotted line shows  $O_2$ -free CVs. ILs used: a)  $[C_1(C_2OC_1)Pyrr][NTf_2]$ , b)  $[C_1(C_2OC_1)Pyrr][C_2F_5COO]$ , c)  $[C_1C_{dma}Pyrr][NTf_2]$ , d)  $[N_{C_1,C_1,C_2,(C_2OC_1)}][NTf_2]$ , e)  $[N_{C_1,C_1,C_2,C_4}][NTf_2]$  (note the different x-axis scale) and f)  $[C_1C_4Pyrr][DCA]$  with inset of magnified CV.

Despite all CVs showing one-electron redox processes in Figure 4.3, Table 4.3 shows that the CVs display varying values of peak-to-peak separation ( $\Delta E_p$ ). The different values of  $\Delta E_p$  indicate that there is variation in the kinetics of

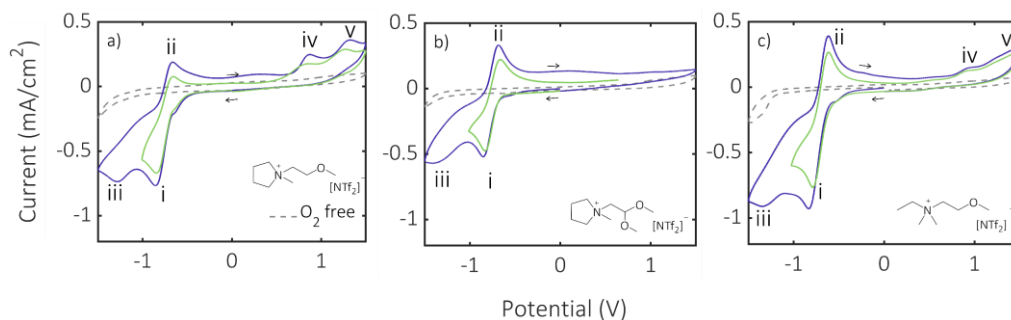
electron transfer across the ILs. Moreover, electrochemically reversible processes display very fast electrode kinetics, thus electrochemical equilibrium is promptly achieved, and the concentration of active species and electrode potential can be described by the Nernst equation. These processes can also be called Nernstian process, and a Nernstian one-electron transfer typically display  $\Delta E_p$  of approximately 57 mV. Therefore, given the  $\Delta E_p$  shown in Table 4.3, the CVs shown in Figure 4.3 are not electrochemically reversible.

Table 4.3 also shows varying oxidation current to reduction current ( $i_{\text{oxi}}/i_{\text{red}}$ ) ratios for the  $\text{O}_2$  CVs in the ILs, with  $[\text{C}_1(\text{C}_2\text{OC}_1)\text{Pyrr}][\text{NTf}_2]$  displaying the lowest ratio and  $[\text{N}_{\text{C}_1,\text{C}_1,\text{C}_2,\text{C}_4}][\text{NTf}_2]$  the greatest. The difference in reduction and oxidation peak currents for  $\text{O}_2$  redox reactions have been previously attributed to the different diffusion coefficients of  $\text{O}_2$  and  $\text{O}_2^-$ .<sup>132</sup> Thus it is possible that the different ratios shown in Table 4.3 are associated with varying  $\text{O}_2^-$  diffusion values in the ILs.

**Table 4.3.** Key information from CVs shown in Figure 4.3: baseline corrected current density for the reduction ( $i_{\text{red}}$ ) and oxidation ( $i_{\text{oxi}}$ ) peaks, the ration between oxidation and reduction currents ( $i_{\text{oxi}}/i_{\text{red}}$ ) and difference between oxidation and reduction peaks ( $\Delta E_p = E_{\text{oxi}} - E_{\text{red}}$ ).

IL	$i_{\text{red}}$ (mA/cm <sup>2</sup> )	$i_{\text{oxi}}$ (mA/cm <sup>2</sup> )	$i_{\text{oxi}}/i_{\text{red}}$	$\Delta E_p$ (mV)
$[\text{C}_1(\text{C}_2\text{OC}_1)\text{Pyrr}][\text{NTf}_2]$	-1.44	0.6264	0.44	151
$[\text{C}_1(\text{C}_2\text{OC}_1)\text{Pyrr}][\text{C}_2\text{F}_5\text{COO}]$	-0.48	0.297109	0.62	120
$[\text{C}_1\text{C}_{\text{dma}}\text{Pyrr}][\text{NTf}_2]$	-0.38	0.2855	0.75	175
$[\text{N}_{\text{C}_1,\text{C}_1,\text{C}_2,(\text{C}_2\text{OC}_1)}][\text{NTf}_2]$	-0.57	0.32386	0.57	168
$[\text{N}_{\text{C}_1,\text{C}_1,\text{C}_2,\text{C}_4}][\text{NTf}_2]$	-0.83	0.8058	0.97	188
$[\text{C}_1\text{C}_4\text{Pyrr}][\text{DCA}]$	-0.23	0.11113	0.49	108

Figure 4.4. shows an extra reduction peak (peak iii) when the CVs are scanned to a more negative cathodic limit. On the anodic scan, other two peaks oxidation peaks (peaks iv and v) become evident for the  $\text{O}_2$  CVs with  $[\text{C}_1(\text{C}_2\text{OC}_1)\text{Pyrr}][\text{NTf}_2]$  and  $[\text{N}_{\text{C}_1,\text{C}_1,\text{C}_2,(\text{C}_2\text{OC}_1)}][\text{NTf}_2]$  (Figure 4.4a and c).



**Figure 4.4.** CVs of  $O_2$ -saturated ILs showing two scans with different cathodic limits: In blue, first scan and more negative cathodic limit, in green second scan and less negative cathodic limit. Note the presence of peak iii with the more negative cathodic limit, and the presence of oxidation peaks iv and v. CVs taken at 100 mV/s using glassy carbon working electrode, Pt coil counter electrode and Ag wire quasi-reference electrode. Arrows show scan direction and grey dotted line shows  $O_2$ -free CVs. ILs used: a)  $[C_1(C_2OC_1)Pyrr][NTf_2]$ , b)  $[C_1C_{dma}Pyrr][NTf_2]$  and c)  $[N_{C_1,C_1,C_2,(C_2OC_1)}][NTf_2]$ .

The reduction peak iii in Figure 4.4 (blue traces) is likely to be associated with reduction of the superoxide anion to peroxide.<sup>44, 133</sup> However, the peak attributed to superoxide oxidation (peak ii) is also present in the anodic scan direction, suggesting that not all  $O_2^-$  is further reduced to peroxide in the cathodic scan.

The peaks iv and v in Figure 4.4a and c were also observed in the absence of peak iii, in CVs with electrolytes containing 300 ppm of water (see orange traces in Figure 4.5). The  $O_2$  CV the electrolyte with 300 ppm of water (orange) in Figure 4.5 shows a significant lower current density for peak ii ( $O_2^-$  oxidation) and greater in current density for peaks iv and v, compared to the electrolyte with 50 ppm of water (blue). This decrease in current density peak ii corroborates with an electro transfer step followed by a chemical step (EC) mechanism, in which  $O_2^-$  reacts with water forming  $H_2O_2$ , according to equations 4.5 and 4.6 shown above. Therefore, peaks iv and v are likely to be associated with oxidation of  $H_2O_2$  and products from  $O_2^-$  side-reactions with traces of water in the IL.<sup>29, 44, 134, 135</sup> Moreover,  $H_2O_2$  can be formed either electrochemically, via reduction of  $O_2^-$  (peak iii) or chemically according to equations 4.5 and 4.6.

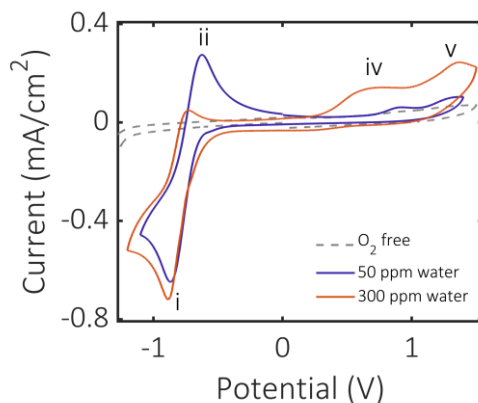


**Figure 4.5.** CVs of  $O_2$ -saturated  $[N_{C_1,C_1,C_2,(C_2OC_1)}][NTf_2]$ , showing effect of water content in the IL: — 50 ppm of water and — 300 ppm of water, measured post experiment using dry and wet  $O_2$  gas lines, respectively.

To further understand the ORR in these ILs and determine key variables for  $O_2$  reactions in the ILs studied herein, voltammetric and amperometric studies are performed in the  $O_2$ -IL systems using a microelectrode, which are discussed in the next section.

### 4.3.3 ORR studies with microdisc electrodes and determination of $O_2$ solubility and diffusion coefficients in ILs

When moving from macroelectrodes to microelectrodes, significant changes in mass transport are observed, which are fully described in Chapter 2. In summary, in cyclic voltammetry using macrodisc electrodes a peak is observed in the CVs because of the decrease on the flux of electroactive species towards the electrode surface during the time scale of the experiment. This is due to the fast electrode kinetics, imposed by the large overpotentials applied. Thus, the fast consumption of electroactive species causes a decrease in the concentration gradient established at the vicinity of the electrode, decreasing the flux of species towards the electrode and the current response. The small dimension of the microdisc electrode means that in the time scale of the experiment, the electrochemical reactions taking place at the electrode cause negligible changes in the concentration gradient established at the vicinity of the electrode. Thus, no significant decrease in the flux of species towards the

electrode is observed, and the CVs display a steady state current instead of the peak shape of the CVs with macroelectrodes.<sup>136, 137</sup>

The steady-state current achieved in microelectrode voltammetry can be described by limiting current equation shown below:

$$i_{ss} = 4nFDc_r \quad (4.8)$$

In addition, time-dependent current response at microelectrodes can be analysed using the equations proposed by Shoup and Szabo, shown below:

$$i = 4nFrDCf(t) \quad (4.9)$$

where  $f(t) = 0.7854 + 0.8862(\tau)^{-1/2} + 0.2146 e^{-0.7823\tau^{-1/2}}$  and  $\tau = \frac{4Dt}{r^2}$ , which allow the simultaneous determination of diffusion and solubility of the electroactive species of interest.

Figure 4.6 shows the CVs of O<sub>2</sub>-saturated ILs using a gold microdisc electrode. The choice of a gold microdisc electrode as oppose to a glassy carbon, as used in to obtain the CVs in the previous section, is due to the inability of making an in-house glassy carbon microdisc electrode. The in-house method used to obtain the microdisc electrode decomposes carbon, thus gold was the material of choice. Negligible differences are expected to be observed in the O<sub>2</sub> electrochemistry when moving from a glassy carbon to a gold working electrode, as pointed out previously in literature.<sup>52</sup> Nevertheless, a CV was obtained with a gold macrodisc electrode which was confirmed to be negligibly different to the CVs obtained with glassy carbon.

Overall, the CVs display one main reduction process that reaches a steady state current, and an oxidation peak in the anodic scan. Moreover, the CVs in [C<sub>1</sub>(C<sub>2</sub>OC<sub>1</sub>)Pyrr][NTf<sub>2</sub>] and [C<sub>1</sub>(C<sub>2</sub>OC<sub>1</sub>)Pyrr][C<sub>2</sub>F<sub>5</sub>COO], the presence of a small peak prior to the main reduction is clear. This has been previously attributed to reduction of O<sub>2</sub> adsorbed at the electrode surface, rather than dissolved in the electrolyte.<sup>48</sup> Alternatively, this may be related to a O<sub>2</sub> electron transfer reaction involving water, impurity molecules or protons in the electrolyte.<sup>128, 138</sup> As soon as the concentration of these molecules drops at the

surface of the electrode, this process diminishes, and  $O_2$  is reduced in a simple electrochemical process forming  $O_2^-$  and displaying the main reduction process in the CVs.

The main reduction process in the voltammograms in Figure 4.6 is attributed to reduction of  $O_2$  to superoxide. The differences in the steady-state current density may be attributed to differences in the solubility and diffusion of  $O_2$  in the ILs, which will be determined below.

The oxidation peak shown in the anodic scan of the CVs in Figure 4.6, is typical of a planar diffusion process in CVs with macroelectrodes, unlike the steady state current expected when using microdisc electrodes. Nevertheless, the peak has been observed before,<sup>132</sup> and is caused by the significant difference in the rates of transport of  $O_2$  and  $O_2^-$  in ILs. Whilst  $O_2$  as a neutral specie diffuses more rapidly through the ILs,  $O_2^-$  being a charged specie diffuses more slowly. This is likely to be associated with the degree of coulombic interactions of the superoxide anion with the IL ions. Thus, different IL structures may lead to different superoxide rate of transport as observed previously for  $[C_4C_1Pyrr][NTf_2]$  and  $[N_{C_2,C_2,C_2,C_6}][NTf_2]$ , with diffusion coefficients of 3.35 and  $1.45 \times 10^{-6} \text{ cm}^2/\text{s}$ , respectively.<sup>139</sup>

The diffusion coefficient and solubility of  $O_2$  in the ILs was determined by fitting the chronoamperometric transients with Shoup and Szabo equations described above. The chronoamperometric data was obtained by stepping the potential from 0 V, at which no Faradaic currents flow, to a potential within the steady-state current region, in which the current is mass transport limited. The experimental and fitted chronoamperograms are shown in Figure 4.7, and the potential applied to each IL is described in the caption of the figure. The experimental data was fitted assuming a one-electron reduction process ( $n=1$ ).

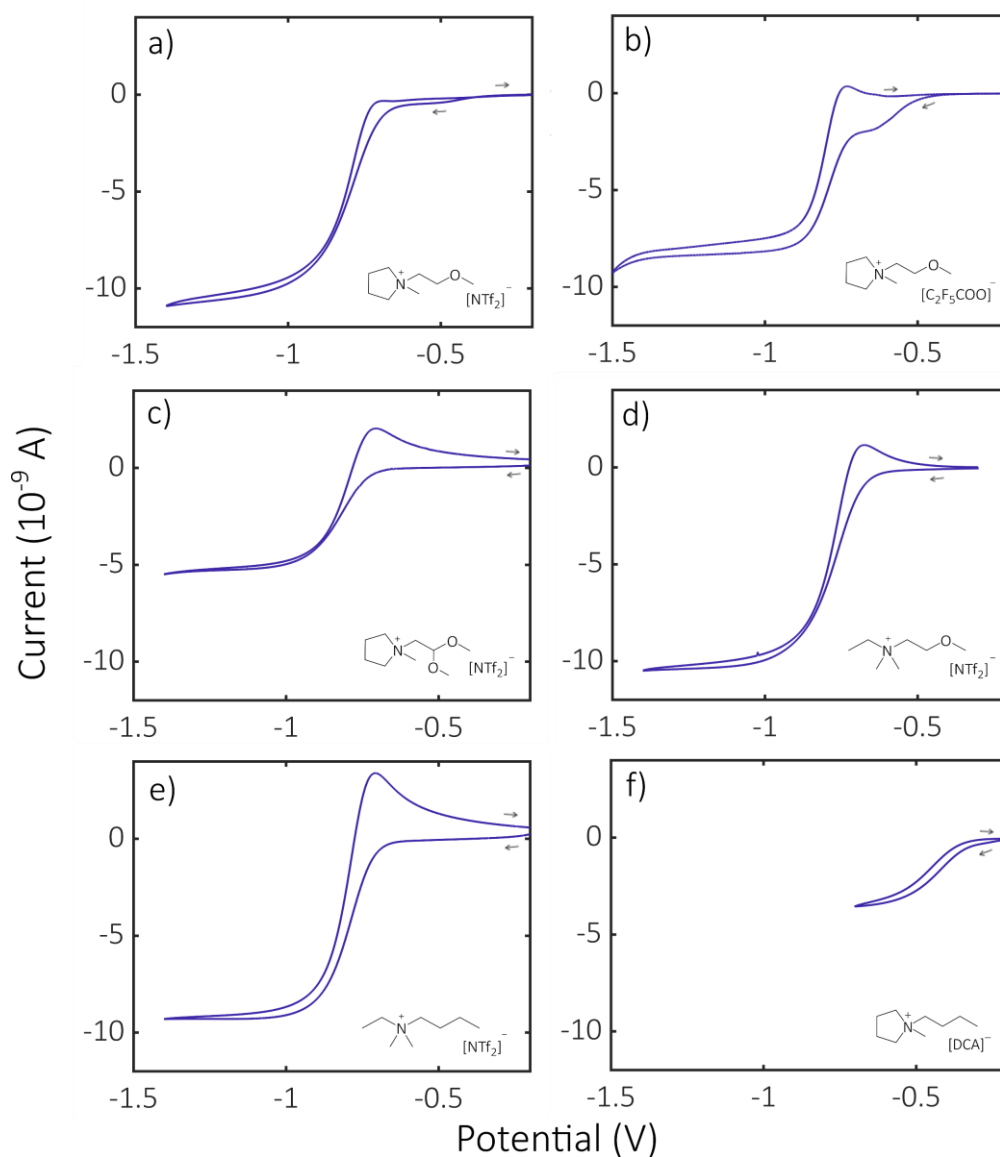


**Figure 4.6.** CVs showing  $1 e^-$  re of  $O_2$ -saturated ILs, at 10 mV/s using a gold microdisc working electrode, Pt coil counter electrode and Ag wire quasi-reference electrode. Arrows show scan direction. ILs used: a)  $[C_1(C_2OC_1)Pyrr][NTf_2]$ , b)  $[C_1(C_2OC_1)Pyrr][C_2F_5COO]$ , c)  $[C_1C_{dma}Pyrr][NTf_2]$ , d)  $[N_{C_1,C_1,C_2,C_2OC_1}][NTf_2]$ , e)  $[N_{C_1,C_1,C_2,C_4}][NTf_2]$  and f)  $[C_1C_4Pyrr][DCA]$ .

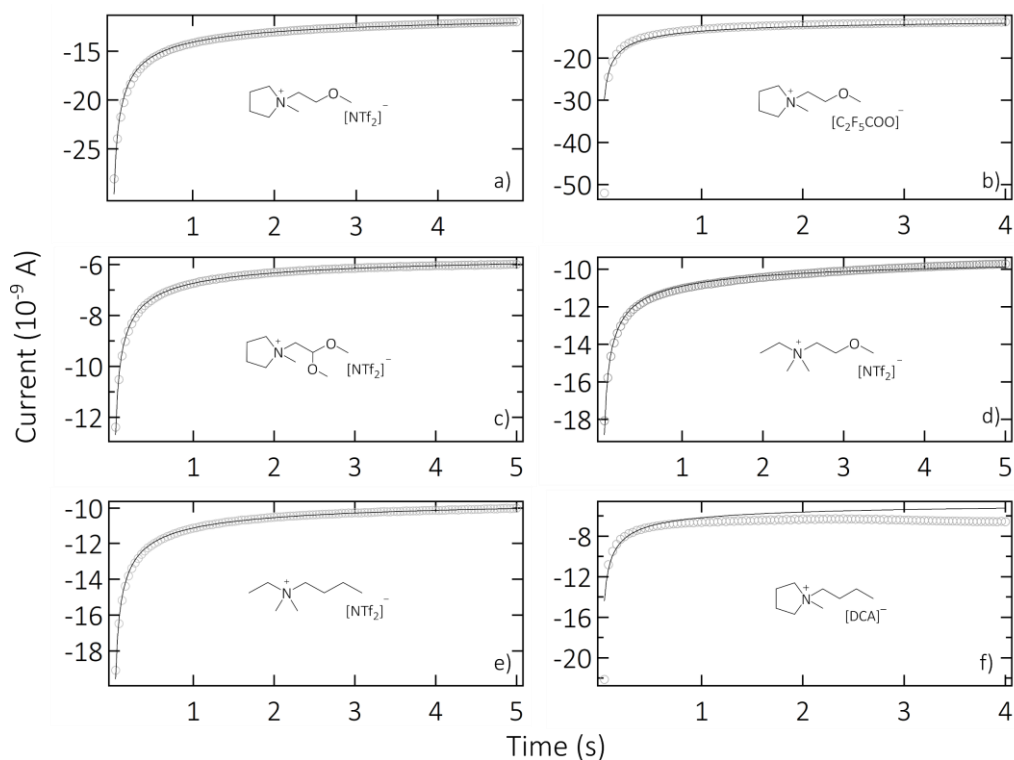


**Figure 4.7.** Potential step chronoamperograms for the reduction of  $O_2$  in saturated ILs, and the potential step applied in each IL is displayed in brackets: a)  $[C_1(C_2OC_1)Pyrr][NTf_2]$  (at -1.4 V), b)  $[C_1(C_2OC_1)Pyrr][C_2F_5COO]$  (at -1.5 V), c)  $[C_1C_{dma}Pyrr][NTf_2]$  (at -1.4 V), d)  $[N_{C_1,C_1,C_2,(C_2OC_1)}][NTf_2]$  (at -1.4 V), e)  $[N_{C_1,C_1,C_2,C_4}][NTf_2]$  (at -1.4 V) and f)  $[C_1C_4Pyrr][DCA]$  (at -0.90 V). The grey circles ( $\circ\circ$ ) show the experimental data and the black lines ( $—$ ) show the fitted data. Repeats of this experiment can be found in Appendix A.3.1.

Figure 4.7 shows that, with the exception of  $[C_1C_4Pyrr][DCA]$ , the fitted transients are a satisfactory representation of the experimental dataset. The solubility and diffusion coefficients of  $O_2$  determined by the fits are displayed in Table 4.4. Some of the coefficients displayed in Table 4.4 differ from those reported in literature (see Table A3.2 in Appendix A.3.1). Previously, Hardacre and co-workers reported  $O_2$  solubility of  $6.67 \times 10^{-6} \text{ mol/cm}^3$  and diffusion coefficient of  $3.76 \times 10^{-6} \text{ cm}^2/\text{s}$  for  $[C_1(C_2OC_1)Pyrr][NTf_2]$ , and AlNashef and co-workers have reported a solubility of  $14.9 \times 10^{-6} \text{ mol/cm}^3$  and diffusion coefficient of  $0.9 \times 10^{-6} \text{ cm}^2/\text{s}$  for  $[N_{C_1,C_1,C_2,(C_2OC_1)}][NTf_2]$ . Those values are rather different than the ones shown on Table 4.4. Nevertheless, it is not unusual to find a lot of variation in the values of  $O_2$  solubility and diffusion coefficients in ILs

reported in literature, even for publications within the same research group, as clearly demonstrated in Appendix A.3.1. This discrepancy may be due to slight variations in temperature during the measurements, accepted fitting quality and even due to different batches of ionic liquid. It is widely known that even small quantities of impurities (such as water content, halide salt, reaction solvent) affect ILs properties. To ensure that different batches of the synthesised ILs in this work would still display the same O<sub>2</sub> solubility and diffusion coefficients, the data displayed in Table 3.3 has been obtained using three repeated experiments conducted over a period of eight months (see repeats in Appendix A.3.1). In addition, the O<sub>2</sub> diffusion coefficient and solubility values were validated with Levich analysis of the data obtained under hydrodynamic conditions. Table 4.6 in the next section shows a comparison of the experimental Levich slope and the slope calculated using the O<sub>2</sub> diffusion coefficient and solubility displayed in Table 4.4. Therefore, despite the values displayed in Table 4.4 being different to those in literature, they are assumed a reliable measure to compare and understand the dataset obtained herein, considering all measurements were conducted following the same protocol.

**Table 4.4.** Average and standard deviation of solubility and diffusion coefficients of O<sub>2</sub> in the ILs determined by fitting of chronoamperometric transients with Shoup and Szabo equations, and viscosity data of ILs. All measurements performed at 20 °C.

IL	C (10 <sup>-6</sup> mol/cm <sup>3</sup> )	D (10 <sup>-6</sup> cm <sup>2</sup> /s)
[C <sub>1</sub> (C <sub>2</sub> OC <sub>1</sub> )Pyrr][NTf <sub>2</sub> ]	13.22 ± 3.76	1.78 ± 0.44
[C <sub>1</sub> (C <sub>2</sub> OC <sub>1</sub> )Pyrr][C <sub>2</sub> F <sub>5</sub> COO]	17.61 ± 5.05	1.10 ± 0.48
[C <sub>1</sub> C <sub>dma</sub> Pyrr][NTf <sub>2</sub> ]	3.55 ± 0.25	3.06 ± 0.45
[N <sub>C<sub>1</sub>,C<sub>1</sub>,C<sub>2</sub>,C<sub>2</sub>,C<sub>2</sub>OC<sub>1</sub></sub> ][NTf <sub>2</sub> ]	3.85 ± 0.20	4.95 ± 0.61
[N <sub>C<sub>1</sub>,C<sub>1</sub>,C<sub>2</sub>,C<sub>4</sub></sub> ][NTf <sub>2</sub> ]	4.39 ± 0.31	4.38 ± 0.31
[C <sub>1</sub> C <sub>4</sub> Pyrr][DCA]	7.73 ± 0.64	1.17 ± 0.04

The O<sub>2</sub> diffusion coefficients were compared to the intrinsic properties of ILs, such as the IL viscosity, density, and molar volume, and can be found in Figure A 37 in Appendix 1.A.3. No clear correlation between the O<sub>2</sub> diffusion

coefficients and the inverse of the IL viscosities was found, despite previous reports,<sup>140</sup> suggesting these systems studied herein disobey the Stokes-Einstein equation that follows:

$$D = \frac{k_b T}{6\pi\eta r} \quad (4.10)$$

This is understandable considering the O<sub>2</sub>-IL system is not exactly equivalent to a system in which the size of the diffusing species is much larger than the size of solvent molecules, and in which the diffusing species are in an infinitely diluted solution, as described by the Stokes-Einstein equation.<sup>141</sup>

Nevertheless, mass transport in ILs has been studied using the holes theory.<sup>65, 141-143</sup> According to the holes theory, species move in solution according to the availability of sites suitable to fit the species in movement.<sup>65, 143, 144</sup> Therefore, the greater the probability of finding voids of size larger than the species in solution, the greater the mass transport in the liquid. Moreover, the size of the holes in a liquid is related to the surface tension in the liquid.<sup>65</sup> The higher the surface tension, the smaller the size of the hole and the lower the free volume in the liquid.<sup>143, 144</sup> Indeed, previous studies<sup>145</sup> have correlated the solubility of gases with the calculated free volume in ILs and have also associated the free volume to the structure of ILs. With this in mind, the O<sub>2</sub> solubility was compared to the density of the ILs, due to the lack of surface tension data on the ILs studied herein, and it is displayed in Figure 4.8. Figure 4.8 shows that the solubility of O<sub>2</sub> seems to decrease with an increase of the IL density and molar volume, if two trends of ILs are considered. Based on this, it is possible that the O<sub>2</sub> solubility in the ILs can be explained by the holes theory, although it is not clear the separation in two trends. However, this present study does not have enough evidence to provide full rationale for these observations.

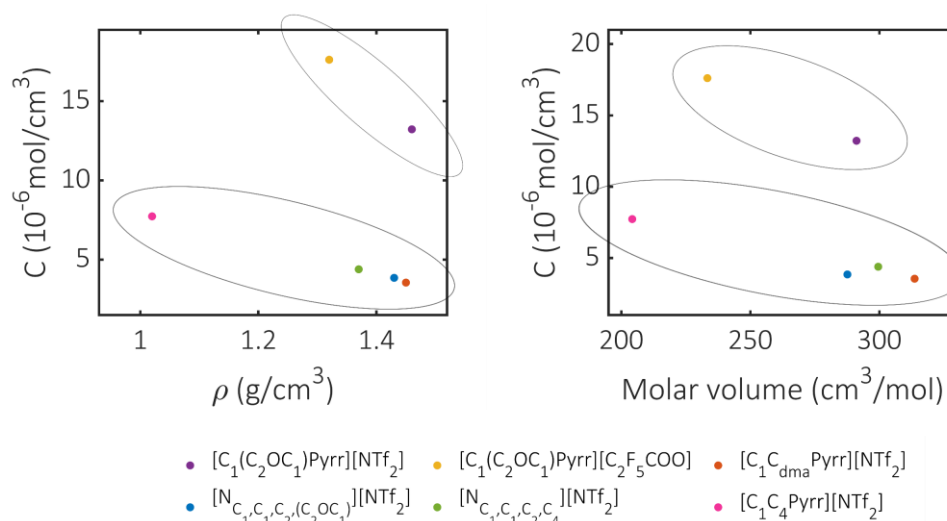


**Figure 4.8.** O<sub>2</sub> solubility (C) in the ILs compared to the IL density (ρ) and molar volume.

#### 4.3.4 Cyclic voltammetry under hydrodynamic conditions and study of electrode kinetics

ORR was also studied in [C<sub>1</sub>(C<sub>2</sub>OC<sub>1</sub>)Pyrr][NTf<sub>2</sub>], [C<sub>1</sub>C<sub>dma</sub>Pyrr][NTf<sub>2</sub>], [N<sub>C<sub>1</sub>,C<sub>1</sub>,C<sub>2</sub>,C<sub>2</sub>OC<sub>1</sub></sub>][NTf<sub>2</sub>] and [N<sub>C<sub>1</sub>,C<sub>1</sub>,C<sub>2</sub>,C<sub>4</sub></sub>][NTf<sub>2</sub>] under hydrodynamic conditions, using a rotating disc electrode (RDE). During RDE, a low flux of O<sub>2</sub> was maintained on the top of the liquid (not immersed) during the experiments. Nevertheless, it was found very challenging to maintain O<sub>2</sub> saturation in the ILs, especially at high rotation rates. Figure 4.9 displays several linear sweep voltammograms (LSVs) recorded at the same rotational speed (1700 RPM) demonstrating the difficulty in keeping a constant O<sub>2</sub> saturation. For this reason, a high flow of O<sub>2</sub> had to be kept in the cell headspace during the experiment. In addition, at least three LSVs were recorded for each rotation speed, with O<sub>2</sub> bubbling in between measurements to ensure the voltammogram recorded was an accurate measurement. The LSVs recorded using RDE are displayed in Figure 4.10. Figure 4.10 shows a pre-peak followed by a large reduction process with onset potential varying in between -0.60 V to -0.80 V.

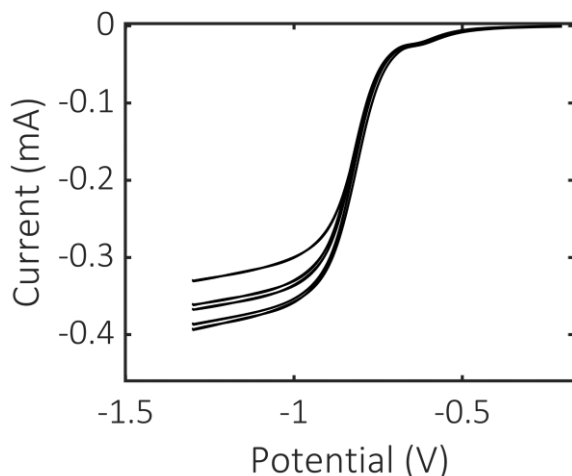


**Figure 4.9.** Multiple LSVs at 1700 RPM, demonstrating variation in the  $O_2$  saturation in the ILs during the experiments. LSVs recorded using a GC RDE as the WE, Pt coil as the CE and Ag wire as the qRE in  $[N_{C_1,C_1,C_2,(C_2OC_1)}][[NTf_2]$  and at 50 mV/s.

The persistent pre-peak, that has already been observed in the previous section, is evident in the majority of the LSVs shown in Figure 4.10. Previously it was suggested the pre-peak could be either associated with an electron transfer reaction involving  $O_2$  and water or impurity molecules, or reduction of  $O_2$  adsorbed on GC surface.<sup>128</sup> Considering this pre-peak is present under hydrodynamic conditions and in all rotation rates, it is likely that it is correlated to superoxide reaction with another ion/molecule. It has been reported that presence of water may lead to side-reactions, as described by equations 4.5 and 4.6.<sup>44 138</sup> Karl Fisher titration before and after the RDE experiments show an increase of the water content in the ILs from 3 to 19 ppm on average. Although the value seems low, it is equivalent to 1.056 mmol/L, which compared to  $O_2$  concentration (Table 4.4) is considerably higher. Furthermore, the shift of the  $O_2$  reduction potential has been previously attributed to the presence of protons in the IL. Thus, it is possible that water acts as the source of protons and the pre-peak is associated with  $O_2$  reduction in the presence of protons. Nevertheless, the concentration of protons rapidly diminishes, and the main reduction process takes place.

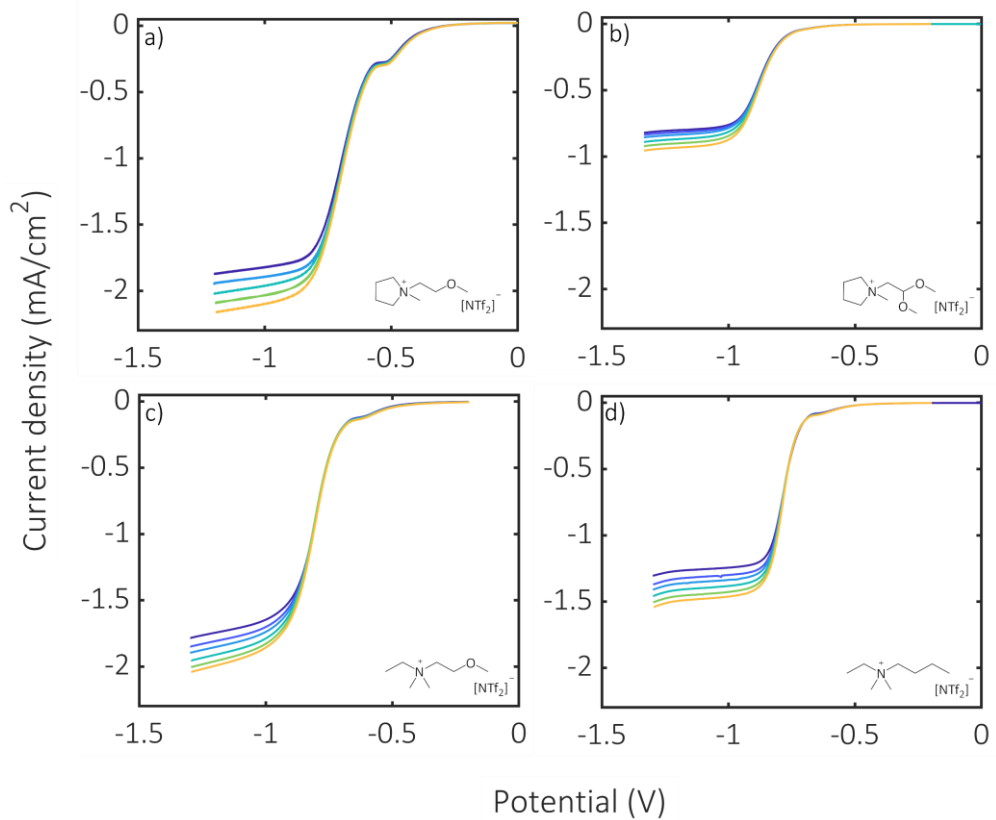


**Figure 4.10.** LSV showing  $1 e^-$   $O_2$  reduction under hydrodynamic conditions using a RDE (GC) of  $O_2$ -saturated ILs, at  $50 \text{ mV/s}$  with rotation rates from  $1300 \text{ RPM}$  to  $1800 \text{ RPM}$ . Pt coil and Ag wire were used as the CE and RE, respectively. a)  $[C_1(C_2OC_1)Pyrr][NTf_2]$ , b)  $[C_1C_{dma}Pyrr][NTf_2]$ , c)  $[N_{C_1,C_1,C_2,(C_2OC_1)}][NTf_2]$  and d)  $[N_{C_1,C_1,C_2,C_4}][NTf_2]$ .

The main reduction process is attributed to a one-electron reduction of  $O_2$  to  $O_2^-$  and pairing with the IL cations. At sufficiently large overpotentials, this process reaches a mass transport limiting current. The mass transport limiting current is a function of square root of the rotation rate according to the Levich equation shown below:

$$i_{lim} = 0.62nFACD^{2/3}\nu^{-1/6}\sqrt{\omega} \quad (4.11)$$

where  $n$  is the number of electrons transferred per molecule,  $F$  is the Faraday constant,  $A$  the area of the electrode (in  $\text{cm}^2$ ),  $C$  the concentration of the analyte (in  $\text{mol/cm}^3$ ),  $D$  the diffusion coefficient of the analyte (in  $\text{cm}^2/\text{s}$ ),  $\nu$  is the kinematic viscosity of the electrolyte (in  $\text{cm}^2/\text{s}$ ), and  $\omega$  the rotation speed (in  $\text{rad/s}$ ). The Levich plots displaying the mass transport limiting current ( $i_{lim}$ ) as a

function of the square root of the rotational speed ( $\omega^{0.5}$ ) are shown in Figure 4.11. The plots show that the limiting current of the main peak is linearly dependent on the square root of rotation rate, indicating that either an E or an EC process is observed in the main reduction event, as described previously.<sup>59</sup>

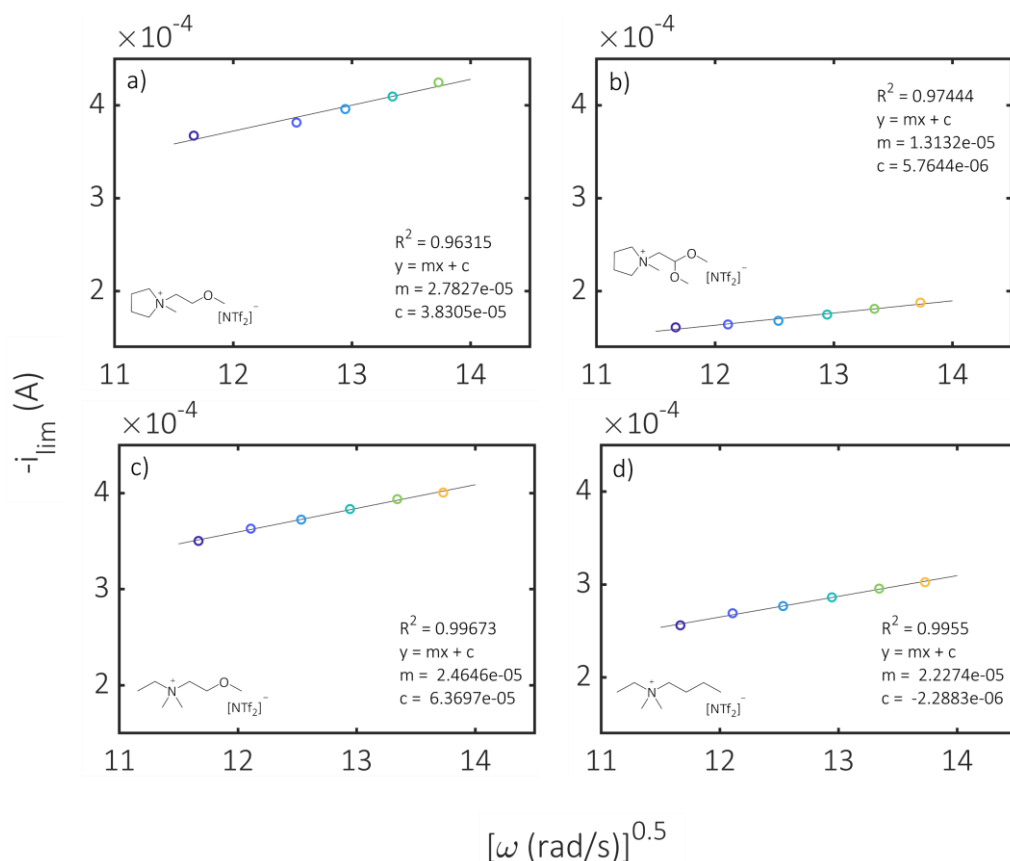


**Figure 4.11.** Levich plots for ORR in the ILs: a)  $[C_1(C_2OC_1)Pyrr][NTf_2]$ , b)  $[C_1C_{dma}Pyrr][NTf_2]$ , c)  $[N_{C_1,C_1,C_2,(C_2OC_1)}][NTf_2]$ , d)  $[N_{C_1,C_1,C_2,C_4}][NTf_2]$ . Note the  $10^{-4}$  value in all currents displayed on the y axis.

Finally, a Tafel analysis was performed on the LSVs shown in Figure 4.10. The Tafel equation is based on the Butler and Volmer equation for electrode reaction kinetics at high overpotentials ( $\eta_E$ ), and is expressed as:

$$\eta_E = a + b \log(i) \quad (4.12)$$

where  $a = (2.3RT/\alpha nF) \log(i_0)$  and  $b = 2.3RT/\alpha nF$ , the Tafel slope for a single step electrochemical reaction. For multistep reactions, including electrochemical and/or chemical steps,  $\alpha$  becomes the apparent charge transfer coefficient, which considers the rate determining step (rds) and any step

precedent to the rds. The apparent coefficient can be summarised as  $(n_{<rds} + n\alpha)$ , in which  $n_{<rds}$  is the number of electrons transferred before the rate determining step, and  $n$  the number of electrons transferred in the rds. Thus, the overall Tafel slope can be written as

$$b = \frac{2.3 RT}{(n_{<rds} + n\alpha)F} \quad (4.13)$$

The typical plots of potential as a function of the log of the mass transport corrected current ( $\log(i_{lim} \times i / (i_{lim} - i))$ ) are displayed in Figure 4.12. Figure 4.12 shows the analysis for the LSV at 1800 RPM, however, the Tafel slopes are independent of the rotation rate as can be seen in Figure A 38.

Figure 4.12 shows each IL display a different Tafel slope, which also changes as the potential is varied. This has been previously associated with a change in the rds, the electrode surface coverage and/or surface morphology caused by the potential sweep.<sup>146, 147</sup> The variation of Tafel slope with potential is more evident for the quaternary ammonium (Figure 4.12c and d) than the pyrrolidinium ILs (Figure 4.12a and b).

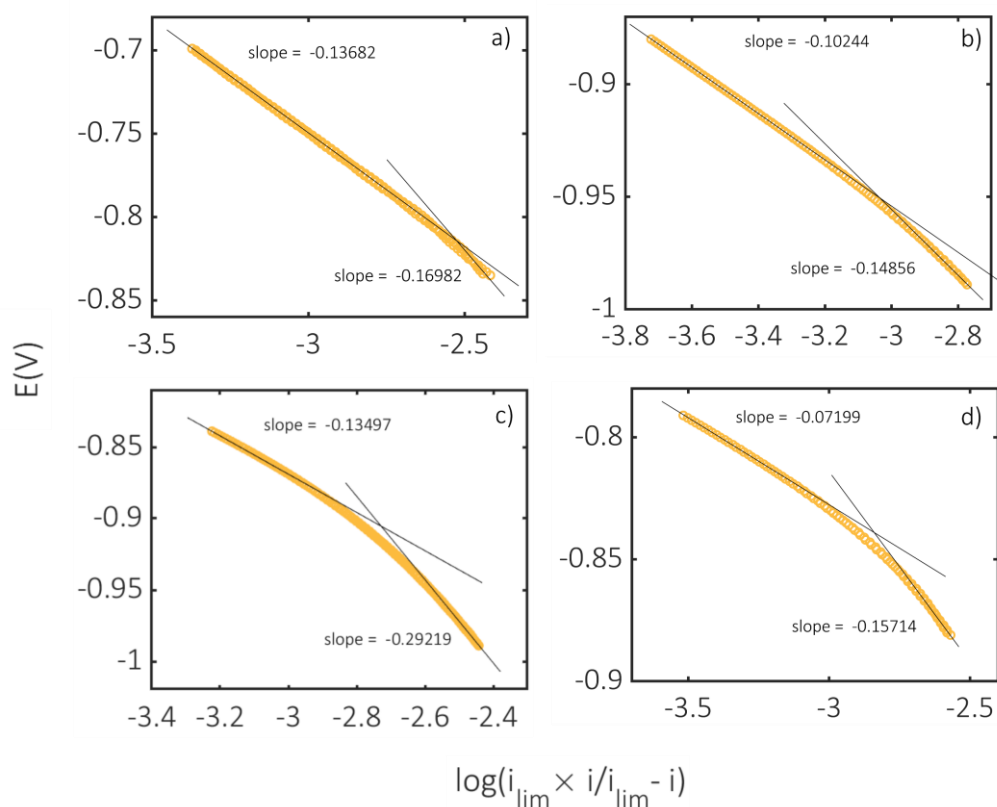


**Figure 4.12.** Tafel analysis of LSVs shown in Figure 4.10 at 1800 RPM, with the dataset range equivalent to percentages of  $i_{lim}$  displayed within brackets for each IL: a)  $[C_1(C_2OC_1)Pyrr][NTf_2]$  ( $0.5i_{lim}$  to  $0.9i_{lim}$ ), b)  $[C_1C_{dma}Pyrr][NTf_2]$  ( $0.5i_{lim}$  to  $0.9i_{lim}$ ), c)  $[N_{C_1,C_1,C_2,(C_2OC_1)}][NTf_2]$  ( $0.6i_{lim}$  to  $0.9i_{lim}$ ), d)  $[N_{C_1,C_1,C_2,C_4}][NTf_2]$  ( $0.5i_{lim}$  to  $0.9i_{lim}$ ).

Table 4.5 shows a summary of the Tafel slopes obtained from Figure 4.12, and the calculated apparent charge transfer coefficient. At less negative potentials,  $[C_1(C_2OC_1)Pyrr][NTf_2]$  and  $[N_{C_1,C_1,C_2,(C_2OC_1)}][NTf_2]$  display very similar slopes, of 137 and 135 mV respectively, perhaps indicating a similar mechanism at this stage. As the potential becomes more negative, the slope in  $[N_{C_1,C_1,C_2,(C_2OC_1)}][NTf_2]$  changes to a greater value of 292 mV, whilst the slope  $[C_1(C_2OC_1)Pyrr][NTf_2]$  only changes at the very negative potentials to 170 mV. At less negative potentials,  $[N_{C_1,C_1,C_2,C_4}][NTf_2]$  and  $[C_1C_{dma}Pyrr][NTf_2]$  display 72 and 102 mV slopes, which increase to 157 and 148 mV, respectively, at more negative potentials.

Tafel slopes reported in literature for ORR typically include values of 60 and 120 mV.<sup>147, 148</sup> A slope of 120 mV for instance, may be associated with a rds

involving one-electron transfer and  $\alpha=0.5$  ( $b = 2.3RT/(0 + 0.5 \times 1 \times F) = 0.118$ ).<sup>147</sup> None of the slopes displayed on Table 4.5 are typical Tafel slopes reported in literature. Furthermore, considering that  $n_{<rds}$  and  $n$  are equal to integer values (0, 1, 2 ... electrons), and given the values obtained for  $(n_{<rds} + n\alpha)$  shown on Table 4.5,  $n_{<rds}$  must be equal to zero, and  $n$  must be equal to one. Therefore, based on these results, the rds involves one electron transfer and no electrons have been transferred prior the rds during the ORR on a GC electrode in the ILs studied herein. Thus, the values for  $(n_{<rds} + n\alpha)$  displayed on Table 4.5 are likely to be simply  $\alpha$  values.

**Table 4.5.** Key information from the Tafel Analysis shown in Figure 4.12: Tafel slopes ( $b$ ) for the less negative (\*) potentials and for the more negative potentials (\*\*), with their respective apparent charge transfer coefficient, at 20 °C.

IL	$b$ * (mV)	$(n_{<rds} + n\alpha)^*$	$b$ * (mV)	$(n_{<rds} + n\alpha)^{**}$
[C <sub>1</sub> (C <sub>2</sub> OC <sub>1</sub> )Pyrr][NTf <sub>2</sub> ]	137	0.42	170	0.34
[C <sub>1</sub> C <sub>dma</sub> Pyrr][NTf <sub>2</sub> ]	102	0.57	148	0.39
[N <sub>C<sub>1</sub>,C<sub>1</sub>,C<sub>2</sub>,C<sub>2</sub>OC<sub>1</sub></sub> ][NTf <sub>2</sub> ]	135	0.43	292	0.20
[N <sub>C<sub>1</sub>,C<sub>1</sub>,C<sub>2</sub>,C<sub>4</sub></sub> ][NTf <sub>2</sub> ]	72	0.81	157	0.37

#### 4.3.5 Comparison of coefficients determined with Shoup-Szabo to Levich slope values

The Levich equation discussed above (equation 4.12) states that the mass transport limiting current ( $i_{lim}$ ) is related to the diffusion and solubility of O<sub>2</sub> ( $D^{2/3}C$ ). Therefore, if the solubility and diffusion coefficients of O<sub>2</sub> are known (as well as the kinematic viscosity of the electrolyte), the Levich slopes ( $0.62nFACD^{2/3}\nu^{-1/6}$ ) can be calculated and compared to the experimental slopes obtained from the Levich plots of  $i_{lim}$  as a function of  $\sqrt{\omega}$  (Figure 4.11).

**Table 4.6.** Calculated Levich slope using O<sub>2</sub> solubility and diffusion coefficients for from Table 4.4 and experimental Levich slope obtained from Figure 4.11, and kinematic viscosity of neat IL ( $\nu$ , at 20 °C) used to calculate the Levich slope.

IL	$\nu$ (cm <sup>2</sup> /s)	Calculated Levich slope	Experimental Levich slope
[C <sub>1</sub> (C <sub>2</sub> OC <sub>1</sub> )Pyrr][NTf <sub>2</sub> ]	0.605	$4.0 \times 10^{-5}$	$2.8 \times 10^{-5}$
[C <sub>1</sub> C <sub>dma</sub> Pyrr][NTf <sub>2</sub> ]	0.983	$1.4 \times 10^{-5}$	$1.3 \times 10^{-5}$
[N <sub>C<sub>1</sub>,C<sub>1</sub>,C<sub>2</sub>,C<sub>2</sub>,C<sub>2</sub>OC<sub>1</sub></sub> ][NTf <sub>2</sub> ]	0.566	$2.3 \times 10^{-5}$	$2.5 \times 10^{-5}$
[N <sub>C<sub>1</sub>,C<sub>1</sub>,C<sub>2</sub>,C<sub>4</sub></sub> ][NTf <sub>2</sub> ]	0.952	$2.2 \times 10^{-5}$	$2.2 \times 10^{-5}$

The solubility and diffusion coefficients determined with the microdisc electrode and the Shoup-Szabo equation (equation 4.9) were used to calculate the Levich slopes, as described above, and the results are shown in Table 4.6. With the exception of [C<sub>1</sub>(C<sub>2</sub>OC<sub>1</sub>)Pyrr][NTf<sub>2</sub>], the calculated Levich slopes are in excellent agreement with the experimental slopes. This confirms the reliability of the solubility and diffusion coefficient values obtained in Section 4.3.3 for these systems.

[C<sub>1</sub>(C<sub>2</sub>OC<sub>1</sub>)Pyrr][NTf<sub>2</sub>] shows the greatest difference among the slopes, and it also shows one of the highest error bands in the solubility coefficient ( $13.22 \pm 3.76$  mol/cm<sup>3</sup>, see Table 4.4). If the lowest solubility value of O<sub>2</sub> in [C<sub>1</sub>(C<sub>2</sub>OC<sub>1</sub>)Pyrr][NTf<sub>2</sub>] is used, the calculated Levich slope becomes  $2.9 \times 10^{-5}$ , which is in high agreement with the experimental slope. Thus, it is possible that either the solubility values obtained in Section 4.3.3 are an overestimation of the solubility, or the IL is not fully O<sub>2</sub>-saturated in the hydrodynamic experiments.

#### 4.4. Conclusions and Future Work

This chapter has demonstrated how small differences in the IL structure can affect key parameters involving O<sub>2</sub> redox reactions. O<sub>2</sub> solubility and diffusion coefficients in ILs have been successfully determined in this chapter,

and it has been demonstrated that the diffusion of O<sub>2</sub> across the range of ILs studied herein does not follow a Stokes-Einstein behaviour. It has been suggested that the O<sub>2</sub> diffusion coefficients in the ILs may be better explained by the holes theory. Additionally, the O<sub>2</sub> solubility has been found to be somewhat dependent on the IL density, and the lower the IL density, the greater the O<sub>2</sub> solubility in the ILs. [C<sub>1</sub>(C<sub>2</sub>OC<sub>1</sub>)Pyrr]-based ILs displayed the highest O<sub>2</sub> solubility whilst [N<sub>C<sub>1</sub>,C<sub>1</sub>,C<sub>2</sub>,C<sub>2</sub>OC<sub>1</sub></sub>][NTf<sub>2</sub>] and [N<sub>C<sub>1</sub>,C<sub>1</sub>,C<sub>2</sub>,C<sub>4</sub></sub>][NTf<sub>2</sub>] displayed the highest rate of O<sub>2</sub> diffusion.

Experiments using RDE show that at sufficiently high overpotentials, a mass transport limited current can be obtained, which was analysed with Levich plots. Moreover, the slope of the Koutecký-Levich plots are potential dependent, suggesting ORR in these ILs are a quasi-reversible reaction. Tafel analysis of the [NTf<sub>2</sub>]-ILs have suggested that no electron transfer has occurred prior to the rds and has also shown that there is a change in the rds as the potential is varied.

Another point that is worth further investigation is to understand the diffusion and the extent of the interactions between the studied ILs and the superoxide anion. This would aid the understanding of the impact of the IL structure not only on O<sub>2</sub>, as demonstrated herein, but also on the O<sub>2</sub><sup>-</sup> stabilisation. Previously Forsyth and co-workers<sup>149</sup> have probed the interaction of O<sub>2</sub><sup>-</sup> with phosphonium compared to quaternary ammonium-based ILs using density functional theory calculations. Therefore, similar calculations could be performed to aid understanding of the interactions of the ILs studied herein with O<sub>2</sub><sup>-</sup>.

Considering a potential battery application, [N<sub>C<sub>1</sub>,C<sub>1</sub>,C<sub>2</sub>,C<sub>2</sub>OC<sub>1</sub></sub>][NTf<sub>2</sub>] seem the most suitable candidate as it displays high O<sub>2</sub> diffusion coefficient and relatively low viscosity.

## 4.5. References

1. Siraki, A. G.; Klotz, L. O.; Kehrer, J. P., Free Radicals and Reactive Oxygen Species. In *Comprehensive Toxicology*, McQueen, C. A., Ed. Elsevier: Oxford, 2018; Vol. 1, pp 262-294.
2. Hayyan, M.; Hashim, M. A.; AlNashef, I. M., Superoxide Ion: Generation and Chemical Implications. *Chem. Rev.* **2016**, *116* (5), 3029-3085.
3. Hayyan, M.; Mjalli, F. S.; Hashim, M. A.; AlNashef, I. M., Generation of Superoxide Ion in Pyridinium, Morpholinium, Ammonium, and Sulfonium-Based Ionic Liquids and the Application in the Destruction of Toxic Chlorinated Phenols. *Ind. Eng. Chem. Res.* **2012**, *51* (32), 10546-10556.
4. Han, X.; Wang, K.; Zhang, G.; Gao, W.; Chen, J., Application of the Electrochemical Oxygen Reduction Reaction (ORR) in Organic Synthesis. *Adv. Synth. Catal.* **2019**, *361* (12), 2804-2824.
5. Khan, A.; Gunawan, C. A.; Zhao, C. Z., Oxygen Reduction Reaction in Ionic Liquids: Fundamentals and Applications in Energy and Sensors. *ACS Sustainable Chem. Eng.* **2017**, *5* (5), 3698-3715.
6. Xiong, L.; Compton, R. G., Amperometric Gas detection: A Review. *Int. J. Electrochem. Sci.* **2014**, *9* (12), 7152-7181.
7. Pozo-Gonzalo, C., Oxygen Reduction Reaction in Ionic Liquids: An Overview. In *Electrochemistry in Ionic Liquids: Volume 2: Applications*, Torriero, A. A. J., Ed. Springer International Publishing: Cham, 2015; pp 507-529.
8. Xu, W.; Xiao, J.; Zhang, J.; Wang, D.; Zhang, J. G., Optimization of Nonaqueous Electrolytes for Primary Lithium/Air Batteries Operated in Ambient Environment. *J. Electrochem. Soc.* **2009**, *156* (10), A773.
9. Kwak, W. J.; Rosy; Sharon, D.; Xia, C.; Kim, H.; Johnson, L. R.; Bruce, P. G.; Nazar, L. F.; Sun, Y. K.; Frimer, A. A.; Noked, M.; Freunberger, S. A.; Aurbach, D., Lithium–Oxygen Batteries and Related Systems: Potential, Status, and Future. *Chem. Rev.* **2020**.
10. Piana, M.; Wandt, J.; Meini, S.; Buchberger, I.; Tsiouvaras, N.; Gasteiger, H. A., Stability of a Pyrrolidinium-Based Ionic Liquid in Li-O<sub>2</sub> Cells. *J. Electrochem. Soc.* **2014**, *161* (14), A1992-A2001.
11. Das, S.; Højberg, J.; Knudsen, K. B.; Younesi, R.; Johansson, P.; Norby, P.; Vegge, T., Instability of Ionic Liquid-Based Electrolytes in Li–O<sub>2</sub> Batteries. *J. Phys. Chem. A* **2015**, *119* (32), 18084-18090.
12. Katayama, Y.; Onodera, H.; Yamagata, M.; Miura, T., Electrochemical Reduction of Oxygen in Some Hydrophobic Room-Temperature Molten Salt Systems. *Journal of The Electrochemical Society* **2004**, *151* (1), A59-A63.
13. Pozo-Gonzalo, C.; Howlett, P. C.; MacFarlane, D. R.; Forsyth, M., Highly reversible oxygen to superoxide redox reaction in a sodium-containing ionic liquid. *Electrochem. Commun.* **2017**, *74*, 14-18.
14. Zhang, Y.; Ortiz-Vitoriano, N.; Acebedo, B.; O'Dell, L.; MacFarlane, D. R.; Rojo, T.; Forsyth, M.; Howlett, P. C.; Pozo-Gonzalo, C., Elucidating the Impact of Sodium Salt Concentration on the Cathode–Electrolyte Interface of Na–Air Batteries. *J. Phys. Chem. C* **2018**, *122* (27), 15276-15286.

15. Allen, C. J.; Hwang, J.; Kautz, R.; Mukerjee, S.; Plichta, E. J.; Hendrickson, M. A.; Abraham, K. M., Oxygen Reduction Reactions in Ionic Liquids and the Formulation of a General ORR Mechanism for Li–Air Batteries. *J. Phys. Chem. C* **2012**, *116* (39), 20755-20764.
16. Neale, A. R.; Li, P.; Jacquemin, J.; Goodrich, P.; Ball, S. C.; Compton, R. G.; Hardacre, C., Effect of cation structure on the oxygen solubility and diffusivity in a range of bis{(trifluoromethyl)sulfonyl}imide anion based ionic liquids for lithium-air battery electrolytes. *Phys. Chem. Chem. Phys.* **2016**, *18* (16), 11251-11262.
17. Zhang, Y.; Pozo-Gonzalo, C., Variations and applications of the oxygen reduction reaction in ionic liquids. *Chem. Commun.* **2018**, *54* (31), 3800-3810.
18. Frith, J. T.; Russell, A. E.; Garcia-Araez, N.; Owen, J. R., An in-situ Raman study of the oxygen reduction reaction in ionic liquids. *Electrochem. Commun.* **2014**, *46*, 33-35.
19. Watanabe, M.; Thomas, M. L.; Zhang, S.; Ueno, K.; Yasuda, T.; Dokko, K., Application of Ionic Liquids to Energy Storage and Conversion Materials and Devices. *Chem. Rev.* **2017**, *117* (10), 7190-7239.
20. Schmeisser, M.; P., I.; Puchta, R.; Zahl, A.; van Eldik, R., Gutmann donor and acceptor numbers for ionic liquids. *Chem. - Eur. J.* **2012**, *18*, 10969-10982.
21. Monaco, S.; Arangio, A. M.; Soavi, F.; Mastragostino, M.; Paillard, E.; Passerini, S., An electrochemical study of oxygen reduction in pyrrolidinium-based ionic liquids for lithium/oxygen batteries. *Electrochim. Acta* **2012**, *83*, 94-104.
22. Walsh, D. A.; Goodwin, S., The Oxygen Reduction Reaction in Room-Temperature Ionic Liquids. In *Encyclopedia of Interfacial Chemistry*, Wandelt, K., Ed. Elsevier: Oxford, 2018; Vol. 5.2, pp 898-907.
23. Rogers, E. I.; Huang, X. J.; Dickinson, E. J. F.; Hardacre, C.; Compton, R. G., Investigating the Mechanism and Electrode Kinetics of the Oxygen|Superoxide (O<sub>2</sub>|O<sub>2</sub><sup>•-</sup>) Couple in Various Room-Temperature Ionic Liquids at Gold and Platinum Electrodes in the Temperature Range 298–318 K. *J. Phys. Chem. C* **2009**, *113* (41), 17811-17823.
24. Compton, R. G.; Banks, C. E., Cyclic Voltammetry at Macroelectrodes. In *Understanding Voltammetry*, World Scientific London, 2007; pp 107-151.
25. Katayama, Y.; Sekiguchi, K.; Yamagata, M.; Miura, T., Electrochemical Behavior of Oxygen/Superoxide Ion Couple in 1-Butyl-1-methylpyrrolidinium Bis(trifluoromethylsulfonyl)imide Room-Temperature Molten Salt. *J. Electrochem. Soc.* **2005**, *152* (8), E247-E250.
26. Balaish, M.; Kraytsberg, A.; Ein-Eli, Y., A critical review on lithium-air battery electrolytes. *Phys. Chem. Chem. Phys.* **2014**, *16* (7), 2801-22.
27. Sanford, A. L.; Morton, S. W.; Whitehouse, K. L.; Oara, H. M.; Lugo-Morales, L. Z.; Roberts, J. G.; Sombers, L. A., Voltammetric Detection of Hydrogen Peroxide at Carbon Fiber Microelectrodes. *Anal. Chem.* **2010**, *82* (12), 5205-5210.
28. Roberts, J. G.; Voinov, M. A.; Schmidt, A. C.; Smirnova, T. I.; Sombers, L. A., The Hydroxyl Radical is a Critical Intermediate in the Voltammetric Detection of Hydrogen Peroxide. *J. Am. Chem. Soc.* **2016**, *138* (8), 2516-2519.

29. Bard, A. J.; Faulkner, L. R., Basic Potential Step Methods. In *Electrochemical methods: fundamentals and applications*, 2nd ed.; Wiley: New York, 2001; pp 156-226.
30. Compton, R. G.; Craig, E. B., Voltammetry at Microelectrodes. In *Understanding Voltammetry*, World Scientific: London, 2010; pp 163-201.
31. Smith, D. E.; Walsh, D. A., The Nature of Proton Shuttling in Protic Ionic Liquid Fuel Cells. *Adv. Energy Mater.* **2019**, *9* (24), 1900744.
32. Huang, X. J.; Rogers E. F.; Hardacre, C.; Compton, R. G., The reduction of oxygen in various room temperature ionic liquids in the temperature range 293-318 K: exploring the applicability of the Stokes-Einstein relationship in room temperature ionic liquids. *J. Phys. Chem. B* **2009**, *113*, 8953-8959.
33. Taylor, A. W.; Licence, P.; Abbott, A. P., Non-classical diffusion in ionic liquids. *Phys. Chem. Chem. Phys.* **2011**, *13* (21), 10147-10154.
34. Abbott, A. P.; Harris, R. C.; Ryder, K. S., Application of Hole Theory to Define Ionic Liquids by their Transport Properties. *J. Phys. Chem. B* **2007**, *111* (18), 4910-4913.
35. Abbott, A. P., Application of hole theory to the viscosity of ionic and molecular liquids. *Chemphyschem* **2004**, *5* (8), 1242-1246.
36. D'Agostino, C., Hole theory as a prediction tool for Brownian diffusive motion in binary mixtures of liquids. *RSC Adv.* **2017**, *7* (82), 51864-51869.
37. Simha, R.; Carri, G., Free volume, hole theory and thermal properties. *J. Polym. Sci. B Polym. Phys.* **1994**, *32* (16), 2645-2651.
38. Shannon, M. S.; Tedstone, J. M.; Danielsen, S. P. O.; Hindman, M. S.; Irvin, A. C.; Bara, J. E., Free Volume as the Basis of Gas Solubility and Selectivity in Imidazolium-Based Ionic Liquids. *Ind. Eng. Chem. Res.* **2012**, *51* (15), 5565-5576.
39. Compton, R. G.; Craig, E. B., Hydrodynamic Electrodes. In *Understanding Voltammetry*, World Scientific: 2010; pp 291-346.
40. Bard, A. J.; Faulkner, L. R., Methods Involving Forced Convection-Hydrodynamic Methods. In *Electrochemical methods: fundamentals and applications*, 2nd ed.; Wiley: New York, 2001; pp 331-367.
41. Wang, H.; Sayed, S. Y.; Lubner, E. J.; Olsen, B. C.; Shirurkar, S. M.; Venkatakrishnan, S.; Tefashe, U. M.; Farquhar, A. K.; Smotkin, E. S.; McCreery, R. L.; Buriak, J. M., Redox Flow Batteries: How to Determine Electrochemical Kinetic Parameters. *ACS Nano* **2020**, *14* (3), 2575-2584.
42. Walsh, D. A.; Ejigu, A.; Smith, J.; Licence, P., Kinetics and mechanism of oxygen reduction in a protic ionic liquid. *Phys. Chem. Chem. Phys.* **2013**, *15* (20), 7548-54.
43. Fang, Y. H.; Liu, Z. P., Tafel Kinetics of Electrocatalytic Reactions: From Experiment to First-Principles. *ACS Catalysis* **2014**, *4* (12), 4364-4376.
44. Holewinski, A.; Lincic, S., Elementary Mechanisms in Electrocatalysis: Revisiting the ORR Tafel Slope. *J. Electrochem. Soc.* **2012**, *159* (11), H864-H870.
45. Pozo-Gonzalo, C.; Howlett, P. C.; Hodgson, J. L.; Madsen, L. A.; MacFarlane, D. R.; Forsyth, M., Insights into the reversible oxygen reduction reaction in a series of phosphonium-based ionic liquids. *Phys. Chem. Chem. Phys.* **2014**, *16* (45), 25062-70.





## 5. Oxygen reduction reaction in the presence of alkali metal cations, and an application in Na-O<sub>2</sub> cells

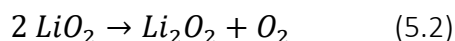
### 5.1. Introduction

The oxygen reduction reaction (ORR) in the presence of metal cations has been extensively studied given its application in metal-O<sub>2</sub> batteries.<sup>45</sup> By far the main focus has been on nonaqueous Li-O<sub>2</sub> systems,<sup>5, 23</sup> and aqueous Zn-O<sub>2</sub>,<sup>150</sup> however the interest in nonaqueous Na-O<sub>2</sub> has been growing<sup>20</sup> and other reports also include K-O<sub>2</sub><sup>151</sup> and Mg-O<sub>2</sub> systems.<sup>152</sup>

In Li-O<sub>2</sub> systems, it has been widely accepted that the reduction of O<sub>2</sub> yields O<sub>2</sub><sup>-</sup>, forming LiO<sub>2</sub> in the presence of Li<sup>+</sup>. Previous studies have shown that depending on the electrolyte, LiO<sub>2</sub> may be partially stabilised in solution or precipitate at the electrode surface right away:<sup>30</sup>



Moreover, LiO<sub>2</sub> undergoes chemical disproportionation to Li<sub>2</sub>O<sub>2</sub> due to the instability of LiO<sub>2</sub>,<sup>153</sup> thus the final discharge product in Li-O<sub>2</sub> batteries has been found to be Li<sub>2</sub>O<sub>2</sub>.<sup>30</sup>



Nevertheless, fundamental studies using cyclic voltammetry have also observed Li<sub>2</sub>O<sub>2</sub> formation via one e<sup>-</sup> reduction of LiO<sub>2</sub>.<sup>127</sup>

In Na-O<sub>2</sub> systems, the ORR in the presence of Na<sup>+</sup> is believed to follow the same first steps as in the Li-O<sub>2</sub> systems, with formation of NaO<sub>2</sub>. Like LiO<sub>2</sub>,

NaO<sub>2</sub> has also been reported to be found either in solution, or at the electrode surface,<sup>32, 53, 54</sup> as shown by equation 5.3. In fact, a previous study on glyme-based electrolytes found that the solubility of NaO<sub>2</sub> is strongly dependent on the solvation properties of the solvent.<sup>32</sup> Furthermore, a recent study using an electrolyte based on dimethoxy ethane (DME) and Na[PF<sub>6</sub>] confirmed that NaO<sub>2</sub> is formed via a solution-mediated nucleation process.<sup>27</sup>



Unlike Li-O<sub>2</sub> systems, NaO<sub>2</sub> is a stable product and it is the discharge product reported by most studies on Na-O<sub>2</sub> cells.<sup>26, 154</sup> This has been attributed to the fact that NaO<sub>2</sub> is the kinetically favoured product, despite being slightly less thermodynamically stable than Na<sub>2</sub>O<sub>2</sub>.<sup>155</sup>

Substantial progress has been achieved in Li-O<sub>2</sub> systems, with reports including mechanistic studies, the use of suitable catalysts and redox mediators. These have been thoroughly reviewed recently.<sup>23, 156</sup> A wide scope of investigation still needs to be covered for Na-O<sub>2</sub> systems to reach the same progress as Li-O<sub>2</sub>. Nevertheless, a recent review has highlighted the latest findings regarding design of the positive electrode and electrolyte, as well as important aspects with respect to the Na electrode.<sup>20</sup>

In both Li and Na systems, the electrolyte choice remains as a challenge in the development of these type of cells, especially in Na systems, considering the increased reactivity of metallic sodium and, more practically, the lesser understanding of the whole system compared to Li-O<sub>2</sub>.<sup>20, 25, 46</sup> Moreover, regarding electrolyte choice, it must be stable in the presence of highly reactive O<sub>2</sub><sup>-</sup> to avoid undesirable side reactions and early electrode blockage with insulating discharge products.<sup>20</sup>

Despite some reports suggesting poor long term stability of ionic liquids (ILs) in Li-O<sub>2</sub> battery cells,<sup>5, 125, 126</sup> research on IL-based electrolytes are worthwhile given their negligible volatility and flammability,<sup>88</sup> which are particularly attractive from a safety aspect in large-scale applications. In addition, the negligible volatility of ILs is beneficial for open-cell structures, an

important requirement for Na-air batteries. This minimizes electrolyte loss overtime in contrast to other commonly used electrolytes.<sup>124</sup>

The high tunability of ILs, which can be explored for instance by the choice of anion and cation combination or by the choice of alkylating reagent in the synthesis process, is another advantage when using IL electrolytes. This can be visualised, for instance, in a study carried out by Monaco *et al.*<sup>48</sup> The study investigated Li-O<sub>2</sub> reactions and O<sub>2</sub> parameters in several pyrrolidinium-based ILs with different choices of anion. The authors found strong correlation between choice of IL anion and O<sub>2</sub> solubility and diffusion coefficient. Furthermore, other studies on Li-O<sub>2</sub> systems have been carried out using an IL-based electrolyte,<sup>47-49, 51, 52, 88, 157-159</sup> however, only a few report the performance of full Li-O<sub>2</sub> cells using IL-based electrolyte.<sup>49, 51, 158, 159</sup>

Studies using ILs as electrolytes in Na-O<sub>2</sub> systems are still under development.<sup>20, 46, 53-55, 160, 161</sup> The main reports to date are due to the efforts of Forsyth, Pozo-Gonzalo, Howlett, McFarlane, and co-workers.<sup>46, 54, 55, 160, 161</sup> The impact of Na<sup>+</sup> salt concentration has been thoroughly evaluated in [C<sub>1</sub>C<sub>4</sub>Pyrr][NTf<sub>2</sub>]-based electrolytes.<sup>54, 55</sup> The authors suggested that at higher Na<sup>+</sup> concentrations, O<sub>2</sub><sup>-</sup> preferably coordinates to Na<sup>+</sup> (instead of [C<sub>1</sub>C<sub>4</sub>Pyrr]<sup>+</sup>)<sup>54</sup> and this improves the discharge capacity and performance of full Na-O<sub>2</sub> cells.<sup>55</sup> Another study compared the O<sub>2</sub> redox reactions in the presence of Na<sup>+</sup> in [C<sub>1</sub>C<sub>4</sub>Pyrr][NTf<sub>2</sub>], [C<sub>1</sub>C<sub>3</sub>Pyrr][NTf<sub>2</sub>] and [C<sub>1</sub>C<sub>3</sub>Pyrr][FSI], and found poor reversibility of the O<sub>2</sub> reactions in [C<sub>1</sub>C<sub>3</sub>Pyrr][FSI].<sup>46</sup>

Despite the progress using IL-based electrolytes in Na-O<sub>2</sub> systems, there is still a vast range of ILs to be investigated, given the high tunability of ILs mentioned earlier. Previous chapters in this thesis have already explored the application of different IL-based electrolytes in Na<sup>0</sup>/Na<sup>+</sup> systems (Chapter 3) and studied fundamental properties of O<sub>2</sub> reactions in these ILs (Chapter 4). Therefore, this chapter aims to fundamentally evaluate the impact that different IL structures and/or cation-anion combinations have in the ORR in the presence of Na<sup>+</sup>. The concentration of Na<sup>+</sup> salts in the electrolytes is ramped from low, additive-like concentrations (25 mM) to concentrations used in electrolytes for

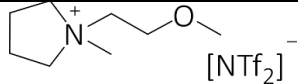
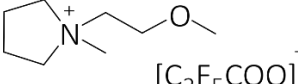
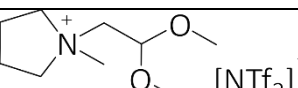
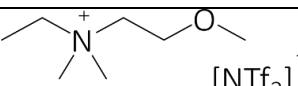
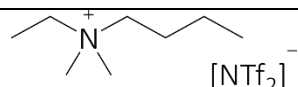
full Na-O<sub>2</sub> cells (0.5 M). Thus, the effect of increasing salt concentration in various IL-based electrolytes can also be observed. This aims to give an insight into the presence of different solvent-solute interactions and transport properties of the active species (O<sub>2</sub>, O<sub>2</sub><sup>-</sup>, Na<sup>+</sup>) in the ILs. Finally, this chapter also includes assembly and cycling of full Na-O<sub>2</sub> cells, containing IL-based electrolytes. Additionally, a brief fundamental study in Li<sup>+</sup>/O<sub>2</sub> system is also performed as an initial step for comparison with the less understood Na<sup>+</sup>/O<sub>2</sub> systems.

## 5.2. Experimental

### 5.2.1 Electrolyte preparation

The structure and nomenclature of the ILs studied in this chapter is displayed in Table 5.1. All ILs were synthesised as described in Chapter 2.

**Table 5.1.** Summary of ILs studied in this chapter.

IL structure	IL abbreviation
	[C <sub>1</sub> (C <sub>2</sub> OC <sub>1</sub> )Pyrr][NTf <sub>2</sub> ]
	[C <sub>1</sub> (C <sub>2</sub> OC <sub>1</sub> )Pyrr][C <sub>2</sub> F <sub>5</sub> COO]
	[C <sub>1</sub> C <sub>dma</sub> Pyrr][NTf <sub>2</sub> ]
	[N <sub>C<sub>1</sub>,C<sub>1</sub>,C<sub>2</sub>,C<sub>2</sub>OC<sub>1</sub>}] [NTf<sub>2</sub>]</sub>
	[N <sub>C<sub>1</sub>,C<sub>1</sub>,C<sub>2</sub>,C<sub>4</sub>}] [NTf<sub>2</sub>]</sub>

Prior to use, all ILs were dried under vacuum ( $\leq 10^{-3}$  mbar) at 65 °C, until their water content was below 40 ppm, confirmed by Karl Fisher titration. Li[NTf<sub>2</sub>], Na[NTf<sub>2</sub>], Li[CF<sub>3</sub>COO] and Na[CF<sub>3</sub>COO] were dried under vacuum at

110 °C for 48 h. The electrolytes were prepared within a glovebox, and the [NTf<sub>2</sub>]-based electrolytes were prepared with Li/Na[NTf<sub>2</sub>], whilst the [C<sub>2</sub>F<sub>5</sub>COO]-based electrolytes were prepared with Li/Na[CF<sub>3</sub>COO], in concentrations of 0.025, 0.05 and 0.5 M of salts. [CF<sub>3</sub>COO]<sup>-</sup> salts were used instead of [C<sub>2</sub>F<sub>5</sub>COO]<sup>-</sup> salts due to Li[C<sub>2</sub>F<sub>5</sub>COO] not being commercially available. Although 0.5 M is a relatively low salt concentration for a battery electrolyte, it was the solubility upper limit of some ILs, like [C<sub>1</sub>C<sub>dma</sub>Pyrr][NTf<sub>2</sub>] for example. For this reason, 0.5 M was selected as the upper limit for all ILs. Before carrying out any set of experiments, dry O<sub>2</sub> (purity ≥ 99.5 %) was bubbled in the ILs for 20 minutes to ensure saturation, and for an additional five minutes between measurements.

### 5.2.2 Cyclic voltammetry

O<sub>2</sub> redox reactions were initially studied with cyclic voltammetry, in an air-tight five necked heart-shaped cell (same cell shown in Figure 4.1, Chapter 4). Glassy carbon (GC, 3 mm diameter) was used as the working electrode (WE) and a platinum coil (Pt coil) was used as the counter electrode (CE). Prior to use, GC electrode was polished with alumina suspension in ultrapure water (miliQ 18.2 Mohm/cm), thoroughly rinsed with acetone and ultrapure water. Ag wire was used as the quasi reference electrode (qRE). The separation of Ag wire from the bulk electrolyte by a glass frit was attempted, however no electrochemical contact could be achieved as the IL did not diffuse through the glass frit, even by heating the IL to higher temperatures. Therefore, no attempt to compare potentials will be discussed in this chapter, only potential difference between anodic and cathodic events. Unless stated, all experiments were performed within a glovebox and iR-compensation was used in all measurements.

### 5.2.3 Hydrodynamic voltammetry

A rotating ring disc electrode (RRDE) WE was used for the hydrodynamic experiments. The RRDE was composed of a glassy carbon disc (5 mm diameter)

and Pt ring. A Pt coil was used as the CE and a Ag wire was used qRE, respectively. Prior to the start of the experiments, O<sub>2</sub> was bubbled into the IL for 20 min, and for another three minutes in between measurements. During the measurements, an O<sub>2</sub> flow was maintained in the headspace, forming an “O<sub>2</sub> blanket” above the solution to avoid any change in O<sub>2</sub> concentration throughout the experiment. iR compensation was used and the experiments were carried out in a five-necked cell within a glovebox (same cell shown in Figure 4.2, Chapter 4). The ring collection efficiency was measured with Fc/Fc<sup>+</sup> redox couple, and the efficiency was considered when plotting the RRDE CVs and analysing the percentual of ring current compared to disc current.

#### 5.2.4 Na-O<sub>2</sub> cells and galvanostatic charge/discharge experiments

The Na-O<sub>2</sub> full cell experiments were performed using a rifle cell based on the design used in the Bruce group at the University of Oxford.<sup>162</sup> The cell schematics are shown in Figure 5.1. The cells were built using Swagelok fittings, and the main cell body was composed of stainless steel (SS) ½ in nuts and ½ in body, and SS rod ( $\varnothing = \frac{1}{2}$  in) fitted with PTFE front and back ferrules. The headspace was composed of a hollow SS rod ( $\varnothing = \frac{1}{2}$  in and approximately 10 cm long) and the O<sub>2</sub> inlet and outlet are also Swagelok parts ( $\varnothing = \frac{1}{2}$  in). The potentiostat connection involved a banana plug in one end of the cell and a crocodile clip in the other. Na electrodes were prepared as described in Chapter 3, by cutting the oxidised parts from a clean Na cube and flattening the cube into a thin Na sheet (< 1 mm thickness) within an Ar filled glovebox. Discs ( $\varnothing = 12$  mm) were cut out and used as the negative electrodes. Glass fibre discs ( $\varnothing = 12.8$  mm, 0.26 mm thickness, 1.6  $\mu$ m pore size) were previously dried under vacuum at 330 °C and used as the separator. The separators were placed in between the electrodes and wet with 105-210  $\mu$ L of electrolyte. A gas diffusion layer (GDL) was used as the O<sub>2</sub> positive electrode and a stainless steel (SS) mesh was used as the current collector. A PTFE film (25  $\mu$ m thickness) was placed on the internal walls of the Swagelok body to prevent short-circuiting. As soon as the cell was assembled, the cell headspace was covered with an

insulating material to prevent short-circuiting, with only the connection to the O<sub>2</sub> line open. The cell was then connected to a dry O<sub>2</sub> line via the inlet and outlet tubes and flushed with O<sub>2</sub> for five minutes. Cells were cycled at either room temperature or placed in an oven at 40 °C.

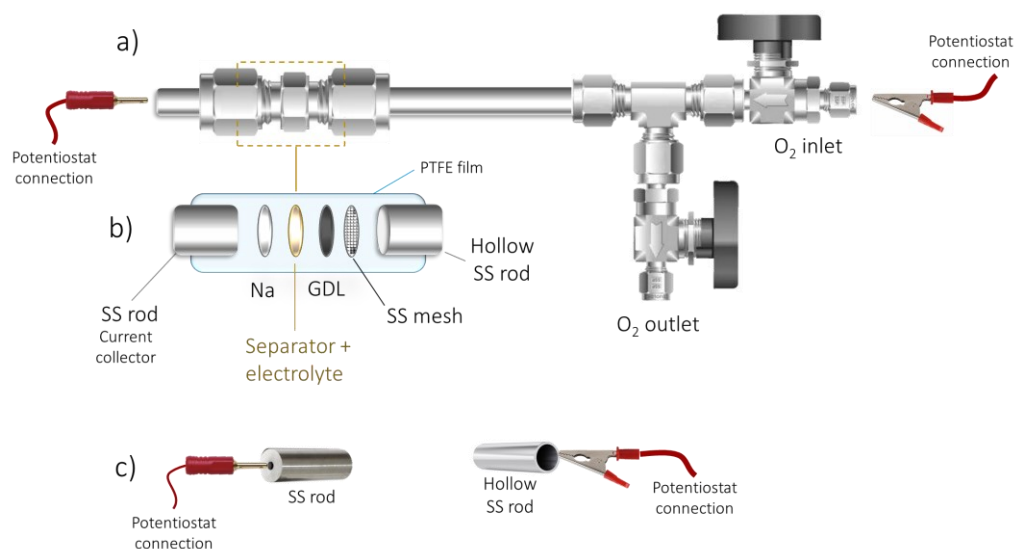


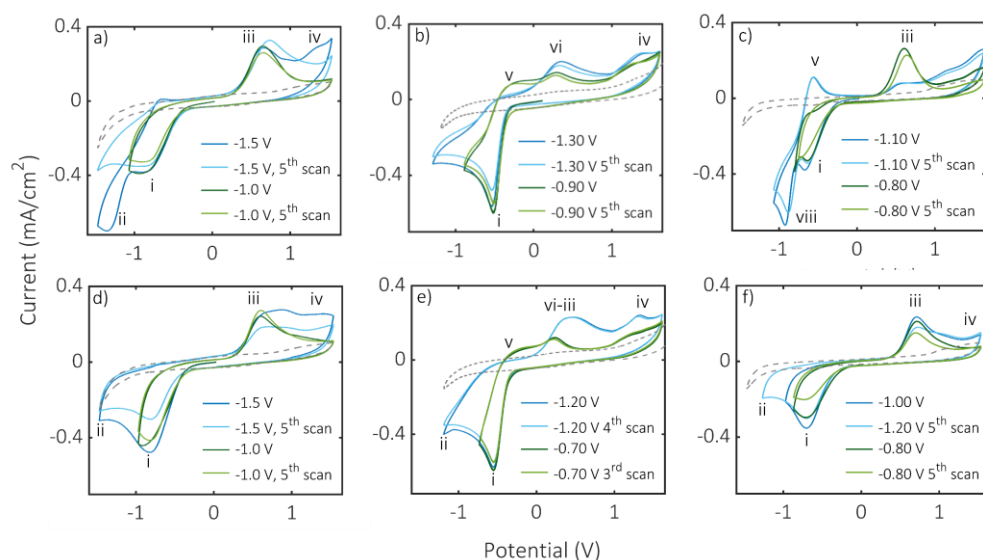
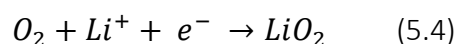
**Figure 5.1.** Na-O<sub>2</sub> cell showing (from left to right) the potentiostat connection to the SS rod current collector, the main cell body, the cell headspace, the O<sub>2</sub> outlet and inlet and the other potentiostat connection **(a)**; the exploded view of the interior of the cell showing the SS current collector, the Na electrode, glass fibre separator with electrolyte, GDL (O<sub>2</sub> electrode), stainless-steel mesh current collector and hollow SS rod current collector enclosed in the PTFE film **(b)**; and a magnified view of the cell connections to the potentiostat **(c)**;

### 5.3. Oxygen reduction reaction in the presence of alkali metal cations

Considering that the O<sub>2</sub> redox reaction in the presence of Li<sup>+</sup> is much more understood than the equivalent Na<sup>+</sup>/O<sub>2</sub> system, the O<sub>2</sub> redox reaction in the presence of alkali metal cations was initially studied with Li<sup>+</sup> salts in some ILs. The ORR was initially studied in the pyrrolidinium-based ILs in the presence of Li<sup>+</sup> cations, and the CVs are shown in Figure 5.2. It is evident that the addition of even small amounts of Li[NTf<sub>2</sub>] significantly changes the ORR in the ILs,

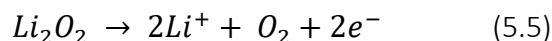
compared to the ORR in the neat ILs shown in the previous chapter (see Figure 4.3 in Chapter 4). Furthermore, Figure 5.2 clearly shows that the choice of IL affects the ORR, thus the shape of the CVs is different across the ILs. Therefore, each IL is briefly discussed individually.

Figure 5.2a shows the CV of  $O_2$ -saturated  $[C_1(C_2OC_1)Pyrr][NTf_2]$  with 25 mM  $Li[NTf_2]$ . The first scan with the more negative cathodic limit (dark blue trace) shows two reduction peaks named i and ii in the cathodic scan, and two oxidation peaks in the anodic scan, named iii and iv. The reduction peak i is attributed to  $O_2$  reduction and pairing with  $Li^+$ , forming  $LiO_2$  according to equation 5.4 below.<sup>48, 50, 52</sup>



**Figure 5.2.** CVs of  $O_2$ -saturated ILs with 25 mM  $Li^+$  (a-c) and 50 mM  $Li^+$  (d-e) showing the effect of  $Li^+$  salts in the ORR in a series of ILs: **a,d**)  $[C_1(C_2OC_1)Pyrr][NTf_2]$  (with  $Li[NTf_2]$ ), **b,e**)  $[C_1(C_2OC_1)Pyrr][C_2F_5COO]$  (with  $Li[CF_3COO]$ ) and **c,f**)  $[C_1C_{dma}Pyrr][NTf_2]$  (with  $Li[NTf_2]$ ). CVs taken using GC WE, Pt coil CE and Ag wire qRE, at 100 mV/s.

The very high charge density of  $Li^+$ , and consequently hard acid character does not form a stable compound with the softer base  $O_2^{\cdot-}$ .<sup>52, 153</sup> Thus, superoxide tends to disproportionate forming  $Li_2O_2$  (equation 5.2) which is then oxidised in peak iii.<sup>48, 52</sup>



A change in the cathodic limit to -1.0 V, so only reduction peak i is scanned (Figure 5.2a, green traces), leads to a single peak in the subsequent anodic scan, oxidation peak iii, corroborating the relation between reduction peak i and oxidation peak iii. Nevertheless, reduction peak ii is likely to be associated with further reduction of superoxide, forming  $\text{Li}_2\text{O}_2$  electrochemically. Alternatively, further superoxide reduction in the presence of trace water can lead to the formation of  $[\text{HO}_2]^-$ ,  $\text{H}_2\text{O}_2$  and  $[\text{OH}]^-$ .<sup>29, 44</sup> These species may then oxidise at more positive potentials, peak iv. However, these reactions do not seem to be persistent as shown by the lower current density of peak iv on the fifth scan (light blue traces).

An increase in the concentration of  $\text{Li}^+$  to 50 mM in  $[\text{C}_1(\text{C}_2\text{OC}_1)\text{Pyrr}][\text{NTf}_2]$  (Figure 5.2d) makes reduction peak ii less evident compared to the lower quantity of  $\text{Li}^+$  (25 mM, Figure 5.2a). This may suggest that most  $\text{O}_2^-$  forms  $\text{LiO}_2$  instead of undergoing further reduction. Furthermore, despite doubling  $\text{Li}^+$  concentration, the current density of the redox peaks increases ever so slightly. This is probably limited by the low  $\text{O}_2$  concentration ( $13.2 \times 10^{-6} \text{ mol/cm}^3$ ) in the electrolyte and poor rate of  $\text{O}_2$  diffusion ( $1.8 \times 10^{-6} \text{ cm}^2/\text{s}$ ). The  $\text{O}_2$  solubility and diffusion coefficients determined in Chapter 4 are shown in Table 5.2. Moreover, the insulating character of the ORR product  $\text{Li}_2\text{O}_2$  may limit the current developed at the electrode.

The CVs for the  $\text{O}_2$ -saturated  $[\text{C}_1(\text{C}_2\text{OC}_1)\text{Pyrr}][\text{C}_2\text{F}_5\text{COO}]$  with 25 mM  $\text{Li}^+$  are displayed in Figure 5.2b. The blue traces in Figure 5.2b shows the reduction peak i, and on the anodic scan the blue traces display oxidation peaks vi and iv. In addition, as the cathodic limit is made less negative (green traces in Figure 5.2b), peak v appears in the anodic scan, and the CV resembles the  $\text{O}_2$  CV in neat  $[\text{C}_1(\text{C}_2\text{OC}_1)\text{Pyrr}][\text{C}_2\text{F}_5\text{COO}]$  (shown and discussed in Chapter 4, Figure 4.3).

The oxidation peak vi has been previously associated with oxidation of  $\text{LiO}_2$ .<sup>48</sup> This is unexpected, considering the poor stability of  $\text{LiO}_2$ . Nevertheless, certain experimental conditions, such as solvent-solute interactions may stabilise  $\text{LiO}_2$  in solution. The  $[\text{C}_1(\text{C}_2\text{OC}_1)\text{Pyrr}][\text{C}_2\text{F}_5\text{COO}]$  IL has greater donating ability compared to the  $[\text{NTf}_2]$ -based ILs, as it is evident by the higher Gutmann

donor number (DN, see Table 5.2) and the Kamlet Taft parameter  $\beta$  (hydrogen bond donating ability) of equivalent ILs,<sup>66</sup>  $\beta = 0.95$  for [EMIM][Ac] and  $\beta = 0.28$  for [EMIM][NTf<sub>2</sub>]. Therefore, the [C<sub>2</sub>F<sub>5</sub>COO]<sup>-</sup> anion is likely to solvate Li<sup>+</sup> more strongly than the [NTf<sub>2</sub>]<sup>-</sup> anion. Thus, as a consequence of [C<sub>2</sub>F<sub>5</sub>COO]<sup>-</sup> solvation, it is possible that Li<sup>+</sup> becomes a softer base, the LiO<sub>2</sub> product becomes more stable in solution and chemical disproportionation happens to a lesser extent. In addition, Li<sup>+</sup> solvation by [C<sub>2</sub>F<sub>5</sub>COO]<sup>-</sup> can diminish the strong Lewis base character of Li<sup>+</sup>, hence superoxide can be stabilised by both Li<sup>+</sup> and IL-cation, as is evident from the presence of both oxidation peaks v and vi.

**Table 5.2.** Properties of ILs studied herein and O<sub>2</sub> transport parameters in the ILs: IL dynamic viscosity ( $\eta$ , in mPa.s), Gutmann donor number (DN), Kamlet Taft parameter ( $\beta$ ), O<sub>2</sub> solubility (in 10<sup>-6</sup> mol/cm<sup>3</sup>) and O<sub>2</sub> diffusion (in 10<sup>-6</sup> cm<sup>2</sup>/s).

IL	$\eta$ (mPa.s)	DN	O <sub>2</sub> solubility (10 <sup>-6</sup> mol/cm <sup>3</sup> )	O <sub>2</sub> diffusion (10 <sup>-6</sup> cm <sup>2</sup> /s)
[C <sub>1</sub> (C <sub>2</sub> OC <sub>1</sub> )Pyrr][NTf <sub>2</sub> ]	74	10.2	13.2	1.8
[C <sub>1</sub> (C <sub>2</sub> OC <sub>1</sub> )Pyrr][C <sub>2</sub> F <sub>5</sub> COO]	107	23.5	17.6	1.1
[C <sub>1</sub> C <sub>dma</sub> Pyrr][NTf <sub>2</sub> ]	120	8.0	3.6	3.0
[N <sub>C<sub>1</sub>,C<sub>1</sub>,C<sub>2</sub>,C<sub>2</sub>OC<sub>1</sub></sub> ][NTf <sub>2</sub> ]	63	9.1	3.8	5.0
[N <sub>C<sub>1</sub>,C<sub>1</sub>,C<sub>2</sub>,C<sub>4</sub></sub> ][NTf <sub>2</sub> ]	115	7.4	4.4	4.4

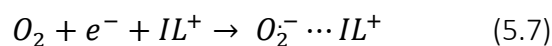
Upon increasing Li<sup>+</sup> concentration in [C<sub>1</sub>(C<sub>2</sub>OC<sub>1</sub>)Pyrr][C<sub>2</sub>F<sub>5</sub>COO] (Figure 5.2e), the oxidation peak vi seems to shift to more positive potentials towards peak iii, which is associated with Li<sub>2</sub>O<sub>2</sub> oxidation. Previous studies<sup>54, 55</sup> using molecular dynamics have described that at low salt concentration, the O<sub>2</sub><sup>-</sup> is found in a complex stabilised by both alkali metal cation and IL cation (Na<sup>+</sup> and [C<sub>1</sub>C<sub>4</sub>Pyrr]<sup>+</sup> in their study). However, with an increase in salt concentration, superoxide is preferentially stabilised by the alkali metal cation only. Thus, it is possible that with higher Li<sup>+</sup> concentration, O<sub>2</sub><sup>-</sup> is more likely to coordinate to Li<sup>+</sup>, forming LiO<sub>2</sub>. In addition, with higher Li<sup>+</sup> concentration, the stabilisation

effect of the  $[\text{C}_2\text{F}_5\text{COO}]^-$  anion is perhaps less pronounced,  $\text{Li}^+$  becomes more acidic and chemical disproportionation of  $\text{LiO}_2$  to  $\text{Li}_2\text{O}_2$  takes place.

Finally, Figure 5.2c shows the CVs of  $\text{O}_2$ -saturated  $[\text{C}_1\text{C}_{\text{dma}}\text{Pyrr}][\text{NTf}_2]$  in the presence of 25 mM  $\text{Li}^+$ . In the cathodic scan, the blue traces display two peaks, peak i and peak viii, whilst the anodic scan shows peak v and at more positive potentials a small peak iii. Reduction peak i is associated with  $\text{O}_2$  reduction and  $\text{LiO}_2$  formation as described by equation 5.4. Peak i is followed by reduction peak viii, which resembles  $\text{O}_2^{\cdot-}$  formation and stabilisation by IL cations, as studied in Chapter 4. The subsequent anodic scan shows the oxidation of the IL-stabilised  $\text{O}_2^{\cdot-}$  in peak v, and a small peak iii related to  $\text{Li}_2\text{O}_2$  oxidation. The significant presence of peaks viii and v implies that  $[\text{C}_1\text{C}_{\text{dma}}\text{Pyrr}][\text{NTf}_2]$  also displays a fine balance between  $\text{LiO}_2$  formation and  $\text{O}_2^{\cdot-}$  interaction with IL cation when scanning towards the more negative cathodic limit (-1.5 V). With -0.80 V cathodic limit, reduction peak i results in oxidation peak iii in the anodic scan, related to  $\text{LiO}_2$  formation and  $\text{Li}_2\text{O}_2$  oxidation, respectively. An increase in  $\text{Li}^+$  concentration in the  $[\text{C}_1\text{C}_{\text{dma}}\text{Pyrr}][\text{NTf}_2]$  IL (Figure 5.2f) eliminates any peaks associated with  $\text{O}_2^{\cdot-}$  stabilisation by IL cations (peaks viii and v) and the CVs bear a resemblance to  $[\text{C}_1(\text{C}_2\text{OC}_1)\text{Pyrr}][\text{NTf}_2]$  CVs with 50mM  $\text{Li}^+$ .

The ORR was also studied in the presence of  $\text{Na}^+$ , and the CVs are shown in Figure 5.3 and Figure 5.4. The reaction was initially studied in  $[\text{C}_1\text{C}_{\text{dma}}\text{Pyrr}][\text{NTf}_2]$  in the presence of 25 mM  $\text{Na}[\text{NTf}_2]$  in two different conditions, under normal ambient conditions (sealed flask at room temperature but outside glovebox, however, still using a dry  $\text{O}_2$  line as the gas source), and under controlled conditions within a glovebox. The CVs are displayed in Figure 5.3a and b, for the ambient and glovebox conditions, respectively. In both conditions, the CVs show the reduction peak i, followed by another reduction peak ii. On the anodic scan, both CVs show peak iii, but the CV in ambient conditions (Figure 5.3a) also display oxidation peaks iv and v. Peak i has been reported in literature<sup>46, 52, 54, 55</sup> to be associated with oxygen reduction and formation of  $\text{NaO}_2$  (equation 5.6 below), whilst the reduction peak ii is likely to

be simply superoxide reduction and stabilisation by IL cations (equation 5.7 below).<sup>46, 54</sup>



Regarding the oxidation peaks, when the reducing potential is limited to -0.70 V in the CV taken in ambient conditions (green traces in Figure 5.3c), the current associated with the oxidation peak iv significantly increases, and the oxidation peak iii disappears. When the cathodic limit is -0.70 V, the CV taken in the glovebox (Figure 5.3d, in green) shows oxidation peaks iv and v, but oxidation peak iii is absent. Therefore, oxidation peak iii is coupled with peak ii. Based on previous studies<sup>46, 54</sup> and on the results displayed in Chapter 4, these peaks can be associated with superoxide reduction and oxidation, stabilised by the  $[C_1C_{dma}Pyrr]^+$  cation. In addition, according to these observations and previous reports,<sup>46, 52, 54</sup> peak iv is related to the oxidation of  $NaO_2$ , the product of a one electron reduction of  $O_2$  and pairing with  $Na^+$  (peak i).

Figure 5.3a and b also show that the current density of peaks iv and v decreases over multiple scans or the peaks are not present at all with the more negative cathodic limits (blue traces). This is likely to be caused by a local decrease in concentration of the  $Na^+$  cations at the electrode surface, even though the bulk concentration of  $Na^+$  in the bulk (25 mM) is higher than the solubility of  $O_2$  in  $[C_1C_{dma}Pyrr][NTf_2]$  (see Table 5.2). As the concentration of  $Na^+$  drops at the electrode surface, superoxide is stabilised by the abundant IL cation, which explains the decrease in current of peak i, iv and v over scanning. Nevertheless, it is intriguing that with cathodic limit at -0.70 V, the oxidation peak iv has much higher current density in the CV taken under ambient conditions (Figure 5.3c) than in the CV taken in the glovebox (Figure 5.3d).

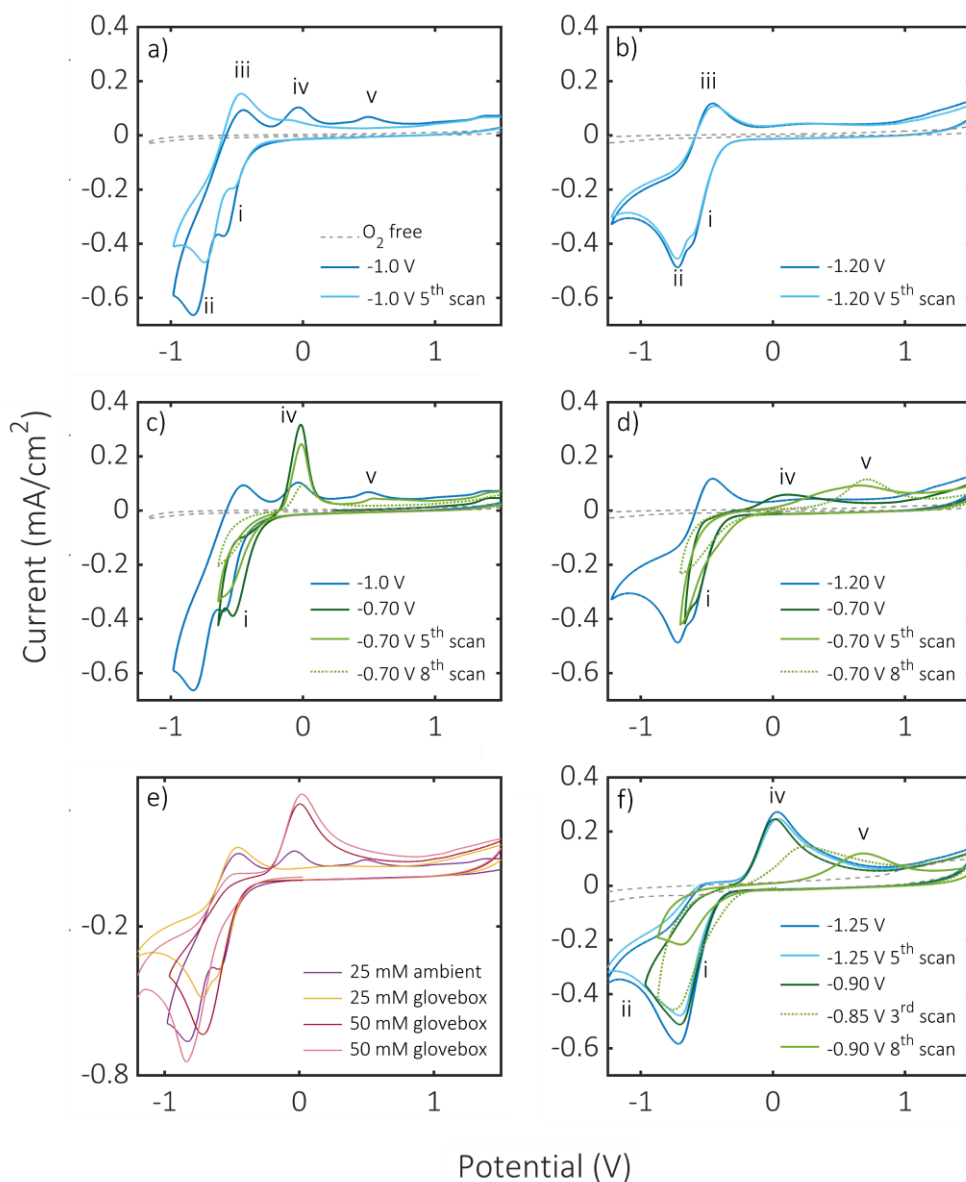


**Figure 5.3.** CVs of  $O_2$ -saturated  $[C_1C_{dma}Pyrr][NTf_2]$  with  $Na^+$  salts: a) in normal ambient conditions (outside glovebox) in the presence of 25 mM  $Na[NTf_2]$ , b) within a glovebox in the presence of 25 mM  $Na[NTf_2]$ , c) in normal ambient conditions in the presence of 25 mM  $Na[NTf_2]$  showing two cathodic limits, d) within a glovebox in the presence of 25 mM  $Na[NTf_2]$  showing two cathodic limits, e) overlap of 25 mM and 50 mM electrolytes showing first scan with the lowest cathodic limit within a glovebox, f) within a glovebox in the presence of 50 mM  $Na[NTf_2]$ . CVs taken with GC WE, Pt coil CE, Ag wire qRE at 100 mV/s.

Although great care has been taken to seal the electrochemical cell in the ambient condition experiment, it was observed that the water content increased from 22 ppm to 320 ppm during the period of the experiment. Thus,

the differences observed in the CVs are likely to be related to the water content in the IL. Higher water content decreases the viscosity of the IL, which can increase the diffusion of active species towards the electrode. This may explain, for example, the higher current shown by the blue traces in Figure 5.3a compared to Figure 5.3b. Furthermore, previous studies<sup>20, 163</sup> have evaluated the role of water as a phase transfer catalyst. Xia *et al*<sup>163</sup> suggested that water-spiked electrolytes have led the formation of HO<sub>2</sub> as a reaction intermediate, which in the presence of Na<sup>+</sup> leads to NaO<sub>2</sub>. Based on these reports, it is possible that in [C<sub>1</sub>C<sub>dma</sub>Pyrr][NTf<sub>2</sub>], the higher water content promotes the formation of NaO<sub>2</sub>, given the greater current associated with the oxidation of NaO<sub>2</sub>. This may either be due to NaO<sub>2</sub> formation via HO<sub>2</sub> or simply due to an enhancement of Na<sup>+</sup> diffusion in a wetter IL.

The ORR in [C<sub>1</sub>C<sub>dma</sub>Pyrr][NTf<sub>2</sub>] was also evaluated in the glovebox in the presence of 50 mM Na<sup>+</sup> (Figure 5.3f). An overlay of the CVs with 25 mM Na<sup>+</sup> taken in and outside the glovebox, and the CV with 50 mM Na<sup>+</sup> (Figure 5.3c) corroborates the assignment of peak iv and v to the oxidation of Na-related products, as peak iv significantly increases with the higher Na<sup>+</sup> concentration. Furthermore, the reduction peaks i and ii seem to be replaced by one single reduction peak named simply peak i, associated with superoxide reduction and NaO<sub>2</sub> formation. Interestingly, with 50 mM Na<sup>+</sup> and cathodic limit of -1.25 V, no major changes can be observed in the CV over scanning. However, with a cathodic limit less negative, as shown by the green traces in Figure 5.3f, there is a clear shift of the oxidation peak iv towards peak v. This shift has also been observed with 25 mM Na<sup>+</sup> in the CV taken in the glovebox (Figure 5.3d), and peak v is also present in the first scan of the CV in ambient condition (Figure 5.3a). Considering that these shifts are observed over multiple scans, the electrode surface is no longer pristine, and it is possible the electrode surface contains any remaining NaO<sub>2</sub> that was not oxidised in the previous cycle. This can alter the formation of NaO<sub>2</sub> in the following cycle, affecting the CVs.

A previous study on the O<sub>2</sub> reduction in [EMIM][NTf<sub>2</sub>] in the presence of 25 mM Na[PF<sub>6</sub>] suggested that the second oxidation peak at more positive

potentials is associated with  $\text{Na}_2\text{O}_2$  oxidation, which the authors suggest to be formed via chemical disproportionation.<sup>52</sup> As discussed above, this has been previously observed in  $\text{Li}^+/\text{O}_2$  systems,<sup>164</sup> and  $\text{Li}_2\text{O}_2$  is now established as the main product of the ORR in the presence of  $\text{Li}^+$ .<sup>5</sup> This has been assigned to the instability of the  $\text{LiO}_2$  product. However, this is not the case for  $\text{NaO}_2$ , in fact,  $\text{NaO}_2$  is the main discharge product found by several reports in a  $\text{Na-O}_2$  cell,<sup>154</sup> despite  $\text{Na}_2\text{O}_2$  being slightly more thermodynamic stable. Some reports attributed the  $\text{NaO}_2$  formation to its lower surface energy, whilst others suggested  $\text{NaO}_2$  is the kinetically favoured product.<sup>154</sup> Considering that  $\text{NaO}_2$  is kinetically favoured, and that peak v is more noticeable at later scans, peak v could perhaps be attributed to  $\text{Na}_2\text{O}_2$  oxidation following  $\text{NaO}_2$  disproportionation as suggested by Allen et al.<sup>52</sup> However *in-situ* measurements would be needed to confirm such a hypothesis given the differences of IL and  $\text{Na}^+$  salt in their study ( $\text{Na}[\text{PF}_6]$  in  $[\text{C}_2\text{C}_1\text{Im}][\text{NTf}_2]$ ) and ours ( $\text{Na}[\text{NTf}_2]$  in  $[\text{C}_1\text{C}_{\text{dma}}\text{Pyrr}][\text{NTf}_2]$ ). Alternatively,  $\text{Na}_2\text{O}_2$  could have been formed electrochemically, given the similar standard potentials for  $\text{NaO}_2$  and  $\text{Na}_2\text{O}_2$ .<sup>26</sup>

Interestingly, another study on the ORR in  $[\text{C}_1\text{C}_4\text{Pyrr}][\text{NTf}_2]$  in the presence of various  $\text{Na}[\text{NTf}_2]$  concentrations observed a shift in the opposite direction to ours (towards less positive potentials, as opposed to more positive potentials in our case - see Figure 5.4f).<sup>53</sup> The authors assigned the peaks at more positive potentials (as peak v) to oxidation of  $\text{NaO}_2$  species at the electrode surface, whilst peaks at less positive potentials (as peak iv) to oxidation of  $\text{NaO}_2$  species in solution. Consequently, the shift towards less positive potentials is described as the dissolution of  $\text{NaO}_2$  species from the surface. Another study using  $\text{Na}[\text{PF}_6]$  in DME demonstrated using operando transmission electronic microscopy that under those electrolyte conditions  $\text{NaO}_2$  formation follows a solution pathway.<sup>27</sup> According to the authors,  $\text{NaO}_2$  is formed in solution and as the electrolyte becomes saturated,  $\text{NaO}_2$  precipitates in a cubic form.<sup>27</sup> This solution/surface hypothesis will be further investigated in Section 5.3.1, with RRDE experiments.

Figure 5.4 shows the ORR in the presence of  $\text{Na}^+$  in the  $[\text{C}_1(\text{C}_2\text{OC}_1)\text{Pyrr}][\text{NTf}_2]$  (Figure 5.4a, c and e) and  $[\text{N}_{\text{C}_1,\text{C}_1,\text{C}_2,(\text{C}_2\text{OC}_1)}][\text{NTf}_2]$  (Figure 5.4b, d and f). The ORR in the presence of 25 mM  $\text{Na}^+$  in  $[\text{C}_1(\text{C}_2\text{OC}_1)\text{Pyrr}][\text{NTf}_2]$  and  $[\text{N}_{\text{C}_1,\text{C}_1,\text{C}_2,(\text{C}_2\text{OC}_1)}][\text{NTf}_2]$  show a slight pre-peak i, followed by peak ii in the cathodic scan. Unlike in  $[\text{C}_1\text{C}_{\text{dma}}\text{Pyrr}][\text{NTf}_2]$ , in  $[\text{C}_1(\text{C}_2\text{OC}_1)\text{Pyrr}][\text{NTf}_2]$  the ORR in the presence of 25 mM  $\text{Na}^+$  does not result in the oxidation peak iii (Figure 5.3b), associated with the superoxide formation and stabilisation by the IL cation. Instead, the CV in  $[\text{C}_1(\text{C}_2\text{OC}_1)\text{Pyrr}][\text{NTf}_2]$  shows clear oxidation peaks v and vi, the former linked to  $\text{Na}_x\text{O}_y$  oxidation and the latter likely to be related to oxidation of  $\text{H}_2\text{O}_2$  or  $[\text{OH}]^-$ , formed in the presence of trace water.<sup>29, 44</sup> In the presence of 25 mM  $\text{Na}^+$  the CV of ORR in  $[\text{N}_{\text{C}_1,\text{C}_1,\text{C}_2,(\text{C}_2\text{OC}_1)}][\text{NTf}_2]$  (Figure 5.4b) shows the oxidation peak v in the first anodic scan. However, with -1.4 V cathodic limit, the current density of peak v decreases over time and peak iii can be observed in later scans (compare dark and light blue traces in Figure 5.4b). This is associated with a drop in the local  $\text{Na}^+$  concentration and superoxide stabilisation by IL cation, as already discussed previously for  $[\text{C}_1\text{C}_{\text{dma}}\text{Pyrr}][\text{NTf}_2]$ .

By adding 50 mM of  $\text{Na}[\text{NTf}_2]$ , the CVs for both  $[\text{C}_1(\text{C}_2\text{OC}_1)\text{Pyrr}][\text{NTf}_2]$  and  $[\text{N}_{\text{C}_1,\text{C}_1,\text{C}_2,(\text{C}_2\text{OC}_1)}][\text{NTf}_2]$  (Figure 5.4c and d, respectively) display a greater distinction between reduction peaks i and ii. Moreover, they feature a new oxidation peak, peak iv, that was not present in the 25 mM CVs. As discussed for  $[\text{C}_1\text{C}_{\text{dma}}\text{Pyrr}][\text{NTf}_2]$ , this peak is associated with oxidation of  $\text{NaO}_2$ . Figure 5.4c shows that in  $[\text{C}_1(\text{C}_2\text{OC}_1)\text{Pyrr}][\text{NTf}_2]$ , regardless of the cathodic limit (either -1.3 or -0.9 V), two oxidation peaks (iv and v) are present in the anodic scan. Moreover, independently of the cathodic limit, the current density of oxidation peak iv decreases over time, and only the oxidation peak v is observed on the fifth scan. As discussed above for  $[\text{C}_1\text{C}_{\text{dma}}\text{Pyrr}][\text{NTf}_2]$ , peak v might be associated with oxidation of insoluble  $\text{Na}_x\text{O}_y$  species at the electrode surface. The solubility of the reduction product will be investigated in Section 5.3.1. Nevertheless, this shift is not observed in the CVs with  $[\text{N}_{\text{C}_1,\text{C}_1,\text{C}_2,(\text{C}_2\text{OC}_1)}][\text{NTf}_2]$ , as shown in Figure 5.4d.

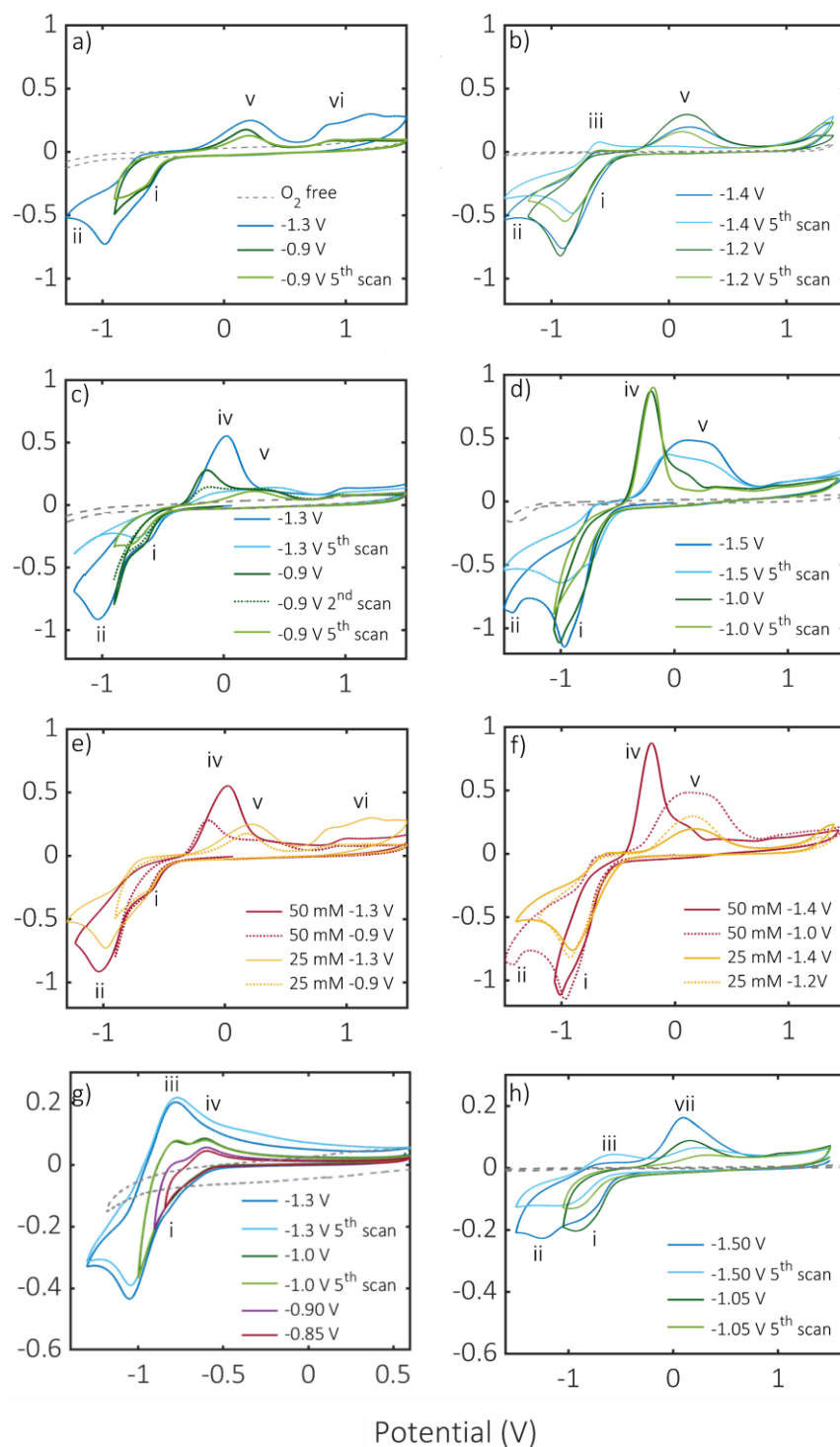


**Figure 5.4.** CVs of  $\text{O}_2$ -saturated ILs with  $\text{Na}^+$  salts taken within a glovebox: **a, c**)  $[\text{C}_1(\text{C}_2\text{OC}_1)\text{Pyrr}][\text{NTf}_2]$  with 25 mM and 50 mM  $\text{Na}[\text{NTf}_2]$  respectively, and **e**) shows an overlay of **a** and **c**. **b, d**)  $[\text{N}_{\text{C}_1,\text{C}_1,\text{C}_2,(\text{C}_2\text{OC}_1)}][\text{NTf}_2]$  with 25 mM and 50 mM  $\text{Na}[\text{NTf}_2]$ , respectively, and **f**) displays an overlay of **b** and **d**. **g**)  $[\text{C}_1(\text{C}_2\text{OC}_1)\text{Pyrr}][\text{C}_2\text{F}_5\text{COO}]$  with 50 mM  $\text{Na}[\text{NTf}_2]$  and **h**)  $[\text{N}_{\text{C}_1,\text{C}_1,\text{C}_2,\text{C}_4}][\text{NTf}_2]$  with 50 mM  $\text{Na}[\text{NTf}_2]$ . CVs taken with GC WE, Pt coil CE and Ag wire qRE at 100 mV/s.

Figure 5.4d shows that in  $[N_{C_1, C_1, C_2, (C_2OC_1)}][NTf_2]$ , when the cathodic limit is -1.5 V, the  $O_2$  CVs in the presence of 50 mM  $Na^+$  CVs show a broad oxidation peak, which seems almost as an overlap of oxidation peaks iv and v. This may be a consequence of the wide cathodic limit causing the formation of a combination of  $Na_xO_y$  products. As a result, the oxidation peaks are poorly defined. With -1.0 V cathodic limit (green traces in Figure 5.4d), both peaks i and iv are very noticeable, and only subtle differences between the first and the fifth scan can be observed. Furthermore, the absence of peak v when the cathodic limit is -1.0 V suggests that in  $[N_{C_1, C_1, C_2, (C_2OC_1)}][NTf_2]$ , the species oxidised in peak v are formed in the cathodic scan with more negative potentials.

The ORR was also evaluated in  $[C_1(C_2OC_1)Pyrr][C_2F_5COO]$  with 50mM  $Na^+$  and the CVs are shown in Figure 5.4g. When the cathodic limit is -1.3 V (blue traces), the CV displays a single reduction peak, and the oxidation peak iii on the anodic scan. Despite the CVs with cathodic limit at -1.3 V not displaying any other clear oxidation events, by changing the cathodic limit to -0.9 V, an extra small oxidation peak iv can be observed, which is probably overlaid with peak iii in the blue CVs (-1.3 V cathodic limit). Moreover, Figure 5.4g shows that as the cathodic limit is changed, it becomes evident that the anodic peak iv is related to the reduction peak i, and this redox couple is likely to be associated with reduction of  $O_2$  and formation of  $NaO_2$  (peak i), followed by oxidation of the latter in peak iv. However, this IL system displays a very distinct CV compared to any of the ILs previously discussed, and this is explained as follows. As briefly discussed above for Figure 5.2b, the  $[C_1(C_2OC_1)Pyrr][C_2F_5COO]$  IL has a much greater donating ability than the other  $[NTf_2]^-$  based ILs. Therefore, it is expected that the  $Na^+$  is more strongly coordinated to the  $[C_2F_5COO]^-$  anion, and consequently, it becomes a softer cation. Thus, the  $[C_2F_5COO]^-$  solvation may change the activity of  $Na^+$  and as a result, may alter the reaction potentials as suggested by the Nernst equation. This explains the overlap of  $O_2$  reduction and formation of  $NaO_2$  and reduction and formation of  $O_2^-$  stabilised by IL cation, as well as the overlap of the oxidation peaks.

Finally, the O<sub>2</sub> CVs in [N<sub>C<sub>1</sub>,C<sub>1</sub>,C<sub>2</sub>,C<sub>4</sub></sub>][NTf<sub>2</sub>] with 50mM (Figure 5.4h) shows the typical reduction peak i, followed by the reduction peak ii, associated with the reactions described in the previous paragraphs. On the anodic scan, the same oxidation peak vii is observed regardless of the cathodic limit, which is associated with Na<sub>x</sub>O<sub>y</sub> species. It is clear that with -1.5 V reduction limit, by the fifth scan, the oxidation peak vii significantly reduces, and the oxidation peak iii appears, associated with the oxidation of IL cation-stabilised O<sub>2</sub><sup>-</sup>. As discussed for [C<sub>1</sub>C<sub>dma</sub>Pyrr][NTf<sub>2</sub>], this is likely to be caused by a drop in the local concentration of Na<sup>+</sup> at the electrode surface in this IL.

Finally, it has been observed that, in contrast to the Li<sup>+</sup> systems, where the variations in the CVs could be clearly associated with the choice of anion, in the Na<sup>+</sup> systems many differences are observed, even among ILs with very similar structure such as [C<sub>1</sub>(C<sub>2</sub>OC<sub>1</sub>)Pyrr][NTf<sub>2</sub>] and [N<sub>C<sub>1</sub>,C<sub>1</sub>,C<sub>2</sub>,C<sub>2</sub>,C<sub>2</sub>OC<sub>1</sub></sub>][NTf<sub>2</sub>], or [C<sub>1</sub>C<sub>dma</sub>Pyrr][NTf<sub>2</sub>] and [C<sub>1</sub>(C<sub>2</sub>OC<sub>1</sub>)Pyrr][NTf<sub>2</sub>]. Thus, these Na<sup>+</sup>/IL systems are further explored with higher Na<sup>+</sup> content, and the type of product formed during the CVs is investigated with RRDE.

Figure 5.5 shows the CVs of O<sub>2</sub>-saturated pyrrolidinium-based ILs in the presence of 0.5 M Na[NTf<sub>2</sub>]. The equivalent CVs for [N<sub>C<sub>1</sub>,C<sub>1</sub>,C<sub>2</sub>,C<sub>2</sub>,C<sub>2</sub>OC<sub>1</sub></sub>][NTf<sub>2</sub>] and [N<sub>C<sub>1</sub>,C<sub>1</sub>,C<sub>2</sub>,C<sub>4</sub></sub>][NTf<sub>2</sub>] are displayed in Figure 5.6. With the exception of [C<sub>1</sub>(C<sub>2</sub>OC<sub>1</sub>)Pyrr][C<sub>2</sub>F<sub>5</sub>COO] (Figure 5.5c and d), all the O<sub>2</sub> CVs with 0.5 M Na<sup>+</sup> show a single reduction and a single oxidation peak, regardless of the cathodic limit used.

An overlay of the CVs with 50 mM Na<sup>+</sup> and 0.5 M Na<sup>+</sup> is shown on the right hand side of Figure 5.5 and Figure 5.6. An analysis of these overlays highlights two main points, firstly the current density of the reduction peaks decreases considerably with the higher salt concentration, with the exception of [N<sub>C<sub>1</sub>,C<sub>1</sub>,C<sub>2</sub>,C<sub>4</sub></sub>][NTf<sub>2</sub>] and [C<sub>1</sub>(C<sub>2</sub>OC<sub>1</sub>)Pyrr][C<sub>2</sub>F<sub>5</sub>COO]. Secondly, the oxidation peak in the CVs with 0.5 M is at potentials similar to those found for peak v in the 50 mM Na<sup>+</sup> CVs. This may indicate formation of insoluble Na<sub>x</sub>O<sub>y</sub> species, as

discussed previously for peak  $v$  in the 50 mM  $\text{Na}^+$  CVs, and it will be further discussed in Section 5.3.1.

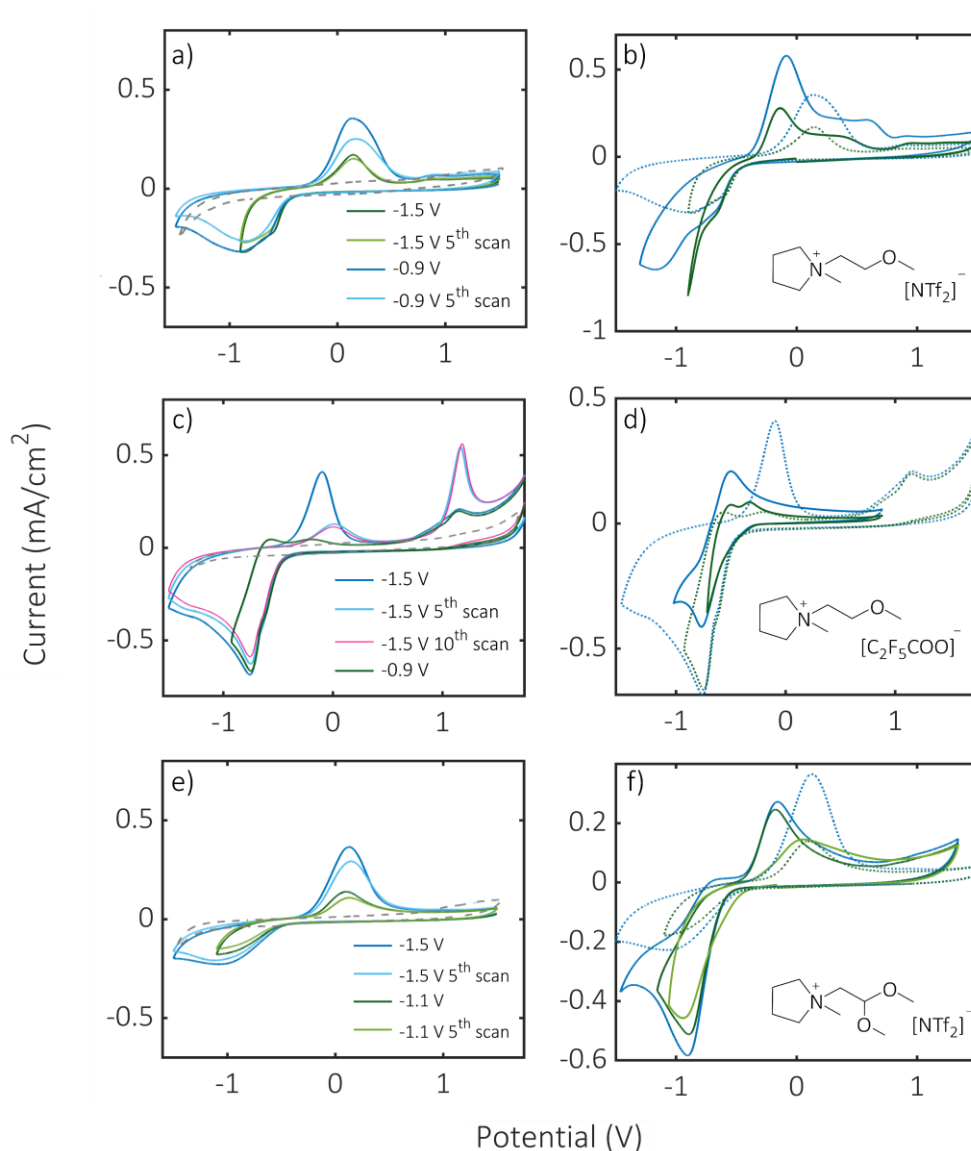


**Figure 5.5.** CV of  $\text{O}_2$ -saturated ILEs in the presence of 0.5 M  $\text{Na}[\text{NTf}_2]$  showing multiple scans and cathodic limits on the left (a, c and e), and an overlay of CVs taken in ILEs with 0.5 M  $\text{Na}^+$  (dashed lines) and 50 mM  $\text{Na}^+$  (continuous line) on the right (b, d and f). a,b)  $[\text{C}_1(\text{C}_2\text{OC}_1)\text{Pyrr}][\text{NTf}_2]$ ; c,d)  $[\text{C}_1(\text{C}_2\text{OC}_1)\text{Pyrr}][\text{C}_2\text{F}_5\text{COO}]$ ; e,f)  $[\text{C}_1\text{C}_{\text{dma}}\text{Pyrr}][\text{NTf}_2]$ . Note that b), d) and f) have different y-axis scales. CVs taken using GC WE, Pt coil CE and Ag wire qRE at 100 mV/s.

Regarding the current density, the addition of higher concentration of  $\text{Na}^+$  salts induces significant changes in the physico-chemical properties of the electrolytes, thus affecting solubility and mass transport within the liquid.

Azaceta *et al*<sup>53</sup> observed that the greater the salt content in the electrolyte, the greater the viscosity, and the lower the solubility of O<sub>2</sub> in the electrolyte. This may explain the decrease in current density observed in some of the electrolytes. In addition, it is possible that with higher Na<sup>+</sup> concentration, more insulating product is formed at the electrode surface, partially blocking it.

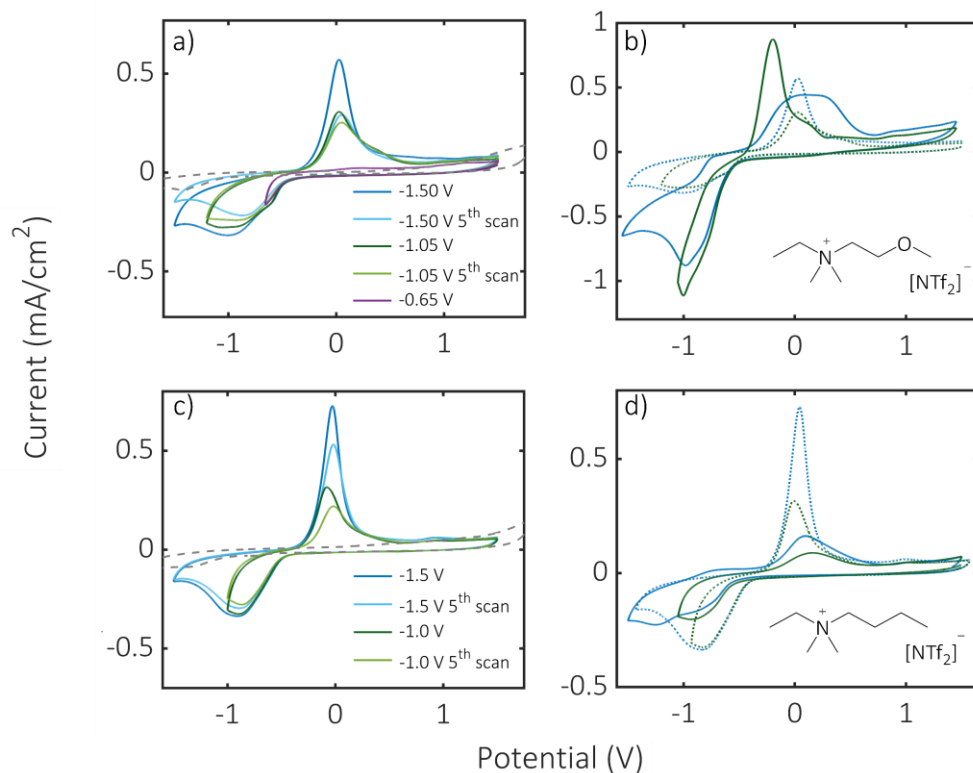


**Figure 5.6.** CV of O<sub>2</sub>-saturated ILs in the presence of 0.5 M Na[NTf<sub>2</sub>] showing multiple scans and cathodic limits on the left (a and c), and an overlay of CVs taken in ILs with 0.5 M Na[NTf<sub>2</sub>] (dashed lines) and 50 mM Na[NTf<sub>2</sub>] (continuous line) on the right (b and d). a,b) [N<sub>C<sub>1</sub>,C<sub>1</sub>,C<sub>2</sub>,C<sub>2</sub>OC<sub>1</sub>][NTf<sub>2</sub>]; c,d) [N<sub>C<sub>1</sub>,C<sub>1</sub>,C<sub>2</sub>,C<sub>4</sub>][NTf<sub>2</sub>]. Note that b) and d) have different y-axis scales.</sub></sub>

Furthermore, regarding the CV with [C<sub>1</sub>(C<sub>2</sub>OC<sub>1</sub>)Pyrr][C<sub>2</sub>F<sub>5</sub>COO], Figure 5.5c shows that an oxidation peak at approximately +1.1 V appears during cycling as the oxidation peak at -0.1 V fades, whilst the reduction peak shows very subtle changes over scanning. This is likely to be associated with an EC mechanism, in which the chemically formed species are oxidised at the more positive potentials. Thus this may be related to oxidation of products from side

reactions of  $O_2^-$  with water.<sup>29, 44</sup> The higher hydrophilicity of this IL means it is more likely to accumulate water than the other [NTf<sub>2</sub>]-based ILs.

### 5.3.1 Hydrodynamic voltammetry to investigate the type of ORR product in the presence of Na<sup>+</sup> salts

The type of product, in terms of product in solution, or product at the electrode surface, was examined with RRDE. A full description of RRDE can be found in Chapter 2. In summary, in a voltammetric experiment using RRDE, the disc potential can be swept within a range of potentials, as a typical linear sweep voltammetry or cyclic voltammetry. The ring potential can be kept constant at a certain potential that reduces or oxidises the species in solution which has just been formed at the disc, providing those species are stable within the time they take to move from the disc towards the ring. However, no current will be detected at the ring if the reaction product adheres to the disc electrode surface.

Figure 5.7 shows the O<sub>2</sub> voltammograms for the experiments using RRDE in ILs with 50 mM Na<sup>+</sup>. Different cathodic limits were chosen to understand the nature (in solution or at the electrode surface) of the product formed at different reduction potentials. Due to the use of a quasi-reference electrode, the cathodic limits cannot be kept the same for all ILs because of the variation in the potential of the ORR within the ILs. To simplify the analysis, the cathodic sweep is shown in Figure 5.7a, d, g and j (figures in the column on the left), whilst both sweeps are displayed in Figure 5.7b, e, h and q (figures in the middle column). The disc current response is shown in continuous lines and the ring current response in dashed lines.

Figure 5.7a, d, g and j (figures in the column on the left) display the O<sub>2</sub> reduction and formation of Na<sub>x</sub>O<sub>y</sub> species in the disc and the oxidation of the soluble Na<sub>x</sub>O<sub>y</sub> in the ring. In addition to these peaks, Figure 5.7b, e, h and q (figures in the middle column) also show the oxidation of Na<sub>x</sub>O<sub>y</sub> species at the disc surface in the anodic scan.

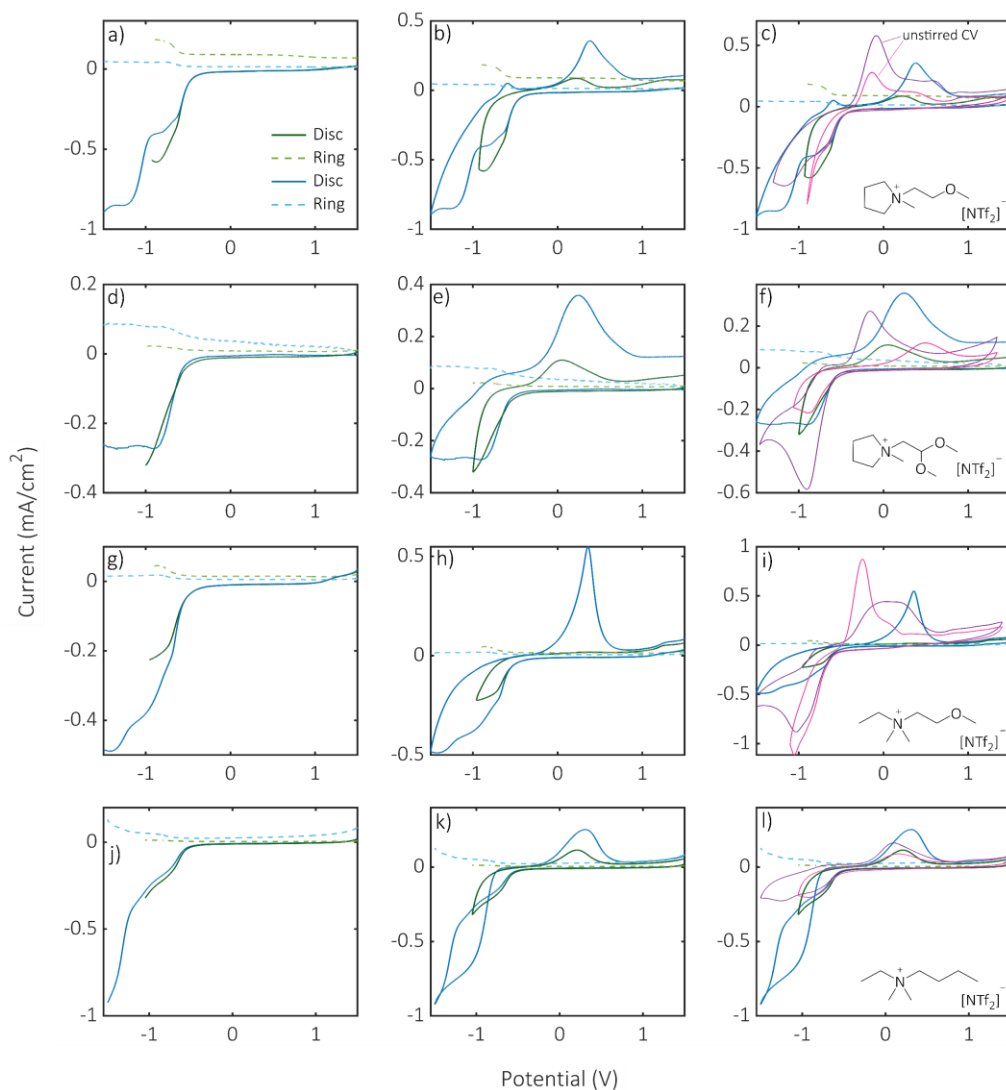


**Figure 5.7.** RRDE LSVs and CVs of O<sub>2</sub>-saturated ILs with 50 mM Na<sup>+</sup> showing the more negative cathodic limits (in blue) and the less negative cathodic limit (green), the disc electrode current (continuous line) and the ring current (dashed line). **c, f, i, and l** show an overlay of the RRDE CVs with the unstirred CVs (in purple and pink) from Figure 5.3f and Figure 5.4c, **d and h**, respectively. **a, b and c** [C<sub>1</sub>(C<sub>2</sub>OC<sub>1</sub>)Pyrr][NTf<sub>2</sub>]; **d, e, and f** [C<sub>1</sub>C<sub>dma</sub>Pyrr][NTf<sub>2</sub>]; **g, h, and i** [N<sub>C<sub>1</sub>,C<sub>1</sub>,C<sub>2</sub>,C<sub>2</sub>OC<sub>1</sub>][NTf<sub>2</sub>]; **j, k and l** [N<sub>C<sub>1</sub>,C<sub>1</sub>,C<sub>2</sub>,C<sub>4</sub>][NTf<sub>2</sub>]. The hydrodynamic CVs were taken with RRDE WE composed of GC disc and Pt ring, Pt coil CE and Aq wire qRE at 100 mV/s. The unstirred CVs were taken with the same conditions but using a GC WE. Different cathodic limits were chosen for each IL according to the reduction peaks observed.</sub></sub>

The ring currents are analysed and compared to the disc current for each IL in each cathodic limit, and these are summarised in Table 5.3. The ring current

analysis shown in Table 5.3 for  $[C_1C_{\text{dma}}\text{Pyrr}][\text{NTf}_2]$  (Figure 5.7d and e) shows that with -1.5 V cathodic limit, the percentage of ring current is considerably higher than when the cathodic limit is -1.0 V. This indicates that the reduction product formed with the more negative cathodic limit displays greater solubility in  $[C_1C_{\text{dma}}\text{Pyrr}][\text{NTf}_2]$  than the product formed within the less negative cathodic limit. Comparing this finding to the unstirred CV shown in Figure 5.3f, it is possible that the higher solubility of the reduction product formed within the wider cathodic scan (-1.5 V limit) contributes to the apparent stability of the redox couple. This apparent stability is suggested based on the almost identical shape and current density of the peaks in the first and fifth scans (dark and light blue traces) in the CV in Figure 5.3f.

The ring current analysis for  $[C_1(C_2OC_1)\text{Pyrr}][\text{NTf}_2]$  (Figure 5.7a and b) and  $[N_{C_1,C_1,C_2,(C_2OC_1)}][\text{NTf}_2]$  (Figure 5.7g and h) in Table 5.3 shows the opposite trend observed in  $[C_1C_{\text{dma}}\text{Pyrr}][\text{NTf}_2]$ . In other words, in  $[N_{C_1,C_1,C_2,(C_2OC_1)}][\text{NTf}_2]$  and  $[C_1(C_2OC_1)\text{Pyrr}][\text{NTf}_2]$  the higher apparent solubility was found for the products formed within the narrower cathodic scan, considering the higher percentual current with less negative cathodic limits. The unstirred CV of these ILs displayed in the previous section have in fact demonstrated different trends than  $[C_1C_{\text{dma}}\text{Pyrr}][\text{NTf}_2]$  (compare Figure 5.4c and d with Figure 5.3).

Overlays of the CVs taken with RRDE and the unstirred CVs (from Figure 5.3f and Figure 5.4) are shown in Figure 5.7c, f, i and l. These overlays clarify some points of discussion from the previous section. As described before, soluble products from the disc electrode reaction on the forward scan move away from the disc as the electrode rotates, whilst insoluble products remain at the disc electrode and are detected on the backwards scan. The overlays in Figure 5.7 show that the oxidation peak (disc current) in the anodic scan of RRDE experiments overlaps with oxidation peak v of the unstirred CVs (see Figure 5.3f, Figure 5.4c, d and h). This confirms the hypothesis discussed above, that peak v is associated with oxidation of  $\text{Na}_x\text{O}_y$  adsorbed at the electrode surface, whilst peak iv is associated with oxidation of soluble  $\text{NaO}_2$ . Further *in-situ* analysis is needed to determine the nature of the  $\text{Na}_x\text{O}_y$  species, however the shifts of peak

iv to peak v observed in the CVs in the previous section can be explained as follows. The shift observed from peak iv to peak v in  $[C_1C_{dma}Pyrr][NTf_2]$  and  $[C_1(C_2OC_1)Pyrr][NTf_2]$  may be linked to a local saturation of soluble  $NaO_2$ , which is followed by precipitation at the electrode surface and oxidation at more positive potentials (peak v). Alternatively,  $NaO_2$  undergoes chemical disproportionation and the insoluble  $Na_2O_2$  is oxidised at more positive potentials, in peak v.

**Table 5.3.** RRDE experiments analysis of ILs with 50 mM  $Na^+$  showing the percentual of the ring current with relation to the disc current for each cathodic limit. The choice of cathodic limit is based on the potential associated with the reduction peaks observed in the CVs (Figure 5.3, Figure 5.4 and Figure 5.7).

IL / $Na^+$ system (50 mM)	Cathodic limit (V)	% ( $i_{ring}/i_{disc}$ )
$[C_1(C_2OC_1)Pyrr][NTf_2]$	-0.9	17.0
	-1.5	3.8
$[C_1C_{dma}Pyrr][NTf_2]$	-1	4.5
	-1.5	25.4
$[N_{C_1,C_1,C_2,(C_2OC_1)}][NTf_2]$	-1.2	12.9
	-1.4	2.6
$[N_{C_1,C_1,C_2,C_4}][NTf_2]$	-1	2.9
	-1.5	10.7

$[N_{C_1,C_1,C_2,C_4}][NTf_2]$  shows slightly higher  $NaO_2$  solubility when the cathodic limit is -1.5 V, compared to -1.0 V. This may be related to the fact that superoxide stabilisation by IL cation could still be observed in  $[N_{C_1,C_1,C_2,C_4}][NTf_2]$ , even at 0.5 M  $Na^+$  concentration. This is demonstrated by peak iii in Figure 5.4h.

RRDE experiments were also performed with the ILs containing 0.5 M  $Na^+$  and the LSVs, CVs and an overlay with the unstirred CVs are shown in Figure 5.8. An analysis of the ring currents for the data shown in Figure 5.8 is displayed in Table 5.4.

## Chapter 5

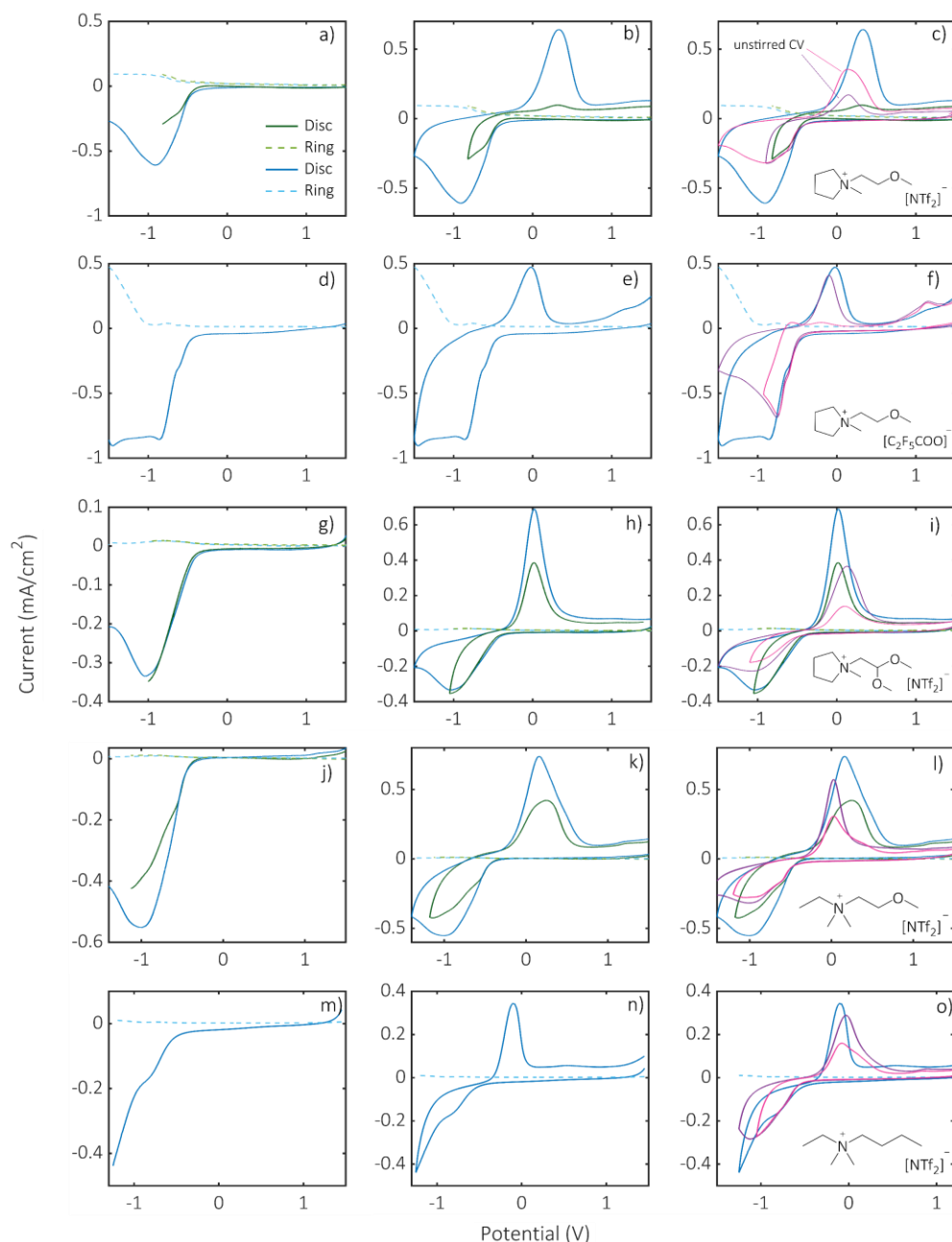


**Figure 5.8.** RRDE LSVs and CVs of  $O_2$ -saturated ILs with 0.5 M  $Na^+$  showing the more negative cathodic limits (in blue) and the less negative cathodic limit (green), the disc electrode current (continuous line) and the ring current (dashed line). **c, f, i, l and o** show an overlay of the RRDE CVs with the unstirred CVs (in purple and pink) from Figure 5.5a, c and e, and Figure 5.6a and c, respectively. The ring potential is stated within brackets: **a, b and c**  $[C_1(C_2OC_1)Pyrr][NTf_2]$ ; **d, e, and f**  $[C_1(C_2OC_1)Pyrr][C_2F_5COO]$  (+0.4 V); **g, h, and i**  $[C_1C_{dma}Pyrr][NTf_2]$ ; **j, k and l**  $[N_{C_1,C_1,C_2,(C_2OC_1)}][NTf_2]$ ; **m, n and o**  $[N_{C_1,C_1,C_2,C_4}][NTf_2]$ . The hydrodynamic CVs were taken with RRDE WE composed of GC disc and Pt ring, Pt coil CE and Aq wire qRE at 100 mV/s. The unstirred CVs were taken with the same conditions but using a GC WE.

The RRDE data in Figure 5.8g-o for  $[N_{C_1,C_1,C_2,(C_2OC_1)}][NTf_2]$ ,  $[N_{C_1,C_1,C_2,C_4}][NTf_2]$  and  $[C_1C_{dma}Pyrr][NTf_2]$  show very small current density at the ring and the presence of a large oxidation peak in the current response at the disc. Moreover, data in Table 5.4 confirms that in  $[N_{C_1,C_1,C_2,(C_2OC_1)}][NTf_2]$ ,  $[N_{C_1,C_1,C_2,C_4}][NTf_2]$  and  $[C_1C_{dma}Pyrr][NTf_2]$  the ORR in the presence of 0.5 M Na $[NTf_2]$  predominantly forms insoluble products. This is evident by the percentual ring current with relation to the disc current, shown in Table 5.4. This is different from the data discussed above for 50 mM Na $^+$ . Therefore, it is possible that with the greater quantity of Na $^+$ , more NaO $_2$  is formed to the extent that Na $_x$ O $_y$  precipitates more readily at the electrode surface. Consequently, less soluble product is detected in these ILs. Moreover, the overlaid CVs of the RRDE and unstirred experiments in Figure 5.8i, l and o show that the oxidation peak in the unstirred CVs with 0.5 M Na $^+$  (Figure 5.5e and Figure 5.6a and c) is related to insoluble Na $_x$ O $_y$  species.

Figure 5.8d and Table 5.4 shows that the percentage of ring current in relation to the disc current for  $[C_1(C_2OC_1)Pyrr][C_2F_5COO]$  is considerably higher than the other ILs studied. Previous studies<sup>30, 165</sup> in Li-O $_2$  systems have demonstrated that solvents with high donating abilities contribute to the dissolution of LiO $_2$  intermediate when discharging Li-O $_2$  batteries. In addition, it has been discussed in the paragraphs above that the high donor number of this IL suggests that  $[C_2F_5COO]^-$  can strongly solvates Na $^+$ . Considering that Na $^+$  is solvated by  $[C_2F_5COO]$ , O $_2^-$  and IL cation are perhaps more available to interact with each other and the NaO $_2$  product actually remains as stable Na $^+$  and O $_2^-$  ions in solution. Therefore, the strong interactions of this IL with the ORR products in the presence of Na $^+$  contributes to the higher solubility of NaO $_2$  demonstrated by the RRDE experiments.

Compared to the other  $[NTf_2]$ -based ILs,  $[C_1(C_2OC_1)Pyrr][NTf_2]$  shows a higher percentage of ring current in relation to the disc current (see Figure 5.8a and Table 5.4). This IL has the higher DN among the  $[NTf_2]$ -based ILs (see Table 5.2), which might contribute to stabilise Na $^+$  and O $_2^-$  in solution. Nevertheless, the difference in DN is very small, so it is possible that the higher apparent

solubility could be promoted by other means. Lutz *et al*<sup>32</sup> observed that other solvent properties than DN influence NaO<sub>2</sub> solubility. With molecular dynamics simulations, the authors identified the degree of solvation and the coordination number of a series of glyme-based solvents and were able to understand the higher NaO<sub>2</sub> solubility in their system. Thus, similar computational studies in the ILs investigated herein would be an insightful analysis.

**Table 5.4.** RRDE experiments analysis of ILs with 0.5 M Na<sup>+</sup> showing the percentual of the ring current with relation to the disc current for each cathodic limit

IL / Na <sup>+</sup> system (0.5 M)	Cathodic limit (V)	% ( <i>i</i> <sub>ring</sub> / <i>i</i> <sub>disc</sub> )
[C <sub>1</sub> (C <sub>2</sub> OC <sub>1</sub> )Pyrr][NTf <sub>2</sub> ]	-0.9	20.1
	-1.5	11.0
[C <sub>1</sub> (C <sub>2</sub> OC <sub>1</sub> )Pyrr][C <sub>2</sub> F <sub>5</sub> COO]	-1.5	48.9
[C <sub>1</sub> C <sub>dma</sub> Pyrr][NTf <sub>2</sub> ]	-1	1.9
	-1.5	2.7
[N <sub>C<sub>1</sub>,C<sub>1</sub>,C<sub>2</sub>,C<sub>2</sub>OC<sub>1</sub></sub> ][NTf <sub>2</sub> ]	-1.2	1.9
	-1.5	0.7
[N <sub>C<sub>1</sub>,C<sub>1</sub>,C<sub>2</sub>,C<sub>4</sub></sub> ][NTf <sub>2</sub> ]	-1.2	1.9

## 5.4. Evaluating a potential application in Na-O<sub>2</sub> cells

A full Na-O<sub>2</sub> battery cell comprises of a metallic Na negative electrode, a Na<sup>+</sup> electrolyte and a positive electrode with a porous material that allows the diffusion of O<sub>2</sub> into the cell. Therefore, when designing an electrolyte for this cell the stability and performance of both electrodes must be considered.

Chapter 3 demonstrated the good performance of [N<sub>C<sub>1</sub>,C<sub>1</sub>,C<sub>2</sub>,C<sub>4</sub></sub>][NTf<sub>2</sub>]-based electrolyte in symmetrical Na|Na cells. [N<sub>C<sub>1</sub>,C<sub>1</sub>,C<sub>2</sub>,C<sub>2</sub>OC<sub>1</sub></sub>][NTf<sub>2</sub>]-based electrolyte displayed inferior behaviour, however [N<sub>C<sub>1</sub>,C<sub>1</sub>,C<sub>2</sub>,C<sub>2</sub>OC<sub>1</sub></sub>][NTf<sub>2</sub>] displays much lower viscosity than [N<sub>C<sub>1</sub>,C<sub>1</sub>,C<sub>2</sub>,C<sub>4</sub></sub>][NTf<sub>2</sub>], which is beneficial for an application in electrochemical devices. Furthermore, it was demonstrated in Chapter 4 that the rate of O<sub>2</sub> diffusion was higher in [N<sub>C<sub>1</sub>,C<sub>1</sub>,C<sub>2</sub>,C<sub>2</sub>OC<sub>1</sub></sub>][NTf<sub>2</sub>] than [N<sub>C<sub>1</sub>,C<sub>1</sub>,C<sub>2</sub>,C<sub>4</sub></sub>][NTf<sub>2</sub>].

Finally, previous sections in this chapter have shown slightly smaller peak-to-peak separation in these ILs (compare Figure 5.5 and Figure 5.6) and high current density of the anodic peak. This could indicate a lower overpotential between charge and discharge steps when cycling the cells, compared to the other ILs. Therefore, these ILs with small structural differences and yet different properties are further investigated in a full Na-O<sub>2</sub> cell.

The cell used for the Na-O<sub>2</sub> experiments was shown in Figure 5.1. Initially, a setup similar to the Na|Na cells from Chapter 3 was attempted but as described below, several parameters had to be adjusted to allow effective cell discharge. These are listed as follows and serve as a guideline when assembling Na-O<sub>2</sub> full cells using the cell from Figure 5.1 with IL electrolytes. The discharge curves for the cells described in the following paragraphs can be found in Appendix 1.A.4.1.

- *Separators:*

The first cell setup was composed of one Na disc as the negative electrode, one glassfibre disc as the separator and one GDL disc as the positive electrode and a disc of stainless-steel mesh as the current collector for the positive electrode. 105  $\mu$ L of electrolyte was used, and the setup was identical to the cells from Chapter 3, except for the GDL electrode. However, the cell short-circuited even before the start of the experiments, in more than one cell assembly. Compared to the symmetrical cell from Chapter 3, the GDL electrode is much more flexible, so perhaps it might have bent and touched the Na electrode. In addition, a strand from the steel mesh might have perforated the separator and contacted the Na electrode. Thus, to suppress this possibility, two glass fibre discs were used as the separators with 210  $\mu$ L of electrolyte.

- *Resting time:*

Initially, the cells were left under open cell potential conditions for two hours. This time is known to be enough to allow adequate wettability of the positive electrode and O<sub>2</sub> diffusion into the GDL/electrolyte interphase for cells with organic solvent electrolytes. However, with this setup the cell reached the

cut-off potential as soon as the current was applied. It was understood that this was caused by poor wettability of the porous carbon electrode and/or instantaneous depletion of  $O_2$  at the GDL/interface. Indeed, the diffusion coefficient of  $O_2$  in DME, for instance, is one order of magnitude greater than the diffusion coefficient determined for the ILs in Chapter 4,<sup>32</sup> which explains the longer resting time needed for the cells with IL. Therefore, the cells were left resting 24 h prior to the discharge experiments.

- *Temperature:*

Although longer resting times and the use of two separators allowed the experiments to occur, the capacity obtained was very low (see Figure A 39b in Appendix 1.A.4.1). Once again,  $O_2$  diffusion in the electrolyte was thought to be responsible for the low capacity. To try to evaluate this, the cells were discharged at 40 °C, instead of the laboratory temperature of ~18 °C. The higher temperature is expected to promote  $O_2$  diffusion in the IL.<sup>48</sup> It was found that the higher temperature was effective in enhancing the cell capacity. Thus, cells were assembled with the optimal conditions of resting time and separators and were cycled at 40 °C. The results are displayed and discussed as follows.

Discharge profiles of Na- $O_2$  cells with  $[N_{C_1,C_1,C_2,C_4}][NTf_2]$  and  $[N_{C_1,C_1,C_2,(C_2OC_1)}][NTf_2]$  electrolytes are shown in Figure 5.9 (a and c, respectively) as well as scanning electron microscopy (SEM) images of the GDL electrode post discharge.

In both cells the voltage sharply decreases as soon as the discharge starts, then in  $[N_{C_1,C_1,C_2,C_4}][NTf_2]$  the voltage reaches a plateau and in  $[N_{C_1,C_1,C_2,(C_2OC_1)}][NTf_2]$  it slowly drops until it reaches the cut-off limit. The voltage drop is caused by different types of losses in the cell, including activation polarisation, concentration polarisation and ohmic polarisation.<sup>60</sup> Whilst the ohmic polarisation is caused by the internal resistance of the cell, the other polarisations are related to the charge transfer at the electrode (activation) and concentration gradient between the electrode and the bulk of active species (concentration).<sup>60</sup>

Compared to previous reports on Na-O<sub>2</sub> cells with ILs,<sup>54, 55</sup> the cell capacity and the abundance of discharge product deposits in the electrode (analysed by SEM) studied herein is considerably inferior. Early cell death in alkali metal-O<sub>2</sub> batteries is often associated with saturation of the porous cathode with discharge products. The SEM images in Figure 5.9b and d clearly show that this is not the case for the cells discharged in Figure 5.9a and c. The SEM images show the long carbon fibres of the GDL electrode with a few white dots attributed to the discharge product Na<sub>x</sub>O<sub>y</sub>, see energy dispersive x-ray analysis (EDX) in Figure A 40. Thus, the early cell termination must be caused by other factors than an electrode blockage. It is believed that the low capacity is caused by depletion of O<sub>2</sub> at the carbon electrode, caused by either slow rate of diffusion of O<sub>2</sub> through the electrolyte, and/or low solubility of O<sub>2</sub> in the IL. It would be interesting to compare these results with the results of a cell with [C<sub>1</sub>(C<sub>2</sub>OC<sub>1</sub>)Pyrr][NTf<sub>2</sub>], for instance, which displays lower O<sub>2</sub> rate of diffusion but much higher O<sub>2</sub> solubility (see Table 4.4 in Chapter 4). In addition, in this IL, Na<sub>x</sub>O<sub>y</sub> displays greater solubility according to RRDE experiments, which may also affect the cell capacity.

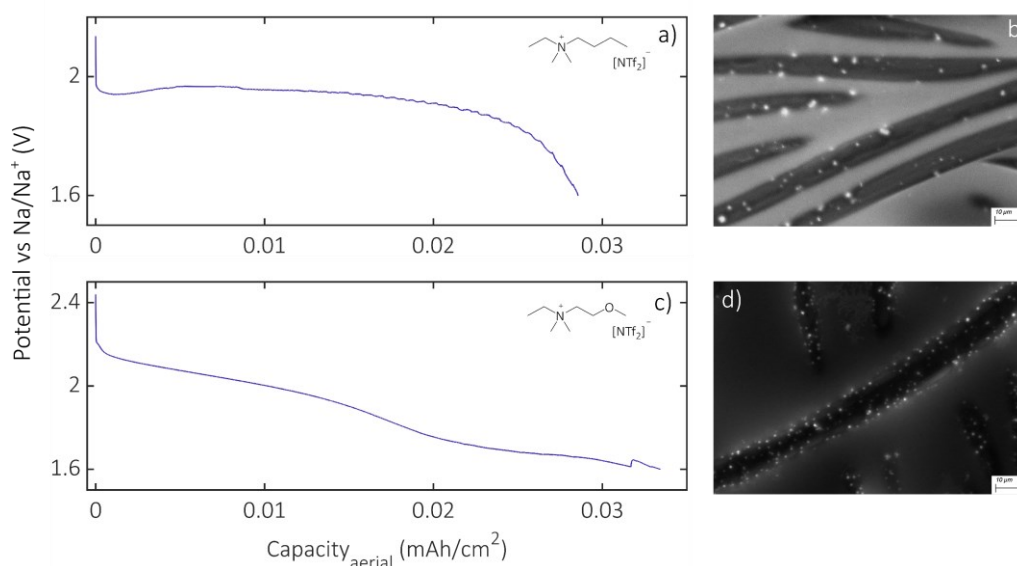


**Figure 5.9.** Discharge profile of Na-O<sub>2</sub> cells with a) [N<sub>C<sub>1</sub>,C<sub>1</sub>,C<sub>2</sub>,C<sub>4</sub>][NTf<sub>2</sub>]-based electrolyte with 0.5 M Na[NTf<sub>2</sub>] and c) [N<sub>C<sub>1</sub>,C<sub>1</sub>,C<sub>2</sub>,C<sub>4</sub>][NTf<sub>2</sub>]-based electrolyte with 0.5 M Na[NTf<sub>2</sub>] with [N<sub>C<sub>1</sub>,C<sub>1</sub>,C<sub>2</sub>,C<sub>4</sub>][NTf<sub>2</sub>] showing a discharge plateau at approximately 1.95 V and [N<sub>C<sub>1</sub>,C<sub>1</sub>,C<sub>2</sub>,C<sub>4</sub>][NTf<sub>2</sub>] displaying a sloping profile. Discharge performed at 10 μA/cm<sup>2</sup></sub></sub></sub></sub>

and 40 °C, with 1.6 V cut-off limit. SEM images of GDL electrode post discharge b) in  $[N_{C_1,C_1,C_2,C_2,C_4}][NTf_2]$  and d) in  $[N_{C_1,C_1,C_2,(C_2OC_1)}][NTf_2]$  (EDX can be found in Appendix A.4).

Finally, a cell with  $[N_{C_1,C_1,C_2,C_4}][NTf_2]$  electrolyte has also been cycled to gain an insight into the cell rechargeability and the discharge and charge curves are displayed in Figure 5.10. Figure 5.10 shows that after the first discharge (continuous line in navy blue), the subsequent charge (dashed navy blue line) is considerably reduced. This implies that although the CVs in Figure 5.6 and Figure 5.8 show an oxidation peak with similar current density as the reduction peak, this is not directly translated into full Na-O<sub>2</sub> cells. Moreover, further substantial capacity loss is observed over cycling, indicating that this system needs further exploring if it is to be considered as a possible cell alternative.

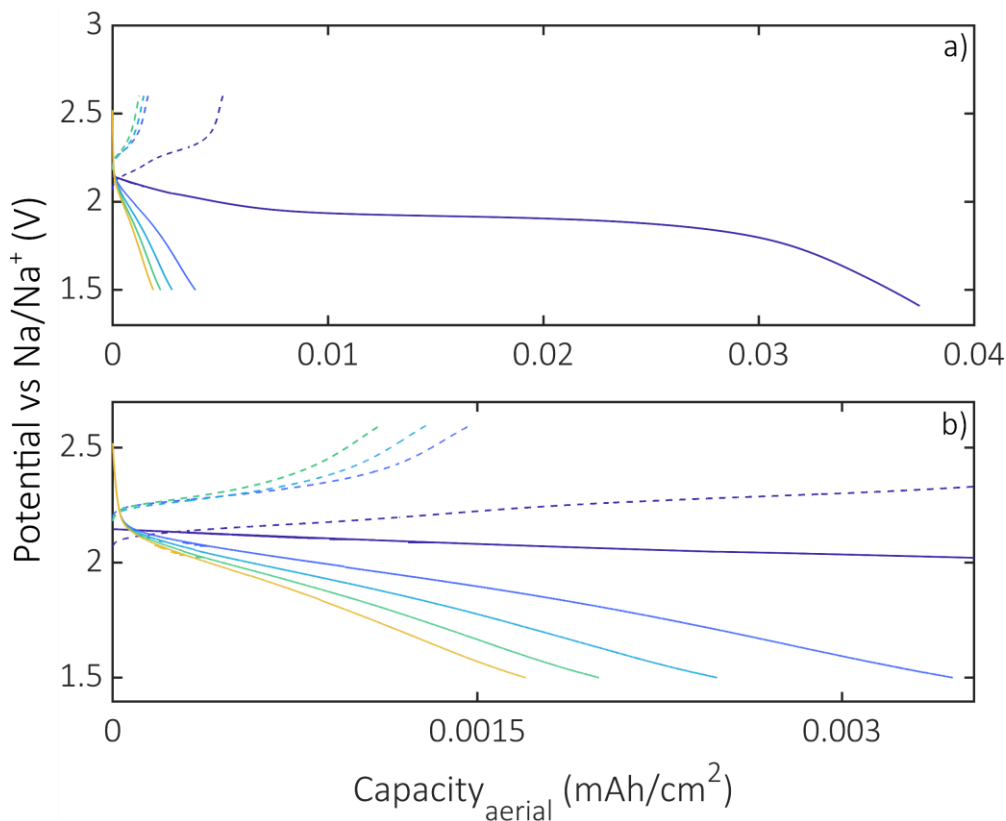


**Figure 5.10.** Cycling of Na-O<sub>2</sub> cells with  $[N_{C_1,C_1,C_2,C_4}][NTf_2]$ -based electrolyte with 0.5 M Na[NTf<sub>2</sub>] showing discharge curves (—) and charge curves (- - -). Note the capacity loss over cycling from first discharge (in navy blue) to fifth discharge (in yellow). Discharge performed at 10 μA/cm<sup>2</sup> and 40 °C, with 1.6 V cut-off limit.

## 5.5. Conclusions and future work

This chapter has evaluated some fundamental aspects of the ORR in ILs in the presence of  $\text{Li}^+$  and  $\text{Na}^+$ . It was found that slight modifications on the IL structure considerably influences the ORR in the presence of  $\text{Li}^+$  and  $\text{Na}^+$ . The effect of the IL anion was evident by the differences in the anodic scans of the  $\text{O}_2$  CVs with  $\text{Li}^+$  in  $[\text{C}_1(\text{C}_2\text{OC}_1)\text{Pyrr}][\text{C}_2\text{F}_5\text{COO}]$ , which suggested the stabilisation of  $\text{LiO}_2$ . This was caused by the strong solvating ability of the  $[\text{C}_2\text{F}_5\text{COO}]^-$  anion, that solvates  $\text{Li}^+$  to a greater extent than  $[\text{NTf}_2]^-$ . Furthermore, it was also demonstrated that the  $[\text{C}_2\text{F}_5\text{COO}]^-$  anion promotes the formation of a substantial percentage of soluble  $\text{NaO}_2$  products during the ORR even in the presence of 0.5 M  $\text{Na}^+$ . At this concentration, the percentage of soluble  $\text{NaO}_2$  in the  $[\text{NTf}_2]$ -based ILs was considerably lower.

The  $\text{O}_2$  CVs in the presence of alkali metals seem to also be influenced by structural differences in the IL cation. This was demonstrated in the system with 25 mM  $\text{Li}^+$  in which superoxide is stabilised by both IL cation and  $\text{Li}^+$  in  $[\text{C}_1\text{C}_{\text{dma}}\text{Pyrr}][\text{NTf}_2]$ , whilst in  $[\text{C}_1(\text{C}_2\text{OC}_1)\text{Pyrr}][\text{NTf}_2]$  it is stabilised by  $\text{Li}^+$  only, based on the assignments of the peaks in the anodic scan. The  $\text{Na}^+$  systems also displayed superoxide stabilisation by both IL cation and  $\text{Na}^+$ , at  $\text{Na}^+$  concentration of 25 mM for  $[\text{N}_{\text{C}_1,\text{C}_1,\text{C}_2,(\text{C}_2\text{OC}_1)}][\text{NTf}_2]$ . Notably this was also observed in  $[\text{C}_1(\text{C}_2\text{OC}_1)\text{Pyrr}][\text{C}_2\text{F}_5\text{COO}]$  and  $[\text{N}_{\text{C}_1,\text{C}_1,\text{C}_2,\text{C}_4}][\text{NTf}_2]$  at  $\text{Na}^+$  concentration as high as 0.5 M. Such differences were attributed to different solvent-solute interactions and mass transport of active species within the IL.

With 50 mM  $\text{Na}^+$  concentration, the  $\text{O}_2$  CVs with  $[\text{NTf}_2]$ -based ILs have displayed different anodic peaks. In  $[\text{C}_1\text{C}_{\text{dma}}\text{Pyrr}][\text{NTf}_2]$  and  $[\text{C}_1(\text{C}_2\text{OC}_1)\text{Pyrr}][\text{NTf}_2]$ , anodic peaks at less positive potentials shifted to more positive potentials over scanning depending on the cathodic limit adopted. This was not observed in  $[\text{N}_{\text{C}_1,\text{C}_1,\text{C}_2,(\text{C}_2\text{OC}_1)}][\text{NTf}_2]$ , but a more negative cathodic limit yielded an oxidation peak at more positive potentials. With the aid of RRDE, it was demonstrated that the oxidation peak at less positive potentials is attributed to oxidation of  $\text{NaO}_2$  species in solution, whilst the peak at more

positive potentials is associated with oxidation of  $\text{Na}_x\text{O}_y$  species adsorbed at the electrode surface.

Finally, full Na- $\text{O}_2$  cells were assembled and discharged, and the cells displayed inferior capacities compared to previous reports in literature. Unlike most cases in Na- $\text{O}_2$  cells, the poor capacity was not associated with electrode blockage, as demonstrated by SEM images. Instead, the capacity is likely to be limited by the solubility and diffusion of active species towards the IL-GDL interphase, mainly  $\text{O}_2$ .

In summary, this chapter has demonstrated that at low salt concentrations (25-50 mM) the structure of both the IL cation and IL anion strongly effects the ORRs, as demonstrated by the shape of the CVs. However, at salt concentrations typically used in practical cells (0.5 M), the choice of anion seems to be the main influencing factor, and strongly donating anions such as  $[\text{C}_2\text{F}_5\text{COO}]^-$  enhances the solubility of  $\text{NaO}_2$ . Nevertheless, the Na- $\text{O}_2$  cells with  $[\text{N}_{\text{C}_1, \text{C}_1, \text{C}_2, (\text{C}_2\text{OC}_1)}][\text{NTf}_2]$  and  $[\text{N}_{\text{C}_1, \text{C}_1, \text{C}_2, \text{C}_4}][\text{NTf}_2]$  demonstrated that substantial work needs to be carried out in order to use these ILs as pure electrolytes in full Na- $\text{O}_2$  cells.

Furthermore, in this chapter several questions remain open to future studies. This includes the understanding of the different solvent-solute interactions of  $\text{Na}^+$  and  $\text{O}_2^-$  species in ILs. Molecular dynamics simulations of the solvation sphere of active species have been shown to aid understanding of electrochemical data,<sup>32, 54</sup> thus it would be an insightful analysis to be carried out in these IL systems. Another point yet to be determined is the nature of the  $\text{Na}_x\text{O}_y$  species. *In-situ* surface enhanced Raman spectroscopy has been previously demonstrated to be a powerful tool for the diagnosis of species formed during cyclic voltammetry experiments.<sup>30, 129</sup> Moreover, it would be interesting to evaluate the capacity and performance of Na- $\text{O}_2$  cells with  $[\text{C}_1(\text{C}_2\text{OC}_1)\text{Pyrr}][\text{NTf}_2]$  considering the higher solubility of  $\text{NaO}_2$  in this IL. Although  $[\text{C}_1(\text{C}_2\text{OC}_1)\text{Pyrr}][\text{C}_2\text{F}_5\text{COO}]$  also displayed high solubility, Chapter 3 has

shown poor stability of metallic Na electrode in contact with  $[\text{C}_1(\text{C}_2\text{OC}_1)\text{Pyrr}][\text{C}_2\text{F}_5\text{COO}]$ .

## 5.6. References

- Walsh, D. A.; Goodwin, S., The Oxygen Reduction Reaction in Room-Temperature Ionic Liquids. In *Encyclopedia of Interfacial Chemistry*, Wandelt, K., Ed. Elsevier: Oxford, 2018; Vol. 5.2, pp 898-907.
- Liu, T.; Vivek, J. P.; Zhao, E. W.; Lei, J.; Garcia-Araez, N.; Grey, C. P., Current Challenges and Routes Forward for Nonaqueous Lithium–Air Batteries. *Chem. Rev.* **2020**.
- Kwak, W. J.; Rosy; Sharon, D.; Xia, C.; Kim, H.; Johnson, L. R.; Bruce, P. G.; Nazar, L. F.; Sun, Y. K.; Frimer, A. A.; Noked, M.; Freunberger, S. A.; Aurbach, D., Lithium–Oxygen Batteries and Related Systems: Potential, Status, and Future. *Chem. Rev.* **2020**.
- Zhang, J.; Zhou, Q.; Tang, Y.; Zhang, L.; Li, Y., Zinc-air batteries: are they ready for prime time? *Chem. Sci.* **2019**, *10* (39), 8924-8929.
- Yadegari, H.; Sun, X., Sodium–Oxygen Batteries: Recent Developments and Remaining Challenges. *Trends Chem.* **2020**, *2* (3), 241-253.
- Qin, L.; Schkeryantz, L.; Zheng, J.; Xiao, N.; Wu, Y., Superoxide-Based K–O<sub>2</sub> Batteries: Highly Reversible Oxygen Redox Solves Challenges in Air Electrodes. *J. Am. Chem. Soc.* **2020**, *142* (27), 11629-11640.
- Li, C.; Sun, Y.; Gebert, F.; Chou, S.-L., Current Progress on Rechargeable Magnesium–Air Battery. *Adv. Energy Mater.* **2017**, *7* (24), 1700869.
- Johnson, L.; Li, C.; Liu, Z.; Chen, Y.; Freunberger, S. A.; Ashok, P. C.; Praveen, B. B.; Dholakia, K.; Tarascon, J. M.; Bruce, P. G., The role of LiO<sub>2</sub> solubility in O<sub>2</sub> reduction in aprotic solvents and its consequences for Li–O<sub>2</sub> batteries. *Nat. Chem.* **2014**, *6* (12), 1091-9.
- McCloskey, B. D.; Scheffler, R.; Speidel, A.; Girishkumar, G.; Luntz, A. C., On the Mechanism of Nonaqueous Li–O<sub>2</sub> Electrochemistry on C and Its Kinetic Overpotentials: Some Implications for Li–Air Batteries. *J. Phys. Chem. C* **2012**, *116* (45), 23897-23905.
- Katayama, Y.; Onodera, H.; Yamagata, M.; Miura, T., Electrochemical Reduction of Oxygen in Some Hydrophobic Room-Temperature Molten Salt Systems. *Journal of The Electrochemical Society* **2004**, *151* (1), A59-A63.
- Lutz, L.; Yin, W.; Grimaud, A.; Alves Dalla Corte, D.; Tang, M.; Johnson, L.; Azaceta, E.; Sarou-Kanian, V.; Naylor, A. J.; Hamad, S.; Anta, J. A.; Salager, E.; Tena-Zaera, R.; Bruce, P. G.; Tarascon, J. M., High Capacity Na–O<sub>2</sub> Batteries: Key Parameters for Solution-Mediated Discharge. *J. Phys. Chem. C* **2016**, *120* (36), 20068-20076.
- Pozo-Gonzalo, C.; Johnson, L. R.; Jónsson, E.; Holc, C.; Kerr, R.; MacFarlane, D. R.; Bruce, P. G.; Howlett, P. C.; Forsyth, M., Understanding of the Electrogenerated Bulk Electrolyte Species in Sodium-Containing Ionic Liquid

Electrolytes During the Oxygen Reduction Reaction. *J. Phys. Chem. C* **2017**, *121* (42), 23307-23316.

13. Azaceta, E.; Lutz, L.; Grimaud, A.; Vicent-Luna, J. M.; Hamad, S.; Yate, L.; Cabanero, G.; Grande, H. J.; Anta, J. A.; Tarascon, J. M.; Tena-Zaera, R., Electrochemical Reduction of Oxygen in Aprotic Ionic Liquids Containing Metal Cations: A Case Study on the Na-O<sub>2</sub> system. *ChemSusChem* **2017**, *10* (7), 1616-1623.

14. Lutz, L.; Dachraoui, W.; Demortiere, A.; Johnson, L. R.; Bruce, P. G.; Grimaud, A.; Tarascon, J. M., Operando Monitoring of the Solution-Mediated Discharge and Charge Processes in a Na-O<sub>2</sub> Battery Using Liquid-Electrochemical Transmission Electron Microscopy. *Nano Lett.* **2018**, *18* (2), 1280-1289.

15. Bender, C. L.; Schroder, D.; Pinedo, R.; Adelhelm, P.; Janek, J., One- or Two-Electron Transfer? The Ambiguous Nature of the Discharge Products in Sodium-Oxygen Batteries. *Angew. Chem.* **2016**, *55* (15), 4640-9.

16. McCloskey, B. D.; Garcia, J. M.; Luntz, A. C., Chemical and Electrochemical Differences in Nonaqueous Li-O<sub>2</sub> and Na-O<sub>2</sub> Batteries. *J. Phys. Chem. Lett.* **2014**, *5* (7), 1230-5.

17. Mekonnen, Y. S.; Christensen, R.; Garcia-Lastra, J. M.; Vegge, T., Thermodynamic and Kinetic Limitations for Peroxide and Superoxide Formation in Na-O<sub>2</sub> Batteries. *J. Phys. Chem. Lett.* **2018**, *9* (15), 4413-4419.

18. Kwak, W. J.; Rosy; Sharon, D.; Xia, C.; Kim, H.; Johnson, L. R.; Bruce, P. G.; Nazar, L. F.; Sun, Y.; Frimer, A. A.; Noked, M.; Freunberger, S. A.; Aurbach, D., Lithium–Oxygen Batteries and Related Systems: Potential, Status, and Future. *Chem. Rev.* **2020**.

19. Das, S. K.; Lau, S.; Archer, L. A., Sodium–oxygen batteries: a new class of metal–air batteries. *J. Mater. Chem. A* **2014**, *2* (32), 12623-12629.

20. Pozo-Gonzalo, C.; Howlett, P. C.; MacFarlane, D. R.; Forsyth, M., Highly reversible oxygen to superoxide redox reaction in a sodium-containing ionic liquid. *Electrochem. Commun.* **2017**, *74*, 14-18.

21. Piana, M.; Wandt, J.; Meini, S.; Buchberger, I.; Tsiouvaras, N.; Gasteiger, H. A., Stability of a Pyrrolidinium-Based Ionic Liquid in Li-O<sub>2</sub> Cells. *J. Electrochem. Soc.* **2014**, *161* (14), A1992-A2001.

22. Das, S.; Højberg, J.; Knudsen, K. B.; Younesi, R.; Johansson, P.; Norby, P.; Vegge, T., Instability of Ionic Liquid-Based Electrolytes in Li–O<sub>2</sub> Batteries. *J. Phys. Chem. A* **2015**, *119* (32), 18084-18090.

23. Watanabe, M.; Thomas, M. L.; Zhang, S.; Ueno, K.; Yasuda, T.; Dokko, K., Application of Ionic Liquids to Energy Storage and Conversion Materials and Devices. *Chem. Rev.* **2017**.

24. Xu, W.; Xiao, J.; Zhang, J.; Wang, D.; Zhang, J. G., Optimization of Nonaqueous Electrolytes for Primary Lithium/Air Batteries Operated in Ambient Environment. *J. Electrochem. Soc.* **2009**, *156* (10), A773.

25. Monaco, S.; Arangio, A. M.; Soavi, F.; Mastragostino, M.; Paillard, E.; Passerini, S., An electrochemical study of oxygen reduction in pyrrolidinium-based ionic liquids for lithium/oxygen batteries. *Electrochim. Acta* **2012**, *83*, 94-104.

26. Cecchetto, L.; Tesio, A. Y.; Olivares-Marín, M.; Espinasa, M. G.; Croce, F.; Tonti, D., Tailoring oxygen redox reactions in ionic liquid based Li/O<sub>2</sub> batteries by means of the Li<sup>+</sup> dopant concentration. *Sustainable Energy Fuels* **2018**, *2* (1), 118-124.
27. Galiote, N. A.; Jeong, S.; Morais, W. G.; Passerini, S.; Huguenin, F., The Role of Ionic Liquid in Oxygen Reduction Reaction for Lithium-air Batteries. *Electrochim. Acta* **2017**, *247*, 610-616.
28. Elia, G. A.; Hassoun, J.; Kwak, W. J.; Sun, Y. K.; Scrosati, B.; Mueller, F.; Bresser, D.; Passerini, S.; Oberhumer, P.; Tsiouvaras, N.; Reiter, J., An advanced lithium-air battery exploiting an ionic liquid-based electrolyte. *Nano Lett.* **2014**, *14* (11), 6572-7.
29. Soavi, F.; Monaco, S.; Mastragostino, M., Catalyst-free porous carbon cathode and ionic liquid for high efficiency, rechargeable Li/O<sub>2</sub> battery. *J. Power Sources* **2013**, *224*, 115-119.
30. Allen, C. J.; Hwang, J.; Kautz, R.; Mukerjee, S.; Plichta, E. J.; Hendrickson, M. A.; Abraham, K. M., Oxygen Reduction Reactions in Ionic Liquids and the Formulation of a General ORR Mechanism for Li-Air Batteries. *J. Phys. Chem. C* **2012**, *116* (39), 20755-20764.
31. Zhang, T.; Wen, Z., A High-Rate Ionic Liquid Lithium-O<sub>2</sub> Battery with LiOH Product. *J. Phys. Chem. C* **2017**, *121* (11), 5968-5973.
32. Olivares-Marín, M.; Sorrentino, A.; Pereiro, E.; Tonti, D., Discharge products of ionic liquid-based Li-O<sub>2</sub> batteries observed by energy dependent soft x-ray transmission microscopy. *J. Power Sources* **2017**, *359*, 234-241.
33. Zhang, Y.; Ortiz-Vitoriano, N.; Acebedo, B.; O'Dell, L.; MacFarlane, D. R.; Rojo, T.; Forsyth, M.; Howlett, P. C.; Pozo-Gonzalo, C., Elucidating the Impact of Sodium Salt Concentration on the Cathode-Electrolyte Interface of Na-Air Batteries. *J. Phys. Chem. C* **2018**, *122* (27), 15276-15286.
34. Ha, T. A.; Fdz De Anastro, A.; Ortiz-Vitoriano, N.; Fang, J.; MacFarlane, D. R.; Forsyth, M.; Mecerreyes, D.; Howlett, P. C.; Pozo-Gonzalo, C., High Coulombic Efficiency Na-O<sub>2</sub> Batteries Enabled by a Bilayer Ionogel/Ionic Liquid. *J. Phys. Chem. Lett.* **2019**, *10* (22), 7050-7055.
35. Ha, T. A.; Pozo-Gonzalo, C.; Nairn, K.; MacFarlane, D. R.; Forsyth, M.; Howlett, P. C., An investigation of commercial carbon air cathode structure in ionic liquid based sodium oxygen batteries. *Sci. Rep.* **2020**, *10* (1), 7123.
36. Gao, X.; Chen, Y.; Johnson, L.; Bruce, P. G., Promoting solution phase discharge in Li-O<sub>2</sub> batteries containing weakly solvating electrolyte solutions. *Nat. Mater.* **2016**, *15* (8), 882-8.
37. De Giorgio, F.; Soavi, F.; Mastragostino, M., Effect of lithium ions on oxygen reduction in ionic liquid-based electrolytes. *Electrochem. Commun.* **2011**, *13*, 3.
38. Pozo-Gonzalo, C., Oxygen Reduction Reaction in Ionic Liquids: An Overview. In *Electrochemistry in Ionic Liquids: Volume 2: Applications*, Torriero, A. A. J., Ed. Springer International Publishing: Cham, 2015; pp 507-529.
39. Balaish, M.; Kraytsberg, A.; Ein-Eli, Y., A critical review on lithium-air battery electrolytes. *Phys. Chem. Chem. Phys.* **2014**, *16* (7), 2801-22.
40. Schmeisser, M.; P., I.; Puchta, R.; Zahl, A.; van Eldik, R., Gutmann donor and acceptor numbers for ionic liquids. *Chem. - Eur. J.* **2012**, *18*, 10969-10982.

41. Xia, C.; Black, R.; Fernandes, R.; Adams, B.; Nazar, L. F., The critical role of phase-transfer catalysis in aprotic sodium oxygen batteries. *Nat. Chem.* **2015**, *7* (6), 496-501.
42. Peng, Z.; Freunberger, S. A.; Hardwick, L. J.; Chen, Y.; Giordani, V.; Bardé, F.; Novák, P.; Graham, D. J.; Tarascon, J. M.; Bruce, P. G., Oxygen Reactions in a Non-Aqueous Li<sup>+</sup> Electrolyte. *Angew. Chem., Int. Ed. Engl.* **2011**, *50* (28), 6351-6355.
43. Lalore, C. O.; Mukerjee, S.; Abraham, K. M.; Plichta, E. J.; Hendrickson, M. A., Influence of Nonaqueous Solvents on the Electrochemistry of Oxygen in the Rechargeable Lithium–Air Battery. *J. Phys. Chem. C* **2010**, *114* (19), 9178-9186.
44. Berg, H., The electrochemical cell. In *Batteries for Electric Vehicles: Materials and Electrochemistry*, Berg, H., Ed. Cambridge University Press: Cambridge, 2015; pp 7-46.
45. Frith, J. T.; Russell, A. E.; Garcia-Araez, N.; Owen, J. R., An in-situ Raman study of the oxygen reduction reaction in ionic liquids. *Electrochem. Commun.* **2014**, *46*, 33-35.



# Final remarks and future work

Among the never-ending challenges of developing new batteries, electrolyte design is a common issue for all emerging technologies. In this thesis the tunability of ILs has been explored to prepare electrolytes aimed at battery applications.

Overall, it was observed that even small structural changes in the IL substantially affect the performance of the electrochemical cells and reaction pathway. Regarding cells with Na electrodes, it was observed that side chains containing oxygen do not appear to form a stable and protective SEI. This was understood to be because of their high reactivity, especially in  $[C_1C_{dma}Pyrr][NTf_2]$ , and potential solubility/diffusion of SEI reaction products in  $[N_{C_1,C_1,C_2,(C_2OC_1)}][NTf_2]$ . Nevertheless,  $[N_{C_1,C_1,C_2,C_4}][NTf_2]$  developed a stable  $R_{surface}$  in open cell experiments, displayed low overpotential during Na|Na cell cycling and a very structured SEI according to 3D OrbiSIMS experiments.

It was demonstrated that the SEI with  $[N_{C_1,C_1,C_2,C_4}][NTf_2]$  has an outermost layer formed by cation-related compounds, including large fragments such as  $[C_{13}H_{30}N]^+$ ,  $[C_9H_{19}NF_3]^+$  and  $[C_{10}H_{24}N]^+$ . In addition, cation-related compounds displayed negligible presence in the inner SEI layers, unlike that observed for the other ILs. Therefore, it was suggested that the outermost layer works as a protective barrier, separating the more reactive SEI products in the inner layers from the remaining bulk electrolyte. The benefits of a structured SEI were evident in the Na|Na cell cycling performance, which displayed relatively low overpotentials even above 300 cycles.

Addition of Na[PF<sub>6</sub>] additive to  $[N_{C_1,C_1,C_2,(C_2OC_1)}][NTf_2]$ -based electrolyte increased the cycling time of the cells until reaching cut-off potentials and displayed stable  $R_{surface}$  after 40h of open cell conditions. Surprisingly, the fluoride content was not the key factor in the improved performance of the electrolyte with Na[PF<sub>6</sub>] additive. Instead, it was proposed that the improved performance was due to the formation of a more organised SEI.

## Final remarks and future work

Regarding the use of IL-based electrolytes in Na<sup>+</sup>/O<sub>2</sub> systems, it was demonstrated that at low Na<sup>+</sup> concentrations, both the IL cation and Na<sup>+</sup> play a role in stabilising O<sub>2</sub><sup>-</sup>. Moreover, differences in the O<sub>2</sub> CVs were observed even among ILs with small structural differences such as [C<sub>1</sub>(C<sub>2</sub>OC<sub>1</sub>)Pyrr][NTf<sub>2</sub>] and [N<sub>C<sub>1</sub>,C<sub>1</sub>,C<sub>2</sub>,C<sub>2</sub>(C<sub>2</sub>OC<sub>1</sub>)</sub>][NTf<sub>2</sub>]. Shifts of the oxidation peak from less to more positive potentials were observed in [C<sub>1</sub>(C<sub>2</sub>OC<sub>1</sub>)Pyrr][NTf<sub>2</sub>] and [C<sub>1</sub>C<sub>dma</sub>Pyrr][NTf<sub>2</sub>], whilst in [N<sub>C<sub>1</sub>,C<sub>1</sub>,C<sub>2</sub>,C<sub>2</sub>(C<sub>2</sub>OC<sub>1</sub>)</sub>][NTf<sub>2</sub>], [N<sub>C<sub>1</sub>,C<sub>1</sub>,C<sub>2</sub>,C<sub>4</sub></sub>][NTf<sub>2</sub>] and [C<sub>1</sub>(C<sub>2</sub>OC<sub>1</sub>)Pyrr][C<sub>2</sub>F<sub>5</sub>COO] the number and potential of the oxidation peaks were dependent on the cathodic limit of the immediately preceding scan. With the aid of RRDE, it was suggested that the oxidation peak at less positive potentials is associated with NaO<sub>2</sub> formed in solution, whilst the oxidation peak at more positive potentials is related to Na<sub>x</sub>O<sub>y</sub> species at the electrode surface.

With higher Na<sup>+</sup> concentration it was found that the IL donor number was the main factor in determining whether the ORR product was found in solution or at the electrode surface. Na<sub>x</sub>O<sub>y</sub> at the electrode surface was the main ORR product in CVs of the [NTf<sub>2</sub>]-based ILs with 0.5 M Na[NTf<sub>2</sub>], whilst [C<sub>1</sub>(C<sub>2</sub>OC<sub>1</sub>)Pyrr][C<sub>2</sub>F<sub>5</sub>COO] also displayed high percentage of product in solution. This demonstrates that although small structural changes in the cation can have an impact on the ORR pathway with low Na<sup>+</sup> concentration, in concentrated electrolytes only ILs with highly solvating anions, like [C<sub>2</sub>F<sub>5</sub>COO]<sup>-</sup> can influence the reaction pathway.

Considering the previous studies in the literature associating a solution mediated discharge with high Na-O<sub>2</sub> battery cell capacities, [C<sub>1</sub>(C<sub>2</sub>OC<sub>1</sub>)Pyrr][C<sub>2</sub>F<sub>5</sub>COO] would be the best candidate for application in a full cell. Nevertheless, it was also found that [C<sub>1</sub>(C<sub>2</sub>OC<sub>1</sub>)Pyrr][C<sub>2</sub>F<sub>5</sub>COO] forms an extremely reactive SEI with Na metal, limiting its application. Na-O<sub>2</sub> cells were assembled with [N<sub>C<sub>1</sub>,C<sub>1</sub>,C<sub>2</sub>,C<sub>4</sub></sub>][NTf<sub>2</sub>], which showed excellent performance in Na|Na cells as discussed above, and [N<sub>C<sub>1</sub>,C<sub>1</sub>,C<sub>2</sub>,C<sub>2</sub>(C<sub>2</sub>OC<sub>1</sub>)</sub>][NTf<sub>2</sub>] which displayed the highest O<sub>2</sub> diffusion among the ILs studied. The full Na-O<sub>2</sub> cells assembled with these two ILs resulted in low cell capacity. Nevertheless, SEM images of the discharged carbon electrodes demonstrated that electrode blockage was not the limiting factor in capacity. Instead the poor O<sub>2</sub> diffusion, hence depletion at the electrode surface, was suggested to be the main factor affecting cell capacity.

To answer some of the questions raised in Chapter 5, *in-situ* techniques such as SERS, would be a good tool to determine the nature of the Na<sub>x</sub>O<sub>y</sub> products observed in the CVs of O<sub>2</sub>

in Na<sup>+</sup> doped ILs. However, even if the nature of Na<sub>x</sub>O<sub>y</sub> is revealed, pure IL-based electrolytes do not seem to be a feasible electrolyte for application in Na-O<sub>2</sub> batteries, given the preliminary discharge experiments demonstrated in Chapter 5. A few studies<sup>5, 163</sup> have evaluated the use of H<sub>2</sub>O as an additive, and the effect of relative humidity in O<sub>2</sub> cell performance, this is particularly important considering an O<sub>2</sub> battery that can operate using atmospheric O<sub>2</sub>. With this in mind, H<sub>2</sub>O-doped ILs could be a potential alternative to use ILs as electrolytes in Na-O<sub>2</sub> cells.

Considering the performance of Na metal electrode with [N<sub>C<sub>1</sub>,C<sub>1</sub>,C<sub>2</sub>,C<sub>4</sub></sub>][NTf<sub>2</sub>], this IL is a very promising electrolyte for other Na metal based batteries. Additionally, design of electrolyte mixtures using [N<sub>C<sub>1</sub>,C<sub>1</sub>,C<sub>2</sub>,C<sub>4</sub></sub>][NTf<sub>2</sub>] aiming to lower the viscosity of [N<sub>C<sub>1</sub>,C<sub>1</sub>,C<sub>2</sub>,C<sub>4</sub></sub>][NTf<sub>2</sub>] without compromising its SEI formation ability could improve the applicability of this IL in full battery cells.

In conclusion, this thesis demonstrated some key aspects to consider when designing electrolytes for emerging battery technologies based on Na metal electrodes, especially IL-based electrolytes. It has also demonstrated the positive impact that a highly organised SEI has on the performance of Na-metal electrodes.

## References

1. Xia, C.; Black, R.; Fernandes, R.; Adams, B.; Nazar, L. F., The critical role of phase-transfer catalysis in aprotic sodium oxygen batteries. *Nat. Chem.* **2015**, 7 (6), 496-501.
2. Kwak, W. J.; Rosy; Sharon, D.; Xia, C.; Kim, H.; Johnson, L. R.; Bruce, P. G.; Nazar, L. F.; Sun, Y. K.; Frimer, A. A.; Noked, M.; Freunberger, S. A.; Aurbach, D., Lithium–Oxygen Batteries and Related Systems: Potential, Status, and Future. *Chem. Rev.* **2020**.

## Final remarks and future work

# Appendices

## A.1. Characterisation of synthesised ILs

### A.1.1. Viscosity of ILs

The viscosity information obtained for the synthesised ILs is displayed in Figure A 1 and Figure A 2. The data shown in Figure A 1 and Figure A 2 confirms that the presence of an oxygen atom in the side chain of the IL cation decreases the viscosity of ILs (compare  $[N_{C_1, C_1, C_2, (C_2OC_1)}][NTf_2]$  and  $[N_{C_1, C_1, C_2, C_4}][NTf_2]$ , blue and green traces respectively). This is caused by an increase in the flexibility of the side chains, which is believed to increase the overall free volume in the liquid, which contributes to molecular movement.<sup>166</sup> This has also been noticed in polyethylene oxide chains, and it was suggested that the oxygen substituent changes the moment of inertia in the molecular liquid, thus altering the dynamic movement of the molecules.<sup>167</sup>

Moreover, the effect of the bulky dimethyl acetate side chain in  $[C_1C_{dma}Pyrr][NTf_2]$  on increasing the viscosity is understood to be caused by the lower flexibility of this side chain which creates resistance to molecular movement.<sup>167</sup>

Finally, a change from  $[NTf_2]$  anion to  $[C_2F_5COO]$  has demonstrated to increase the viscosity of the ILs. Molecular interactions are known to be one of the main factors dictating the viscosity in molecular liquids. Thus considering the much higher donor number of  $[C_1(C_2OC_1)Pyrr][C_2F_5COO]$ , the stronger cation-anion interaction in this IL compared to  $[C_1(C_2OC_1)Pyrr][NTf_2]$ , plays a role increasing  $[C_1(C_2OC_1)Pyrr][C_2F_5COO]$  viscosity.

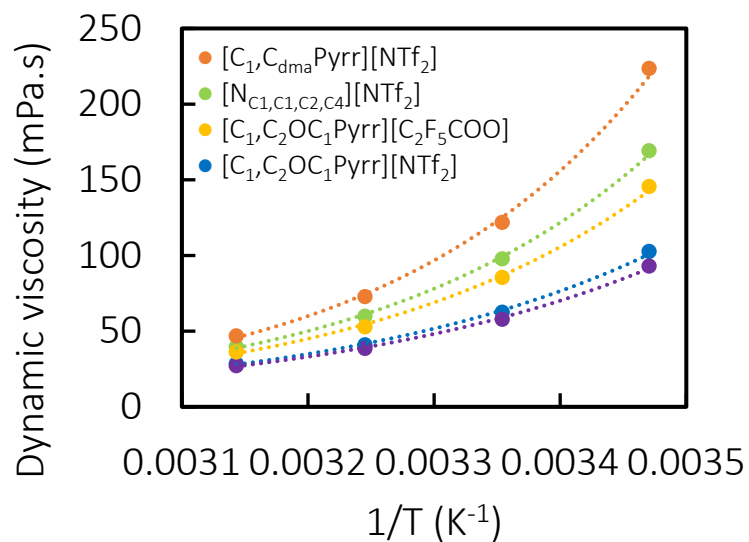


**Figure A 1.** Dynamic viscosity as a function of the inverse of temperature, showing that the dataset follows the Arrhenius exponential equation

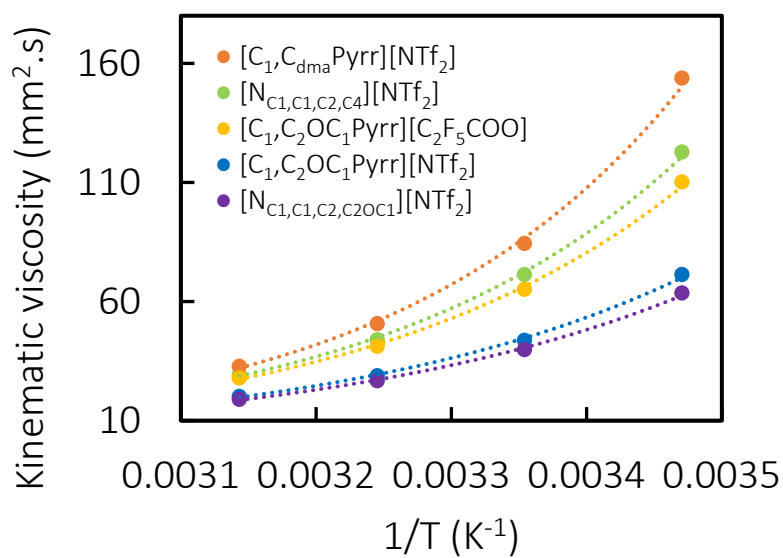


**Figure A 2.** Kinematic viscosity as a function of the inverse of temperature, showing that the dataset follows the Arrhenius exponential equation

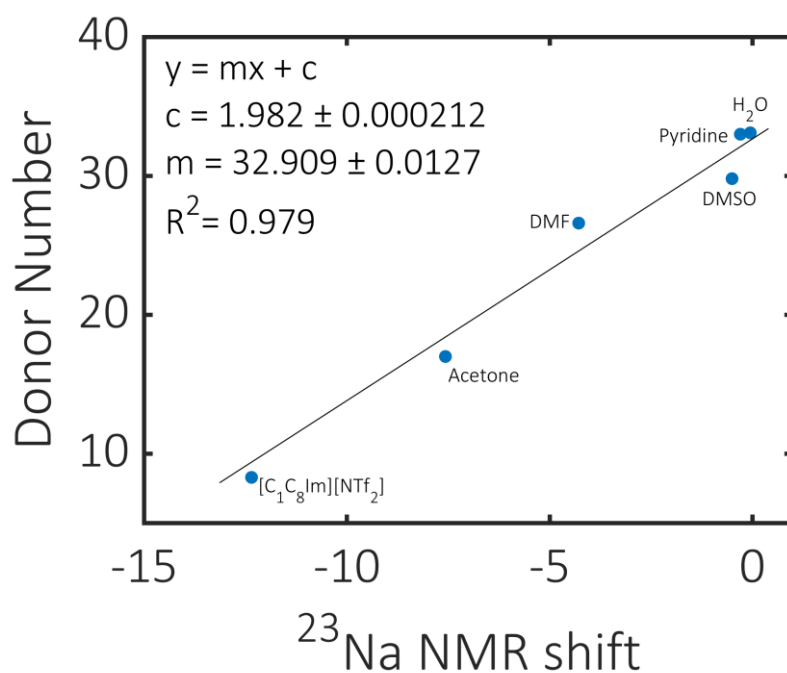
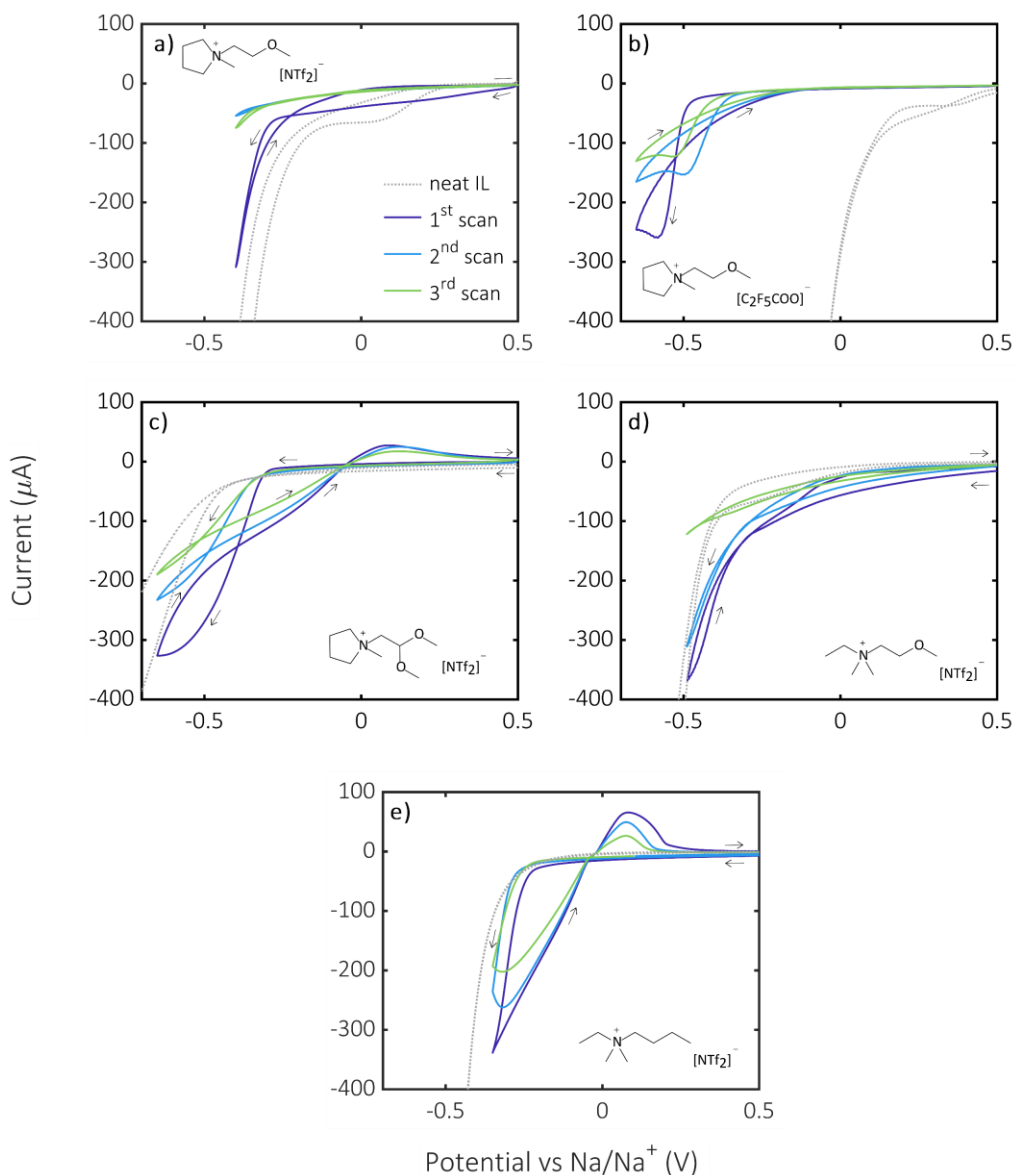
A.1.2. Donor number  $^{23}\text{Na}$  shift and calibration


Figure A 3. Donor Number calibration line with solvents previously reported in literature.<sup>66</sup>

Table A1.1. DN dataset showing  $^{23}\text{Na}$  shift for two measurements, average  $^{23}\text{Na}$  shift and calculated DN.

IL	$^{23}\text{Na}$ shift <sup>(1)</sup>	$^{23}\text{Na}$ shift <sup>(2)</sup>	$^{23}\text{Na}$ shift <sup>(avg)</sup>	DN
$[\text{N}_{\text{C}_1, \text{C}_1, \text{C}_2, (\text{C}_2\text{OC}_1)}][\text{NTf}_2]$	-11.96	-12.04	-12.0	9.1
$[\text{C}_1(\text{C}_2\text{OC}_1)\text{Pyrr}][\text{NTf}_2]$	-11.38	-11.56	-11.47	10.2
$[\text{C}_1\text{C}_{\text{dma}}\text{Pyrr}][\text{NTf}_2]$	-12.59	-12.54	-12.56	8.0
$[\text{N}_{\text{C}_1, \text{C}_1, \text{C}_2, \text{C}_4}][\text{NTf}_2]$	-12.91	-12.8	-12.85	7.4
$[\text{C}_1(\text{C}_2\text{OC}_1)\text{Pyrr}][\text{C}_2\text{F}_5\text{COO}]$	-4.71	-4.75	-4.73	23.5
$[\text{P}_{6,6,6,14}][\text{NTf}_2]$	-15.84	-15.11	-15.48	2.5

A.2. Electrochemical performance and stability of Na metal electrode and IL-based electrolytes



**Figure A 4.** Cyclic voltammograms (CVs) of 0.5 M Na<sup>+</sup> in the IL based electrolytes showing three scans, at 100 mV.s<sup>-1</sup> and using glassy carbon working electrode, Pt coil counter electrode and Na flag reference electrode. Arrows show scanning direction. a) [C<sub>1</sub>(C<sub>2</sub>OC<sub>1</sub>)Pyrr][NTf<sub>2</sub>], b) [C<sub>1</sub>(C<sub>2</sub>OC<sub>1</sub>)Pyrr][C<sub>2</sub>F<sub>5</sub>COO], c) [C<sub>1</sub>C<sub>dma</sub>Pyrr][NTf<sub>2</sub>], d) [N<sub>C<sub>1</sub>,C<sub>1</sub>,C<sub>2</sub>,C<sub>2</sub>OC<sub>1</sub>}] [NTf<sub>2</sub>], and e) [N<sub>C<sub>1</sub>,C<sub>1</sub>,C<sub>2</sub>,C<sub>4</sub>}] [NTf<sub>2</sub>] IL-based electrolytes</sub></sub>

A.2.1. Solid-electrolyte interphase studies with electrochemical impedance spectroscopy

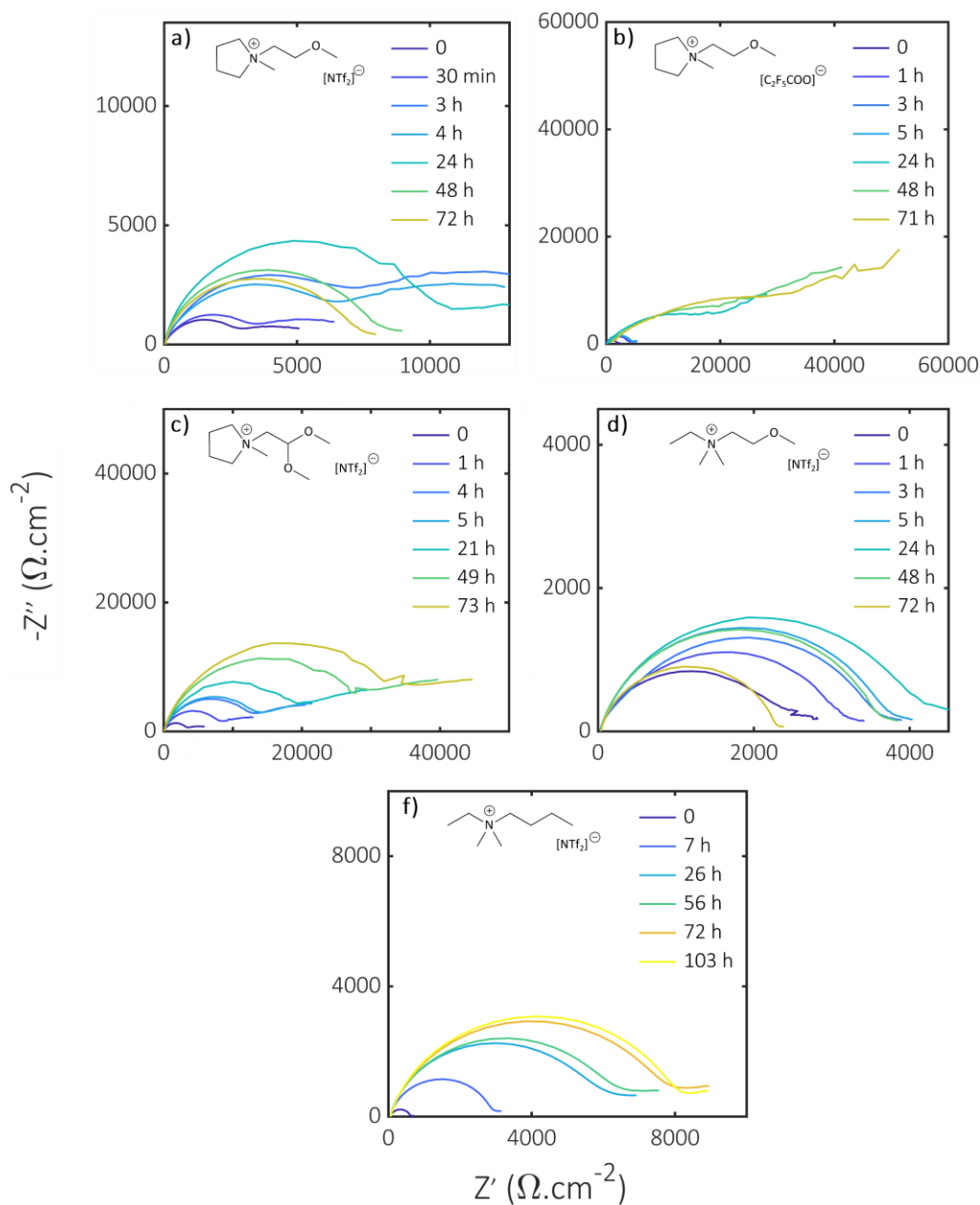


**Figure A 5.** Nyquist plots of electrochemical impedance spectroscopy (EIS) of Na|Na symmetrical cells during open circuit conditions for over 70 h, using the various IL electrolytes: 0.5 M Na<sup>+</sup> in a)  $[C_1(C_2OC_1)Pyrr][NTf_2]$ , b)  $[C_1(C_2OC_1)Pyrr][C_2F_5COO]$ , c)  $[C_1C_{dma}Pyrr][NTf_2]$ , d)  $[N_{C_1,C_1,C_2,(C_2OC_1)}][NTf_2]$ , e)  $[N_{C_1,C_1,C_2,C_4}][NTf_2]$ ; Na<sup>+</sup> counter ion accordingly to IL anion. Inserts show pictures of one of Na electrodes post analysis (cell disassembled within a glovebox).

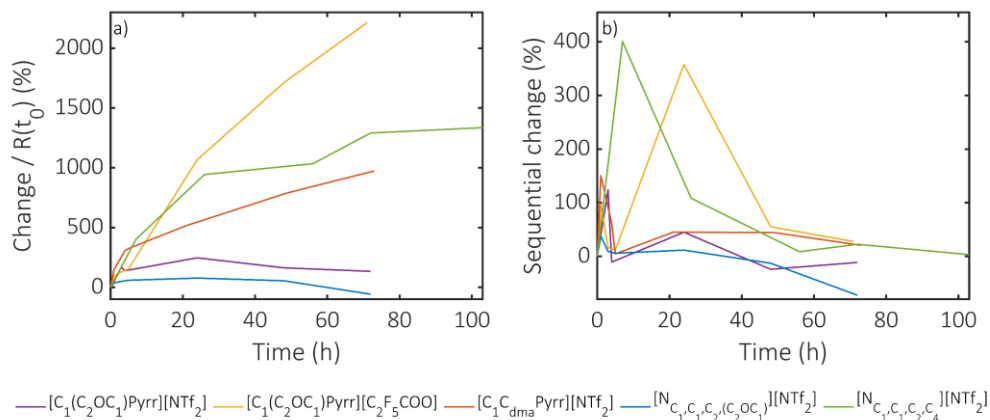


**Figure A 6.** Analysis of electrochemical impedance data (EIS) of Na | Na symmetrical cells using IL-based electrolytes (0.5 M Na<sup>+</sup> salts in the ILs displayed in the figure legend); a) Change/R(t<sub>0</sub>): Percentual change of surface resistance over time with respect to the resistance at the initial time (t<sub>0</sub>); b) Sequential change: Percentual change of surface resistance over time with respect to the resistance of the immediately preceding measurement.

### A.2.2. Na | Na cell galvanostatic cycling

The cells were initially cycled at 10 μA/cm<sup>2</sup>, and the voltage profiles are shown in Figure A 7. With 10 μA/cm<sup>2</sup> current density, no cells reach the cut-off limit despite cycling it for over 300 cycles, as demonstrated by the voltage profiles in Figure A 7. Nevertheless, [C<sub>1</sub>C<sub>dma</sub>Pyrr][NTf<sub>2</sub>] displays the highest overpotential across the whole experiment. [N<sub>C<sub>1</sub>,C<sub>1</sub>,C<sub>2</sub>,C<sub>2</sub>OC<sub>1</sub></sub>][NTf<sub>2</sub>] show an increase in overpotential from approximately 75 to 200 h of cycling, whilst the overpotential for [N<sub>C<sub>1</sub>,C<sub>1</sub>,C<sub>2</sub>,C<sub>4</sub></sub>][NTf<sub>2</sub>] increases slightly above 150 h of cycling. The voltage profiles for all cells display the same shape, therefore it is concluded that at 10 μA/cm<sup>2</sup>, the effect of IL in cell performance is subtle, mainly expressed in a difference in overpotential.

## Appendices

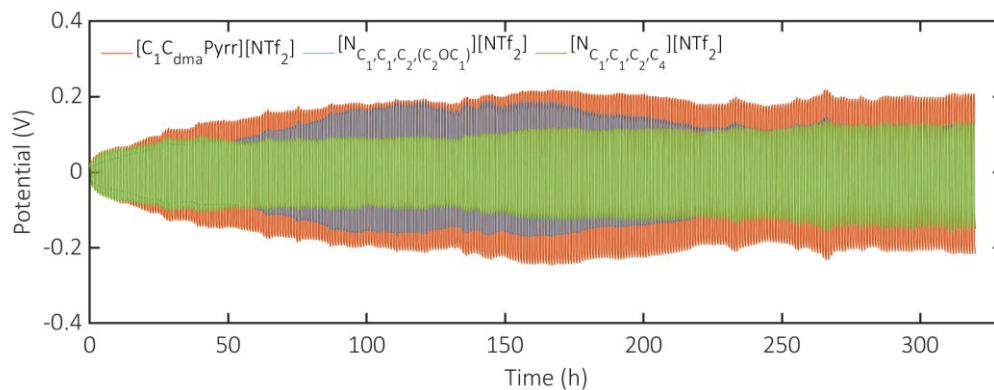


**Figure A 7.** Na|Na symmetrical cycling at  $10 \mu\text{A}/\text{cm}^2$  showing cells with  $[\text{C}_1\text{C}_{\text{dma}}\text{Pyrr}][\text{NTf}_2]$  (—),  $[\text{N}_{\text{C}_1,\text{C}_1,\text{C}_2,(\text{C}_2\text{OC}_1)}][\text{NTf}_2]$  (—), and  $[\text{N}_{\text{C}_1,\text{C}_1,\text{C}_2,\text{C}_4}][\text{NTf}_2]$  (—). Note that with this small current density no cell reaches the cut-off potentials, even after 300 cycles.

Repeats were carried on for all Na|Na cells at  $0.1\text{mA}/\text{cm}^2$ , and although showing the same trends, galvanostatic cycling of cells assembled in different days display differences in the voltage traces. Figure A 8 shows galvanostatic cycling of cells assembled in different days, but with electrolytes from the same batch, which have not been taking outside glovebox in between measurements, and metallic sodium from the same batch as well. The cell components (Swagelok parts and separator) were also cleaned and dried under the same conditions). Despite great care has been taken to ensure that the conditions are kept the same, it is possible than small changes might have happened, including electrolyte volume, or pressure on closing the Swagelok cells, etc.

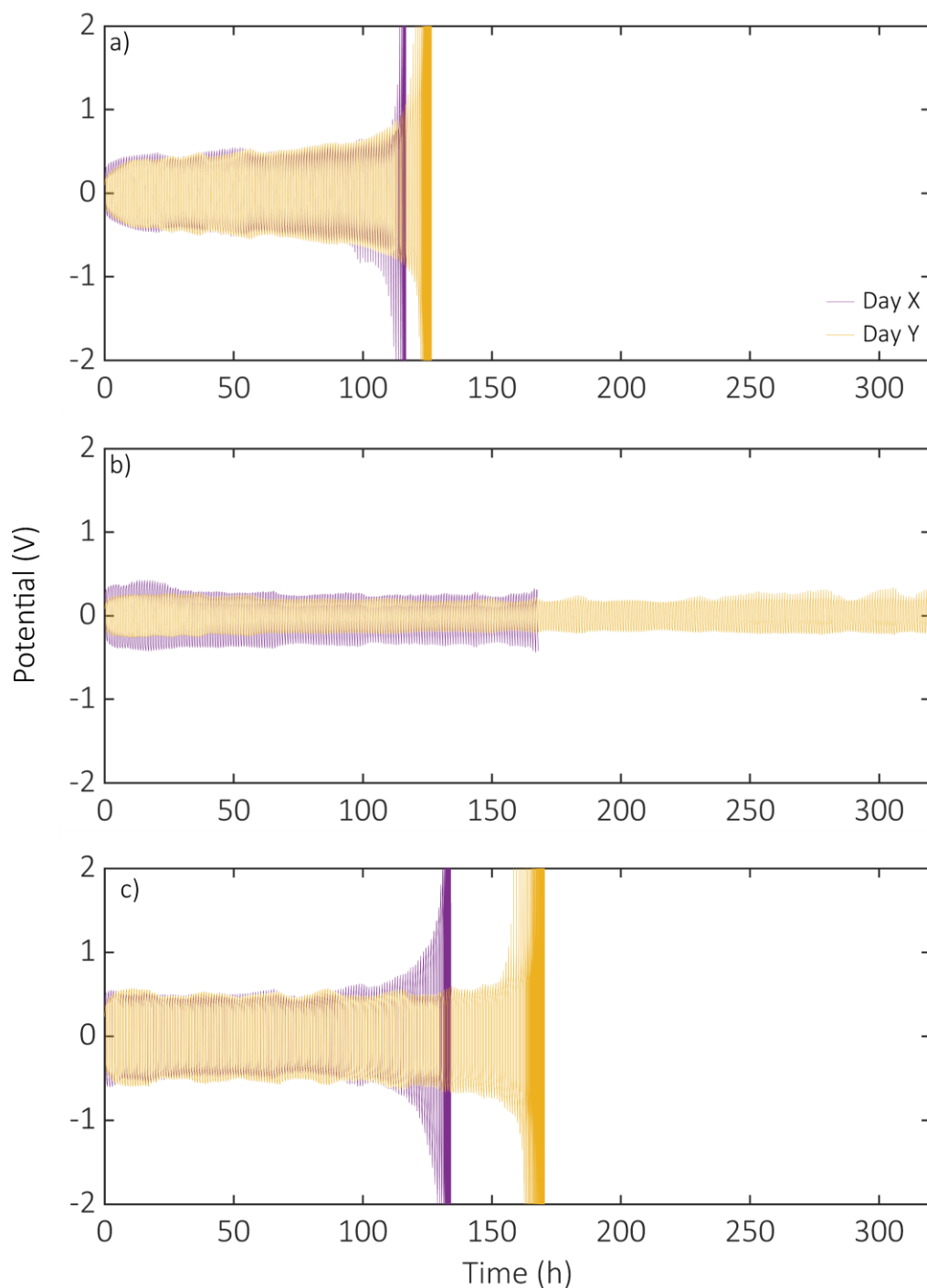


**Figure A 8.** Galvanostatic cycling of Na|Na symmetrical cells assembled in different days: yellow traces display day X (—), and purple traces display day Y (—). Cells cycled at  $0.1 \text{ mA}\cdot\text{cm}^{-2}$ , with 30 minutes polarisation time and  $105 \mu\text{L}$  of  $0.5 \text{ M Na}[\text{NTf}_2]$  in a)  $[\text{N}_{\text{C}_1, \text{C}_1, \text{C}_2, (\text{C}_2\text{OC}_1)}][\text{NTf}_2]$ , b)  $[\text{N}_{\text{C}_1, \text{C}_1, \text{C}_2, \text{C}_4}][\text{NTf}_2]$  and c)  $[\text{N}_{\text{C}_1, \text{C}_1, \text{C}_2, (\text{C}_2\text{OC}_1)}][\text{NTf}_2]$  with  $\text{Na}[\text{NTf}_2]$  and  $\text{Na}[\text{PF}_6]$ . Cell cycling displayed in b) was purposely stopped at 160 h (—) and 320 h (—), of running time despite not having reached cut-off limits.

Another factor that might have contributed to the differences in the cells is the glovebox environment during cell assembly. Metallic Li and Na are highly reactive metals that promptly form a passivation layer on their surface even without direct contact with any electrolytes. This layer is referred in literature as the native layer of metallic Li and Na, and despite pre-treatment or polishing of the metals, it may still be present and/or redevelop at the metal surface. The environment in which these metals are handled also has an impact on the formation and on the characteristics of this layer.

All cells have been handled and assembled within a glovebox, with O<sub>2</sub>, H<sub>2</sub>O and solvent catalysts and purifiers to ensure a dry and inert atmosphere within the box. Despite O<sub>2</sub> and H<sub>2</sub>O levels being both below 1 ppm in both days, it is interesting that the catalysts and the solvent purifier have been just regenerated on the day before the cells assembled on day Y. Perhaps the presence of volatiles, not detected by the O<sub>2</sub> and H<sub>2</sub>O sensors, have affected the Na electrode surface to an extent to cause differences in the galvanostatic cycling.

### A.2.3. Na-IL interphase studies with OrbiSIMS: a multivariate analysis study

The following figures display the depth profile of all peaks obtained in the Na-IL SEI SIMS analysis.

## Appendices

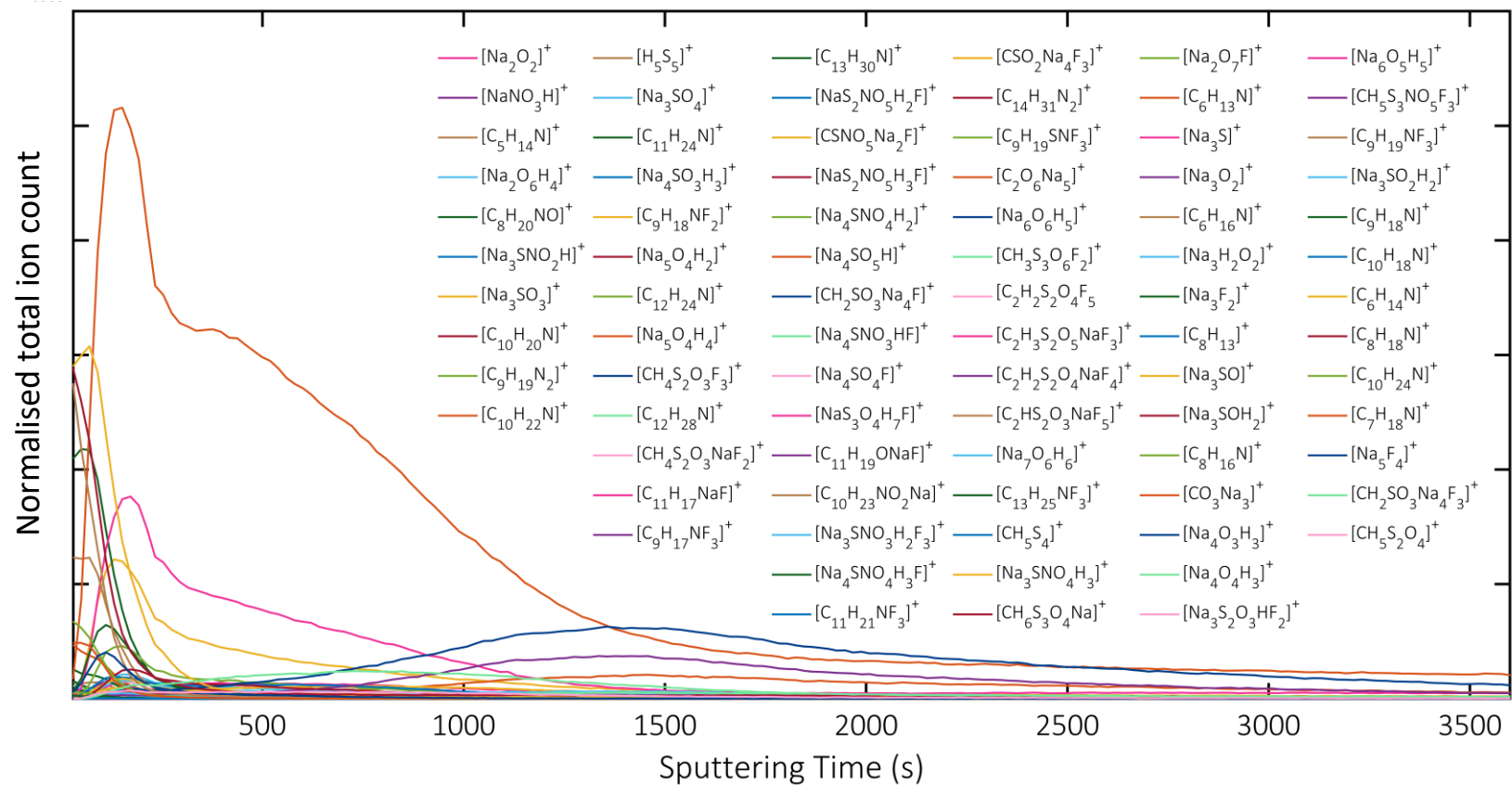


**Figure A 9.** Positive ion depth profile of  $\text{Na}-[\text{N}_{C_1,C_1,C_2,C_4}][\text{NTf}_2]$  interphase (with 0.5 M  $\text{Na}[\text{NTf}_2]$ ) using  $20 \text{ keV Ar}_{3000}^+$  for sputtering and analysis.

## Appendices

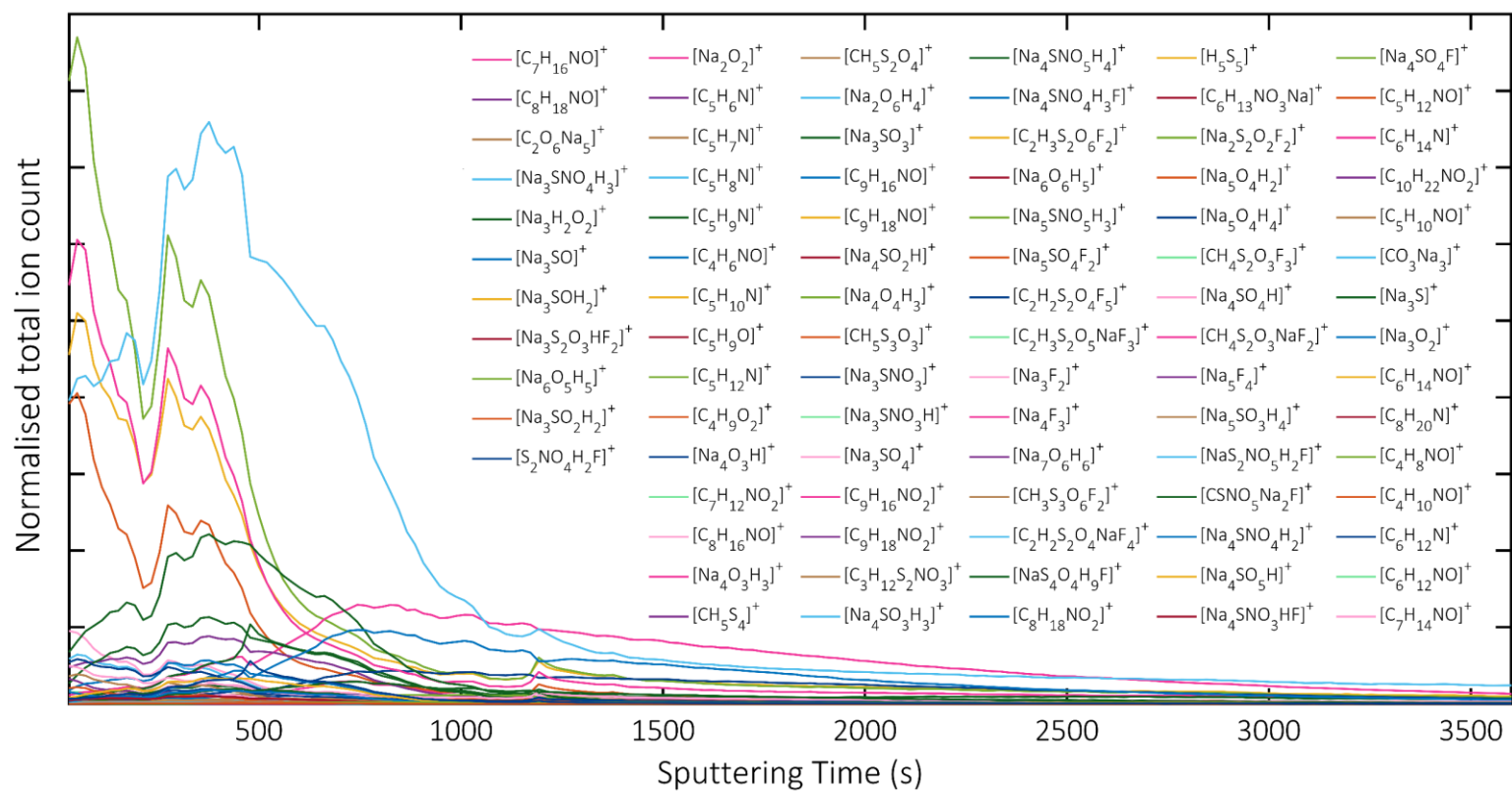


Figure A 10. Positive ion depth profile of Na-[C<sub>1</sub>C<sub>dma</sub>Pyrr][NTf<sub>2</sub>] interphase (with 0.5 M Na[NTf<sub>2</sub>]) using 20 keV Ar<sub>3000</sub><sup>+</sup> for sputtering and analysis.

Appendices

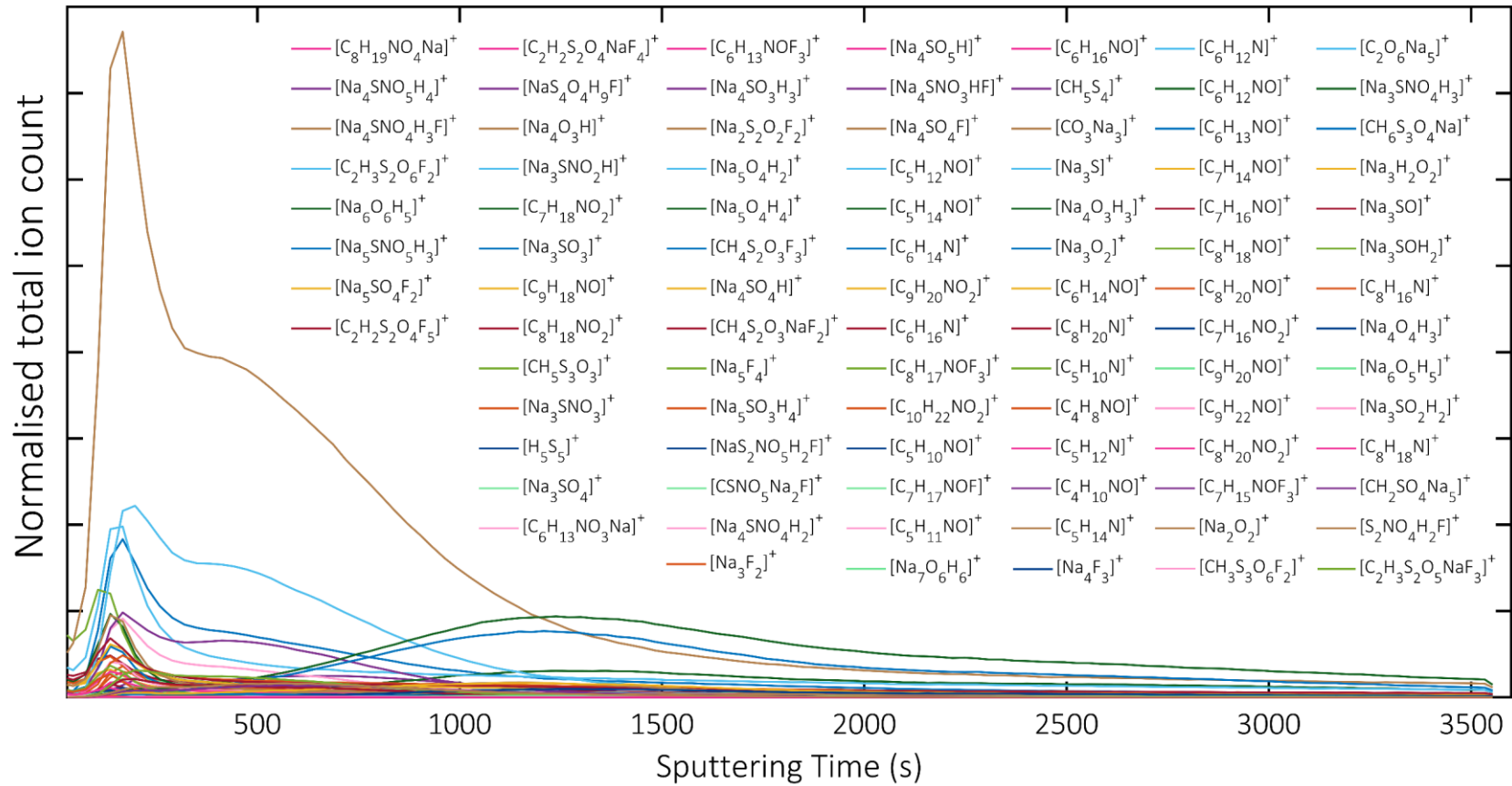
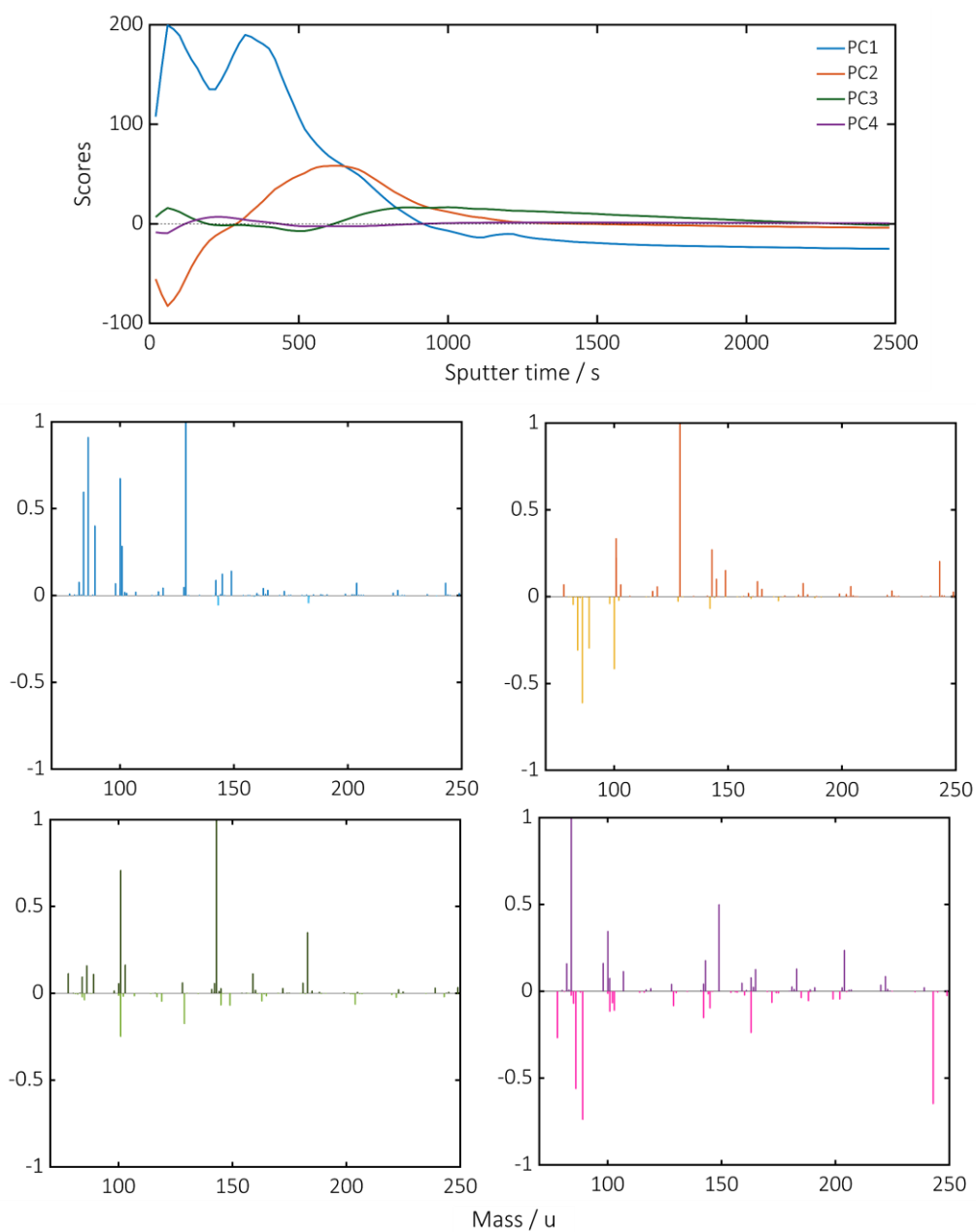


Figure A 11. Positive ion depth profile of Na-[N<sub>C<sub>1</sub>,C<sub>1</sub>,C<sub>2</sub>,C<sub>2</sub>OC<sub>1</sub>][NTf<sub>2</sub>] interphase (with 0.5 M Na[NTf<sub>2</sub>]) using 20 keV Ar<sub>3000</sub><sup>+</sup> for sputtering and analysis</sub>

## Appendices

The following figures display the PCA of the 3D OrbiSIMS dataset.



**Figure A 12.** Principal component analysis (PCA) for solid electrolyte interphase (SEI) of Na and  $[C_1C_{dma}Pyrr][NTf_2]$ -based electrolyte (0.5 M  $Na[NTf_2]$ ).

## Appendices

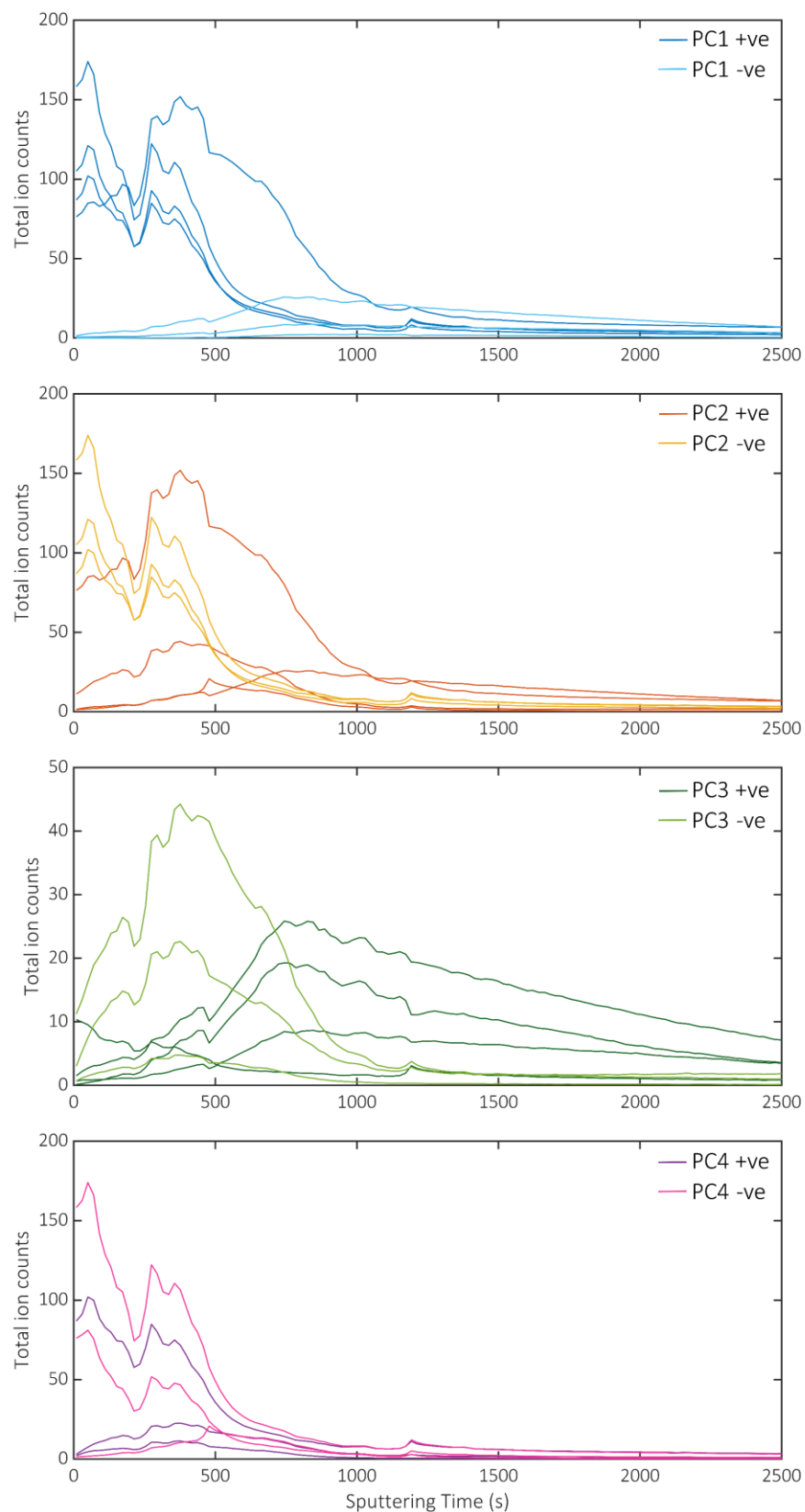


**Figure A 13.** Analysis of PCA results to determine number of endmembers for NMF analysis of Na-[C<sub>1</sub>C<sub>dma</sub>Pyrr][NTf<sub>2</sub>] SEI dataset: depth profile plot for assignments with the most significant (highest loadings) assignments in each PC.

## Appendices

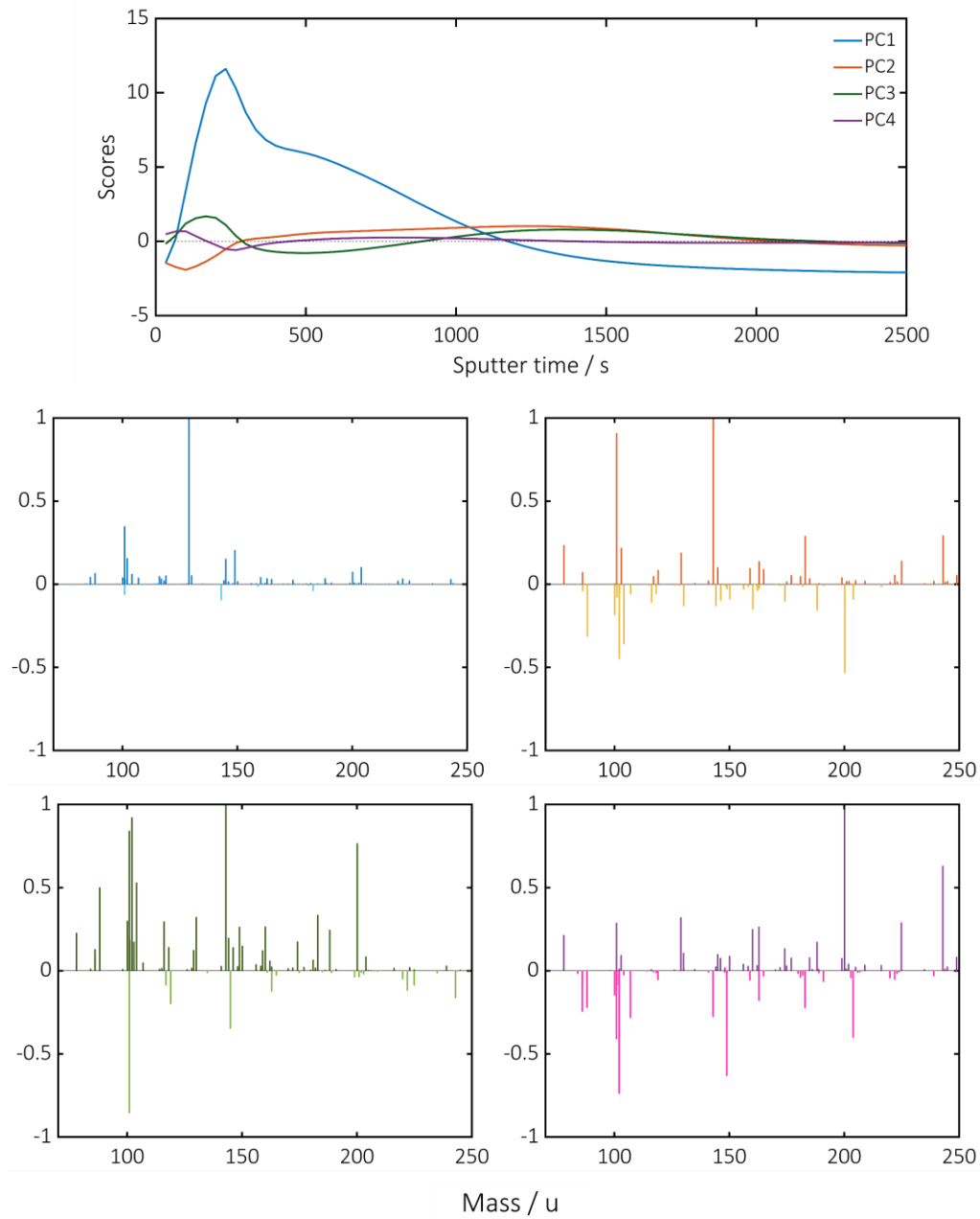


**Figure A 14.** Principal component analysis (PCA) for solid electrolyte interphase (SEI) of Na and  $[N_{C_1,C_1,C_2,(C_2OC_1)}][NTf_2]$  based electrolyte (0.5 M Na[NTf<sub>2</sub>]).

## Appendices

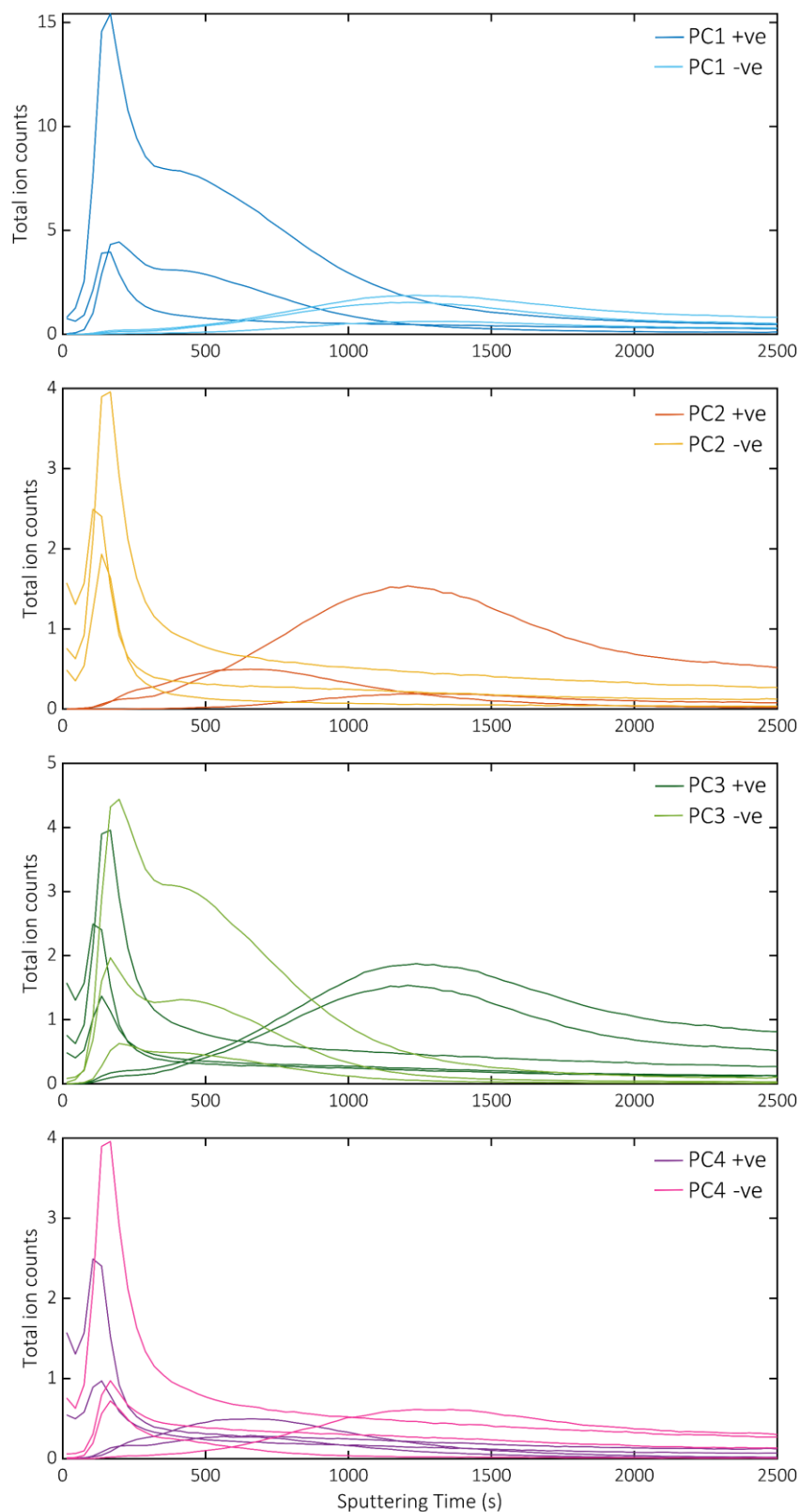


**Figure A 15.** Analysis of PCA results to determine number of endmembers for NMF analysis of  $\text{Na}[\text{N}_{\text{C}_1, \text{C}_1, \text{C}_2, (\text{C}_2\text{OC}_1)}][\text{NTf}_2]$  SEI dataset: depth profile plot for assignments with the most significant (highest loadings) assignments in each PC.

## Appendices

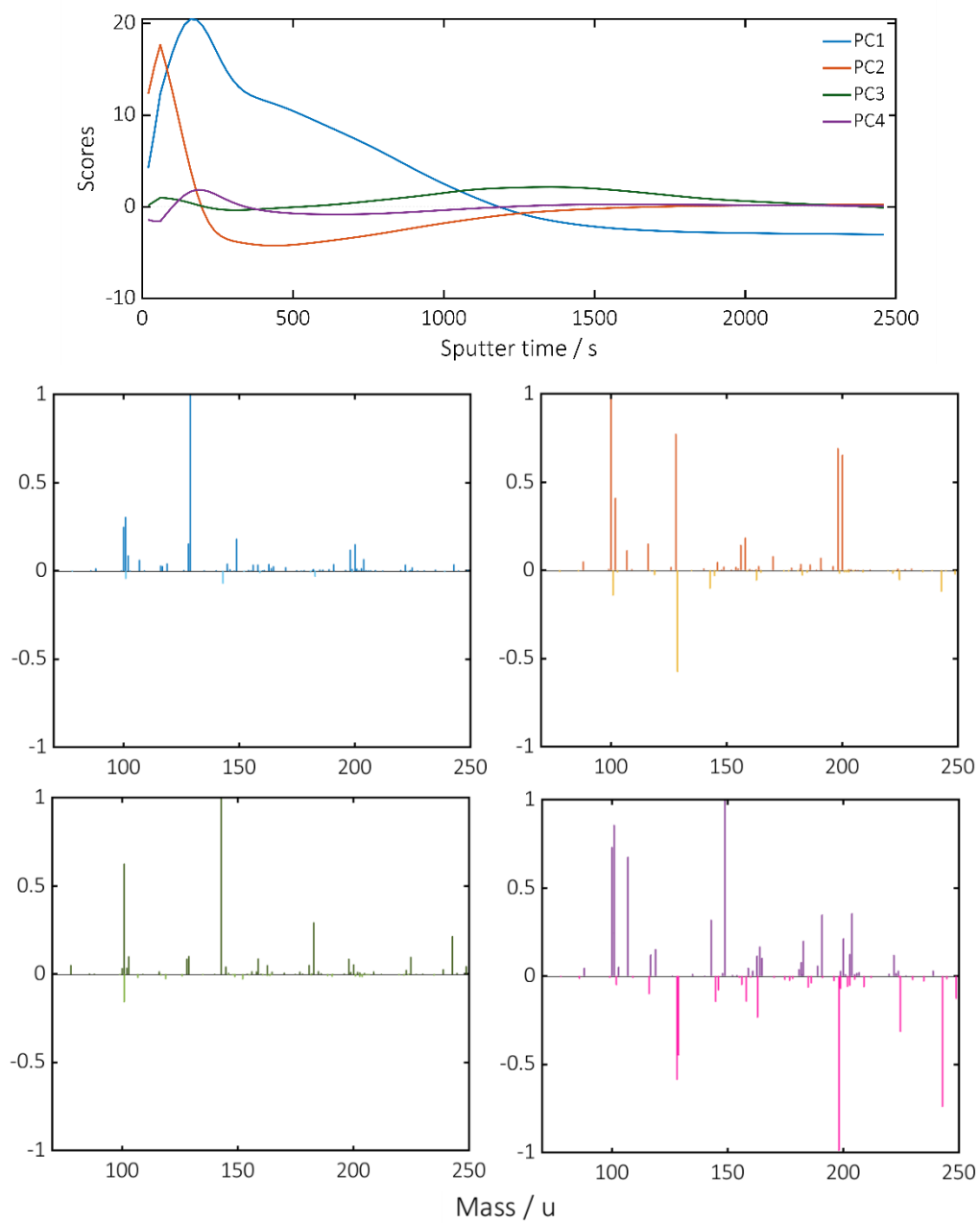


**Figure A 16.** Principal component analysis (PCA) for solid electrolyte interphase (SEI) of Na and  $[N_{C_1,C_1,C_2,C_4}][NTf_2]$  based electrolyte (0.5 M Na[NTf<sub>2</sub>]).

## Appendices

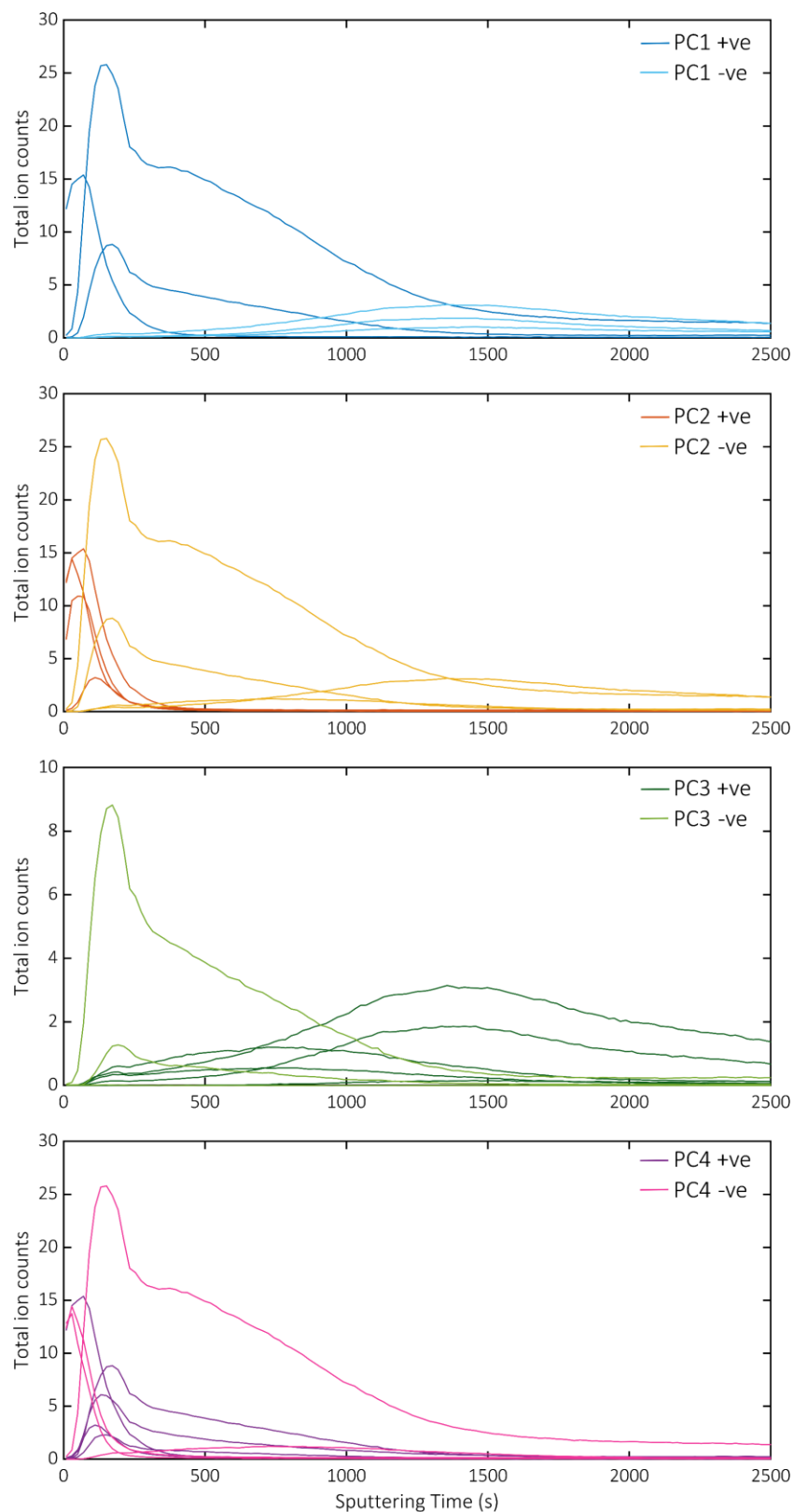


**Figure A 17.** Analysis of PCA results to determine number of endmembers for NMF analysis of  $\text{Na}[\text{N}_{\text{C}_1, \text{C}_1, \text{C}_2, \text{C}_4}][\text{NTf}_2]$  SEI dataset: depth profile plot for assignments with the most significant (highest loadings) assignments in each PC.

## Appendices

The following figures display the lack of fit for the NMF analysis, followed by NMF analysis of 3D OrbiSIMS assignments with lower intensity.

The raw 3D OrbiSIMS dataset and MVA of the SEI with the mixed electrolyte are also displayed afterwards.

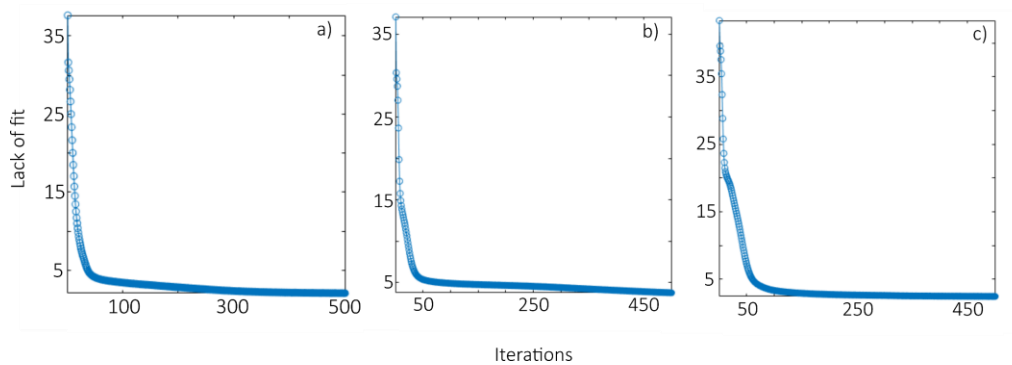


**Figure A 18.** Lack of fit for NMF analysis of a) Na-[C<sub>1</sub>C<sub>dma</sub>Pyrr][NTf<sub>2</sub>] SEI, b) Na-[N<sub>C<sub>1</sub>,C<sub>1</sub>,C<sub>2</sub>,C<sub>2</sub>OC<sub>1</sub></sub>][NTf<sub>2</sub>] SEI and c) Na-[N<sub>C<sub>1</sub>,C<sub>1</sub>,C<sub>2</sub>,C<sub>4</sub></sub>][NTf<sub>2</sub>] SEI.

## Appendices

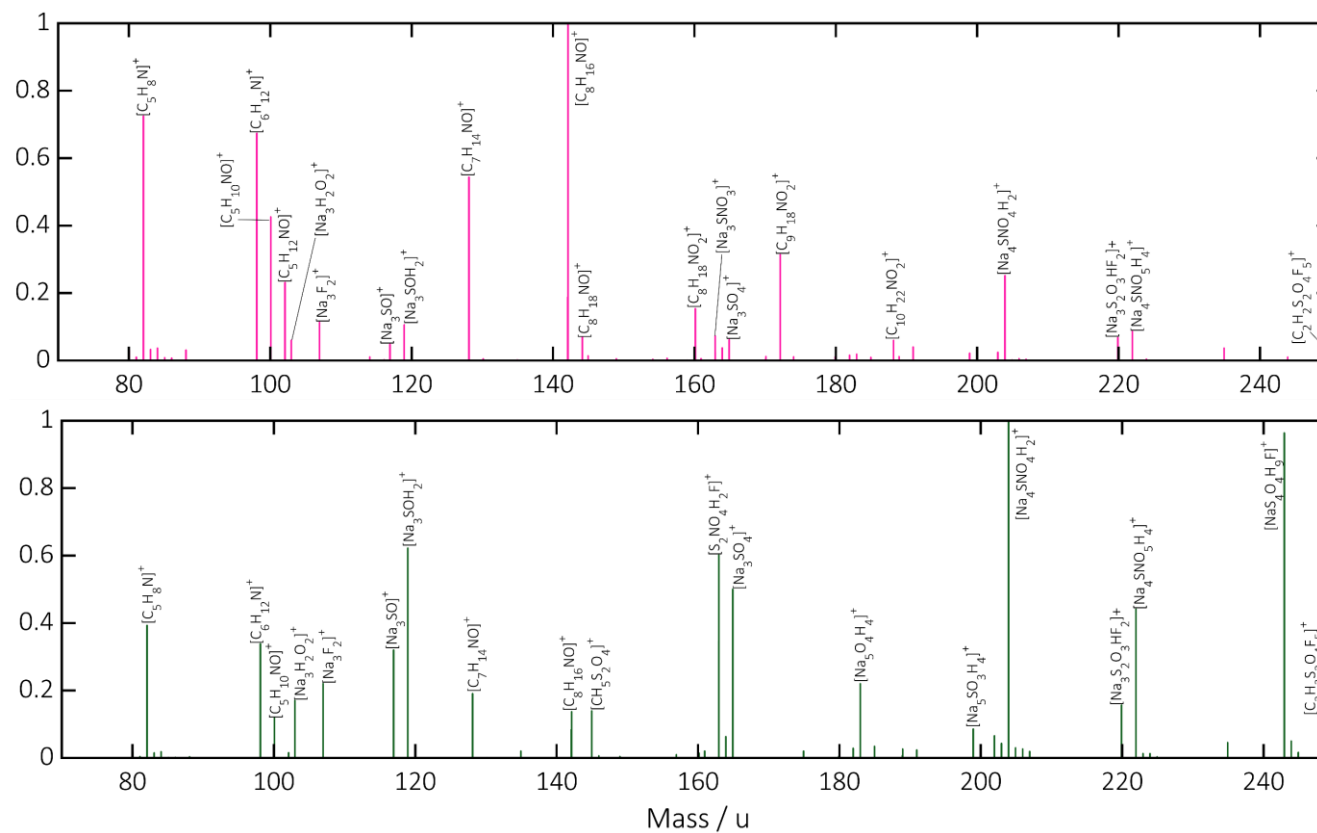


**Figure A 19.Part I.** NMF characteristic spectra of Na-[C<sub>1</sub>C<sub>dma</sub>Pyrr][NTf<sub>2</sub>] (0.5 M Na[NTf<sub>2</sub>]) interphase without high intensity assignments showing endmembers 1 (pink) and 2 (green).

## Appendices

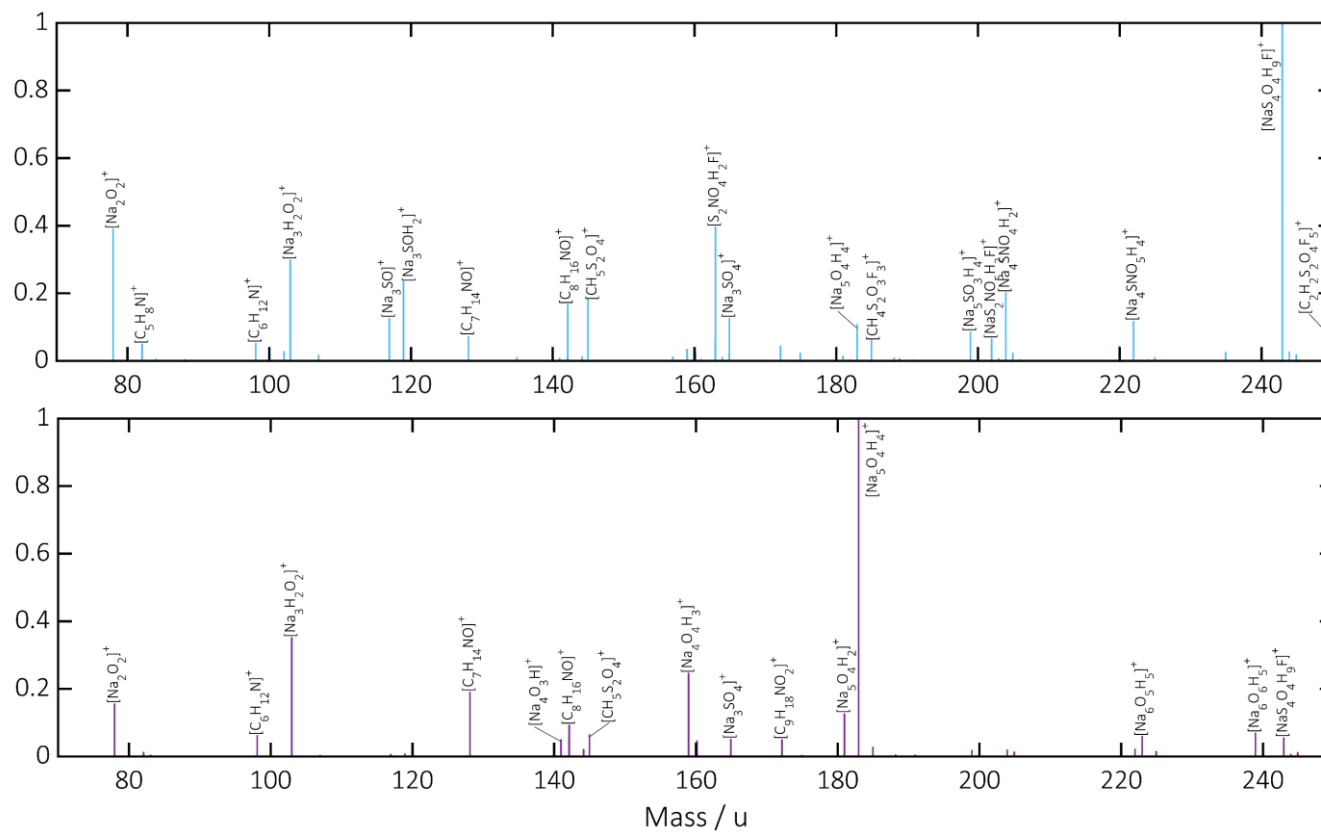


**Figure A 20.Part II:** NMF characteristic spectra of Na-[C<sub>1</sub>C<sub>dma</sub>Pyrr][NTf<sub>2</sub>] (0.5 M Na[NTf<sub>2</sub>]) interphase without high intensity assignments showing endmembers 3 (blue) and 4 (purple).

## Appendices

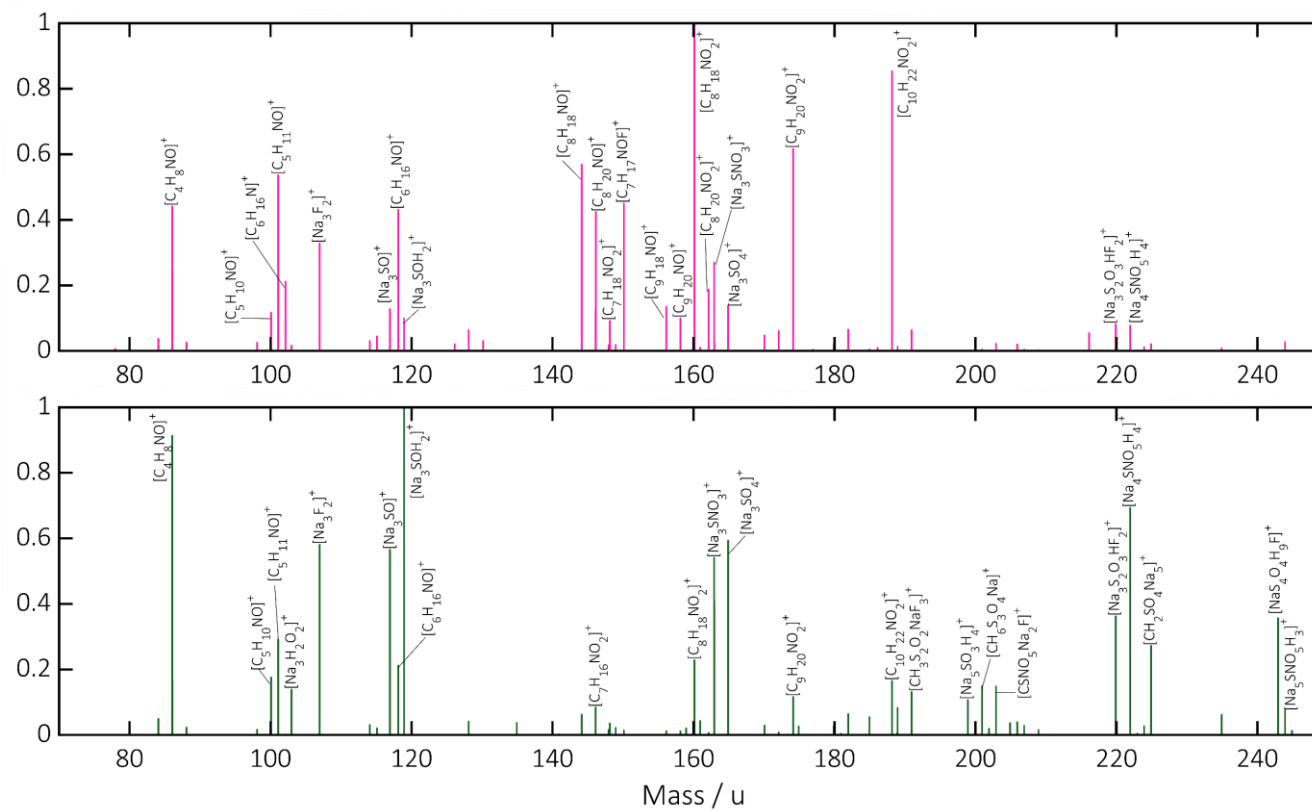


**Figure A 21.Part I.** NMF characteristic spectra of  $\text{Na}-[\text{N}_{\text{C}_1,\text{C}_1,\text{C}_2,(\text{C}_2\text{OC}_1)}][\text{NTf}_2]$  (0.5 M  $\text{Na}[\text{NTf}_2]$ ) interphase without high intensity assignments showing endmembers 1 (pink) and 2 (green)..

## Appendices

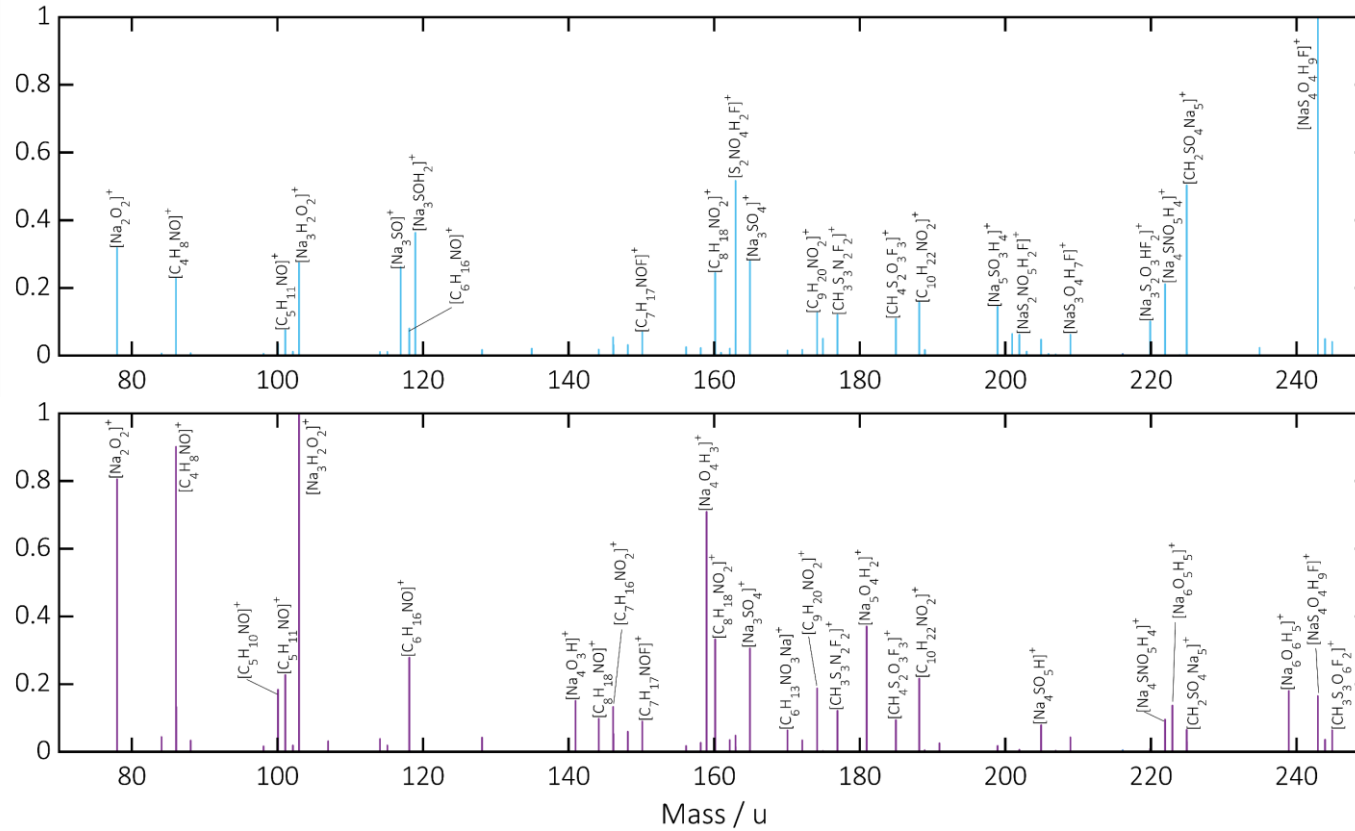


**Figure A 22.Part II:** NMF characteristic spectra of Na-[N<sub>C<sub>1</sub>,C<sub>1</sub>,C<sub>2</sub>,C<sub>2</sub>OC<sub>1</sub>][NTf<sub>2</sub>] (0.5 M Na[NTf<sub>2</sub>]) interphase without high intensity assignments showing endmembers 3 (blue) and 4 (purple).</sub>

# Appendices

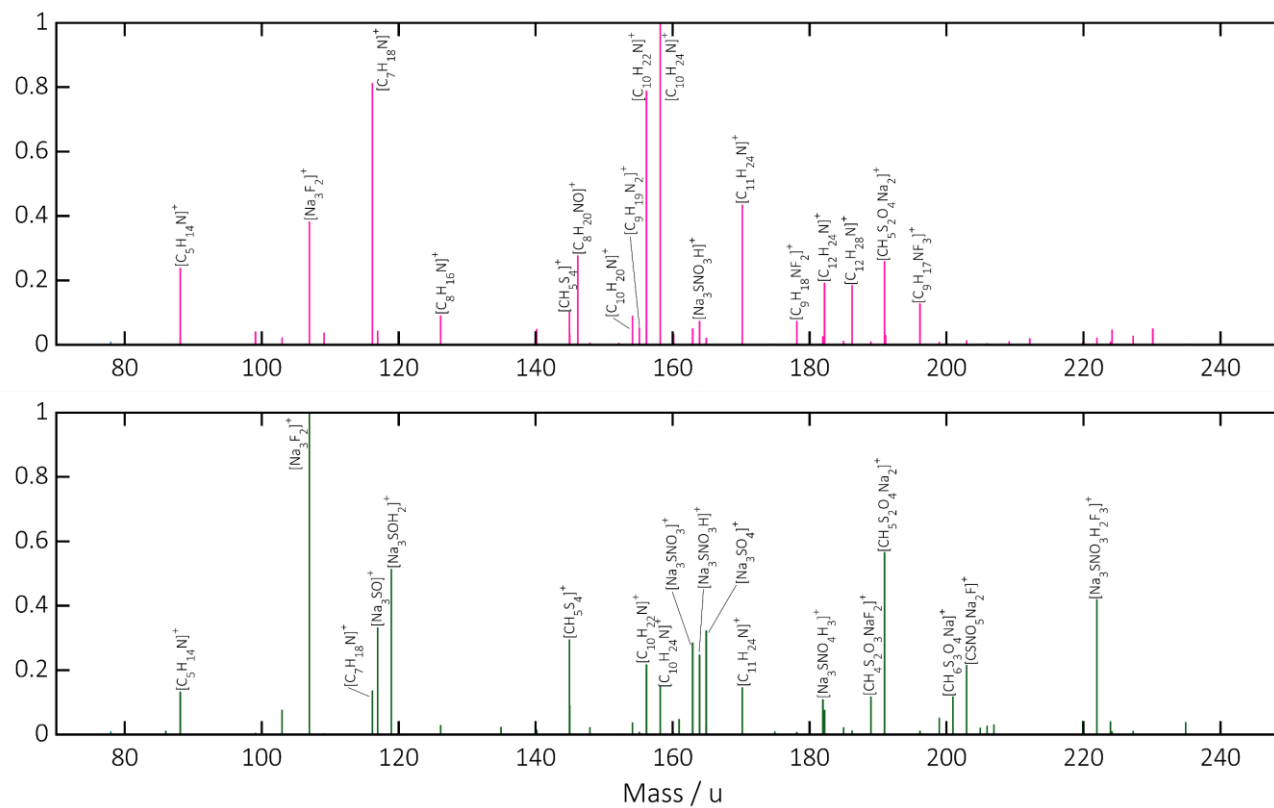


**Figure A 23.Part I.** NMF characteristic spectra of Na-[N<sub>C<sub>1</sub>,C<sub>1</sub>,C<sub>2</sub>,C<sub>4</sub></sub>][NTf<sub>2</sub>] (0.5 M Na[NTf<sub>2</sub>]) interphase without high intensity assignments showing endmembers 1 (pink) and 2 (green).

## Appendices

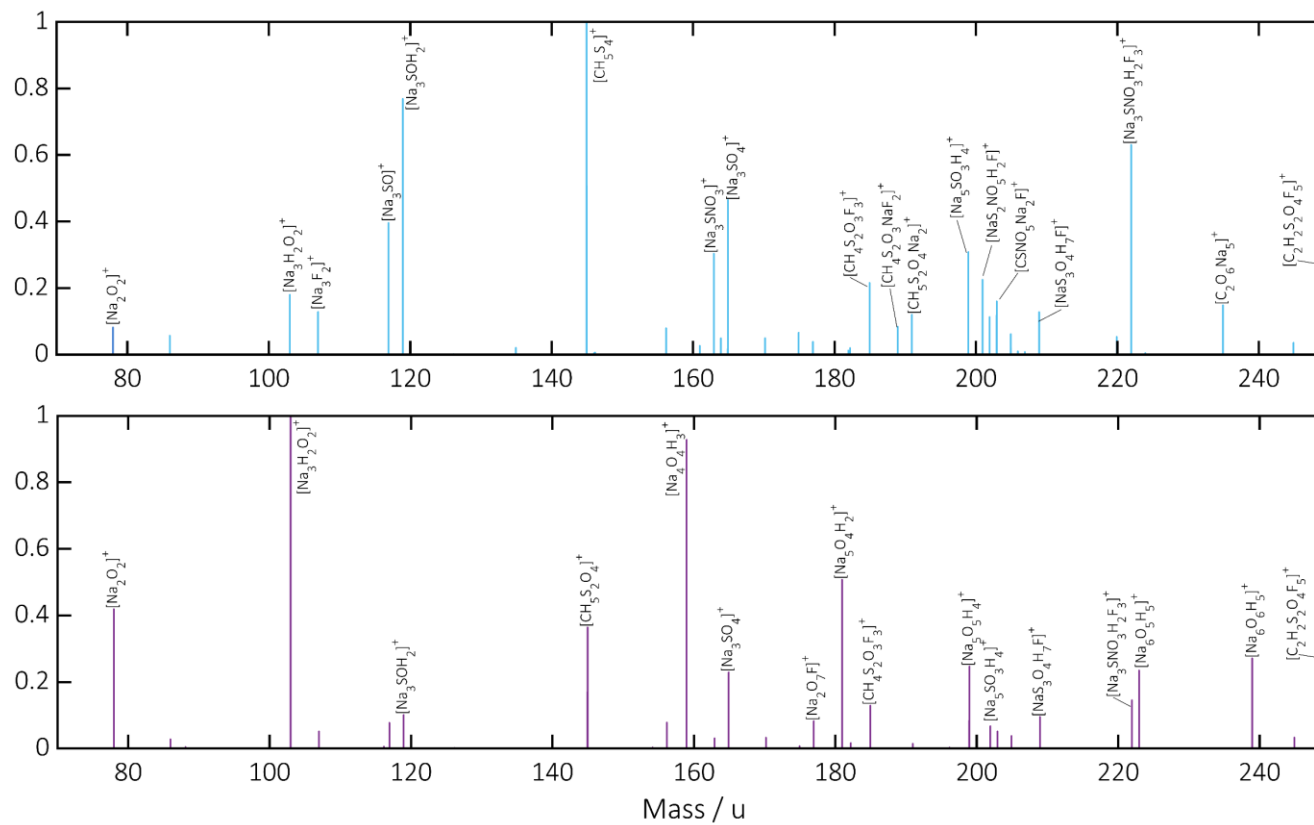


**Figure A 24.Part II:** NMF characteristic spectra of  $Na-[N_{C_1,C_1,C_2,C_4}][NTf_2]$  (0.5 M  $Na[NTf_2]$ ) interphase without high intensity assignments showing endmembers 3 (blue) and 4 (purple).

## Appendices

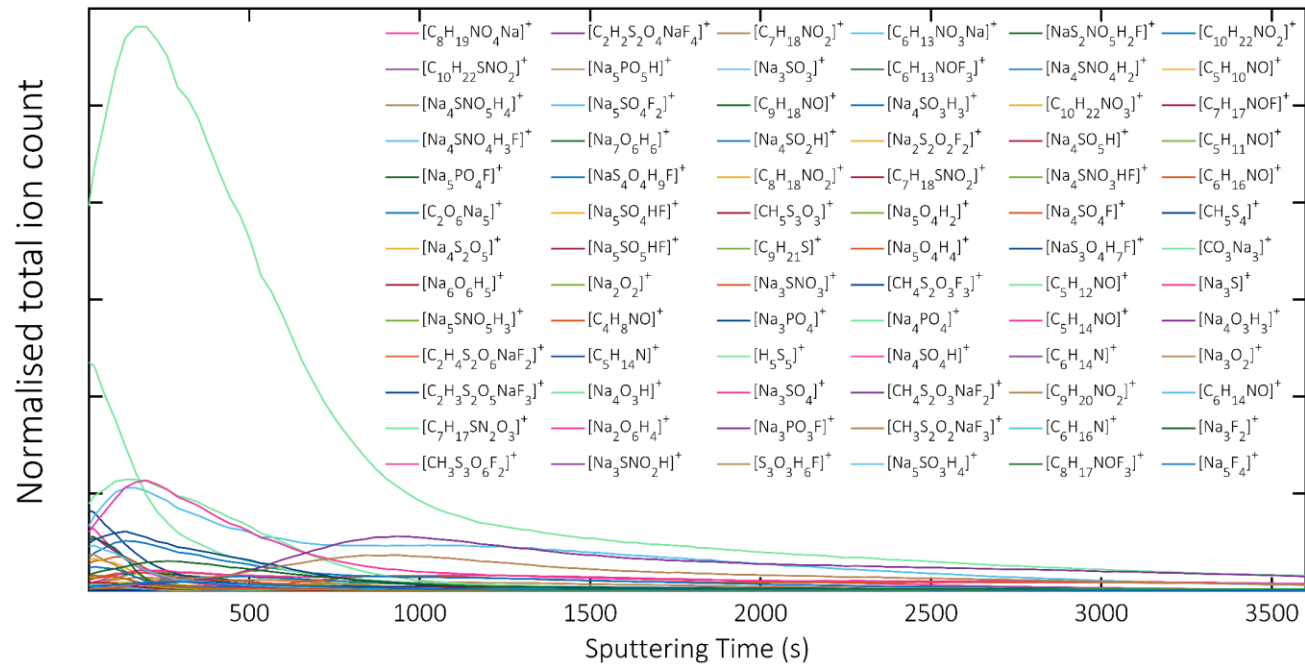


**Figure A 25.** Positive ion depth profile of Na-[N<sub>C<sub>1</sub>,C<sub>1</sub>,C<sub>2</sub>,C<sub>2</sub>(C<sub>2</sub>O<sub>C<sub>1</sub>)</sub>][NTf<sub>2</sub>] interphase (with 0.5 M Na<sup>+</sup> salts, 50 % Na[NTf<sub>2</sub>] and 50 % Na[PF<sub>6</sub>]) using 20 keV Ar<sub>3000</sub><sup>+</sup> for sputtering and analysis</sub>

## Appendices

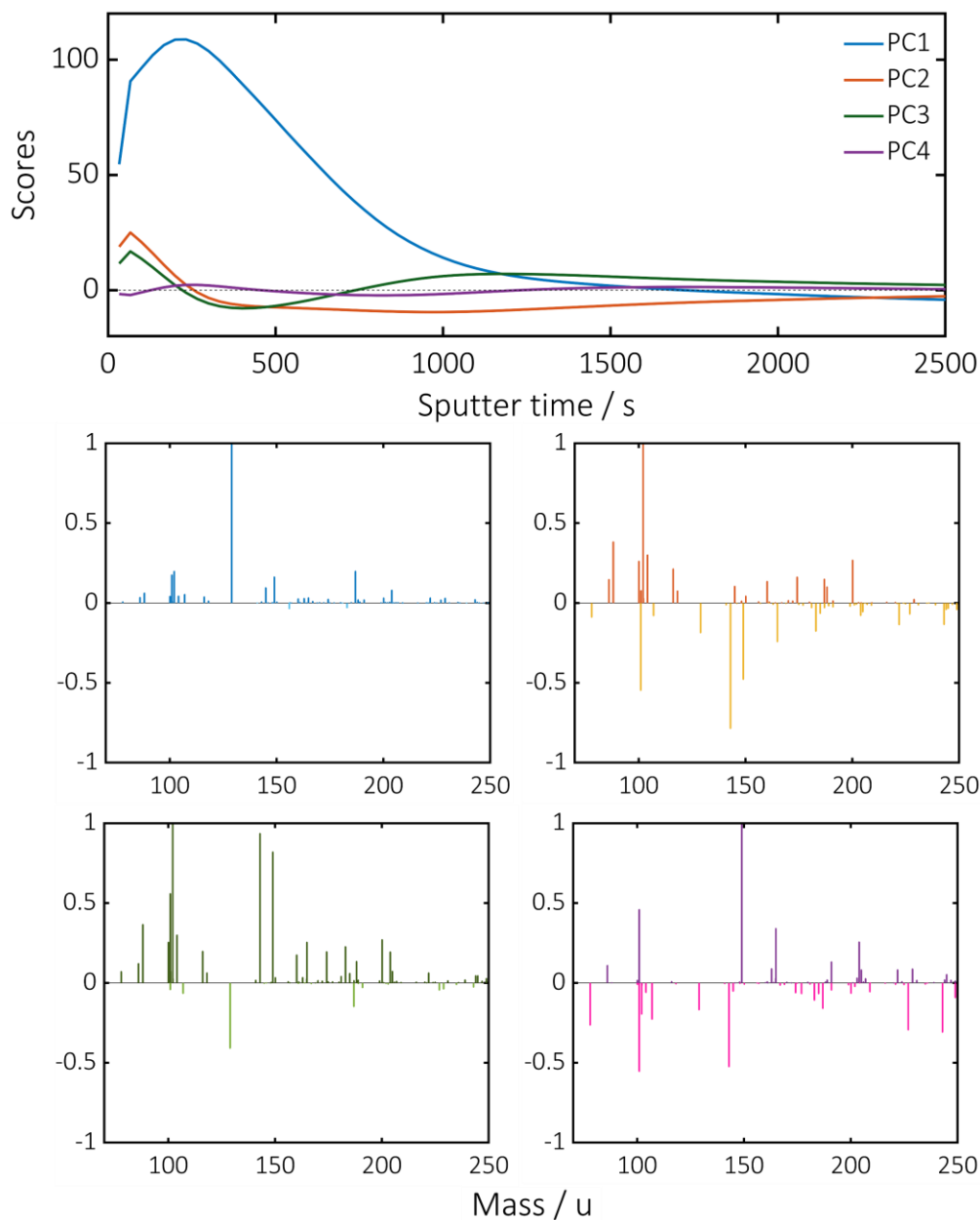


**Figure A 26.** Analysis of PCA results to determine number of endmembers for NMF analysis of  $\text{Na}[\text{N}_{\text{C}_1, \text{C}_1, \text{C}_2, (\text{C}_2\text{OC}_1)}][\text{NTf}_2]$  (with 0.5 M  $\text{Na}^+$ , 50 %  $\text{Na}[\text{PF}_6]$  and 50 %  $\text{Na}[\text{NTf}_2]$ ) SEI dataset: depth profile plot for assignments with the most significant (highest loadings) assignments in each PC.

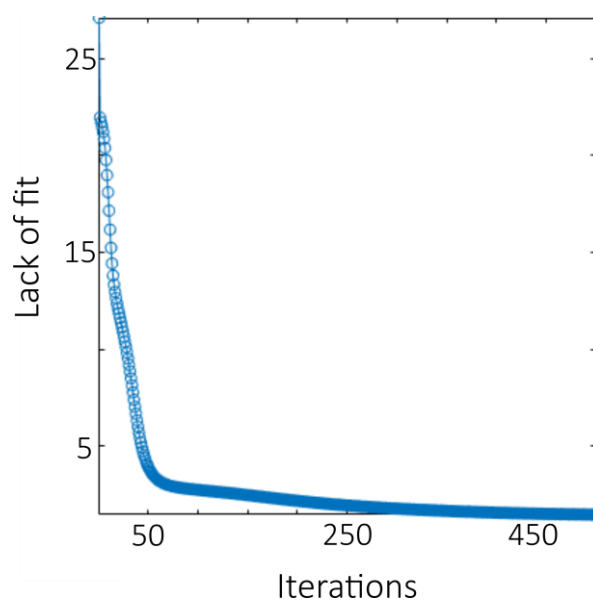


**Figure A 27.** Lack of fit for NMF analysis of  $\text{Na}[\text{N}_{\text{C}_1, \text{C}_1, \text{C}_2, (\text{C}_2\text{OC}_1)}][\text{NTf}_2]$  with 50 %  $\text{Na}[\text{PF}_6]$  and 50%  $\text{Na}[\text{NTf}_2]$  SEI.

## Appendices

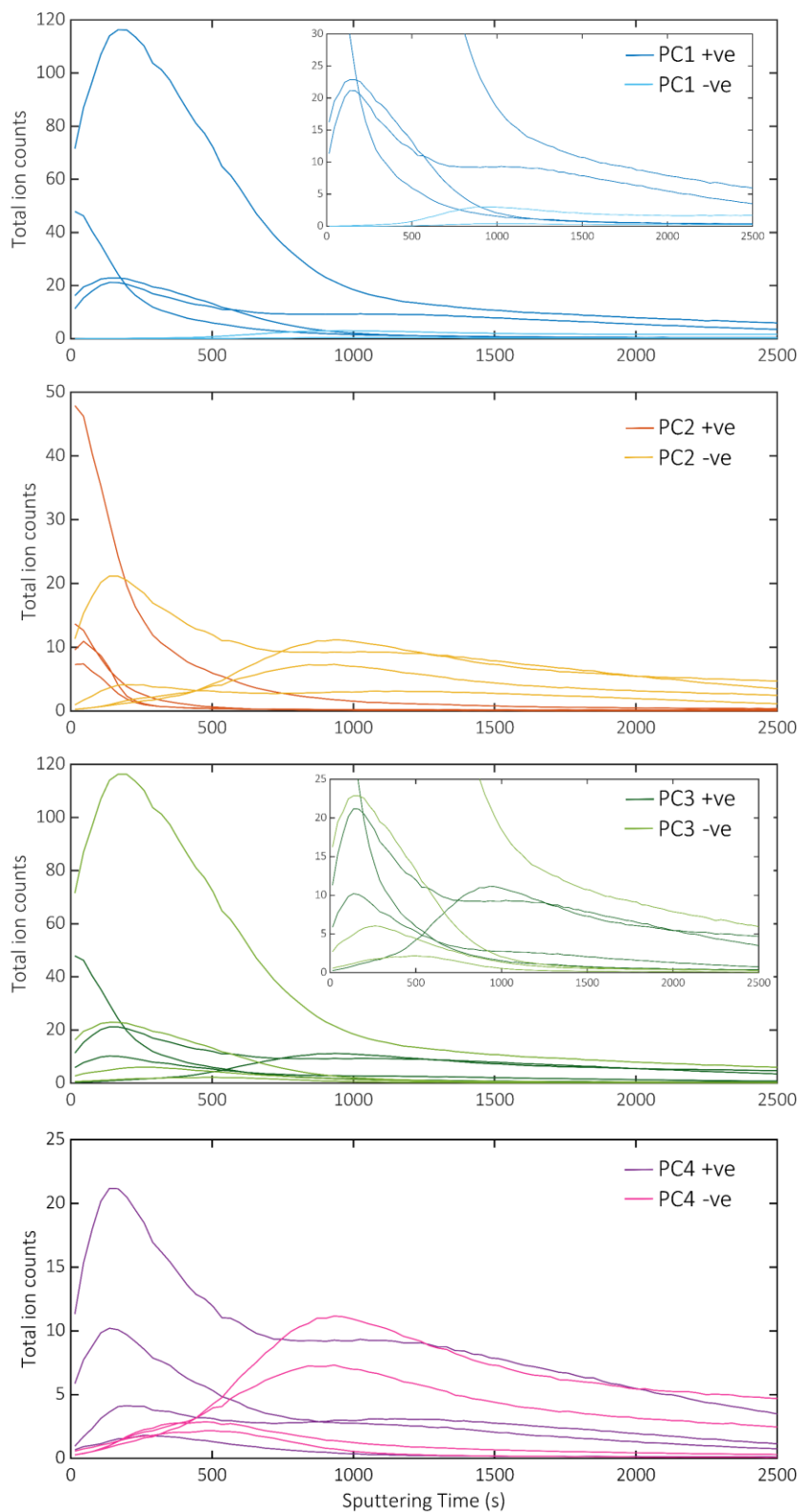


**Figure A 28.** Analysis of PCA results to determine number of endmembers for NMF analysis of  $\text{Na}[\text{N}_{\text{C}_1, \text{C}_1, \text{C}_2, (\text{C}_2\text{OC}_1)}][\text{NTf}_2]$  (0.5 M  $\text{Na}^+$ , 50 %  $\text{Na}[\text{NTf}_2]$  and 50 %  $\text{Na}[\text{PF}_6]$ ) SEI dataset: depth profile plot for assignments with the most significant (highest loadings) assignments in each PC.

# Appendices

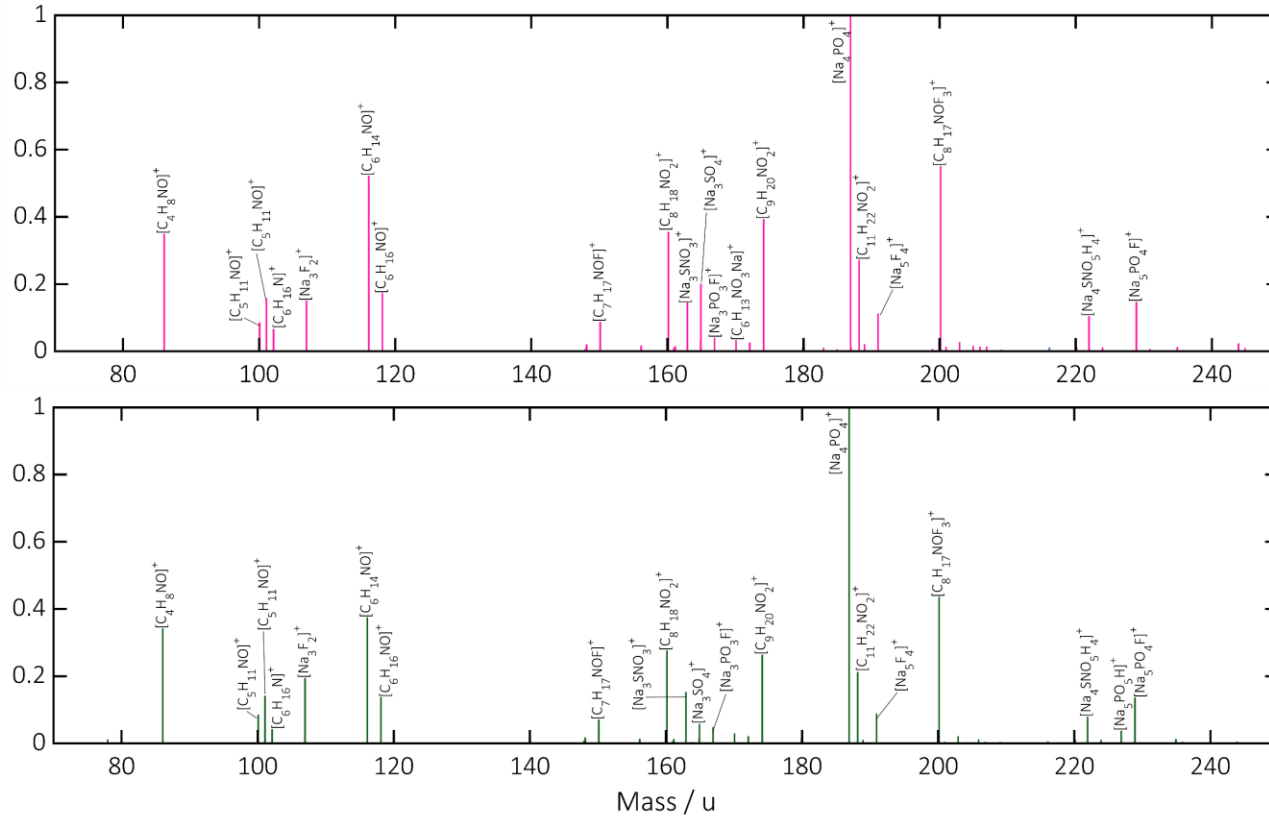
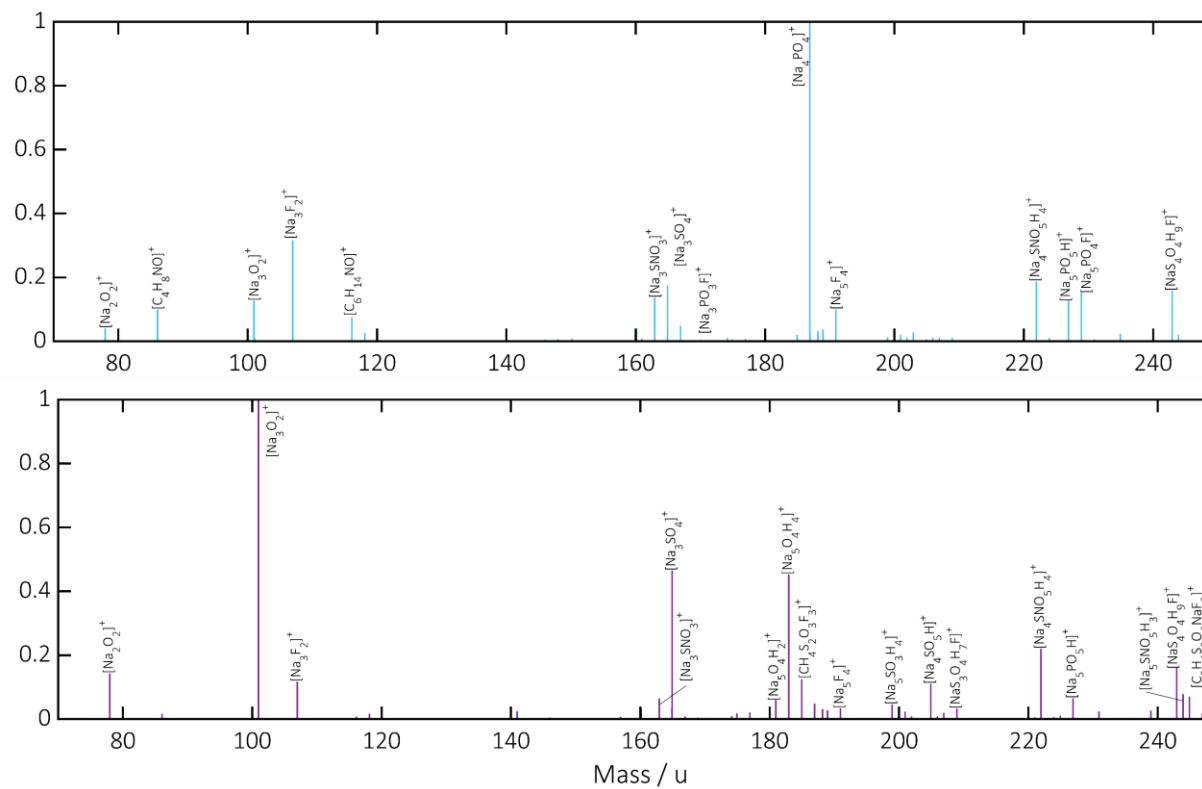


Figure A 29.Part I. NMF characteristic spectra of Na-[N<sub>C<sub>1</sub>,C<sub>1</sub>,C<sub>2</sub>,C<sub>2</sub>OC<sub>1</sub></sub>][NTf<sub>2</sub>] (0.5 M Na<sup>+</sup>, 50 % Na[NTf<sub>2</sub>], 50 % Na[PF<sub>6</sub>]) interphase without high intensity assignments showing endmembers 1 (pink) and 2 (green).

## Appendices



**Figure A 30.Part II:** NMF characteristic spectra of Na-[N<sub>C<sub>1</sub>,C<sub>1</sub>,C<sub>2</sub>,C<sub>2</sub>OC<sub>1</sub>][NTf<sub>2</sub>] (0.5 M Na<sup>+</sup>, 50 % Na[NTf<sub>2</sub>], 50 % Na[PF<sub>6</sub>]) interphase without high intensity assignments showing endmembers 3 (blue) and 4 (purple).</sub>

## A.3. Fundamental studies in the ORR in ILs

## A.3.1. Potential step chronoamperometry using a microdisc electrode

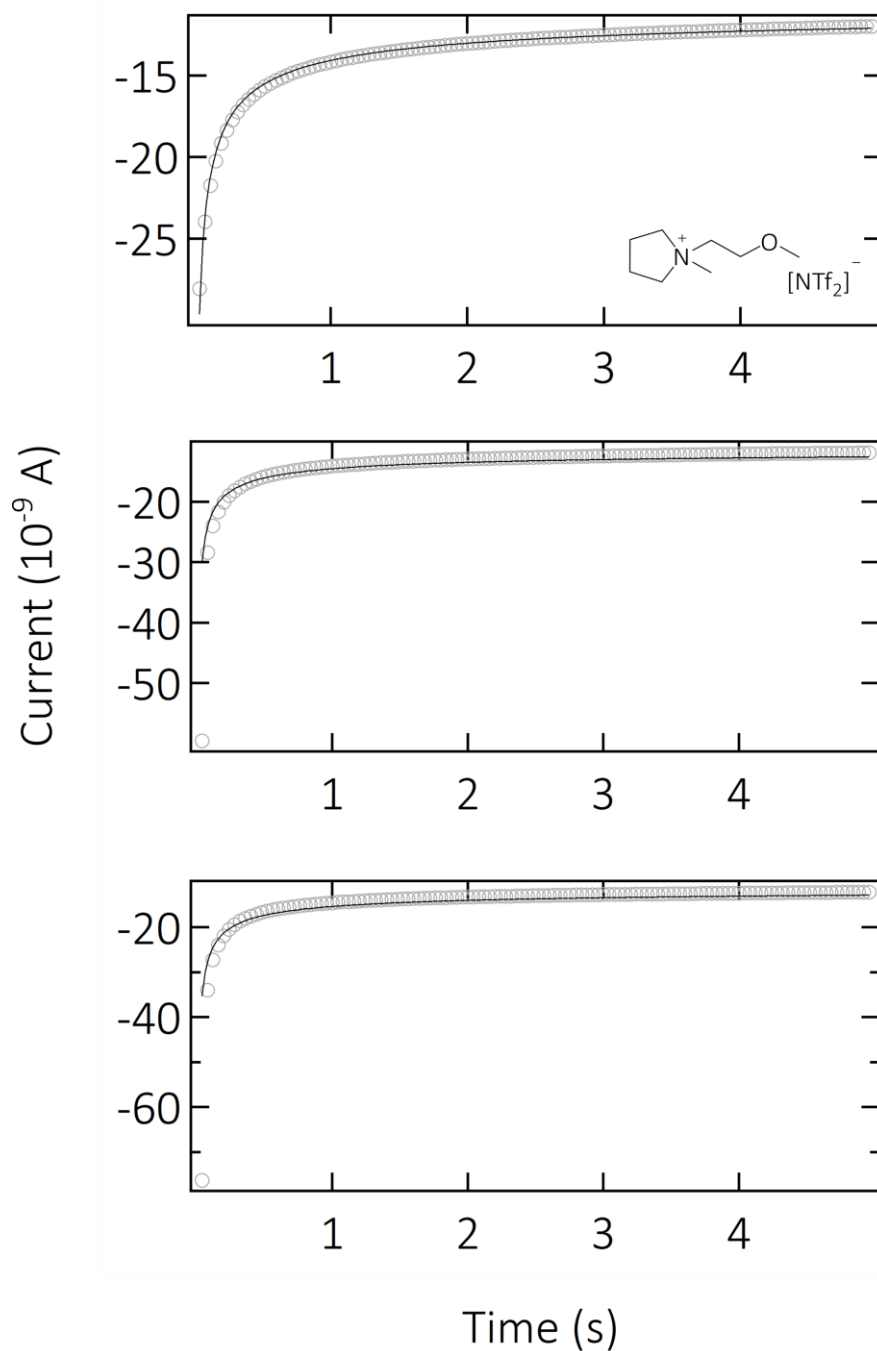


**Figure A 31.** Potential step chronoamperogram for the reduction of  $\text{O}_2$  in  $[\text{C}_1(\text{C}_2\text{OC}_1)\text{Pyr}][\text{NTf}_2]$  at  $-1.4$  V. The grey circles ( $\circ\circ$ ) show the experimental data and the black lines ( $—$ ) show the fitted data.

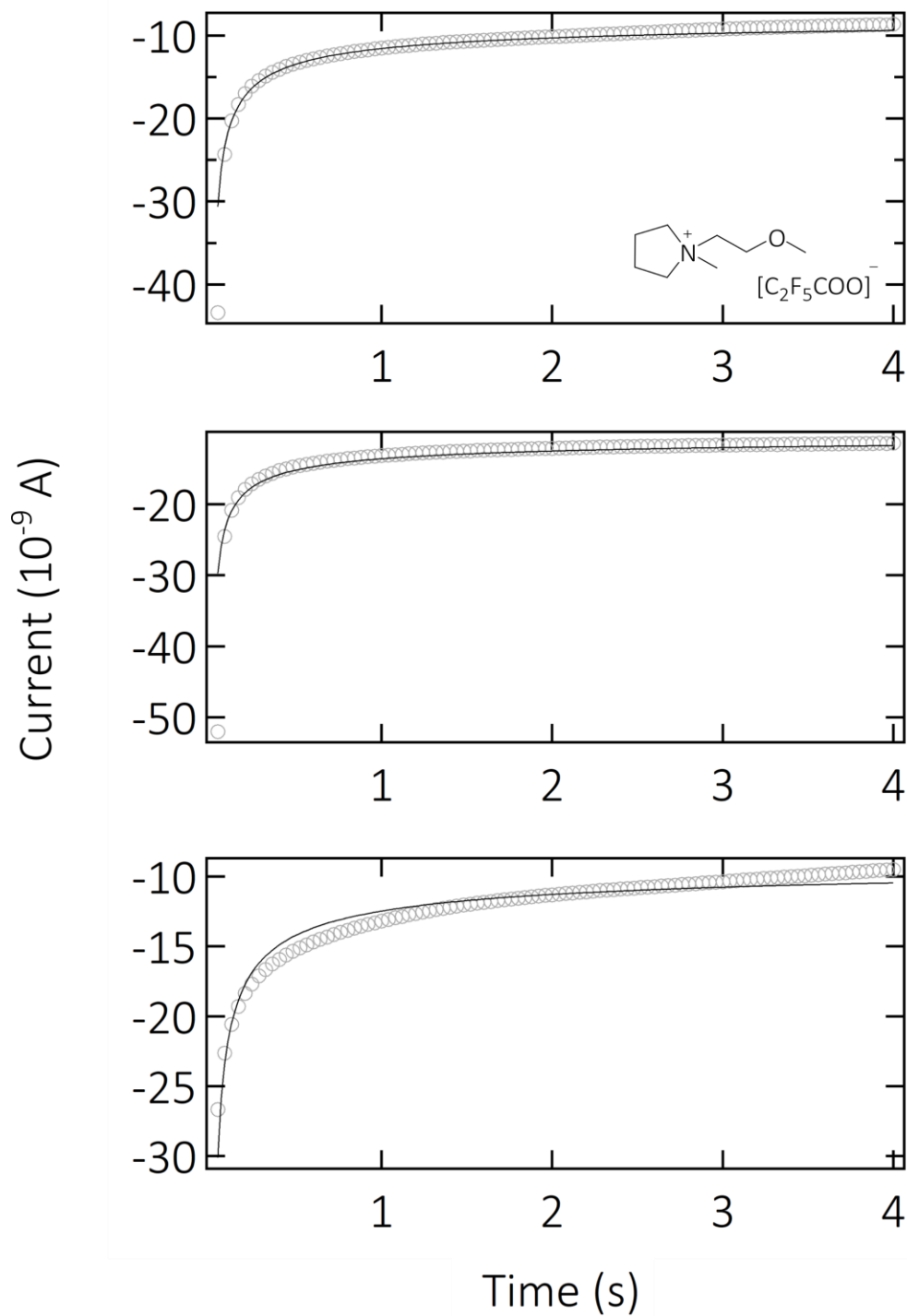


**Figure A 32.** Potential step chronoamperogram for the reduction of  $O_2$  in  $[C_1(C_2OC_1)Pyrr][C_2F_5COO]$  at  $-1.5$  V. The grey circles ( $\circ\circ$ ) show the experimental data and the black lines ( $—$ ) show the fitted data.

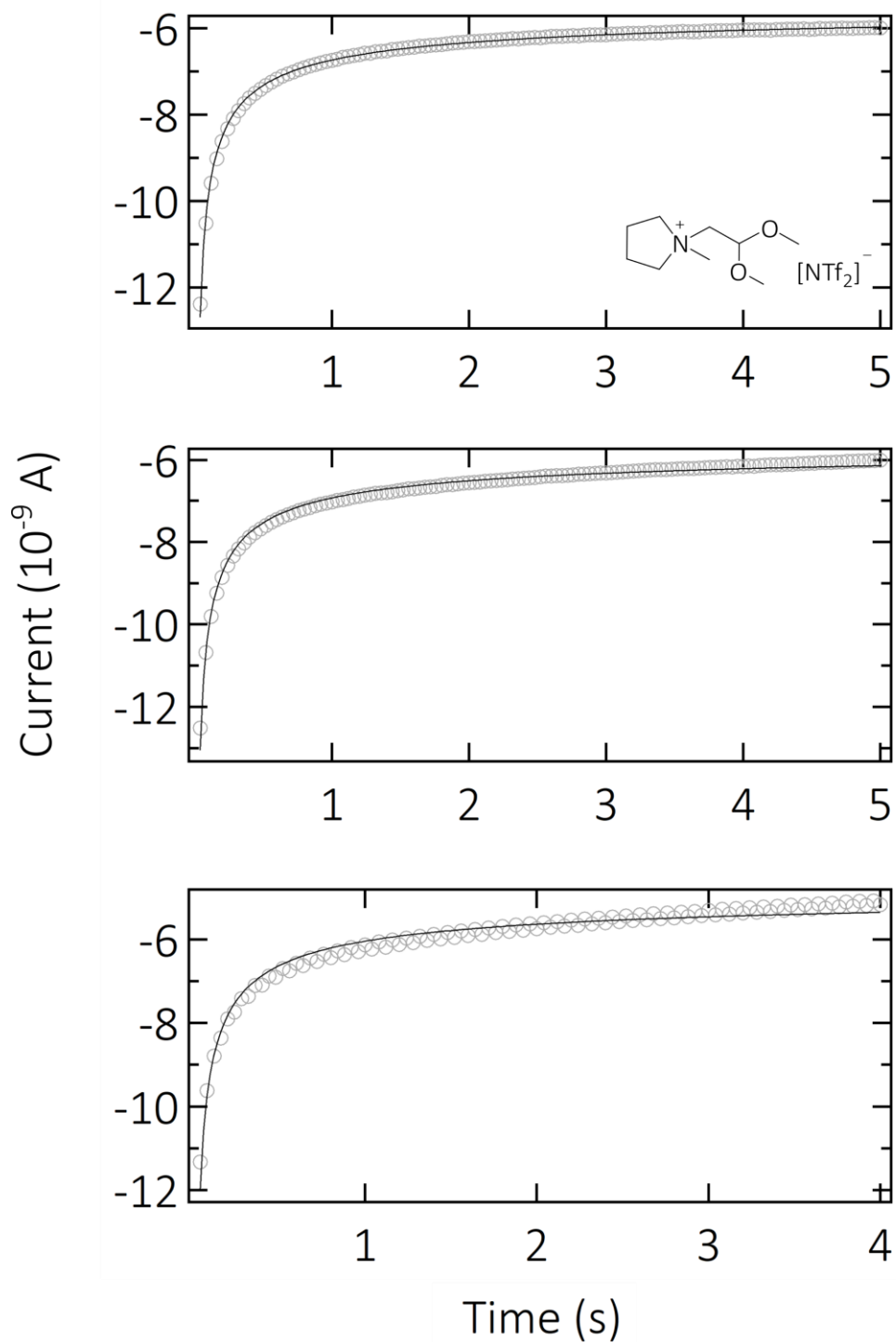


**Figure A 33.** Potential step chronoamperogram for the reduction of  $O_2$   $[C_1C_{dma}Pyrr][NTf_2]$  at  $-1.4$  V. The grey circles ( $\circ$ ) show the experimental data and the black lines ( $—$ ) show the fitted data.

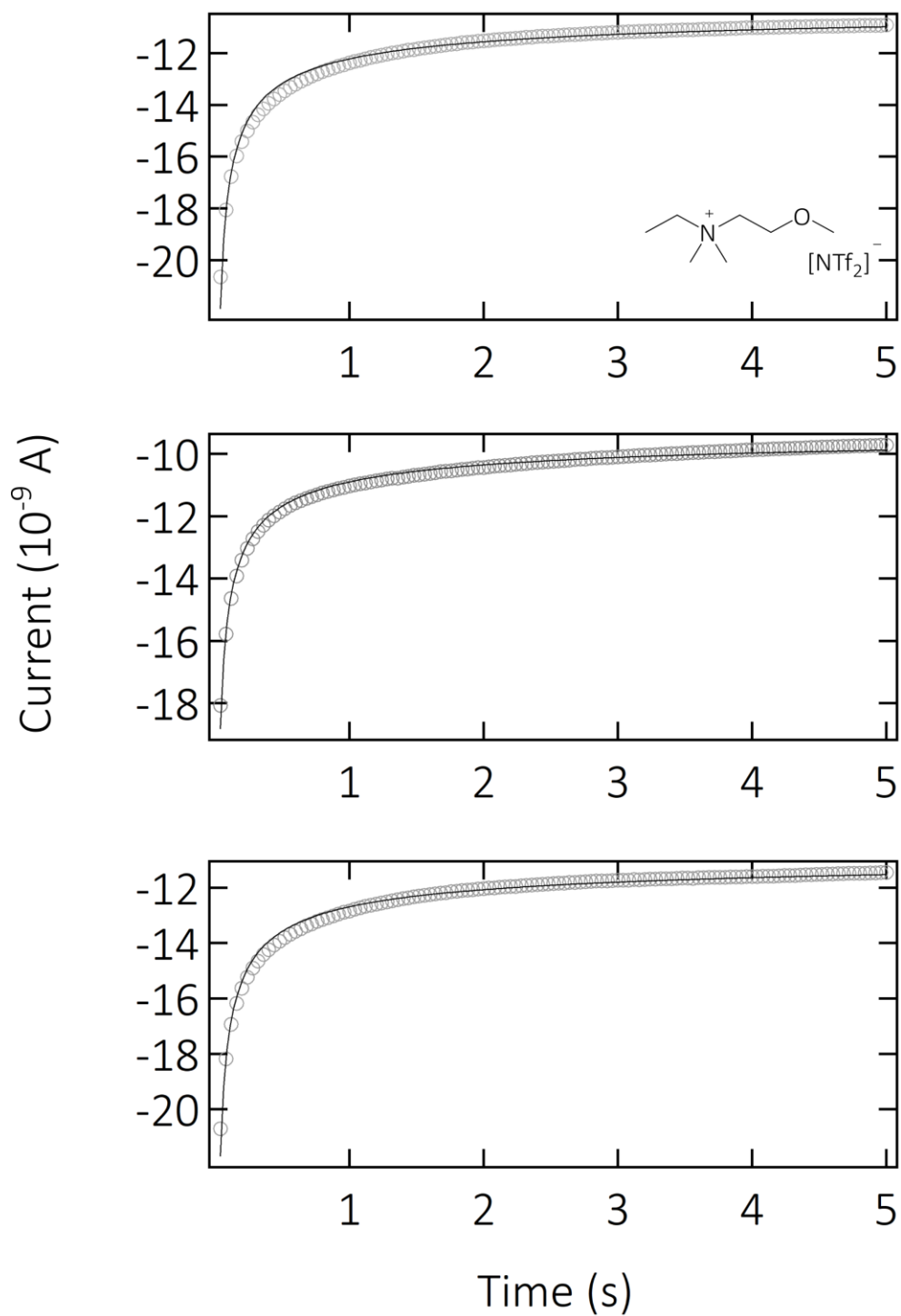


**Figure A 34.** Potential step chronoamperogram for the reduction of  $O_2$  in  $[N_{C_1,C_1,C_2,(C_2OC_1)}][NTf_2]$  at  $-1.4$  V. The grey circles ( $\circ\circ$ ) show the experimental data and the black lines ( $-$ ) show the fitted data.

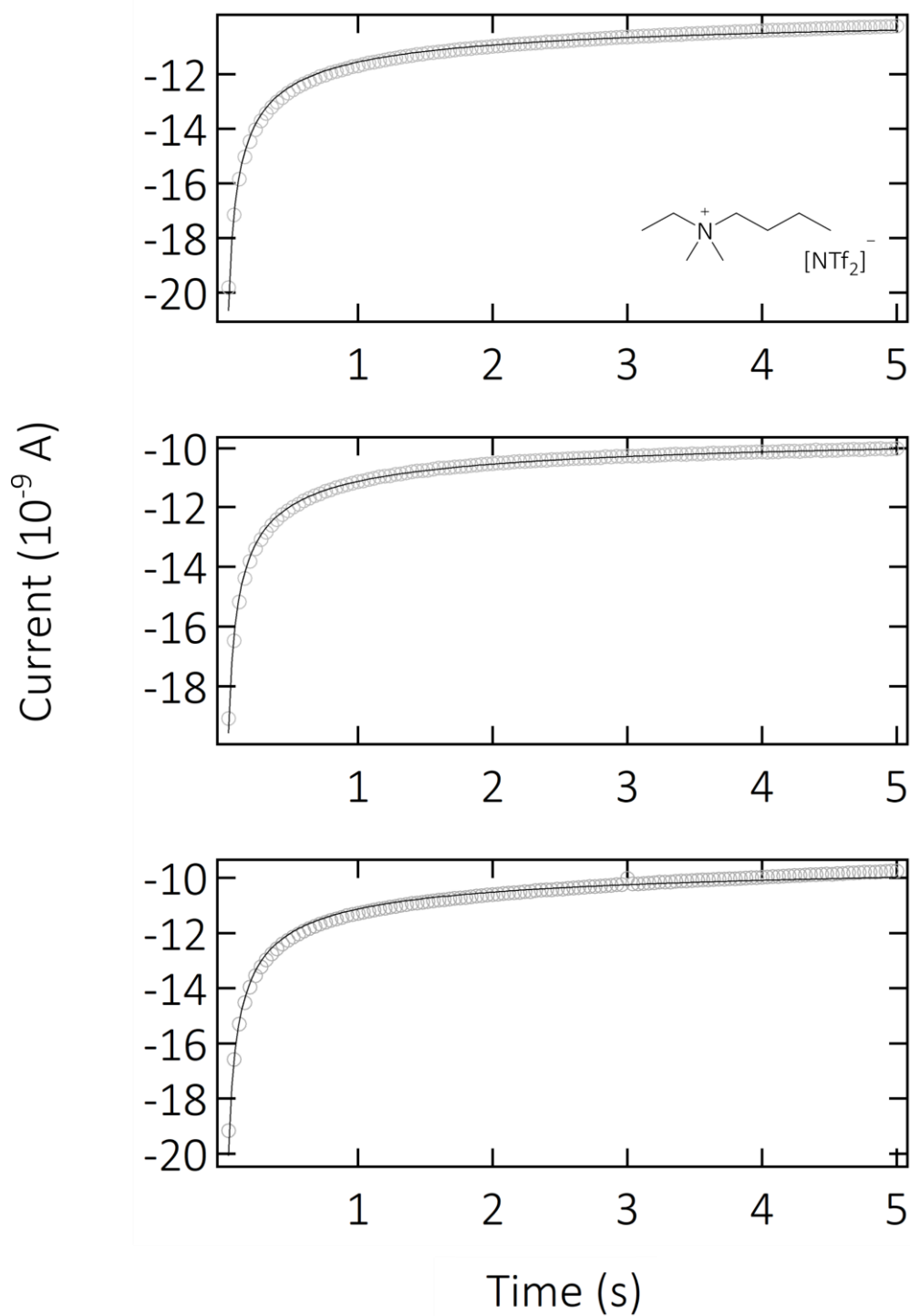


**Figure A 35.** Potential step chronoamperogram for the reduction of O<sub>2</sub> in [N<sub>C<sub>1</sub>,C<sub>1</sub>,C<sub>2</sub>,C<sub>4</sub></sub>][NTf<sub>2</sub>] at -1.4 V. The grey circles (oo) show the experimental data and the black lines (—) show the fitted data.

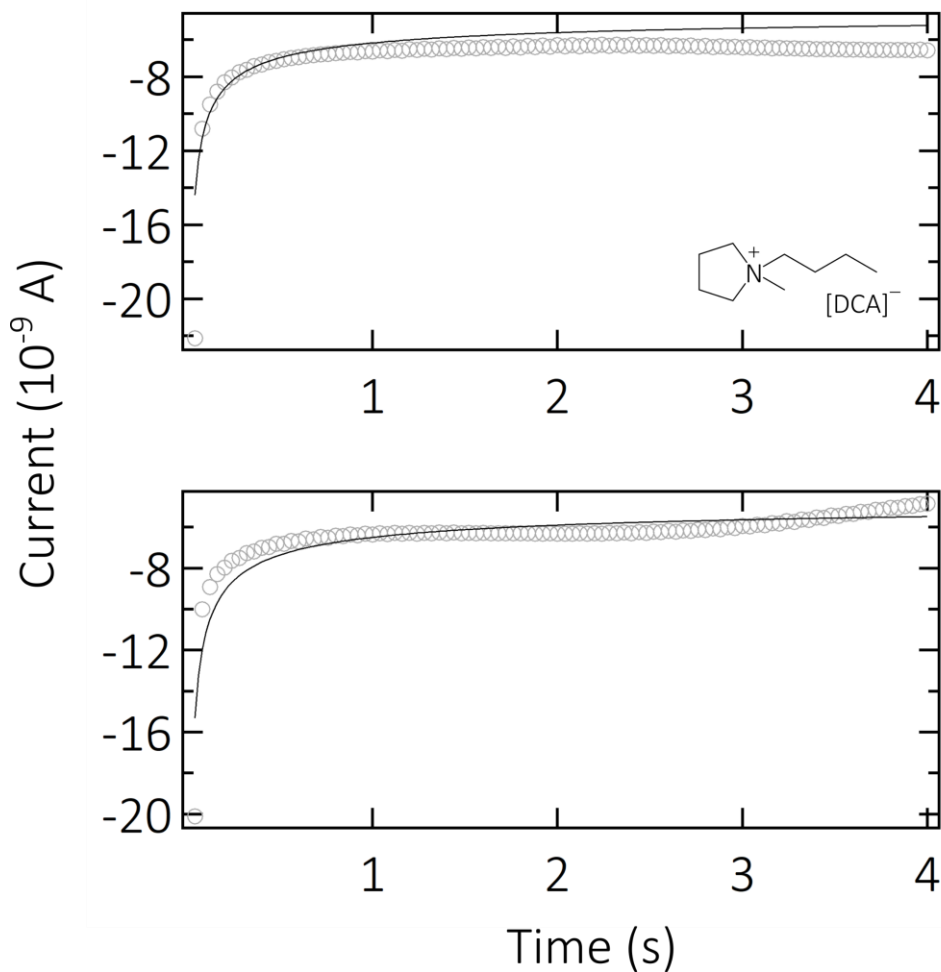


**Figure A 36.** Potential step chronoamperogram for the reduction of  $O_2$  in  $[C_1C_4Pyrr][NTf_2]$  at  $-1.4$  V. The grey circles ( $\circ\circ$ ) show the experimental data and the black lines ( $—$ ) show the fitted data.

#### *Calculated vs experimental steady state current*

To verify the values obtained with Shoup and Szabo equations, the solubility and diffusion coefficients obtained for  $O_2$  in the ILs were used to calculate the steady-state current (see steady-state current equation described at the beginning of this section). The calculated values were compared to the experimental steady-state currents obtained from the CVs in Figure 4.6 in the main text. The calculated and experimental currents, and the percentual difference between the values are displayed in Table A3.1 .

Most of the calculated currents are in good agreement with the experimental currents, with the exception of  $[C_1C_4Pyrr][DCA]$  which reflects the

## Appendices

poor fittings observed for this IL, and  $[N_{C_1,C_1,C_2,(C_2OC_1)}][NTf_2]$ . The fact that the experimental current in  $[N_{C_1,C_1,C_2,(C_2OC_1)}][NTf_2]$  is higher than the calculated suggests that solubility and diffusion coefficient of  $O_2$  are greater than those calculated. However, the values for  $[C_1C_4Pyrr][DCA]$  appear to be an overestimation.

**Table A3.1.** Calculated and experimental steady-state current ( $i_{ss}$ ) for the  $O_2$  reduction in the ILs, also showing the percentual difference between the two values.

IL	$i_{ss}$ calculated ( $10^{-9}$ A)	$i_{ss}$ experimental ( $10^{-9}$ A)	% difference
$[C_1(C_2OC_1)Pyrr][NTf_2]$	11.4	10.9	3.9
$[C_1(C_2OC_1)Pyrr][C_2F_5COO]$	9.35	9.27	0.90
$[C_1C_{dma}Pyrr][NTf_2]$	5.23	5.48	4.8
$[N_{C_1,C_1,C_2,(C_2OC_1)}][NTf_2]$	9.18	10.4	12.7
$[N_{C_1,C_1,C_2,C_4}][NTf_2]$	9.27	9.30	0.3
$[C_1C_4Pyrr][DCA]$	4.37	3.52	19.5

## Appendices

**Table A3.2.** Solubility (C, in  $10^{-6}$  mol/cm<sup>3</sup>) and diffusion coefficients (D, in  $10^{-6}$  mol/cm<sup>3</sup>) of O<sub>2</sub> in various IL reported in the literature.

Ionic liquid	T (°C)	C	D	References
[C <sub>1</sub> C <sub>4</sub> Pyrr][NTf <sub>2</sub> ]	25	13.6	1.8	Miura and co-workers <sup>133</sup>
	25	9.15	2.67	Hardacre and co-workers <sup>128</sup>
	25	3.6	5.49	Compton and co-workers <sup>140</sup>
	25	6.7	5.0	Fransaer and co-workers <sup>168</sup>
	30	2.9	12	Passerini and co-workers <sup>48</sup>
	35	3.7	7.41	Compton and co-workers <sup>140</sup>
	35	6.1	5.2	Compton and co-workers <sup>139</sup>
[C <sub>1</sub> (C <sub>2</sub> OC <sub>2</sub> )Pyrr][NTf <sub>2</sub> ]	25	6.67	3.76	Hardacre and co-workers <sup>128</sup>
	30	3.0	11	Passerini and co-workers <sup>48</sup>
[C <sub>1</sub> (C <sub>2</sub> OC <sub>1</sub> CF <sub>3</sub> )Pyrr][NTf <sub>2</sub> ]	25	26.0	0.8	Fransaer and co-workers <sup>168</sup>
[N <sub>C<sub>2</sub>,C<sub>2</sub>,C<sub>2</sub>,C<sub>6</sub></sub> ][NTf <sub>2</sub> ]	25	3.9	4.55	Compton and co-workers <sup>140</sup>
	35	3.8	6.0	Compton and co-workers <sup>140</sup>
	35	3.2	8.9	Compton and co-workers <sup>140</sup>
[N <sub>C<sub>1</sub>,C<sub>1</sub>,C<sub>2</sub>,C<sub>2</sub>OC<sub>1</sub></sub> ][NTf <sub>2</sub> ]	25	14.9	0.9	AlNashef and co-workers <sup>120</sup>
	35	11.2	2.4	AlNashef and co-workers <sup>120</sup>
[N <sub>C<sub>1</sub>,C<sub>2</sub>,C<sub>2</sub>,C<sub>2</sub>OC<sub>2</sub></sub> ][NTf <sub>2</sub> ]	25	5.1	4.8	Fransaer and co-workers <sup>168</sup>

## Appendices

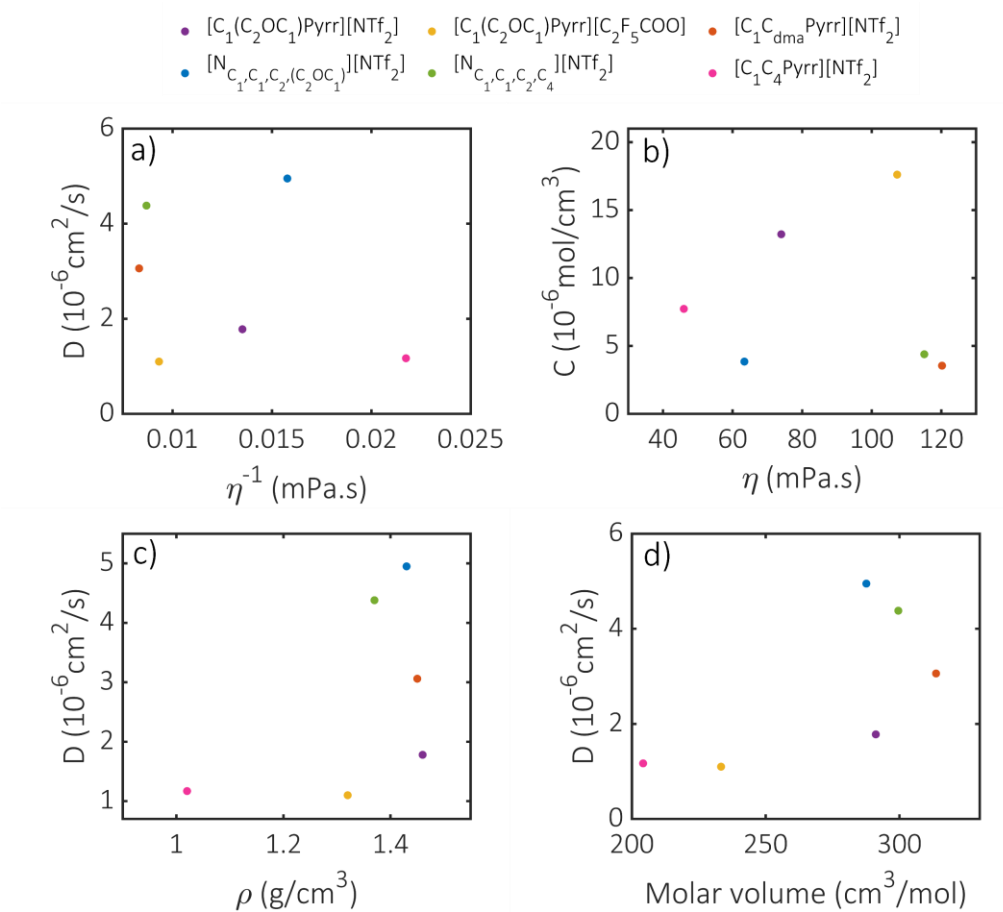


**Figure A 37.** Diffusion of  $O_2$  as a function of IL viscosity (a), density (c) and molar volume (d). Solubility of  $O_2$  as a function of IL viscosity (b), all measurements taken at 20 °C.

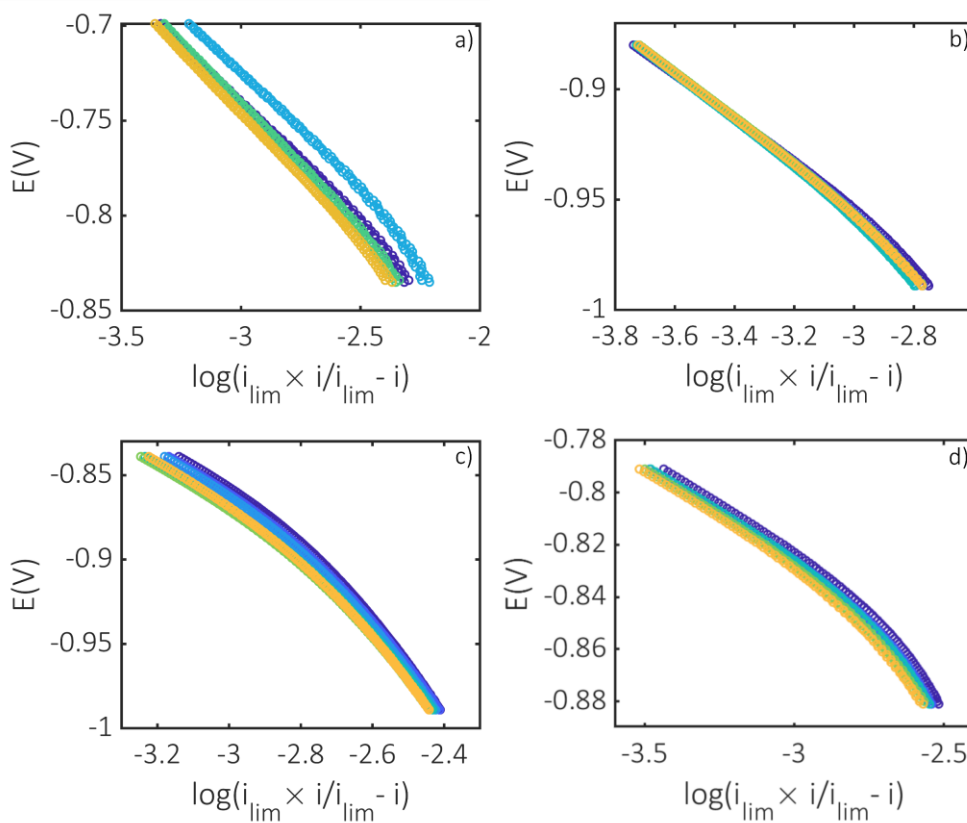


**Figure A 38.** Tafel analysis of LSVs of O<sub>2</sub> reduction in ILs, with rotational speed from — 1300 RPM to — 1800 RPM: a) [C<sub>1</sub>(C<sub>2</sub>OC<sub>1</sub>)Pyrr][NTf<sub>2</sub>], b) [C<sub>1</sub>C<sub>dma</sub>Pyrr][NTf<sub>2</sub>], c) [N<sub>C<sub>1</sub>,C<sub>1</sub>,C<sub>2</sub>,C<sub>2</sub>OC<sub>1</sub></sub>][NTf<sub>2</sub>], d) [N<sub>C<sub>1</sub>,C<sub>1</sub>,C<sub>2</sub>,C<sub>4</sub></sub>][NTf<sub>2</sub>].

## A.4. Oxygen reduction reaction in the presence of alkali metal cations, and an application in Na-O<sub>2</sub> cells

### A.4.1. Potential application in Na-O<sub>2</sub> cells

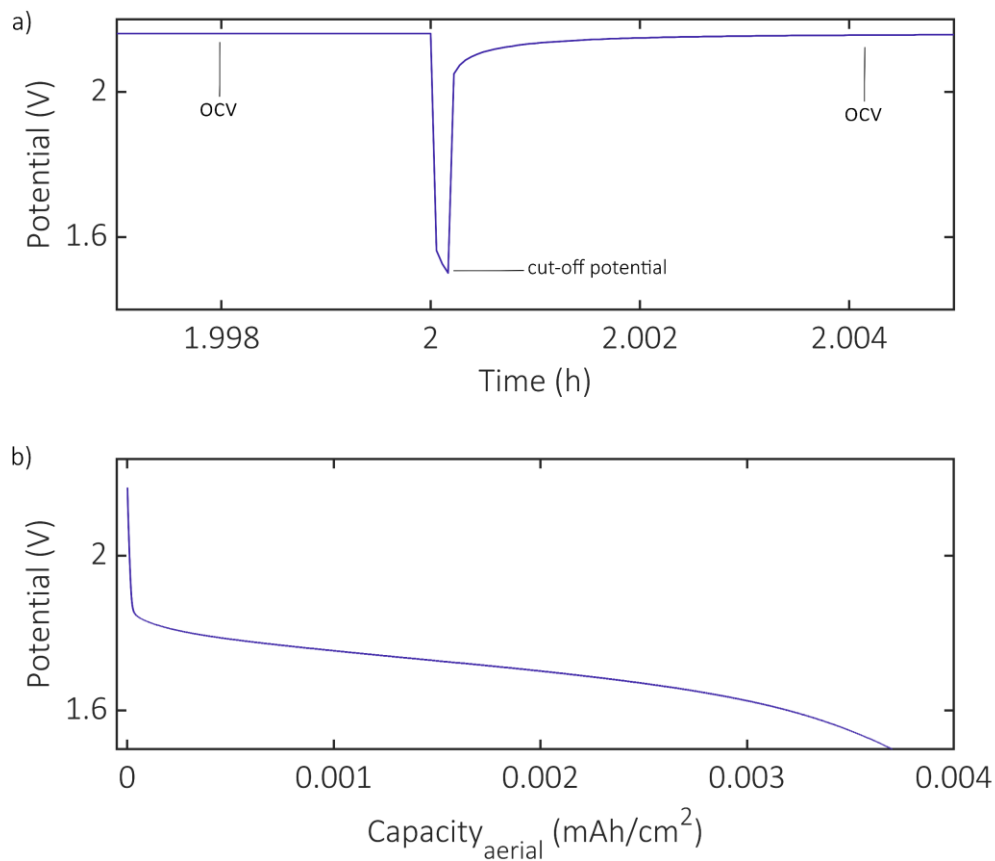


**Figure A 39.** Discharge profile of Na-O<sub>2</sub> cell a) with 2 h of resting before the beginning of the discharge showing that the cell instantly reaches the cut-off potential and returns automatically to the open cell voltage (opv) monitoring; and b) with 24 h of resting before the beginning of the discharge but showing low capacity. Both profiles were obtained with cells using a metallic Na negative electrode, gas diffusion layer positive electrode, two layers of separator with 210  $\mu$ L of electrolyte and run in room temperature.

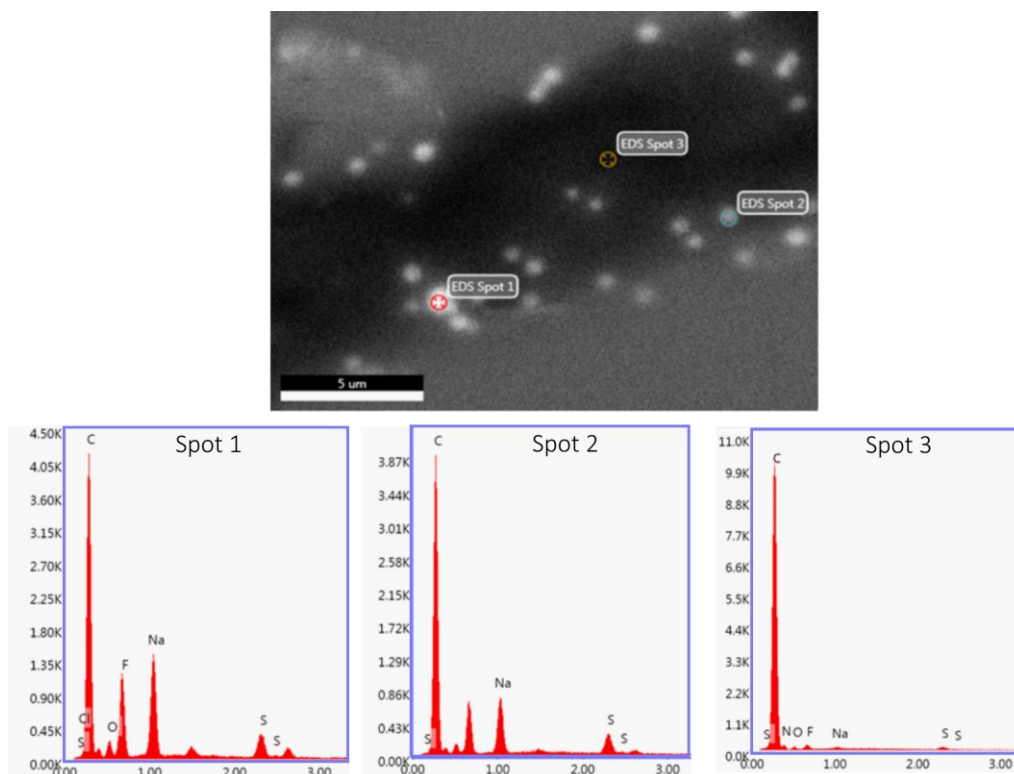


**Figure A 40.** Energy dispersive x-ray analysis (EDX) analysis of scanning electron microscopy image (SEM) of discharged GDL using  $[N_{C_1,C_1,C_2,(C_2OC_1)}][NTf_2]$  IL, showing dark area to be composed in its vast majority by carbon, and the white dots with higher Na content.

## A.5. References

1. Waite, C. Final UK greenhouse gas emissions national statistics. <https://data.gov.uk/dataset/final-uk-greenhouse-gas-emissions-national-statistics> (accessed 27/07/2020).
2. Desai, M.; Camobreco, V. Sources of Greenhouse Gas Emissions. <https://www.epa.gov/ghgemissions/sources-greenhouse-gas-emissions> (accessed 27/07/2020).
3. Albertus, P.; Babinec, S.; Litzelman, S.; Newman, A., Status and challenges in enabling the lithium metal electrode for high-energy and low-cost rechargeable batteries. *Nat. Energy* **2017**, *3* (1), 16-21.
4. Charlton, A. The longest range electric cars of 2020: new EVs with the most charge. <https://www.carmagazine.co.uk/electric/longest-range-electric-cars-ev/> (accessed 25/07/2020).
5. Kwak, W. J.; Rosy; Sharon, D.; Xia, C.; Kim, H.; Johnson, L. R.; Bruce, P. G.; Nazar, L. F.; Sun, Y. K.; Frimer, A. A.; Noked, M.; Freunberger, S. A.; Aurbach, D., Lithium–Oxygen Batteries and Related Systems: Potential, Status, and Future. *Chem. Rev.* **2020**.

6. Sapunkov, O.; Pande, V.; Khetan, A.; Choomwattana, C.; Viswanathan, V., Quantifying the promise of 'beyond' Li-ion batteries. *Transl. Mater. Res.* **2015**, *2* (4), 045002.
7. Lee, B.; Paek, E.; Mitlin, D.; Lee, S. W., Sodium Metal Anodes: Emerging Solutions to Dendrite Growth. *Chem. Rev.* **2019**, *119* (8), 5416-5460.
8. Zheng, X.; Bommier, C.; Luo, W.; Jiang, L.; Hao, Y.; Huang, Y., Sodium metal anodes for room-temperature sodium-ion batteries: Applications, challenges and solutions. *Energy Stor. Mater.* **2019**, *16*, 6-23.
9. Berg, H., Lithium battery materials. In *Batteries for Electric Vehicles: Materials and Electrochemistry*, Cambridge University Press: Cambridge, 2015; pp 83-125.
10. Liu, Z.; Lu, P.; Zhang, Q.; Xiao, X.; Qi, Y.; Chen, L. Q., A Bottom-Up Formation Mechanism of Solid Electrolyte Interphase Revealed by Isotope-Assisted Time-of-Flight Secondary Ion Mass Spectrometry. *J. Phys. Chem. Lett.* **2018**, *9* (18), 5508-5514.
11. Wood, K. N.; Kazyak, E.; Chadwick, A. F.; Chen, K.-H.; Zhang, J.-G.; Thornton, K.; Dasgupta, N. P., Dendrites and Pits: Untangling the Complex Behavior of Lithium Metal Anodes through Operando Video Microscopy. *ACS Cent. Sci.* **2016**, *2* (11), 790-801.
12. Rodriguez, R.; Loeffler, K. E.; Nathan, S. S.; Sheavly, J. K.; Dolocan, A.; Heller, A.; Mullins, C. B., In Situ Optical Imaging of Sodium Electrodeposition: Effects of Fluoroethylene Carbonate. *ACS Energy Lett.* **2017**, *2* (9), 2051-2057.
13. Deng, Y.; Zheng, J.; Warren, A.; Yin, J.; Choudhury, S.; Biswal, P.; Zhang, D.; Archer, L. A., On the Reversibility and Fragility of Sodium Metal Electrodes. *Adv. Energy Mater.* **2019**, *9* (39).
14. Chen, K.-H.; Wood, K. N.; Kazyak, E.; LePage, W. S.; Davis, A. L.; Sanchez, A. J.; Dasgupta, N. P., Dead lithium: mass transport effects on voltage, capacity, and failure of lithium metal anodes. *J. Mater. Chem. A* **2017**, *5* (23), 11671-11681.
15. Matios, E.; Wang, H.; Wang, C.; Li, W., Enabling Safe Sodium Metal Batteries by Solid Electrolyte Interphase Engineering: A Review. *Ind. Eng. Chem. Res.* **2019**, *58* (23), 9758-9780.
16. Wang, H.; Yu, D.; Kuang, C.; Cheng, L.; Li, W.; Feng, X.; Zhang, Z.; Zhang, X.; Zhang, Y., Alkali Metal Anodes for Rechargeable Batteries. *Chem* **2019**, *5* (2), 313-338.
17. Wang, Y.; Wang, Y.; Wang, Y.; Feng, X.; Chen, W.; Ai, X.; Yang, H.; Cao, Y., Developments and Perspectives on Emerging High-Energy-Density Sodium-Metal Batteries. *Chem* **2019**, *5* (10), 2547-2570.
18. Ma, L. B.; Cui, J.; Yao, S.; Liu, X.; Luo, Y.; Shen, X.; Kim, J., Dendrite-free lithium metal and sodium metal batteries. *Energy Stor. Mater.* **2020**, *27*, 522-554.
19. Sun, B.; Xiong, P.; Maitra, U.; Langsdorf, D.; Yan, K.; Wang, C.; Janek, J.; Schroder, D.; Wang, G., Design Strategies to Enable the Efficient Use of Sodium Metal Anodes in High-Energy Batteries. *Adv. Mater.* **2020**, *32* (18), e1903891.
20. Yadegari, H.; Sun, X., Sodium-Oxygen Batteries: Recent Developments and Remaining Challenges. *Trends Chem.* **2020**, *2* (3), 241-253.

21. Bruce, P. G.; Freunberger, S. A.; Hardwick, L. J.; Tarascon, J., Li–O<sub>2</sub> and Li–S batteries with high energy storage. *Nat. Mat.* **2012**, *11* (1), 19-29.
22. Shen, X.; Liu, H.; Cheng, X.-B.; Yan, C.; Huang, J.-Q., Beyond lithium ion batteries: Higher energy density battery systems based on lithium metal anodes. *Energy Storage Materials* **2018**, *12*, 161-175.
23. Liu, T.; Vivek, J. P.; Zhao, E. W.; Lei, J.; Garcia-Araez, N.; Grey, C. P., Current Challenges and Routes Forward for Nonaqueous Lithium–Air Batteries. *Chem. Rev.* **2020**.
24. Landa-Medrano, I.; Li, C.; Ortiz-Vitoriano, N.; Ruiz de Larramendi, I.; Carrasco, J.; Rojo, T., Sodium-Oxygen Battery: Steps Toward Reality. *J. Phys. Chem. Lett.* **2016**, *7* (7), 1161-6.
25. Das, S. K.; Lau, S.; Archer, L. A., Sodium–oxygen batteries: a new class of metal–air batteries. *J. Mater. Chem. A* **2014**, *2* (32), 12623-12629.
26. Bender, C. L.; Schroder, D.; Pinedo, R.; Adelhelm, P.; Janek, J., One- or Two-Electron Transfer? The Ambiguous Nature of the Discharge Products in Sodium-Oxygen Batteries. *Angew. Chem.* **2016**, *55* (15), 4640-9.
27. Lutz, L.; Dachraoui, W.; Demortiere, A.; Johnson, L. R.; Bruce, P. G.; Grimaud, A.; Tarascon, J. M., Operando Monitoring of the Solution-Mediated Discharge and Charge Processes in a Na-O<sub>2</sub> Battery Using Liquid-Electrochemical Transmission Electron Microscopy. *Nano Lett.* **2018**, *18* (2), 1280-1289.
28. Zhao, N.; Guo, X., Cell Chemistry of Sodium–Oxygen Batteries with Various Nonaqueous Electrolytes. *J. Phys. Chem. C* **2015**, *119* (45), 25319-25326.
29. Balaish, M.; Kraysberg, A.; Ein-Eli, Y., A critical review on lithium-air battery electrolytes. *Phys. Chem. Chem. Phys.* **2014**, *16* (7), 2801-22.
30. Johnson, L.; Li, C.; Liu, Z.; Chen, Y.; Freunberger, S. A.; Ashok, P. C.; Praveen, B. B.; Dholakia, K.; Tarascon, J. M.; Bruce, P. G., The role of LiO<sub>2</sub> solubility in O<sub>2</sub> reduction in aprotic solvents and its consequences for Li-O<sub>2</sub> batteries. *Nat. Chem.* **2014**, *6* (12), 1091-9.
31. Aldous, I. M.; Hardwick, L. J., Solvent-Mediated Control of the Electrochemical Discharge Products of Non-Aqueous Sodium-Oxygen Electrochemistry. *Angew. Chem. Int. Ed. Engl.* **2016**, *55* (29), 8254-7.
32. Lutz, L.; Yin, W.; Grimaud, A.; Alves Dalla Corte, D.; Tang, M.; Johnson, L.; Azaceta, E.; Sarou-Kanian, V.; Naylor, A. J.; Hamad, S.; Anta, J. A.; Salager, E.; Tena-Zaera, R.; Bruce, P. G.; Tarascon, J. M., High Capacity Na–O<sub>2</sub> Batteries: Key Parameters for Solution-Mediated Discharge. *J. Phys. Chem. C* **2016**, *120* (36), 20068-20076.
33. Lutz, L.; Alves Dalla Corte, D.; Tang, M.; Salager, E.; Deschamps, M.; Grimaud, A.; Johnson, L.; Bruce, P. G.; Tarascon, J.-M., Role of Electrolyte Anions in the Na–O<sub>2</sub> Battery: Implications for NaO<sub>2</sub> Solvation and the Stability of the Sodium Solid Electrolyte Interphase in Glyme Ethers. *Chem. Mater.* **2017**, *29* (14), 6066-6075.
34. Seh, Z. W.; Sun, J.; Sun, Y.; Cui, Y., A Highly Reversible Room-Temperature Sodium Metal Anode. *ACS Cent. Sci.* **2015**, *1* (8), 449-55.
35. Forsyth, M.; Hilder, M.; Zhang, Y.; Chen, F.; Carre, L.; Rakov, D. A.; Armand, M.; Macfarlane, D. R.; Pozo-Gonzalo, C.; Howlett, P. C., Tuning Sodium

Interfacial Chemistry with Mixed-Anion Ionic Liquid Electrolytes. *ACS Appl. Mater. Interfaces* **2019**, *11* (46), 43093-43106.

36. Doi, K.; Yamada, Y.; Okoshi, M.; Ono, J.; Chou, C. P.; Nakai, H.; Yamada, A., Reversible Sodium Metal Electrodes: Is Fluorine an Essential Interphasial Component? *Angew. Chem. Int. Ed. Engl.* **2019**, *58* (24), 8024-8028.

37. Singh, S. K.; Savoy, A. W., Ionic liquids synthesis and applications: An overview. *J. Mol. Liq.* **2020**, *297*, 112038.

38. Earle, M. J.; Seddon, K. R., Ionic Liquids: Green Solvents for the Future. In *Clean Solvents*, American Chemical Society: 2002; Vol. 819, pp 10-25.

39. Sun, H.; Zhu, G.; Xu, X.; Liao, M.; Li, Y.; Angell, M.; Gu, M.; Zhu, Y.; Hung, W.; Li, J.; Kuang, Y.; Meng, Y.; Lin, M.; Peng, H.; Dai, H., A safe and non-flammable sodium metal battery based on an ionic liquid electrolyte. *Nat. Commun.* **2019**, *10* (1), 3302.

40. Delorme, A.; Sans, V.; Licence, P.; Walsh, D. A., Tuning the Reactivity of TEMPO during Electrocatalytic Alcohol Oxidations in Room-Temperature Ionic Liquids. *ACS Sust. Chem. Eng.* **2019**, *7*.

41. Anderson, J. L.; Clark, K. D., Ionic liquids as tunable materials in (bio)analytical chemistry. *Anal. Bioanal. Chem.* **2018**, *410* (19), 4565-4566.

42. Chen, Z.; Zhang, S., Extraction of Heavy Metal Ions Using Ionic Liquids. In *Encyclopedia of Ionic Liquids*, Zhang, S., Ed. Springer Singapore: Singapore, 2019; pp 1-8.

43. Zhang, Y.; Pozo-Gonzalo, C., Variations and applications of the oxygen reduction reaction in ionic liquids. *Chem. Commun.* **2018**, *54* (31), 3800-3810.

44. Pozo-Gonzalo, C., Oxygen Reduction Reaction in Ionic Liquids: An Overview. In *Electrochemistry in Ionic Liquids: Volume 2: Applications*, Torriero, A. A. J., Ed. Springer International Publishing: Cham, 2015; pp 507-529.

45. Walsh, D. A.; Goodwin, S., The Oxygen Reduction Reaction in Room-Temperature Ionic Liquids. In *Encyclopedia of Interfacial Chemistry*, Wandelt, K., Ed. Elsevier: Oxford, 2018; Vol. 5.2, pp 898-907.

46. Pozo-Gonzalo, C.; Howlett, P. C.; MacFarlane, D. R.; Forsyth, M., Highly reversible oxygen to superoxide redox reaction in a sodium-containing ionic liquid. *Electrochem. Commun.* **2017**, *74*, 14-18.

47. Galiote, N. A.; Jeong, S.; Morais, W. G.; Passerini, S.; Huguenin, F., The Role of Ionic Liquid in Oxygen Reduction Reaction for Lithium-air Batteries. *Electrochim. Acta* **2017**, *247*, 610-616.

48. Monaco, S.; Arangio, A. M.; Soavi, F.; Mastragostino, M.; Paillard, E.; Passerini, S., An electrochemical study of oxygen reduction in pyrrolidinium-based ionic liquids for lithium/oxygen batteries. *Electrochim. Acta* **2012**, *83*, 94-104.

49. Elia, G. A.; Hassoun, J.; Kwak, W. J.; Sun, Y. K.; Scrosati, B.; Mueller, F.; Bresser, D.; Passerini, S.; Oberhumer, P.; Tsiouvaras, N.; Reiter, J., An advanced lithium-air battery exploiting an ionic liquid-based electrolyte. *Nano Lett.* **2014**, *14* (11), 6572-7.

50. De Giorgio, F.; Soavi, F.; Mastragostino, M., Effect of lithium ions on oxygen reduction in ionic liquid-based electrolytes. *Electrochem. Commun.* **2011**, *13*, 3.

51. Soavi, F.; Monaco, S.; Mastragostino, M., Catalyst-free porous carbon cathode and ionic liquid for high efficiency, rechargeable Li/O<sub>2</sub> battery. *J. Power Sources* **2013**, *224*, 115-119.
52. Allen, C. J.; Hwang, J.; Kautz, R.; Mukerjee, S.; Plichta, E. J.; Hendrickson, M. A.; Abraham, K. M., Oxygen Reduction Reactions in Ionic Liquids and the Formulation of a General ORR Mechanism for Li–Air Batteries. *J. Phys. Chem. C* **2012**, *116* (39), 20755-20764.
53. Azaceta, E.; Lutz, L.; Grimaud, A.; Vicent-Luna, J. M.; Hamad, S.; Yate, L.; Cabanero, G.; Grande, H. J.; Anta, J. A.; Tarascon, J. M.; Tena-Zaera, R., Electrochemical Reduction of Oxygen in Aprotic Ionic Liquids Containing Metal Cations: A Case Study on the Na-O<sub>2</sub> system. *ChemSusChem* **2017**, *10* (7), 1616-1623.
54. Pozo-Gonzalo, C.; Johnson, L. R.; Jónsson, E.; Holc, C.; Kerr, R.; MacFarlane, D. R.; Bruce, P. G.; Howlett, P. C.; Forsyth, M., Understanding of the Electrogenerated Bulk Electrolyte Species in Sodium-Containing Ionic Liquid Electrolytes During the Oxygen Reduction Reaction. *J. Phys. Chem. C* **2017**, *121* (42), 23307-23316.
55. Zhang, Y.; Ortiz-Vitoriano, N.; Acebedo, B.; O’Dell, L.; MacFarlane, D. R.; Rojo, T.; Forsyth, M.; Howlett, P. C.; Pozo-Gonzalo, C., Elucidating the Impact of Sodium Salt Concentration on the Cathode–Electrolyte Interface of Na–Air Batteries. *J. Phys. Chem. C* **2018**, *122* (27), 15276-15286.
56. Rakov, D. A.; Chen, F.; Ferdousi, S. A.; Li, H.; Pathirana, T.; Simonov, A. N.; Howlett, P. C.; Atkin, R.; Forsyth, M., Engineering high-energy-density sodium battery anodes for improved cycling with superconcentrated ionic-liquid electrolytes. *Nat. Mater.* **2020**.
57. Hosokawa, T.; Matsumoto, K.; Nohira, T.; Hagiwara, R.; Fukunaga, A.; Sakai, S.; Nitta, K., Stability of Ionic Liquids against Sodium Metal: A Comparative Study of 1-Ethyl-3-methylimidazolium Ionic Liquids with Bis(fluorosulfonyl)amide and Bis(trifluoromethylsulfonyl)amide. *J. Phys. Chem. C* **2016**, *120* (18), 9628-9636.
58. Noviandri, I.; Brown, K. N.; Fleming, D. S.; Gulyas, P. T.; Lay, P. A.; Masters, A. F.; Phillips, L., The Decamethylferrocenium/Decamethylferrocene Redox Couple: A Superior Redox Standard to the Ferrocenium/Ferrocene Redox Couple for Studying Solvent Effects on the Thermodynamics of Electron Transfer. *J. Phys. Chem. B* **1999**, *103* (32), 6713-6722.
59. Compton, R. G.; Craig, E. B., Hydrodynamic Electrodes. In *Understanding Voltammetry*, World Scientific: 2010; pp 291-346.
60. Berg, H., The electrochemical cell. In *Batteries for Electric Vehicles: Materials and Electrochemistry*, Berg, H., Ed. Cambridge University Press: Cambridge, 2015; pp 7-46.
61. Passarelli, M. K.; Pirkl, A.; Moellers, R.; Grinfeld, D.; Kollmer, F.; Havelund, R.; Newman, C. F.; Marshall, P. S.; Arlinghaus, H.; Alexander, M. R.; West, A.; Horning, S.; Niehuis, E.; Makarov, A.; Dollery, C. T.; Gilmore, I. S., The 3D OrbiSIMS—label-free metabolic imaging with subcellular lateral resolution and high mass-resolving power. *Nat. Methods* **2017**, *14* (12), 1175-1183.
62. Zubarev, R. A.; Makarov, A., Orbitrap mass spectrometry. *Anal. Chem.* **2013**, *85* (11), 5288-96.

63. Graham, D. J.; Castner, D. G., Multivariate analysis of ToF-SIMS data from multicomponent systems: the why, when, and how. *Biointerphases* **2012**, *7* (1-4), 49.
64. de Juan, A.; Jaumot, J.; Tauler, R., Multivariate Curve Resolution (MCR). Solving the mixture analysis problem. *Anal. Methods* **2014**, *6* (14), 4964-4976.
65. Abbott, A. P., Application of hole theory to the viscosity of ionic and molecular liquids. *Chemphyschem* **2004**, *5* (8), 1242-1246.
66. Schmeisser, M.; P., I.; Puchta, R.; Zahl, A.; van Eldik, R., Gutmann donor and acceptor numbers for ionic liquids. *Chem. - Eur. J.* **2012**, *18*, 10969-10982.
67. Blundell, R. K.; Licence, P., Quaternary ammonium and phosphonium based ionic liquids: a comparison of common anions. *Phys Chem Chem Phys* **2014**, *16* (29), 15278-88.
68. Dinarès, I.; Garcia de Miguel, C.; Ibáñez, A.; Mesquida, N.; Alcalde, E., Imidazolium ionic liquids: A simple anion exchange protocol. *Green Chemistry* **2009**, *11* (10), 1507.
69. Moreno, M.; Montanino, M.; Carewska, M.; Appetecchi, G. B.; Jeremias, S.; Passerini, S., Water-soluble, triflate-based, pyrrolidinium ionic liquids. *Electrochimica Acta* **2013**, *99*, 108-116.
70. Schmidt, O.; Hawkes, A.; Gambhir, A.; Staffell, I., The future cost of electrical energy storage based on experience rates. *Nat. Energy* **2017**, *2* (8), 17110.
71. Zhao, H.; Deng, N.; Yan, J.; Kang, W.; Ju, J.; Ruan, Y.; Wang, X.; Zhuang, X.; Li, Q.; Cheng, B., A review on anode for lithium-sulfur batteries: Progress and prospects. *Chem. Eng. J. (Amsterdam, Neth.)* **2018**, *347*, 343-365.
72. Wang, Y. R.; Chen, R. P.; Chen, T.; Lv, H. L.; Zhu, G. Y.; Ma, L. B.; Wang, C. X.; Jin, Z.; Liu, J., Emerging non-lithium ion batteries. *Energy Stor. Mater.* **2016**, *4*, 103-129.
73. Yabuuchi, N.; Kubota, K.; Dahbi, M.; Komaba, S., Research Development on Sodium-Ion Batteries. *Chem. Rev.* **2014**, *114* (23), 11636-11682.
74. Palomares, V.; Serras, P.; Villaluenga, I.; Hueso, K. B.; Carretero-González, J.; Rojo, T., Na-ion batteries, recent advances and present challenges to become low cost energy storage systems. *Energy Environ. Sci.* **2012**, *5* (3), 5884-5901.
75. Cheng, X. B.; Zhang, R.; Zhao, C. Z.; Wei, F.; Zhang, J. G.; Zhang, Q., A Review of Solid Electrolyte Interphases on Lithium Metal Anode. *Adv. Sci. (Weinheim, Ger.)* **2016**, *3* (3), 1500213.
76. Goodenough, J. B.; Kim, Y., Challenges for Rechargeable Li Batteries. *Chem. Mater.* **2010**, *22* (3), 587-603.
77. Wang, A.; Kadam, S.; Li, H.; Shi, S.; Qi, Y., Review on modeling of the anode solid electrolyte interphase (SEI) for lithium-ion batteries. *npj Comput. Mater.* **2018**, *4* (1).
78. Markevich, E.; Salitra, G.; Chesneau, F.; Schmidt, M.; Aurbach, D., Very Stable Lithium Metal Stripping–Plating at a High Rate and High Areal Capacity in Fluoroethylene Carbonate-Based Organic Electrolyte Solution. *ACS Energy Lett.* **2017**, *2* (6), 1321-1326.
79. Brown, Z. L.; Jurng, S.; Nguyen, C. C.; Lucht, B. L., Effect of Fluoroethylene Carbonate Electrolytes on the Nanostructure of the Solid

Electrolyte Interphase and Performance of Lithium Metal Anodes. *ACS Appl. Energy Mater.* **2018**, *1* (7), 3057-3062.

80. Iermakova, D. I.; Dugas, R.; Palacín, M. R.; Ponrouch, A., On the Comparative Stability of Li and Na Metal Anode Interfaces in Conventional Alkyl Carbonate Electrolytes. *J. Electrochem. Soc.* **2015**, *162* (13), A7060-A7066.

81. Wang, H.; Wang, C.; Matios, E.; Li, W., Facile Stabilization of the Sodium Metal Anode with Additives: Unexpected Key Role of Sodium Polysulfide and Adverse Effect of Sodium Nitrate. *Angew. Chem., Int. Ed. Engl.* **2018**, *57* (26), 7734-7737.

82. Yu, J.; Gao, N.; Peng, J.; Ma, N.; Liu, X.; Shen, C.; Xie, K.; Fang, Z., Concentrated LiODFB Electrolyte for Lithium Metal Batteries. *Front. Chem.* **2019**, *7* (494).

83. Schafzahl, L.; Ehmman, H.; Kriechbaum, M.; Sattelkow, J.; Ganner, T.; Plank, H.; Wilkening, M.; Freunberger, S. A., Long-Chain Li and Na Alkyl Carbonates as Solid Electrolyte Interphase Components: Structure, Ion Transport, and Mechanical Properties. *Chem. Mater.* **2018**, *30* (10), 3338-3345.

84. Wang, H.; Liu, Y.; Li, Y.; Cui, Y., Lithium Metal Anode Materials Design: Interphase and Host. *Electrochem. Energy Rev.* **2019**, *2* (4), 509-517.

85. Aurbach, D.; Pollak, E.; Elazari, R.; Salitra, G.; Kelley, C. S.; Affinito, J., On the Surface Chemical Aspects of Very High Energy Density, Rechargeable Li-Sulfur Batteries. *J. Electrochem. Soc.* **2009**, *156* (8), A694.

86. Fiedler, C.; Luerssen, B.; Rohnke, M.; Sann, J.; Janek, J., XPS and SIMS Analysis of Solid Electrolyte Interphases on Lithium Formed by Ether-Based Electrolytes. *J. Electrochem. Soc.* **2017**, *164* (14), A3742-A3749.

87. Jankowski, P.; Wieczorek, W.; Johansson, P., Functional ionic liquids: Cationic SEI-formers for lithium batteries. *Energy Stor. Mater.* **2019**, *20*, 108-117.

88. Watanabe, M.; Thomas, M. L.; Zhang, S.; Ueno, K.; Yasuda, T.; Dokko, K., Application of Ionic Liquids to Energy Storage and Conversion Materials and Devices. *Chem. Rev.* **2017**.

89. Zhang, J.; Brown, J.; Scurr, D. J.; Bullen, A.; MacLellan-Gibson, K.; Williams, P.; Alexander, M. R.; Hardie, K. R.; Gilmore, I. S.; Rakowska, P. D., Cryo-OrbiSIMS for 3D Molecular Imaging of a Bacterial Biofilm in Its Native State. *Anal. Chem.* **2020**, *92* (13), 9008-9015.

90. De Vos, N.; Maton, C.; Stevens, C. V., Electrochemical Stability of Ionic Liquids: General Influences and Degradation Mechanisms. *ChemElectroChem* **2014**, *1* (8), 1258-1270.

91. Clayden, J.; Greeves, N.; Warren, S., Sulfur, silicon, and phosphorous in organic chemistry. In *Organic Chemistry*, Oxford University Press Inc. : New York, 2001.

92. Clayden, J.; Greeves, N.; Warren, S., Radical Reactions. In *Organic Chemistry*, Oxford University Press Inc. : New York, 2001.

93. Trindade, G. F.; Abel, M.-L.; Watts, J. F., simsMVA: A tool for multivariate analysis of ToF-SIMS datasets. *Chemom. Intell. Lab. Syst.* **2018**, *182*, 180-187.

94. Fröba, A. P.; Kremer, H.; Leipertz, A., Density, Refractive Index, Interfacial Tension, and Viscosity of Ionic Liquids [EMIM][EtSO<sub>4</sub>], [EMIM][NTf<sub>2</sub>],

- [EMIM][N(CN)<sub>2</sub>], and [OMA][NTf<sub>2</sub>] in Dependence on Temperature at Atmospheric Pressure. *J. Phys. Chem. B* **2008**, *112* (39), 12420-12430.
95. Rinaldi, A.; Wang, Y.; Tan, K. S.; Wijaya, O.; Yazami, R., Lithium-air batteries for medium- and large-scale energy storage. In *Advances in Batteries for Medium and Large-Scale Energy Storage*, Menictas, C.; Skyllas-Kazacos, M.; Lim, T. M., Eds. Woodhead Publishing: 2015; pp 387-440.
96. Zhang, S.; Qi, X.; Ma, X.; Lu, L.; Deng, Y., Hydroxyl Ionic Liquids: The Differentiating Effect of Hydroxyl on Polarity due to Ionic Hydrogen Bonds between Hydroxyl and Anions. *J. Phys. Chem. B* **2010**, *114* (11), 3912-3920.
97. Isik, M.; Sardon, H.; Mecerreyes, D., Ionic Liquids and Cellulose: Dissolution, Chemical Modification and Preparation of New Cellulosic Materials. *Int. J. Mol. Sci.* **2014**, *15*, 11922-11940.
98. Richard G Compton, C. E. B., Diffusion. In *Understanding Voltammetry*, WORLD SCIENTIFIC: 2007; pp 77-106.
99. Richard G Compton, C. E. B., Cyclic Voltammetry at Macroelectrodes. In *Understanding Voltammetry*, WORLD SCIENTIFIC: 2007; pp 107-151.
100. Rosol, Z. P.; German, N. J.; Gross, S. M., Solubility, ionic conductivity and viscosity of lithium salts in room temperature ionic liquids. *Green Chem.* **2009**, *11* (9).
101. Tong, J.; Wu, S.; von Solms, N.; Liang, X.; Huo, F.; Zhou, Q.; He, H.; Zhang, S., The Effect of Concentration of Lithium Salt on the Structural and Transport Properties of Ionic Liquid-Based Electrolytes. *Front. Chem.* **2019**, *7*, 945.
102. Bonhôte, P.; Dias, A.-P.; Papageorgiou, N.; Kalyanasundaram, K.; Grätzel, M., Hydrophobic, Highly Conductive Ambient-Temperature Molten Salts. *Inor. Chem.* **1996**, *35* (5), 1168-1178.
103. Berg, H., Battery usage and degradation. In *Batteries for Electric Vehicles: Materials and Electrochemistry*, Berg, H., Ed. Cambridge University Press: Cambridge, 2015; pp 194-229.
104. Zheng, J.; Gu, M.; Chen, H.; Meduri, P.; Engelhard, M. H.; Zhang, J.-G.; Liu, J.; Xiao, J., Ionic liquid-enhanced solid state electrolyte interface (SEI) for lithium-sulfur batteries. *J. Mater. Chem. A* **2013**, *1* (29).
105. Bieker, G.; Winter, M.; Bieker, P., Electrochemical in situ investigations of SEI and dendrite formation on the lithium metal anode. *Phys. Chem. Chem. Phys.* **2015**, *17* (14), 8670-9.
106. Matsumoto, K.; Hwang, J.; Kaushik, S.; Chen, C.; Hagiwara, R., Advances in sodium secondary batteries utilizing ionic liquid electrolytes. *Energy Environ. Sci.* **2019**, *12* (11), 3247-3287.
107. Kanamura, K.; Tamura, H.; Takehara, Z.-i., XPS analysis of a lithium surface immersed in propylene carbonate solution containing various salts. *J. Electroanal. Chem.* **1992**, *333* (1), 127-142.
108. Bessette, S.; Hovington, P.; Demers, H.; Golozar, M.; Bouchard, P.; Gauvin, R.; Zaghbi, K., In-Situ Characterization of Lithium Native Passivation Layer in A High Vacuum Scanning Electron Microscope. *Microsc. Microanal.* **2019**, *25* (4), 866-873.

109. Clough, M. T.; Geyer, K.; Hunt, P. A.; Mertes, J.; Welton, T., Thermal decomposition of carboxylate ionic liquids: trends and mechanisms. *Phys. Chem. Chem. Phys.* **2013**, *15* (47), 20480-95.
110. Prasad, M. R. R.; Krishnan, K.; Ninan, K. N.; Krishnamurthy, V. N., Thermal decomposition of tetraalkyl ammonium tetrafluoroborates. *Thermochim. Acta* **1997**, *297* (1), 207-210.
111. Steinruck, H. P., Recent developments in the study of ionic liquid interfaces using X-ray photoelectron spectroscopy and potential future directions. *Phys. Chem. Chem. Phys.* **2012**, *14* (15), 5010-29.
112. Zhou, Z. B.; Matsumoto, H.; Tatsumi, K., Cyclic quaternary ammonium ionic liquids with perfluoroalkyltrifluoroborates: synthesis, characterization, and properties. *Chem. - Eur. J.* **2006**, *12* (8), 2196-212.
113. Girard, G. M. A.; Hilder, M.; Dupre, N.; Guyomard, D.; Nucciarone, D.; Whitbread, K.; Zavorine, S.; Moser, M.; Forsyth, M.; MacFarlane, D. R.; Howlett, P. C., Spectroscopic Characterization of the SEI Layer Formed on Lithium Metal Electrodes in Phosphonium Bis(fluorosulfonyl)imide Ionic Liquid Electrolytes. *ACS Applied Materials & Interfaces* **2018**, *10* (7), 6719-6729.
114. Freire, M. G.; Neves, C. M. S. S.; Marrucho, I. M.; Coutinho, J. A. P.; Fernandes, A. M., Hydrolysis of Tetrafluoroborate and Hexafluorophosphate Counter Ions in Imidazolium-Based Ionic Liquids. *J. Phys. Chem. A* **2010**, *114* (11), 3744-3749.
115. Wang, B.; Qin, L.; Mu, T.; Xue, Z.; Gao, G., Are Ionic Liquids Chemically Stable? *Chem. Rev.* **2017**, *117* (10), 7113-7131.
116. Wu, F.; Maier, J.; Yu, Y., Guidelines and trends for next-generation rechargeable lithium and lithium-ion batteries. *Chem. Soc. Rev.* **2020**, *49* (5), 1569-1614.
117. Kong, L.; Xing, Y.; Pecht, M. G., *In-Situ* Observations of Lithium Dendrite Growth. *IEEE Access* **2018**, *6*, 8387-8393.
118. Siraki, A. G.; Klotz, L. O.; Kehler, J. P., Free Radicals and Reactive Oxygen Species. In *Comprehensive Toxicology*, McQueen, C. A., Ed. Elsevier: Oxford, 2018; Vol. 1, pp 262-294.
119. Hayyan, M.; Hashim, M. A.; AlNashef, I. M., Superoxide Ion: Generation and Chemical Implications. *Chem. Rev.* **2016**, *116* (5), 3029-3085.
120. Hayyan, M.; Mjalli, F. S.; Hashim, M. A.; AlNashef, I. M., Generation of Superoxide Ion in Pyridinium, Morpholinium, Ammonium, and Sulfonium-Based Ionic Liquids and the Application in the Destruction of Toxic Chlorinated Phenols. *Ind. Eng. Chem. Res.* **2012**, *51* (32), 10546-10556.
121. Han, X.; Wang, K.; Zhang, G.; Gao, W.; Chen, J., Application of the Electrochemical Oxygen Reduction Reaction (ORR) in Organic Synthesis. *Adv. Synth. Catal.* **2019**, *361* (12), 2804-2824.
122. Khan, A.; Gunawan, C. A.; Zhao, C. Z., Oxygen Reduction Reaction in Ionic Liquids: Fundamentals and Applications in Energy and Sensors. *ACS Sustainable Chem. Eng.* **2017**, *5* (5), 3698-3715.
123. Xiong, L.; Compton, R. G., Amperometric Gas detection: A Review. *Int. J. Electrochem. Sci.* **2014**, *9* (12), 7152-7181.

124. Xu, W.; Xiao, J.; Zhang, J.; Wang, D.; Zhang, J. G., Optimization of Nonaqueous Electrolytes for Primary Lithium/Air Batteries Operated in Ambient Environment. *J. Electrochem. Soc.* **2009**, *156* (10), A773.
125. Piana, M.; Wandt, J.; Meini, S.; Buchberger, I.; Tsiouvaras, N.; Gasteiger, H. A., Stability of a Pyrrolidinium-Based Ionic Liquid in Li-O<sub>2</sub> Cells. *J. Electrochem. Soc.* **2014**, *161* (14), A1992-A2001.
126. Das, S.; Højberg, J.; Knudsen, K. B.; Younesi, R.; Johansson, P.; Norby, P.; Vegge, T., Instability of Ionic Liquid-Based Electrolytes in Li-O<sub>2</sub> Batteries. *J. Phys. Chem. A* **2015**, *119* (32), 18084-18090.
127. Katayama, Y.; Onodera, H.; Yamagata, M.; Miura, T., Electrochemical Reduction of Oxygen in Some Hydrophobic Room-Temperature Molten Salt Systems. *Journal of The Electrochemical Society* **2004**, *151* (1), A59-A63.
128. Neale, A. R.; Li, P.; Jacquemin, J.; Goodrich, P.; Ball, S. C.; Compton, R. G.; Hardacre, C., Effect of cation structure on the oxygen solubility and diffusivity in a range of bis{(trifluoromethyl)sulfonyl}imide anion based ionic liquids for lithium-air battery electrolytes. *Phys. Chem. Chem. Phys.* **2016**, *18* (16), 11251-11262.
129. Frith, J. T.; Russell, A. E.; Garcia-Araez, N.; Owen, J. R., An in-situ Raman study of the oxygen reduction reaction in ionic liquids. *Electrochem. Commun.* **2014**, *46*, 33-35.
130. Watanabe, M.; Thomas, M. L.; Zhang, S.; Ueno, K.; Yasuda, T.; Dokko, K., Application of Ionic Liquids to Energy Storage and Conversion Materials and Devices. *Chem. Rev.* **2017**, *117* (10), 7190-7239.
131. Rogers, E. I.; Huang, X. J.; Dickinson, E. J. F.; Hardacre, C.; Compton, R. G., Investigating the Mechanism and Electrode Kinetics of the Oxygen|Superoxide (O<sub>2</sub>|O<sub>2</sub>•<sup>-</sup>) Couple in Various Room-Temperature Ionic Liquids at Gold and Platinum Electrodes in the Temperature Range 298–318 K. *J. Phys. Chem. C* **2009**, *113* (41), 17811-17823.
132. Compton, R. G.; Banks, C. E., Cyclic Voltammetry at Macroelectrodes. In *Understanding Voltammetry*, World Scientific London, 2007; pp 107-151.
133. Katayama, Y.; Sekiguchi, K.; Yamagata, M.; Miura, T., Electrochemical Behavior of Oxygen/Superoxide Ion Couple in 1-Butyl-1-methylpyrrolidinium Bis(trifluoromethylsulfonyl)imide Room-Temperature Molten Salt. *J. Electrochem. Soc.* **2005**, *152* (8), E247-E250.
134. Sanford, A. L.; Morton, S. W.; Whitehouse, K. L.; Oara, H. M.; Lugo-Morales, L. Z.; Roberts, J. G.; Sombers, L. A., Voltammetric Detection of Hydrogen Peroxide at Carbon Fiber Microelectrodes. *Anal. Chem.* **2010**, *82* (12), 5205-5210.
135. Roberts, J. G.; Voinov, M. A.; Schmidt, A. C.; Smirnova, T. I.; Sombers, L. A., The Hydroxyl Radical is a Critical Intermediate in the Voltammetric Detection of Hydrogen Peroxide. *J. Am. Chem. Soc.* **2016**, *138* (8), 2516-2519.
136. Bard, A. J.; Faulkner, L. R., Basic Potential Step Methods. In *Electrochemical methods: fundamentals and applications*, 2nd ed.; Wiley: New York, 2001; pp 156-226.
137. Compton, R. G.; Craig, E. B., Voltammetry at Microelectrodes. In *Understanding Voltammetry*, World Scientific: London, 2010; pp 163-201.

138. Smith, D. E.; Walsh, D. A., The Nature of Proton Shuttling in Protic Ionic Liquid Fuel Cells. *Adv. Energy Mater.* **2019**, *9* (24), 1900744.
139. Evans, R. G.; Klymenko, O. V.; Saddoughi, S. A.; Hardacre, C.; Compton, R. G., Electroreduction of Oxygen in a Series of Room Temperature Ionic Liquids Composed of Group 15-Centered Cations and Anions. *J. Phys. Chem. B* **2004**, *108* (23), 7878-7886.
140. Huang, X. J.; Rogers E. F; Hardacre, C.; Compton, R. G., The reduction of oxygen in various room temperature ionic liquids in the temperature range 293-318 K: exploring the applicability of the Stokes-Einstein relationship in room temperature ionic liquids. *J. Phys. Chem. B* **2009**, *113*, 8953-8959.
141. Taylor, A. W.; Licence, P.; Abbott, A. P., Non-classical diffusion in ionic liquids. *Phys. Chem. Chem. Phys.* **2011**, *13* (21), 10147-10154.
142. Abbott, A. P.; Harris, R. C.; Ryder, K. S., Application of Hole Theory to Define Ionic Liquids by their Transport Properties. *J. Phys. Chem. B* **2007**, *111* (18), 4910-4913.
143. D'Agostino, C., Hole theory as a prediction tool for Brownian diffusive motion in binary mixtures of liquids. *RSC Adv.* **2017**, *7* (82), 51864-51869.
144. Simha, R.; Carri, G., Free volume, hole theory and thermal properties. *J. Polym. Sci. B Polym. Phys.* **1994**, *32* (16), 2645-2651.
145. Shannon, M. S.; Tedstone, J. M.; Danielsen, S. P. O.; Hindman, M. S.; Irvin, A. C.; Bara, J. E., Free Volume as the Basis of Gas Solubility and Selectivity in Imidazolium-Based Ionic Liquids. *Ind. Eng. Chem. Res.* **2012**, *51* (15), 5565-5576.
146. Walsh, D. A.; Ejigu, A.; Smith, J.; Licence, P., Kinetics and mechanism of oxygen reduction in a protic ionic liquid. *Phys. Chem. Chem. Phys.* **2013**, *15* (20), 7548-54.
147. Fang, Y. H.; Liu, Z. P., Tafel Kinetics of Electrocatalytic Reactions: From Experiment to First-Principles. *ACS Catalysis* **2014**, *4* (12), 4364-4376.
148. Holewinski, A.; Linic, S., Elementary Mechanisms in Electrocatalysis: Revisiting the ORR Tafel Slope. *J. Electrochem. Soc.* **2012**, *159* (11), H864-H870.
149. Pozo-Gonzalo, C.; Howlett, P. C.; Hodgson, J. L.; Madsen, L. A.; MacFarlane, D. R.; Forsyth, M., Insights into the reversible oxygen reduction reaction in a series of phosphonium-based ionic liquids. *Phys. Chem. Chem. Phys.* **2014**, *16* (45), 25062-70.
150. Zhang, J.; Zhou, Q.; Tang, Y.; Zhang, L.; Li, Y., Zinc-air batteries: are they ready for prime time? *Chem. Sci.* **2019**, *10* (39), 8924-8929.
151. Qin, L.; Schkeryantz, L.; Zheng, J.; Xiao, N.; Wu, Y., Superoxide-Based K-O<sub>2</sub> Batteries: Highly Reversible Oxygen Redox Solves Challenges in Air Electrodes. *J. Am. Chem. Soc.* **2020**, *142* (27), 11629-11640.
152. Li, C.; Sun, Y.; Gebert, F.; Chou, S.-L., Current Progress on Rechargeable Magnesium-Air Battery. *Adv. Energy Mater.* **2017**, *7* (24), 1700869.
153. McCloskey, B. D.; Scheffler, R.; Speidel, A.; Girishkumar, G.; Luntz, A. C., On the Mechanism of Nonaqueous Li-O<sub>2</sub> Electrochemistry on C and Its Kinetic Overpotentials: Some Implications for Li-Air Batteries. *J. Phys. Chem. C* **2012**, *116* (45), 23897-23905.

154. McCloskey, B. D.; Garcia, J. M.; Luntz, A. C., Chemical and Electrochemical Differences in Nonaqueous Li-O<sub>2</sub> and Na-O<sub>2</sub> Batteries. *J. Phys. Chem. Lett.* **2014**, *5* (7), 1230-5.
155. Mekonnen, Y. S.; Christensen, R.; Garcia-Lastra, J. M.; Vegge, T., Thermodynamic and Kinetic Limitations for Peroxide and Superoxide Formation in Na-O<sub>2</sub> Batteries. *J. Phys. Chem. Lett.* **2018**, *9* (15), 4413-4419.
156. Kwak, W. J.; Rosy, Sharon, D.; Xia, C.; Kim, H.; Johnson, L. R.; Bruce, P. G.; Nazar, L. F.; Sun, Y.; Frimer, A. A.; Noked, M.; Freunberger, S. A.; Aurbach, D., Lithium–Oxygen Batteries and Related Systems: Potential, Status, and Future. *Chem. Rev.* **2020**.
157. Cecchetto, L.; Tesio, A. Y.; Olivares-Marín, M.; Espinasa, M. G.; Croce, F.; Tonti, D., Tailoring oxygen redox reactions in ionic liquid based Li/O<sub>2</sub> batteries by means of the Li<sup>+</sup> dopant concentration. *Sustainable Energy Fuels* **2018**, *2* (1), 118-124.
158. Zhang, T.; Wen, Z., A High-Rate Ionic Liquid Lithium-O<sub>2</sub> Battery with LiOH Product. *J. Phys. Chem. C* **2017**, *121* (11), 5968-5973.
159. Olivares-Marín, M.; Sorrentino, A.; Pereiro, E.; Tonti, D., Discharge products of ionic liquid-based Li-O<sub>2</sub> batteries observed by energy dependent soft x-ray transmission microscopy. *J. Power Sources* **2017**, *359*, 234-241.
160. Ha, T. A.; Fdz De Anastro, A.; Ortiz-Vitoriano, N.; Fang, J.; MacFarlane, D. R.; Forsyth, M.; Mecerreyes, D.; Howlett, P. C.; Pozo-Gonzalo, C., High Coulombic Efficiency Na-O<sub>2</sub> Batteries Enabled by a Bilayer Ionogel/Ionic Liquid. *J. Phys. Chem. Lett.* **2019**, *10* (22), 7050-7055.
161. Ha, T. A.; Pozo-Gonzalo, C.; Nairn, K.; MacFarlane, D. R.; Forsyth, M.; Howlett, P. C., An investigation of commercial carbon air cathode structure in ionic liquid based sodium oxygen batteries. *Sci. Rep.* **2020**, *10* (1), 7123.
162. Gao, X.; Chen, Y.; Johnson, L.; Bruce, P. G., Promoting solution phase discharge in Li-O<sub>2</sub> batteries containing weakly solvating electrolyte solutions. *Nat. Mater.* **2016**, *15* (8), 882-8.
163. Xia, C.; Black, R.; Fernandes, R.; Adams, B.; Nazar, L. F., The critical role of phase-transfer catalysis in aprotic sodium oxygen batteries. *Nat. Chem.* **2015**, *7* (6), 496-501.
164. Peng, Z.; Freunberger, S. A.; Hardwick, L. J.; Chen, Y.; Giordani, V.; Bardé, F.; Novák, P.; Graham, D. J.; Tarascon, J. M.; Bruce, P. G., Oxygen Reactions in a Non-Aqueous Li<sup>+</sup> Electrolyte. *Angew. Chem., Int. Ed. Engl.* **2011**, *50* (28), 6351-6355.
165. Laroche, C. O.; Mukerjee, S.; Abraham, K. M.; Plichta, E. J.; Hendrickson, M. A., Influence of Nonaqueous Solvents on the Electrochemistry of Oxygen in the Rechargeable Lithium–Air Battery. *J. Phys. Chem. C* **2010**, *114* (19), 9178-9186.
166. Chen, Z. J.; Xue, T.; Lee, J., What causes the low viscosity of ether-functionalized ionic liquids? Its dependence on the increase of free volume. *RSC Advances* **2012**, *2* (28).
167. Li, H.; Ibrahim, M.; Agberemi, I.; Kobrak, M. N., The relationship between ionic structure and viscosity in room-temperature ionic liquids. *J. Chem. Phys.* **2008**, *129* (12), 124507.

## Appendices

168. Vanhoutte, G.; Hojniak, S. D.; Bardé, F.; Binnemans, K.; Fransaer, J., Fluorine-functionalized ionic liquids with high oxygen solubility. *RSC Adv.* **2018**, *8* (9), 4525-4530.